

AD-A101 064

STANFORD UNIV CALIF DEPT OF PHYSICS

I. SPIN-LATTICE RELAXATION OF DILUTE SOLUTIONS OF POLARIZED HE3--ETC(U)

AUG 78 M A TABER

F/G 14/2

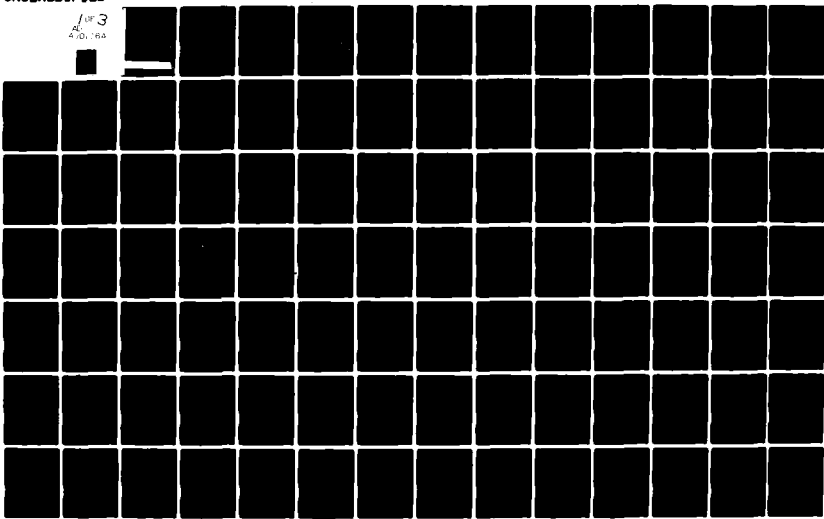
F44620-75-C-0022

NL

AFOSR-TR-81-0522

UNCLASSIFIED

1 of 3  
4/10/84



AFOSR TR. 81-0522

AD A101064

LEVEL

(P)

- I. SPIN-LATTICE RELAXATION OF DILUTE SOLUTIONS OF POLARIZED  $\text{He}^3$  IN LIQUID  $\text{He}^4$  IN LOW MAGNETIC FIELDS AT 4 K.
- II. AN ANALYSIS OF A PROPOSED CRYOGENIC  $\text{He}^3$  NUCLEAR GYROSCOPE AND ITS APPLICATION TO A NUCLEAR ELECTRIC-DIPOLE MOMENT EXPERIMENT.

FILE COPY

by  
Michael A. Taber

DTIC  
SELECTED  
JUL 7 1987  
S D C

Approved for public release;  
distribution unlimited.



LOW TEMPERATURE PHYSICS GROUP  
Department of PHYSICS  
STANFORD UNIVERSITY

Supported by the Air Force Office of Scientific Research  
under Contract F44620-75-C-0022, and Grant F49620-78-C-0088

81 7 06 017

## UNCLASSIFIED

SECURITY CLASSIFICATION OF THIS PAGE (When Data Entered)

REPORT DOCUMENTATION PAGE		READ INSTRUCTIONS BEFORE COMPLETING FORM
1. REPORT NUMBER <b>AFOSR-TR- 81 -0522</b>	2. GOVT ACCESSION NO. <b>AD-A101 064</b>	3. RECIPIENT'S CATALOG NUMBER
4. TITLE (and Subtitle) I. SPIN-LATTICE RELAXATION OF DILUTE SOLUTIONS OF POLARIZED He <sup>3</sup> IN LIQUID He <sup>4</sup> IN LOW MAGNETIC FIELDS AT 4 K. II. AN ANALYSIS OF A PROPOSED CRYOGENIC He <sup>3</sup> NUCLEAR GYROSCOPE AND ITS APPLICATION TO A NUCLEAR	5. TYPE OF REPORT & PERIOD COVERED	
7. AUTHOR(s) <b>ÉLECTRIC-DIPOLE MOMENT EXPERIMENT</b>  Michael A Taber	6. PERFORMING ORG. REPORT NUMBER	
9. PERFORMING ORGANIZATION NAME AND ADDRESS Department of Physics Stanford University Stanford, CA 94305	8. CONTRACT OR GRANT NUMBER(s) <b>F44620-75-C-0022</b>	
11. CONTROLLING OFFICE NAME AND ADDRESS AFOSR/NP Bolling AFB Wash DC 20332	10. PROGRAM ELEMENT, PROJECT, TASK AREA & WORK UNIT NUMBERS <b>61102F 2301/A5</b>	
14. MONITORING AGENCY NAME & ADDRESS (if different from Controlling Office)	12. REPORT DATE <b>AUG 1978</b>	
	13. NUMBER OF PAGES <b>234</b>	
16. DISTRIBUTION STATEMENT (of this Report)  <b>Approved for public release; distribution unlimited.</b>	15. SECURITY CLASS. (of this report) <b>unclassified</b>	
17. DISTRIBUTION STATEMENT (of the abstract entered in Block 20, if different from Report)	15a. DECLASSIFICATION/DOWNGRADING SCHEDULE	
18. SUPPLEMENTARY NOTES		
19. KEY WORDS (Continue on reverse side if necessary and identify by block number)		
20. ABSTRACT (Continue on reverse side if necessary and identify by block number)  Measurements were made of the spin-lattice nuclear relaxation time of 0.07% solutions of polarized helium-3 in liquid helium-4 at 4 K by use of an rf-biased SQUID (Superconducting Quantum Interference Device) magnetometer in magnetic fields ranging between 30 microGauss and 3 milliGauss. After the effect of magnetic-gradient-induced relaxation was subtracted by extrapolation to large magnetic fields, it was found that the relaxation time was 40 hours in a 1 cm-diameter Pyrex cell. When the sample cell was pre-filled with an		

UNCLASSIFIED

SECURITY CLASSIFICATION OF THIS PAGE(When Data Entered)

amount of hydrogen estimated to be equivalent to uniform wall coating of 30 molecular layers thickness, the extrapolated relaxation time increased to 5 days. It is estimated that this result was dominated by intrinsic relaxation due to helium-3 dipole-dipole interactions in the bulk of the sample. As a potential application, the performance of a proposed cryogenic nuclear gyroscope utilizing a helium-4 — polarized helium-3 gas mixture with SQUID magnetometer readout in zero magnetic field is theoretically analyzed. The possibility of using a modified version of this device based on a polarized helium-3 — superfluid helium-4 mixture for the purpose of an experimental search for an electri-dipole moment in the helium-3 nucleus is also discussed.

UNCLASSIFIED

SECURITY CLASSIFICATION OF THIS PAGE(When Data Entered)

I. SPIN-LATTICE RELAXATION OF DILUTE SOLUTIONS OF POLARIZED  $\text{He}^3$   
IN LIQUID  $\text{He}^4$  IN LOW MAGNETIC FIELDS AT 4 K.

II. AN ANALYSIS OF A PROPOSED CRYOGENIC  $\text{He}^3$  NUCLEAR GYROSCOPE AND  
ITS APPLICATION TO A NUCLEAR ELECTRIC-DIPOLE MOMENT EXPERIMENT.

A DISSERTATION  
SUBMITTED TO THE DEPARTMENT OF PHYSICS  
AND THE COMMITTEE ON GRADUATE STUDIES  
OF STANFORD UNIVERSITY  
IN PARTIAL FULFILLMENT OF THE REQUIREMENTS  
FOR THE DEGREE OF  
DOCTOR OF PHILOSOPHY

by

Michael A. Taber



AIR FORCE OFFICE OF SCIENTIFIC RESEARCH (AFSC)  
NOTICE OF TRANSMITTAL TO DDC  
This technical report has been reviewed and is  
approved for public release IAW AFR 190-12 (7b).  
Distribution is unlimited.  
A. D. BLOSE  
Technical Information Officer

August, 1978

## ABSTRACT

Measurements were made of the spin-lattice nuclear relaxation time of 0.07% solutions of polarized helium-3 in liquid helium-4 at 4 K by use of an rf-biased SQUID (Superconducting Quantum Interference Device) magnetometer in magnetic fields ranging between 30 microGauss and 3 milliGauss. After the effect of magnetic-gradient-induced relaxation was subtracted by extrapolation to large magnetic fields, it was found that the relaxation time was 40 hours in a 1 cm-diameter Pyrex cell. When the sample cell was prefilled with an amount of hydrogen estimated to be equivalent to uniform wall coating of 30 molecular layers thickness, the extrapolated relaxation time increased to 5 days. It is estimated that this result was dominated by intrinsic relaxation due to helium-3 dipole-dipole interactions in the bulk of the sample.

As a potential application, the performance of a proposed cryogenic nuclear gyroscope utilizing a helium-4 - polarized helium-3 gas mixture with SQUID magnetometer readout in zero magnetic field is theoretically analyzed. The possibility of using a modified version of this device based on a polarized helium-3 - superfluid helium-4 mixture for the purpose of an experimental search for an electric-dipole moment in the helium-3 nucleus is also discussed.

Accession No.	
Ref. No.	
BYRIG File	<input type="checkbox"/>
Unannounced	<input type="checkbox"/>
Justification	
By	
Distribution/	
Availability Codes	
Avail and/or	
Dist	Special

## ACKNOWLEDGMENTS

It is my pleasure to acknowledge the efforts and advice of the numerous people who have made this work possible.

First, I must thank my advisor, Professor William Fairbank who suggested the topic and provided the necessary support.

Also of great importance were the efforts of my colleagues and the many helpful conversations I had with them. In particular, I would like to thank Isaac Bass and Terry Jach who were involved in the early stages of this project. Particularly invaluable were the contributions of Blas Cabrera who was responsible for the superconducting shield used in my experiments and who worked with me on the dewar modifications. In addition, Robin Giffard was of great help in setting up the SQUID magnetometer and providing the electronics necessary for its operation.

Credit is also due to the technical staff who provided a range of skills that would be difficult for any one individual to master. Specifically I would like to express my gratitude to Gerry Sander for his excellent mechanical design, Wolfgang Jung, John Murphy and Joe Ascorra for their quality machine work, Frank Peters for his skilled glass-blowing, and Sylvia Harris for the fine drawings which contribute significantly to this thesis. In addition, special thanks are due to Norva Shick whose typing skills and organizational ability were essential for the efficient completion of this work.

## TABLE OF CONTENTS

	<u>Page</u>
ABSTRACT . . . . .	iii
ACKNOWLEDGMENTS . . . . .	iv
LIST OF FIGURES . . . . .	viii
CHAPTER 1: BACKGROUND AND OUTLINE . . . . .	1
1.1 Introduction . . . . .	1
1.2 Electric Dipole Moments . . . . .	3
1.3 Essential Elements of the $\text{He}^3$ ZFNG . . . . .	6
1.3.1 Polarization of the $\text{He}^3$ . . . . .	6
1.3.2 Zero Magnetic Field . . . . .	7
1.3.3 ZFNG Readout . . . . .	10
1.3.4 Long Nuclear Relaxation Time . . . . .	12
1.4 Outline and Scope of Thesis . . . . .	16
CHAPTER 2: EXPERIMENTAL APPARATUS AND PROCEDURE . . . . .	19
2.1 Apparatus and Ancillary Procedures . . . . .	19
2.1.1 Dewar and Magnetic Shields . . . . .	19
2.1.2 Optical Pumping Apparatus and Procedure . .	25
2.1.3 Gas Handling and Purification . . . . .	29
2.1.4 Magnetometer and Electronics . . . . .	35
2.1.5 Cryostat Probe . . . . .	38
2.2 Experimental Procedures . . . . .	44
2.2.1 $\text{He}^4$ Requirement . . . . .	44
2.2.2 $\text{He}^3$ Density . . . . .	46
2.2.3 Start-up Procedure . . . . .	47
2.2.4 $T_1$ Measurement Procedure . . . . .	50
2.2.5 Full Free-Precession Decay Measurements .	54
2.2.6 Ambient Field Estimation . . . . .	56
CHAPTER 3: THEORY OF $\text{He}^3$ NUCLEAR RELAXATION . . . . .	59
3.1 General Theory . . . . .	60
3.2 A Simple Example . . . . .	63

3.3 Relaxation Due to Diffusion Through Magnetic Field Gradients . . . . .	72
3.3.1 Unspecified Sample Geometry . . . . .	73
3.3.2 Spherical Sample . . . . .	78
3.3.3 Relaxation When the Motional Narrowing Condition is Violated . . . . .	83
3.4 Intrinsic Relaxation . . . . .	90
3.5 Wall-Induced Relaxation . . . . .	98
CHAPTER 4: EXPERIMENTAL RESULTS AND ANALYSIS . . . . .	104
4.1 Initial Experimental Results . . . . .	104
4.1.1 Effect of Sample Condensation on $\text{He}^3$ Relaxation . . . . .	104
4.1.2 Initial $T_1$ Measurements . . . . .	105
4.1.3 Field-Dependent Longitudinal Relaxation . .	107
4.2 Measurement of the $\text{He}^3$ Diffusion Coefficient . . . .	108
4.3 Relaxation Due to a Nearby Ferromagnetic Dipole . .	111
4.3.1 Results of Model Calculation . . . . .	111
4.3.2 Comparison of the Dipole Model with the Data . . . . .	114
4.4 Wall-Induced Relaxation and Intrinsic Relaxation in the Bulk . . . . .	121
4.4.1 Effect of $\text{He}^4$ . . . . .	121
4.4.2 Cryogenic Wall Coatings . . . . .	128
4.4.3 Effect of $\text{O}_2$ Contamination . . . . .	135
4.5 Conclusions . . . . .	136
CHAPTER 5: $\text{He}^3$ ZERO FIELD NUCLEAR GYROSCOPE . . . . .	138
5.1 Introduction . . . . .	138
5.2 $\text{He}^3$ Nuclear Relaxation Considerations . . . . .	140
5.2.1 Intrinsic Relaxation . . . . .	141
5.2.2 Wall-Induced Relaxation . . . . .	142
5.2.3 Gradient-Induced Relaxation . . . . .	143
5.3 $\text{He}^3$ ZFNG Angular Readout Resolution . . . . .	146
5.4 Residual Magnetic Torques . . . . .	153

5.4.1	Drifts Proportional to the Sample Magnetization . . . . .	153
5.4.1.1	Interaction of the Magnetization with Passive Elements . . . . .	153
5.4.1.2	Interaction of the Magnetization with the Readout Magnetometers: Effect of Finite Loop Gain . . . . .	159
5.4.2	Motion of the Sample Magnetization Due to Magnetometer Noise and Drift. . . . .	163
5.4.3	Effect of the London Moment . . . . .	170
5.5	Conclusion . . . . .	171
CHAPTER 6: $\text{He}^3$ NUCLEAR ELECTRIC DIPOLE MOMENT EXPERIMENT . . .		173
6.1	Introduction . . . . .	173
6.2	Frequency Resolution Estimate . . . . .	177
6.3	Stability of the Larmor Frequency . . . . .	183
6.3.1	Method of Analysis . . . . .	184
6.3.2	Effects Due to Magnetometer Noise and Drift . . . . .	188
6.3.3	Variations in the Larmor Frequency Due to Asymmetries . . . . .	190
6.3.4	Effect of Mechanical Motion . . . . .	192
6.3.5	Effect of Temperature Stability on $\omega_0$ . . . . .	193
6.4	Relaxation Time Considerations . . . . .	196
6.5	Electric Field Requirement. . . . .	197
6.6	Conclusions . . . . .	199
APPENDIX A: GRADIENT-INDUCED RELAXATION DUE TO A NEARBY FERROMAGNETIC DIPOLE . . . . .		200
APPENDIX B: FORMAL RELATIONSHIP BETWEEN $\vec{B}_{\text{loc}}$ AND $\vec{M}$ FOR A UNIFORMLY MAGNETIZED REGION IN A PERFECTLY DIAMAGNETIC SHIELD . . . . .		207
APPENDIX C: FIRST ORDER CALCULATION OF $\vec{B}_{\text{loc}}$ IN A NEARLY SPHERICAL SAMPLE IN A NEARLY SPHERICAL SUPERCONDUCTING SHIELD . . . . .		212
REFERENCES . . . . .		222

LIST OF FIGURES

	<u>Page</u>
Fig. 2.1 Schematic depiction of the bottom portion of the cryostat probe . . . . .	20
Fig. 2.2 General experimental configuration . . . . .	21
Fig. 2.3 $\text{He}^3$ optical-pumping apparatus and absorption monitor . . . . .	26
Fig. 2.4 Gas-handling and purification apparatus . . . . .	31
Fig. 2.5 Detail of Vycor superleak $\text{He}^4$ purifier . . . . .	33
Fig. 2.6 Schematic diagram of SQUID magnetometer system . .	36
Fig. 2.7 Compensation electronics . . . . .	39
Fig. 2.8 Detail of sample cell and coil assembly . . . . .	41
Fig. 2.9 Typical condensation signal . . . . .	49
Fig. 2.10 Diagram of the transitory precession technique . .	51
Fig. 2.11 Typical data record of two sequential measurements of the sample magnetization . . . . .	53
Fig. 2.12 Example of a full precession decay . . . . .	55
Fig. 2.13 Precession and decay in the ambient magnetic field . . . . .	58
Fig. 4.1 Data from a sequence of $T_1$ measurements made under nominally constant conditions . . . . .	106
Fig. 4.2 Measurement of the $\text{He}^3$ diffusion coefficient in liquid $\text{He}^4$ . . . . .	110
Fig. 4.3 Geometry and coordinate system used to estimate the relaxation due to an external ferromagnetic dipole . . . . .	113
Fig. 4.4 $T_1$ as a function of $B_0$ in the bare Pyrex sample cell . . . . .	116
Fig. 4.5 Detail of sample cell and pickup coil form showing possible location of a ferromagnetic dipole . . . . .	117

Fig. 4.6	Cabrera's measurement of remanent magnetization associated with Delrin . . . . .	119
Fig. 4.7	Estimates of the wall-induced relaxation, $T_{1w}^{-1}$ , and the relaxation rate in the adsorbed phase, $T_{1Ad}^{-1}$ . . . . .	127
Fig. 4.8	Relaxation rate data obtained with solid-H <sub>2</sub> wall coatings . . . . .	132
Fig. 4.9	Relaxation rate data obtained when the sample cell was prefilled with argon prior to cooldown . .	134
Fig. 5.1	Schematic depiction of the He <sup>3</sup> zero-field nuclear gyroscope . . . . .	139
Fig. 5.2	One of the SQUID readout systems for the He <sup>3</sup> ZFNG . . . . .	147
Fig. 6.1	Schematic depiction of an apparatus that might be used for He <sup>3</sup> nuclear electric dipole moment experiment . . . . .	175
Fig. 8.1	A uniformly magnetized region R located entirely in a volume bounded by a surface S . . . . .	208

## CHAPTER 1

### BACKGROUND AND OUTLINE

#### 1.1 Introduction

The nucleus of the  $\text{He}^3$  atom has intrinsic spin angular momentum of  $\frac{1}{2}\hbar$ . Thus, by the Wigner-Eckart theorem, the  $\text{He}^3$  nucleus can possess no electromagnetic multipole moments higher than a dipole. Since the nuclear magnetic dipole moment is represented by a vector operator,  $\vec{\mu}$ , the Wigner-Eckart theorem also specifies that  $\langle \vec{\mu} \rangle = \gamma \hbar \langle \vec{I} \rangle$  where  $\vec{I}$  is the nuclear angular momentum operator. The gyromagnetic ratio  $\gamma$  has been experimentally determined to be  $-2.038 \times 10^4 \text{ rad sec}^{-1} \text{ G}^{-1}$  for  $\text{He}^3$ . A similar relation could be written for the electric dipole moment  $\vec{\mu}_e$ , but for reasons that will be discussed shortly,  $\vec{\mu}_e$  is either extremely small or zero and can be ignored for the moment. Hence, at low energies, the only significant interaction between  $\langle \vec{I} \rangle$  and external electromagnetic fields is through the magnetic dipole moment.

If we now consider a collection of a large number of  $\text{He}^3$  atoms in the form of a classical gas or liquid where the nuclear polarization is such that the components of the total nuclear-spin angular momentum are much larger than  $\hbar$ , then the magnetization,  $\vec{M}$ , of the sample can be treated as a classical variable. Secondly, if the interactions experienced by the individual nuclei are of only two types, 1) that of a dipole in a uniform constant field  $\vec{B}_0 = B_0 \hat{k}$ , and 2) random fluctuating interactions which are modulated by thermally-driven atomic motion and which have only a weak effect during the time interval characteristic

of these fluctuations, then Bloch's equations describe the motion of  $\vec{M}$ :<sup>1</sup>

$$dM_z/dt = - (M_z - M_0)/T_1$$

$$dM_{x,y}/dt = \gamma(\vec{M} \times \vec{B}_0)_{x,y} - M_{x,y}/T_2 .$$

In these expressions,  $\vec{M}_0 = M_0 \hat{k}$  is the equilibrium magnetization,  $T_1$  and  $T_2$  are the longitudinal and transverse relaxation times respectively, and it is necessary to assume that  $\omega_0 T_{1,2} \gg 1$ , where  $\omega_0 = -\gamma B_0$  is the Larmor precession frequency.

The most notable aspect of this result is that the effects of the random fluctuating interactions are manifested only through the exponential-decay time constants  $T_1$  and  $T_2$  provided that the "motional narrowing" condition expressed in 2) above holds. These fluctuating interactions can arise from a number of sources:  $^{3\text{He}}\text{-}^{3\text{He}}$  dipole-dipole interactions,  $^{3\text{He}}$ -foreign spin (electronic or nuclear) dipole-dipole or scalar interactions, and motion through macroscopic magnetic-field gradients.

This being the case, we now ask the question of what happens if  $\vec{B}_0 = 0$ . If we assume that the macroscopic magnetic field is identically zero over the sample volume and the microscopic relaxation mechanisms are isotropic, the answer is clear: Having removed the anisotropy introduced by  $\vec{B}_0$  and having assumed that no other anisotropy exists, the relaxation rate (the reciprocal of the relaxation time) must now be a scalar and Bloch's equations are simply

$$d\vec{M}/dt = - \vec{M}/T_R .$$

Thus  $\vec{M}/|\vec{M}|$  is a constant of the motion and  $|\vec{M}|$  decays exponentially with a time constant  $T_R$ . The system would then behave as a nuclear gyroscope.

There are, of course, considerable technical problems in actually achieving zero magnetic field over the sample volume. One must devise a stable shielding technique to eliminate ambient magnetic fields, find suitable materials that are devoid of ferromagnetic contamination, and consider the question of the macroscopic B-field generated by the sample magnetization itself. With discovery of flux quantization in superconductivity,<sup>2,3</sup> however, it was pointed out by Fairbank and Hamilton<sup>4</sup> that the problem of a stable shield that completely excluded magnetic flux was theoretically solvable. Using this concept they proposed that not only could a  $\text{He}^3$  nuclear gyroscope be built (which we shall call the  $\text{He}^3$  zero-field nuclear gyroscope,  $\text{He}^3\text{ZFNG}$ ), but that with the addition of an electric field, such a device could be used to search for the  $\text{He}^3$  nuclear electric dipole moment as well.

This proposal constituted the motivation for this thesis. In the following section of this chapter we will briefly review the reason for scientific interest in the electric dipole moments (EDM) of elementary particles and how it is possible to look for an EDM of the  $\text{He}^3$  nucleus using neutral atoms. The succeeding sections will then deal with the key elements of the ZFNG and how they might be implemented with current technology and with the goals and scope of this present work.

## 1.2 Electric Dipole Moments

It is well known that a quantum system that is in an eigenstate of its total angular momentum cannot have an electric dipole moment unless parity is violated. This is particularly obvious if one uses the Wigner-Eckart theorem to express the expectation value of the

electric-dipole moment operator:  $\langle \vec{\mu}_e \rangle = \gamma_e \hbar \langle \vec{I} \rangle$ . The "gyroelectric ratio",  $\gamma_e$ , is clearly a pseudoscalar which can be nonzero only if parity is not conserved.

On the other hand, it was pointed out by Landau that the violation of parity in weak interactions does not guarantee that electric dipole moments would exist.<sup>5</sup> He observed that if charge conjugation were violated in such a way that CP were still valid then there would still be no electric dipoles. Thus, the CPT theorem implies that time reversal would have to be violated as well if electric dipole moments were to exist.

The connection between time reversal invariance and electric dipoles can be made more directly apparent by means of a simple argument.<sup>6</sup> If a particle has an electric dipole moment and is subjected to an electric field  $\vec{E}$ , there will be a term in the Hamiltonian of the form  $-\vec{\mu}_e \cdot \vec{E}$ . The energy shift introduced by such a term would then be  $-\gamma_e \hbar \langle \vec{I} \rangle \cdot \vec{E}$ . Now under a time reversal  $\langle \vec{I} \rangle \rightarrow -\langle \vec{I} \rangle$ ,  $\vec{E} \rightarrow \vec{E}$ , and this term would change sign. In comparison, the energy of a magnetic dipole in a magnetic field will not change sign under time reversal since the direction of the currents that generate the magnetic field will also change.

Thus, while the original experiment to search for an EDM on neutrons that was done by Smith, Purcell and Ramsey over 25 years ago was motivated by the hypothesis that parity was not inviolate, continued activity in EDM experiments has been sustained by interest in time reversal violation. This has been particularly the case since evidence of CP violation was reported by Christenson, Cronin, Fitch, and Turlay in the

decay of  $K_2^0$  mesons.<sup>7</sup>

At the present, the upper limit of the EDM of the neutron has been reported by Dress, *et al.* as  $|\mu_e(n)/e| < 3 \times 10^{-24}$  cm<sup>8</sup> where e is the charge of the electron. The limit on the size of the EDM of the electron stands at virtually the same level as the neutron<sup>9,10</sup> while the limit on the EDM of the proton is several orders of magnitude larger.<sup>11,12</sup>

The basis for the Fairbank and Hamilton proposal to use a ZFNG to measure the EDM of the He<sup>3</sup> nucleus (which could arise from the unpaired neutron) was an analysis by Schiff on the measurability of nuclear EDMs.<sup>13</sup> The primary problem, of course, is that the nucleus is charged, and the application of an external electric field merely polarizes the electron cloud so that the net electric field seen at the nucleus remains zero. Schiff discovered, however, that there are small first order effects which prevent exact cancelation and thus allow a small electric field to be present at the nucleus. The largest of these effects is due to the force generated by the interaction of the nuclear *magnetic* dipole moment with the magnetic field gradient produced by currents in the polarized electron cloud. This effect causes the nucleus to be subjected to an electric field approximately  $10^{-7}$  times the external field.<sup>13</sup>

Although this result is not terribly encouraging in comparison with free neutrons which can be exposed to an unattenuated electric field, there is at least one compensatory factor in the Fairbank and Hamilton proposal. That is, if a dilute mixture of He<sup>3</sup> in liquid He<sup>4</sup> is used (one part in  $10^5$  was originally suggested), it might be possible to achieve nuclear relaxation times on the order of days or longer. Thus

the  $\text{He}^3$  nuclei could be exposed to the electric field for  $\sim 10^5$  sec instead of the  $\sim 10^{-2}$  sec typical of neutrons in the neutron-beam EDM experiment.

Thus it appears that the ZFNG approach to the  $\text{He}^3$  nuclear EDM has sufficient merit to justify more detailed consideration given the importance of time reversal invariance. It is clear from the outset, however, that this approach will not be without its problems. As an indication of the difficulty involved, we note the rate of angular precession that would be obtained in an applied field of  $10^5$  V/cm would be  $\sim 10^{-11}$  rad  $\text{sec}^{-1}$  if  $|\mu_e/e| = 10^{-24}$  cm. This is equivalent to the effect of a magnetic field of less than  $10^{-15}$  G!

### 1.3 Essential Elements of the $\text{He}^3$ ZFNG

From our rough description of the  $\text{He}^3$  ZFNG, it is clear that there are four essential elements necessary for a useful device: 1) polarized  $\text{He}^3$ , 2) a shielded region that has zero magnetic field, 3) a means of measuring the orientation of the magnetization of the polarized  $\text{He}^3$ , and 4) a usefully long relaxation time. In this section we will briefly discuss the best techniques and devices that are currently available for the realization of these requirements. As this is only an introductory discussion, however, no attempt will be made at this point to evaluate how well a ZFNG would perform with these techniques.

#### 1.3.1 *Polarization of the $\text{He}^3$*

Since we are contemplating the use of dilute  $\text{He}^3$ -liquid  $\text{He}^4$  mixture, it is necessary that the  $\text{He}^3$  be substantially polarized. While significant "brute force" polarization could be achieved with currently available

superconducting magnets and dilution refrigerators (it is assumed that the  $\text{He}^3$  is sufficiently dilute that Fermi degeneracy is not a factor), *in situ* application of this technique would be difficult at best. For one thing, polarization times would be very long (by design!), and for another, the use of large magnetic fields is basically incompatible with the zero-field requirement. This does not preclude, however, the possibility of polarizing the  $\text{He}^3$  in one place and then piping into the zero-field region.

Fortunately, Colegrove, Schearer, and Walters developed an easier solution. They discovered a fairly simple optical pumping process which readily yields a nuclear polarization of 10-20% in  $\text{He}^3$  gas in the vicinity of 1 Torr pressure at room temperature.<sup>14</sup> We will not discuss the nature of this process here,<sup>15</sup> but a description of the technique and apparatus involved will be found in Chapter 2.

It should be pointed out that the most serious limitation of this process is that it is restricted to low  $\text{He}^3$  densities. In order to achieve useful densities for some applications it is necessary to use mechanical compression or low temperatures after polarization. Since the  $\text{He}^3$  ZFNG is intended to be a low temperature device anyway, this does not present a serious problem: The  $\text{He}^3$  can be optically pumped at room temperature, mixed with  $\text{He}^4$ , and the mixture condensed into the zero-field region via a glass capillary.

### 1.3.2 *Zero Magnetic Field*

We have already noted the advantage of using a superconductor as a magnetic shield. Some technique must be developed, however, for cooling the shield in such a way as to "degauss" the shield, *i.e.* to minimize

or prevent trapped flux. Although it might be thought that the Meissner effect would tend to expel the magnetic flux when the shield is cooled through its transition, it is usually found in actual practice that the shield tends to trap the ambient field. This is because even a type I superconductor rarely exhibits strong Meissner effect unless it is a single crystal having low impurity and dislocation densities.

Superconducting shields have been made and degaussed by a variety of techniques, but probably the best and most useful for ultralow field applications is the one refined by Cabrera<sup>16,17</sup> making use of an expansion technique. This technique makes use of cylindrical lead foil shields which are closed at the bottom. The virtue of a foil shield is that it can be pleated and folded flat prior to cooling and then opened to its full diameter after cooling. It is then possible to cool a new folded shield inside of a previously established shield. The old shield is then torn away prior to expanding the new one. This cascading process can be continued until a satisfactory shield is obtained. Cabrera has obtained 4" diameter shields with fields below  $10^{-8}$  G over 20" along their axes using this technique.<sup>16,17</sup> As a point of reference, we note that a field of  $10^{-8}$  G would yield a precessional period of over 8 h in  $\text{He}^3$ .

In the original Fairbank and Hamilton scheme, a cylindrical shield of the sort that Cabrera has developed would constitute an outer shield inside of which a spherical superconducting shield that was concentric with the  $\text{He}^3$  sample cell would be cooled. It was this inner spherical shield that was specified to have zero trapped flux. The practicality of such a shield has yet to be demonstrated.

In this regard a valid question may be asked: Is it in fact necessary to achieve the zero-flux state? It would seem possible to cancel out the uniform field component (*i.e.*, the average field) over the sample volume. Provided then that the residual gradient were small enough such that the motional narrowing condition held, that is, that the diffusion time through the sample would be short compared to the differential Larmor period, it would seem that the effect of the gradient would be averaged out.

As far as it goes, this conjecture is correct. Unfortunately, the anisotropy introduced by the residual gradient makes the relaxation rate also anisotropic. Thus, the direction of  $\vec{M}$  is still in general not a constant of the motion even though the average magnetic field is zero. This issue will be examined in detail in Chapters 3 and 5.

Even though the trapped flux is zero, however, it is obvious that there are other possible sources of magnetic fields that can affect the motion of the sample magnetization. One such possibility is the remanent magnetization due to ferromagnetic contaminants. Cabrera has measured the remanent magnetization of a wide variety of materials in a low-field environment at 4.2 K,<sup>17,18</sup> and has found several materials that appear to have promise in ultralow-field applications. For example, samples of fused silica, AL 300 alumina ceramic, and Corning Macor (machinable glass-ceramic) were found to not have any detectable dipole moments ( $\lesssim 10^{-8}$  G cm<sup>3</sup> for the ceramics,  $\lesssim 10^{-9}$  G cm<sup>3</sup> for the quartz).<sup>17</sup> In general, clean insulators are preferable to clean normal metals since the latter can produce thermoelectric currents in the presence of thermal gradients.<sup>17</sup>

There are two remaining sources of magnetic field that are intrinsic to the ZFNG technique under discussion. One is the magnetic field produced by a superconductor when it is subject to rotations, that is, the London moment.<sup>19</sup> This phenomenon, however, is not a significant problem for two reasons: the effect is small and it is quite predictable. We will show in Chapter 5 that the uncorrected London moment will cause a relative error of  $\sim 10^{-3}$  in the readout of an angular displacement.

The other source of magnetic field that is intrinsic to the ZFNG is the field produced by the sample magnetization itself. This problem must be resolved by maintaining proper symmetry. For instance, it is clear without any detailed consideration that if the sample cell and the superconducting shield (which is perfectly diamagnetic) are both spherical and concentric, then the average macroscopic flux density (*i.e.*, the magnetic induction,  $\vec{B}$ ) must always be collinear with  $\vec{M}$  and therefore cannot cause any torque on the magnetization. The issue of whether sufficient symmetry can be achieved in actual practice will also be discussed in detail in Chapter 5.

### 1.3.3 ZFNG Readout

The most likely candidate for readout is the SQUID (Superconducting Quantum Interference Device) magnetometer. Such a device can be flux-coupled to the sample volume by means of a persistent superconducting loop consisting of two coils connected in series. One coil is inductively coupled to the SQUID and the other to the sample volume. This type of system has a number of advantages to commend it: 1) close coupling, 2) vector field response, *i.e.*, the output is proportional

to the component of the magnetic field normal to the plane of the sensing coil, 3) it is a low temperature device compatible with other aspects of the proposed ZFNG, and 4) excellent energy sensitivity. With regard to sensitivity, for example, a commercially available rf-biased SQUID has a typical energy sensitivity of  $5 \times 10^{-29}$  J/Hz for frequencies above 0.1 Hz.<sup>20</sup> This corresponds to a magnetic field sensitivity of  $\sim 4 \times 10^{-10}$  G Hz<sup>-1/2</sup> when referred to a 1 cm diameter sensing coil.

We will not discuss here the theory of operation of the rf SQUID<sup>21,22</sup> or the improved dc SQUID.<sup>23</sup> It should be pointed out however, that the basic response of the SQUID is a periodic function of applied flux where the periodicity is associated with the quantum of flux  $\phi_0 = 2.07 \times 10^{-7}$  G cm<sup>2</sup>. In general, the output of the SQUID is "linearized" by applying an af sweep with an amplitude of  $\frac{1}{2}\phi_0$  to the SQUID. The output of the SQUID is then synchronously detected, filtered, and the resulting low-frequency signal is fed back to the SQUID causing the system to lock onto a single flux quantum.<sup>22,23</sup> This feedback signal is then linearly related to the input magnetic flux (as long as the system remains locked and the loop gain is much larger than unity) and serves as the output signal.

In application to the He<sup>3</sup> ZFNG the feedback signal is coupled directly into the input coupling circuit rather than into the SQUID (see Fig. 2.6 in Chapter 2). This guarantees that the current in the superconducting coupling circuit remains constant to within a small error specified by the loop gain and the magnetometer noise. Thus if the current in the coupling circuit is initially nulled, it will remain

that way except for this error. Since the sensing coil is closely coupled to the sample, it is clear that finite loop gain and magnetometer noise and drift will have an effect on the  $\text{He}^3$  ZFNG. These factors as well as the angular resolution that might be expected from the SQUID readout system are also discussed in detail in Chapter 5.

#### 1.3.4 Long Nuclear Relaxation Time

The last element necessary for a useful ZFNG is the requirement of sufficiently long relaxation times in the zero-field condition. Just how long is sufficient depends, of course, on the particular application. In the case of the  $\text{He}^3$  nuclear EDM experiment, it will be seen that it is probably necessary to achieve relaxation times on the order of several days or longer (*i.e.*,  $\gtrsim 2 \times 10^5$  sec) if this approach is to be competitive with the neutron beam technique.

As we have already noted, Fairbank and Hamilton proposed using dilute  $\text{He}^3$ -liquid  $\text{He}^4$  mixtures in order to obtain relaxation times of this magnitude. The logic of this proposal is clear. The intrinsic longitudinal relaxation time of pure liquid  $\text{He}^3$  lies in the range 300-500 sec.<sup>24</sup> (By the term "intrinsic relaxation" we mean relaxation due to  $\text{He}^3$  dipole-dipole interactions in the bulk of the sample. For this mechanism,  $T_1 = T_2$  in liquids and gases subjected to low magnetic fields.<sup>1</sup>) Since it is well known that the intrinsic relaxation of a monatomic species is inversely proportional to the spin density,<sup>1</sup> however, it is clear that a  $\text{He}^3$  density  $\approx 10^{-3} \times$  liquid density should be used. This is on the order of gas density under STP conditions. Although  $\text{He}^3$  gas could be acceptable for gyro applications it certainly is not for the EDM experiment:  $\text{He}$  gas would electrically break down

at electric field levels much less than the  $10^5$  V/cm that is feasible for liquid He. Hence there is no alternative but to use  $\text{He}^3$ -liquid  $\text{He}^4$  mixtures.

The necessity of using dilute  $\text{He}^3$ -liquid  $\text{He}^4$  mixtures in order to obtain the requisite relaxation times is clear. Because there are other potential relaxation mechanisms, however, a low  $\text{He}^3$  density is not sufficient to guarantee long relaxation times. In particular, there are at least two additional relaxation mechanisms that can be important under the proposed experimental conditions: relaxation due to motion through magnetic field gradients and wall-induced relaxation.

Nuclear relaxation due to magnetic field gradients can be very effective when the average field is reduced to zero. Since this mechanism is well understood, it is more of a technical problem (although a difficult one if the diffusion coefficient is small) than a scientific problem. This relaxation mechanism will be thoroughly reviewed in Chapter 5.

Wall-induced relaxation is an inherently more complex problem to deal with, and while some research has been done on the subject in recent years, there is still quite a bit to be learned. It was found in early  $\text{He}^3$  NMR experiments that some wall materials (especially metallic surfaces) can be very effective in relaxing  $\text{He}^3$  at low temperatures.<sup>25</sup> It was also found, however, that when Pyrex or quartz cells were used, the spin-lattice relaxation time of liquid  $\text{He}^3$  was not much shorter than the theoretically expected intrinsic value thus indicating that these surfaces are only weakly relaxing.<sup>26,27</sup> Subsequent work obtained good agreement between theory and experiment when the Pyrex cell was carefully plasma cleaned and a more sophisticated theoretical result was used.<sup>24</sup>

Unfortunately, no relaxation time measurements have been made on very dilute ( $\leq 0.1\%$ )  $\text{He}^3$ -liquid  $\text{He}^4$  mixtures in Pyrex or quartz cells. Measurements have been made at moderate dilutions by Romer<sup>26</sup> ( $T_1 = 90$  min for 3.5%  $\text{He}^3$ , and  $T_1 = 120$  min for 1.7%  $\text{He}^3$ , both at 1.25 K) and Horvitz<sup>24</sup> ( $500 < T_1 < 700$  sec for 33%  $\text{He}^3$  in a plasma-cleaned cell for temperatures ranging between 1.2 and 1.8 K), but these data are insufficient to allow extrapolation to lower  $\text{He}^3$  densities. The primary problem is that the relative contribution of  $\text{He}^3$ - $\text{He}^3$  interactions on the wall and the  $\text{He}^3$ -foreign spin interactions is not known. The former contribution should depend on the  $\text{He}^3$  concentration while the latter should not.

Thus it needs to be demonstrated whether or not relaxation times on the order of days can be obtained in dilute  $\text{He}^3$ -liquid  $\text{He}^4$  mixtures. Results of  $T_1$  measurements made on  $\sim 0.1\%$   $\text{He}^3$ -liquid  $\text{He}^4$  mixtures in low magnetic fields at 4.2 K will be discussed in Chapter 4.

Although  $\text{He}^3$  gas cannot be used in the presence of the larger electric fields necessary for an EDM experiment, it still remains a candidate for gyro applications. In fact, the rapid diffusion associated with the gas phase is quite advantageous since relaxation due to residual field gradients would be considerably reduced. For this reason, we will briefly review results of  $T_1$  measurements on  $\text{He}^3$  gas in glass cells at low temperatures. This subject will also be discussed in greater detail in Chapter 4.

Fitzsimmons, Tankersley, and Walters have shown that it is possible to obtain a relaxation time of  $9 \times 10^5$  sec ( $\sim 9$  days) at a temperature of 373 K provided that a glass of low permeability to helium is used for the sample cell.<sup>28</sup> As the temperature is lowered below 100 K,

however, the fraction of the time that a given atom spends adsorbed on the surface becomes progressively longer. Because of the longer correlation times and the greater density of spins associated with the adsorbed phase and the wall surface, the relaxation time for an adsorbed atom is much shorter than in the bulk. Thus the relaxation time for  $\text{He}^3$  gas at low temperatures can become very short.<sup>28-30</sup>

When the temperature becomes sufficiently low and the gas density sufficiently high that the wall becomes effectively saturated (*i.e.*, the adsorption isotherm varies only slowly with gas density) the probability that a given atom is in the adsorbed phase varies inversely with the gas density. In that case, the relaxation time varies approximately linearly with the density until the intrinsic relaxation in the bulk becomes dominant.<sup>31</sup> Above that density the relaxation time varies inversely with density until liquid density is approached. It is clear, then, that for a given cell size and material there is an optimal  $\text{He}^3$  density that yields the maximum relaxation time. Chapman and Richards have found that in a 1 cm diameter, plasma-cleaned, Pyrex cell the optimal density at 4.2 K is  $\sim 10^{-2} \text{ g cm}^{-2}$  (equivalent to 75 atm STP) and that the relaxation time under these conditions is  $\sim 5 \times 10^3$  sec (80 min).<sup>31</sup>

Although the prospects for  $\text{He}^3$  gas at low temperature do not seem very bright on the basis of this kind of result, the situation is improved markedly by the discovery of Barbé, Laloë, and Brossel that certain frozen-gas wall coatings could be very effective in reducing wall-induced relaxation of low-density  $\text{He}^3$  over various temperature ranges.<sup>32</sup> For example, they found that a wall coating of solid  $\text{H}_2$  at 4.2 K would

yield a relaxation time of  $60 \pm 10$  h in a sealed 3 cm-diameter cell that had been filled with 0.5 Torr  $\text{He}^3$  at room temperature. In the bare Pyrex cell the relaxation time was less than 1 sec and estimated to be  $\sim 10^{-2}$  sec. The solid  $\text{H}_2$  wall coating gave good relaxation times between 2 and 6.5 K. Other wall coating materials such as  $\text{D}_2$ ,  $\text{Ne}$ ,  $\text{Ar}$ ,  $\text{Kr}$ , and  $\text{Xe}$  also proved to be effective over higher temperature ranges, but only  $\text{H}_2$  was effective at 4 K.

These measurements were made at densities that are probably too low to be useful for our purposes. Since the  $\text{He}^3$  adsorption on top of the solid  $\text{H}_2$  was probably well below monolayer coverage<sup>53</sup> (this will be discussed in Chapter 4), it is difficult to say what the relaxation time would be at higher densities. Nonetheless this is an encouraging result.

#### 3.4 Outline and Scope of Thesis

The work that will be discussed in the following chapters will be concerned with achieving two primary objectives: 1) measurement of the nuclear relaxation times of dilute  $\text{He}^3$ -liquid  $\text{He}^4$  mixtures at 4 K, and 2) analysis of the expected performance of the  $\text{He}^3$  ZFNG based on currently known technology in light of the requirements of the  $\text{He}^3$  nuclear MRI experiment.

In achieving the first objective, it was considered important to gain as much experience as possible in the techniques that were proposed for the  $\text{He}^3$  ZFNG. Thus the relaxation time measurements were made in low magnetic fields ( $\leq 3$  mG) using a SQUID magnetometer to measure the magnetization, and the  $\text{He}^3$  was polarized at room temperature using optical

pumping.\*

It should be noted that the elucidation of the basic physics involved in the various relaxation mechanisms, particularly wall-induced relaxation, was not a primary objective although any data that might be useful in this regard was certainly welcome. The constraints imposed by the primary objective of demonstrating long relaxation times and the desire to use low magnetic fields made it difficult and time consuming to make significant progress on this issue as well.

In the first part of the thesis, Chapters 2-4, we deal primarily with the relaxation problem. In Chapter 2, the experimental apparatus and techniques are described. Chapter 3 reviews the theory of  $\text{He}^3$  nuclear relaxation with particular emphasis placed on the relaxation arising from diffusion through magnetic field gradients. This subject is important for both the analysis of our data and the evaluation of the ZFNG concept. In Chapter 4 the experimental results are presented and analyzed.

The remaining portion of the thesis deals with the ZFNG and the  $\text{He}^3$  nuclear EDM experiment. In Chapter 5 the ZFNG is dealt with. A general analysis is made, but specific numerical estimates are based

---

\* It should be noted that an approach similar to ours, but involving different technology and experimental conditions, has been reported by Cohen-Tannoudji, *et al.*<sup>34</sup> Using a  $\text{Rb}^{87}$  magnetometer, they detected the magnetic field generated by optically-pumped  $\text{He}^3$  atoms located in an adjacent cell in ambient fields of 2  $\mu\text{G}$  and lower. Their experiments were done at room temperature using nested  $\mu$ -metal shields. This type of shield is not sufficiently stable for our purposes although independent field measurement or stabilization may be possible for less critical applications.

on a 3.8 cm-diameter *gas gyro*. With the possible exception of the gradient-induced relaxation rate, this configuration is found to be superior to a smaller  $\text{He}^3$ -liquid  $\text{He}^4$  configuration.

The final Chapter deals with the EDM experiment. Because the LMG results in Chapter 5 are found to be discouraging, the zero-field concept is discarded as being inessential anyway. We note that it is the magnetic-field stability that is crucial to the EDM experiment. It will be seen that more promising performance estimates can be obtained by considering the magnetization to be freely precessing about a non-zero uniform field,  $\vec{B}_0$ . The applied electric field must then be in the same direction as  $\vec{B}_0$ . In order to obtain the rapid diffusion necessary to minimize gradient-induced relaxation and still have the ability to apply large electric fields, we propose using a  $\text{He}^3$ -superfluid at a temperature of  $\lesssim 0.9$  K.

## CHAPTER 2

### EXPERIMENTAL APPARATUS AND PROCEDURE

As was noted in Chapter 1, the basic experimental approach was to build a crude prototype of the  $\text{He}^3$  ZFNG in order to do relaxation measurements and to experimentally determine the difficulties involved in some of the practical aspects of the device. This concept can be seen in the schematic depiction of the lower portion of the experimental cryostat probe shown in Fig. 2.1. In actual execution the experimental apparatus in some regards fell short of our expectations. Nevertheless, we were able to extract a reasonable amount of information despite the fact that the prototype could not function as a gyro in any real sense.

In the first part of this chapter, we will describe the apparatus used in our experiments and some of the ancillary procedures. In the second part, those considerations and procedures that were more directly relevant to the relaxation measurements will be reviewed and examples of the raw data shown.

#### 2.1 Apparatus and Ancillary Procedures

##### 2.1.1 *Dewar and Magnetic Shields*

Our experiments were performed in a non-magnetic Cryogenic Associates dewar having a liquid helium well of 8 in diam  $\times$  6½ ft length. (See Fig. 2.2.) The dewar had been modified by cutting it open and replacing the aluminum-foil vapor-cooled radiation shields with one

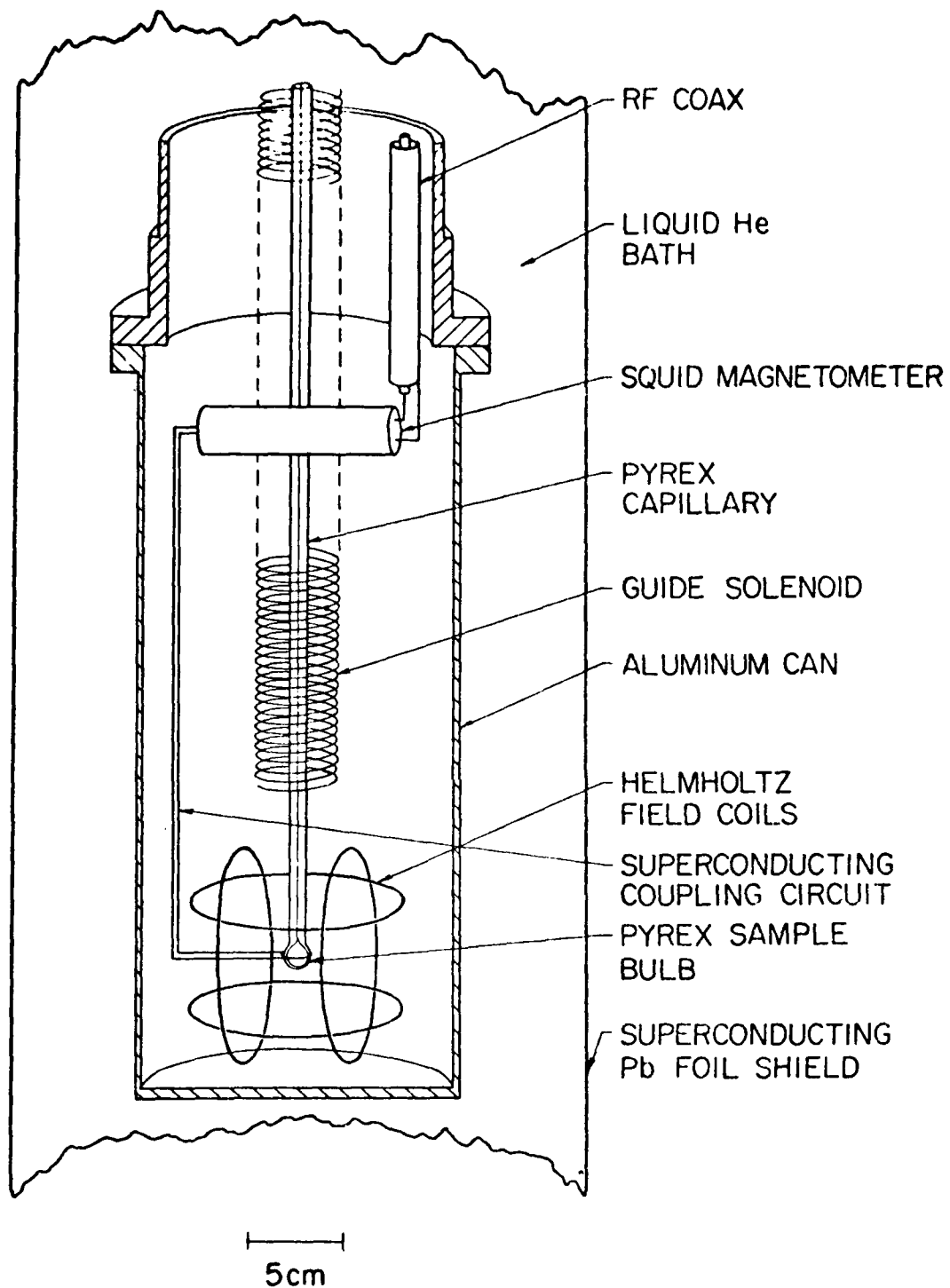


Fig. 2.1 Schematic depiction of the bottom portion of the cryostat probe.

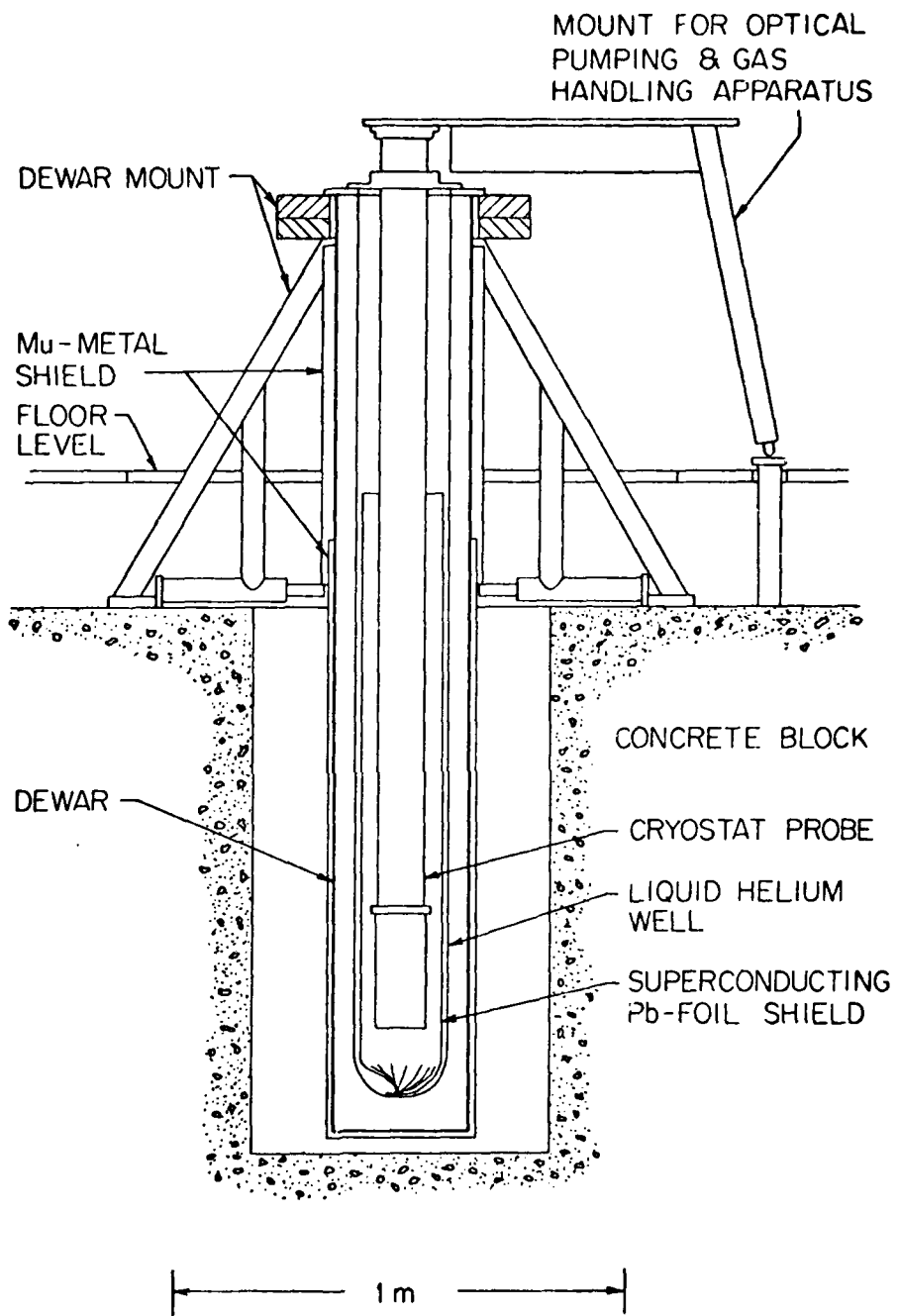


Fig. 2.2 General experimental configuration. Not shown are the field coils for the optical pumping, the optical pumping apparatus and the gas-handling apparatus.

1/16 in thick vapor-cooled shield and a liquid nitrogen jacket. This modification was deemed necessary in order to reduce the liquid helium consumption rate. Helium consumption became an important consideration since it was time consuming and expensive to establish a degaussed superconducting shield. It was therefore advantageous to keep the shield cold continuously until it was no longer needed. The unmodified dewar consumed  $\sim 0.25 \text{ lh}^{-1}$ . After modification, this figure dropped to  $0.09 \text{ lh}^{-1}$  but later deteriorated to  $0.14 \text{ lh}^{-1}$  and stabilized at that level. The reason for this deterioration has not been determined.

Because of its length, the dewar was mounted in a pit by suspending it from its top-plate flange in a sturdy tripod arrangement. This left sufficient head room for the experimental apparatus to be hoisted in and out of the dewar.

The inside of the dewar was lined with a degaussed superconducting shield made of 0.0025 in thick lead foil having a length of 56 in prior to installation. The degaussing and installation procedures were outlined in Chapter 1 and will not be discussed further since they are described in detail in Cabrera's thesis.<sup>17</sup> Details concerning the construction and performance of the actual shield utilized in our experiments will also be found there. Some aspects of the shield, however, had a sufficiently important impact on our experiment to warrant a short discussion here.

The 8 in shield was degaussed, installed and checked while the dewar was located in two nested  $\mu$ -metal shields in Cabrera's laboratory. While located there, the measured magnetic field on the axis of the shield was  $< 0.1 \mu\text{G}$  at points 60, 80 and 100 cm below the top of the

shield. The dewar and shield were then transported to the author's laboratory for actual use. Because it was feared that the top edge of the open shield could not tolerate exposure to the earth's magnetic field (~ 0.6 G), a  $\mu$ -metal collar was installed around the dewar in the vicinity of the top of the shield prior to transportation. This collar then became an integral part of a 1/16 in thick single-layer  $\mu$ -metal shield which housed the dewar in its permanent location.

After relocation, the internal magnetic field was once again measured, and it was discovered that although the field on the shield axis was still < 0.1  $\mu$ G in the region of 60-70 cm from the top, the field became progressively higher as one proceeded below this region. At the lowest point that could be measured with the magnetometer (100 cm from the top of the shield, ~ 34 cm from the bottom) the magnitude of the field was ~ 5  $\mu$ G.

There are two possible reasons for this unfortunate turn of events. Flux penetration occurred during exposure of the lower portion of the shield to the earth's field because of the deeply convoluted folds near the bottom of the shield,<sup>17</sup> and/or the internal field inside the author's single  $\mu$ -metal shield generated larger fringing fields through small tears in the superconducting shield than the field in Cabrera's double  $\mu$ -metal shield. This latter possibility was not even suspected until a post-mortem examination revealed the presence of a number of small tears caused by the process of expanding the shield from its folded state.

The ratio of the internal fields 100 cm below the top of the superconducting shield before and after transportation was on the order of

50 to 1 whereas the field measured in the author's  $\mu$ -metal shield was 2.5 mG as compared to 0.25 mG in Cabrera's shield, yielding a ratio of only 10 to 1. It may still be possible, though, that the fringing mechanism was solely responsible for what was observed because of a non-linear effect arising from the additional magnetic loading of the  $\mu$ -metal shield by the presence of a large perfect diamagnet--the superconducting shield. A single  $\mu$ -metal shield is near saturation in the earth's magnetic field but the inner shield of a nested set is not. Thus it could be possible that the leakage field inside the superconducting shield would not scale linearly with the fields measured in the *empty*  $\mu$ -metal shields.

If it were possible to locate the sample cell in the minimum field region (60-70 cm from the top), this situation would not have been particularly troublesome. Unfortunately, however, the cryostat probe was designed and constructed with the intention of locating the sample cell near the bottom of the shield. As a consequence, stainless-to-copper transitions which occurred in internal tubes in the cryostat probe were located too high in the probe to allow the sample cell to be placed in the minimal field position. Attempting to locate the sample cell in the minimal field region would result in an unacceptable heat leak and excessive helium consumption. Since it was feared that the magnetic field would continue to increase below the lowest measured point, it was decided to position the sample cell at the 100 cm point where the helium consumption was acceptable. Almost all of our data were taken at this position.

It was necessary therefore to locate the sample cell in an ambient

field of a few microgauss. Since the direction and homogeneity were not very well known, most of our data were taken in applied fields which were at least a factor of ten larger than the ambient field. The applied field was generated by the Helmholtz coils depicted schematically in Fig. 2.1. Ambient-field estimation is discussed in Section 2.2.6.

#### 2.1.2 *Optical Pumping Apparatus and Procedure*

The physical principles involved in the nuclear polarization of  $\text{He}^3$  by optical pumping are amply discussed in the original paper by Colegrove, Schearer, and Walters (CSW).<sup>14</sup> They also discuss a number of practical aspects such as sample preparation, pumping bulb cleaning, monitoring the absorption of the resonant  $1.083 \mu\text{m}$  light, circular polarizer construction, and the advantage of a  $\text{He}^4$  (rather than  $\text{He}^3$ ) lamp to provide resonant pumping light.

The optical pumping apparatus is depicted schematically in Fig. 2.3. The optical pumping cell and lamp were slightly modified versions of units that had been designed and built for another application. The optical pumping system was designed to accomodate two pumping lamps, one above, and one below, the optical pumping cell. In actual practice, however, only one was ever used.

The optical pumping cell was a cylindrically shaped Pyrex bulb having 2 in diam  $\times$  6 in external dimensions and an internal volume of  $\sim 300 \text{ cm}^3$ . The weak electrodeless discharge in the optical pumping cell (necessary to populate the metastable  $2^3\text{S}_1$  state) was excited by a power oscillator at a frequency of  $\sim 600 \text{ kHz}$ .

The pumping lamp consisted of a linear discharge tube (with

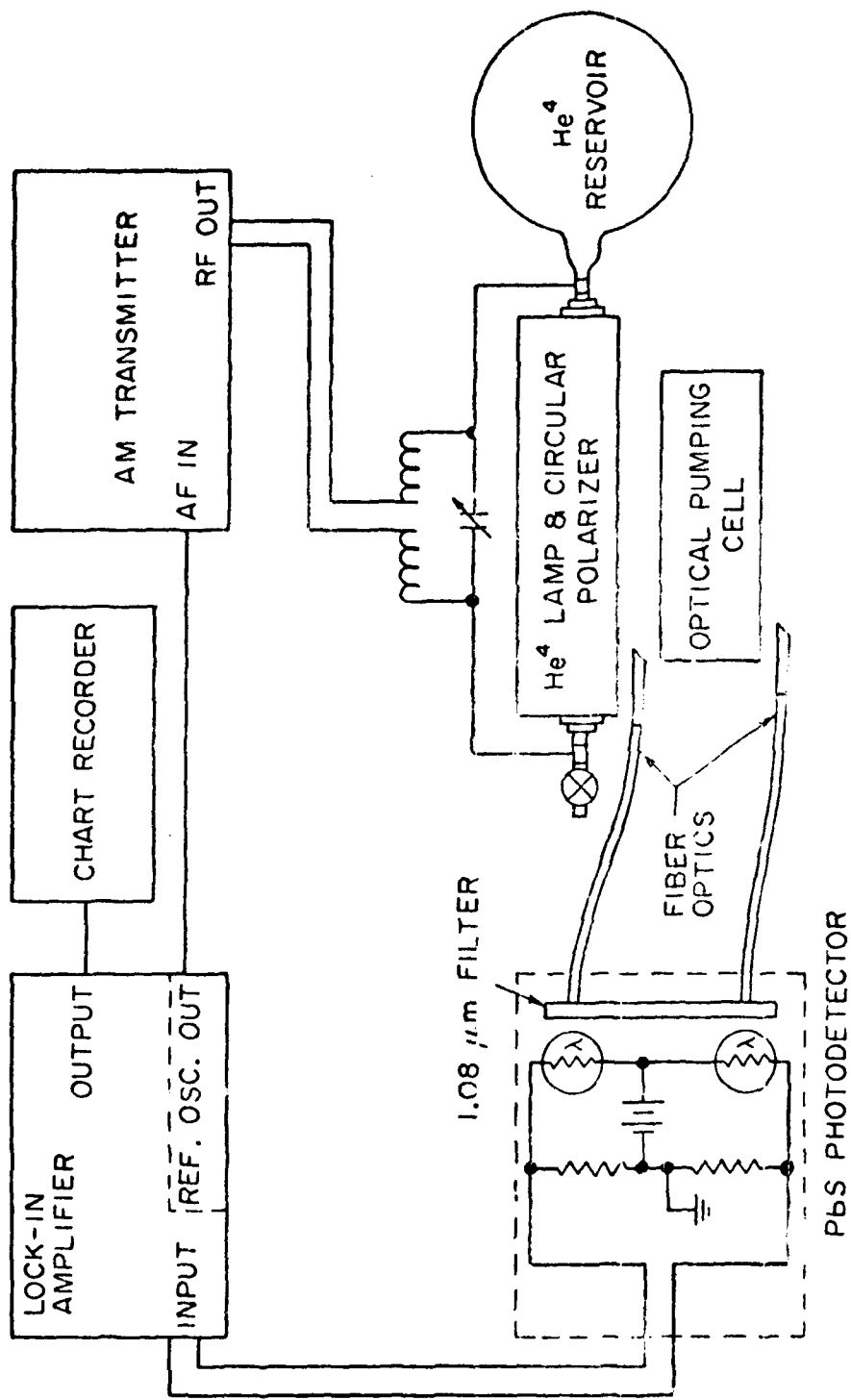


Fig. 2.3  $\text{He}^3$  optical-pumping apparatus and absorption monitor. The external electrodes for igniting a weak discharge in the optical-pumping cell are not shown.

reservoir) and a cylindrical mirror, both of the same length as the pumping cell. The lamp was driven by a radio amateur transmitter at 13.56 MHz (industrial frequency).

The progress of the optical pumping process was monitored by use of the absorption monitor shown in Fig. 2.3. This is the same technique originally used by CSW and relies on the close coupling between the nuclear polarization of the ground state atoms and the polarization of the metastable atoms which are responsible for the absorption of the resonant  $1.083 \mu\text{m}$  light ( $2^3\text{S}_1 \rightarrow 2^3\text{P}$ ). To relate the polarization to the light absorption, we used the expression given by Greenhow,<sup>35</sup>

$$\begin{aligned}\Delta I/I &= P(15 - 10P + 3P^2)/(6 + 2P^2) \\ &\approx 5P/2, \quad \text{if } P \ll 1,\end{aligned}$$

where  $P = (N_+ - N_-)/(N_+ + N_-)$  is the ground state polarization,  $I$  is the intensity of the light absorbed by the metastable atoms, and  $\Delta I$  is the change in the absorbed light intensity that occurs when the polarization is destroyed. In actual practice, we made polarization measurements by adiabatically reversing the magnetic field ( $\sim 10$  G, generated by 3 ft diam Helmholtz coils) for a few seconds and then returning it to its original direction. In this case the change in light absorption was  $2\Delta I$  when  $P \ll 1$ .

The absorption monitor shown in Fig. 2.3 should be discussed briefly. Light was sampled by two glass prisms coupled to two glass fiber optic bundles, one viewing the lamp directly, the other viewing the lamp through the optical pumping cell. This was done to make the

optical pumping assembly as compact as possible. Light from both of the fiber optic bundles were then passed through the same interference filter so that only 1.08  $\mu\text{m}$  light reached the PbS photodetectors. The lamp rf drive and consequently the lamp intensity were amplitude modulated by a 500 Hz signal from the reference oscillator of a lock-in amplifier. Modulation depth was kept small in order to avoid non-linear effects from the lamp which occur when the rf level drops too low. The outputs of the photodetector were then coupled into the differential inputs of the lock-in preamplifier. By making small adjustments in the light-collecting prisms, the lock-in output can be nulled and small changes in the absorption can be detected while small changes in the lamp intensity are rejected.

The total 1.08  $\mu\text{m}$  absorbed by the metastable atoms in the pumping cell is on the order of 1-2% depending on the weak discharge level. Since we were interested in the value of  $\Delta I/I$ , however, it is not necessary to accurately know the absorption coefficient and the monitoring system was not intended for that purpose.

It should also be noted that there was a price to be paid for the compactness of the fiber optic scheme: The overall optical efficiency of the system was quite low and as a consequence the signal-to-noise ratio was inferior to the value that would be obtained in a more conventional system.

In actual use the optical pumping system performed adequately. When operated in isolation, 10% polarizations were typically obtained. When it was assembled together with the cryostat probe and operated in its working position (about 15 in above the dewar top), 5% polariza-

tion that could be achieved. A possible reason for this degradation in performance was the reduction in magnetic field homogeneity due to the nearby  $\mu$ -metal shield around the outside of the dewar. It was discovered, however, that a 5% initial polarization yielded a condensed sample magnetization that was quite adequate for our purpose (see Sec. 4.1.1 of Chapter 4). Hence, no further efforts were made to improve the optical pumping system performance.

#### 2.1.3 *Gas Handling and Purification*

The gas-handling and purification apparatus consisted of two major parts. The first part is a gas-handling table. It was originally designed for the purpose of producing sealed-off  $\text{He}^3$  optical pumping cells and thus included vacuum pumps (mechanical and air-cooled diffusion pump), pressure gauges (oil manometer, thermocouple, and ionization), gas storage bulbs ( $\text{He}^3$ ,  $\text{He}^4$ ,  $\text{H}_2$ , etc.), an activated-charcoal trap that was cooled by liquid nitrogen, and a calibrated leak. The  $\text{He}^4$  and  $\text{H}_2$  were useful for cleaning glass surfaces by means of a hot rf plasma discharge.

This system was modified by the addition of a stainless steel flexible hose with O-ring sealed quick-coupler that allowed connection to the second, remotely located, part of the gas handling system.

The second part of the gas handling and purification system consisted of that portion in proximity to the optical pumping cell. In an earlier version, this consisted simply of an additional  $\text{LN}_2$ -cooled charcoal trap, an ionization-gauge tube and 1 cm-bore vacuum stopcocks for the charcoal trap. This system was all glass and when carefully cleaned achieved  $10^{-7}$  Torr. The additional trap served as both an

additional purifier for the helium and as a sorption pump for other gases and vapors. In our most recent version of this part of the apparatus (Fig. 2.4) two changes were made: 1) Viton-sealed stainless steel bellows valves and tubing were used, and 2) a  $\text{He}^4$  superleak purifier and a 1 liter  $\text{He}^4$  storage volume were added.

The change to stainless steel was motivated primarily by safety considerations. In particular, the large bore vacuum stopcocks with vacuum cups for plug retention eventually require excessive amount of torque as a result of slow extrusion of the vacuum grease, and they consequently become liable to breakage. In addition, the  $\text{He}^4$  storage container would potentially be a hazard if it were made of glass since it would be subjected to several atmospheres of pressure. The stainless plumbing and ionization-gauge tube were located outside the large Helmholz coils that provided the magnetic field for the optical pumping in order to keep ferromagnetic parts away from the optical pumping cell. Only glass plumbing was used inside these field coils.

The price that had to be paid for the ruggedness of the stainless plumbing was a poorer quality vacuum. The base pressure for this system was  $2 \times 10^{-6}$  Torr. The stainless could not be plasma cleaned, and with the presence of Viton seals, could be subjected to only very mild (150° C) bakeout temperatures. CSW estimated that a vacuum system capable of an ultimate pressure well below  $10^{-4}$  Torr should be sufficient for optical pumping of  $\text{He}^3$ , however, and as we have noted, our optical pumping system performed adequately.

In order to purify the  $\text{He}^4$  needed for our experiments, it was elected to construct a Vycor superleak purifier. Since we were going

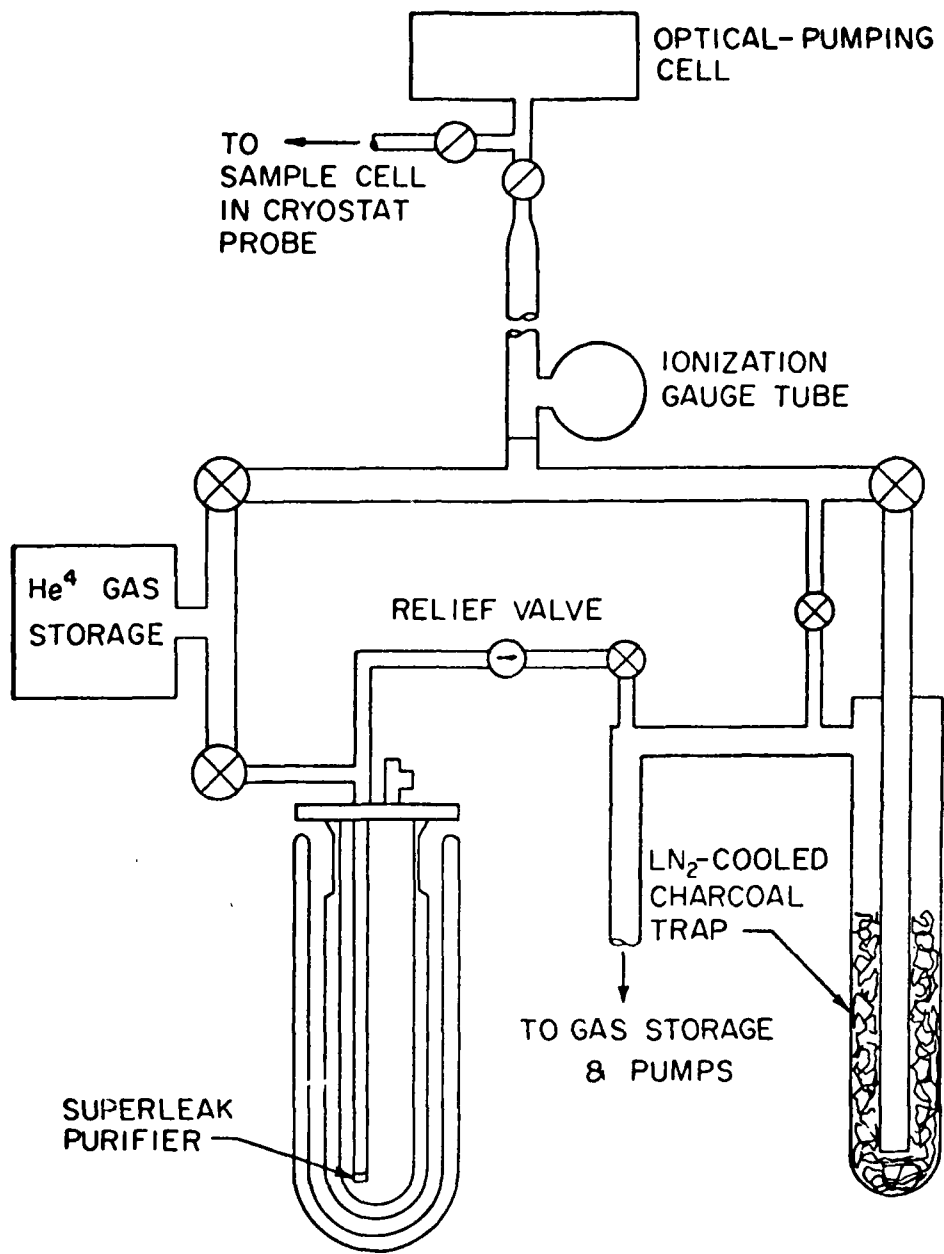


Fig. 2.4 Gas-handling and purification apparatus.

to be studying dilute  $\text{He}^3$ -liquid  $\text{He}^4$  mixtures, it was obvious that the purity of the  $\text{He}^4$  would be of greater importance than that of the  $\text{He}^3$ . Of greatest concern was contamination by molecular oxygen since it exhibits electronic paramagnetism. As will be noted in the next chapter, the interaction with an electronic spin is approximately  $10^6$  times more effective in inducing nuclear relaxation than is the interaction with another nuclear spin. Since most of our experiments had  $\text{He}^3$  concentrations in the neighborhood of 1 part in  $10^3$ , the  $\text{O}_2$  concentration in the  $\text{He}^4$  should be kept below  $10^{-9}$ ,

Our design of the superleak purifier was based on data published by Brewer, Champeney, and Mendelssohn<sup>36</sup> on superfluidity of  $\text{He}^4$  in porous Vycor (Corning Glass No. 7930). Details of the purifier design are shown in Fig. 2.5.

The Vycor disc (0.050 in thick  $\times$  0.30 in diam) was sealed with indium and clamped by pressure exerted by a stack of loaded stainless steel Belleville spring washers. Indium was also used on the unsealed side in order to provide cushioning. The spring washers were compressed sufficiently to provide  $\sim 30$  lb of clamping force as estimated from the manufacturer's specifications. This was approximately ten times the maximum force that would occur from gas pressure on the clean side of the purifier so that there was no danger of the Vycor button becoming unseated during use.

The operation of the superleak was straightforward. The 1½ in i.d. glass helium dewar which was used with the superleak was filled with liquid helium and then cooled through the lambda point by pumping on the bath. At the same time the superleak tube was open to the storage

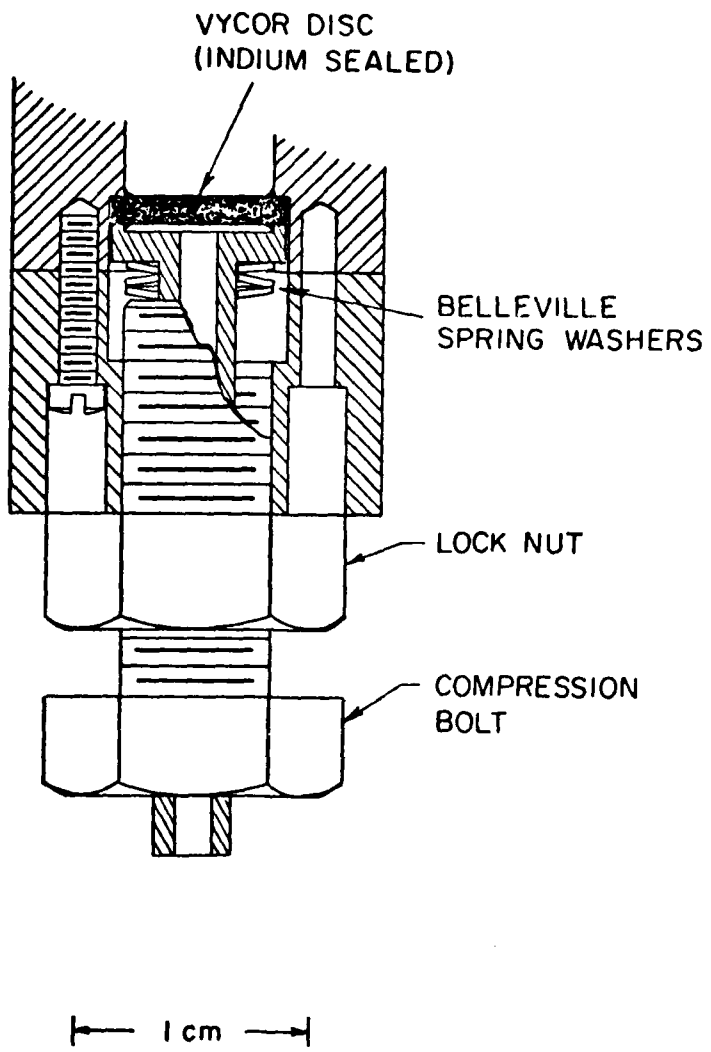


Fig. 2.5 Detail of Vycor superleak  $\text{He}^4$  purifier.

container and was being pumped on by the small mechanical pump associated with the gas-handling table. In order to prevent back streaming of pump oil vapors, this pump was throttled sufficiently to keep pressure in the pumping line above 0.2 Torr. When the onset of superfluid flow occurred in the Vycor (at a temperature well below the lambda transition in the bulk liquid) a rapid rise in pressure was noted in the pumping line and the valve to the small pump was closed, leaving the superleak open only to the storage container. Pumping on the bath was continued until 10-15 minutes had elapsed after minimum bath pressure was reached. This allowed ample time for the liquid levels to equilibrate.

After this point the pump was shut off and the dewar backfilled with an atmosphere of helium gas. The bath was then boiled away by inserting a copper rod into the dewar. After a short delay, the liquid in the superleak tube would also vaporize and start to warm up. When the pressure in the storage volume reached a preset value, the relief valve (see Fig. 2.4) would fire and the valve between the superleak and the storage container would be closed. This completed the purification procedure.

In actual use, the superleak worked quite reliably. In order to obtain greatest consistency in performance, however, it was found to be helpful to maintain the Vycor in a helium atmosphere when it was not in use. Since exposure of a glass dewar to helium at room temperature will quickly cause the thermal vacuum to become soft, it was necessary to replace the dewar with a brass can between purification runs. Exposure of the Vycor to a normal atmosphere between purification

runs was found to gradually reduce the flow rate of superfluid through the superleak and thus require longer equilibration times. Since porous Vycor is known to be hygroscopic (it can be used as a dessicant) it was speculated that water adsorption was responsible for a reduction in the average pore size.

As a rough check on the purifier, a sample of the purified helium was sent to an analytical lab<sup>37</sup> for mass spectrometer analysis. All impurities were found to be below the limit of detectability: 1 ppm, except for water and hydrogen which had 3 ppm detectability limits.

#### 2.1.4 *Magnetometer and Electronics*

A block diagram of our magnetometer system is shown in Fig. 2.6. Both the SQUID sensor and the mode of operation of the sensor in a magnetometer system are virtually identical to those described by Zimmerman, Thiene, and Harding,<sup>21</sup> and Giffard, Webb and Wheatley.<sup>22</sup> For this reason, we will discuss only those aspects of our system which may be unique or unusual.

The SQUID sensor and the sample cell were separated by ~ 20 cm in order to minimize the effect of a relatively large piece of niobium on the sample magnetization. The two were coupled by the superconducting input circuit which was made entirely of 0.002 in diam insulated niobium wire. Coupling to the sample cell was accomplished with a 6-turn, 1.07 cm diam coil wound in a V-groove on a Delrin<sup>38</sup> form. For maximum coupling efficiency, the inductance of this coil (~ 1  $\mu$ H) approximately matched the inductance of the signal coil mounted in the SQUID.

In addition to these two coils, there was a small series inductance consisting of one turn around a 2.8 mm diameter close-wound solenoid of

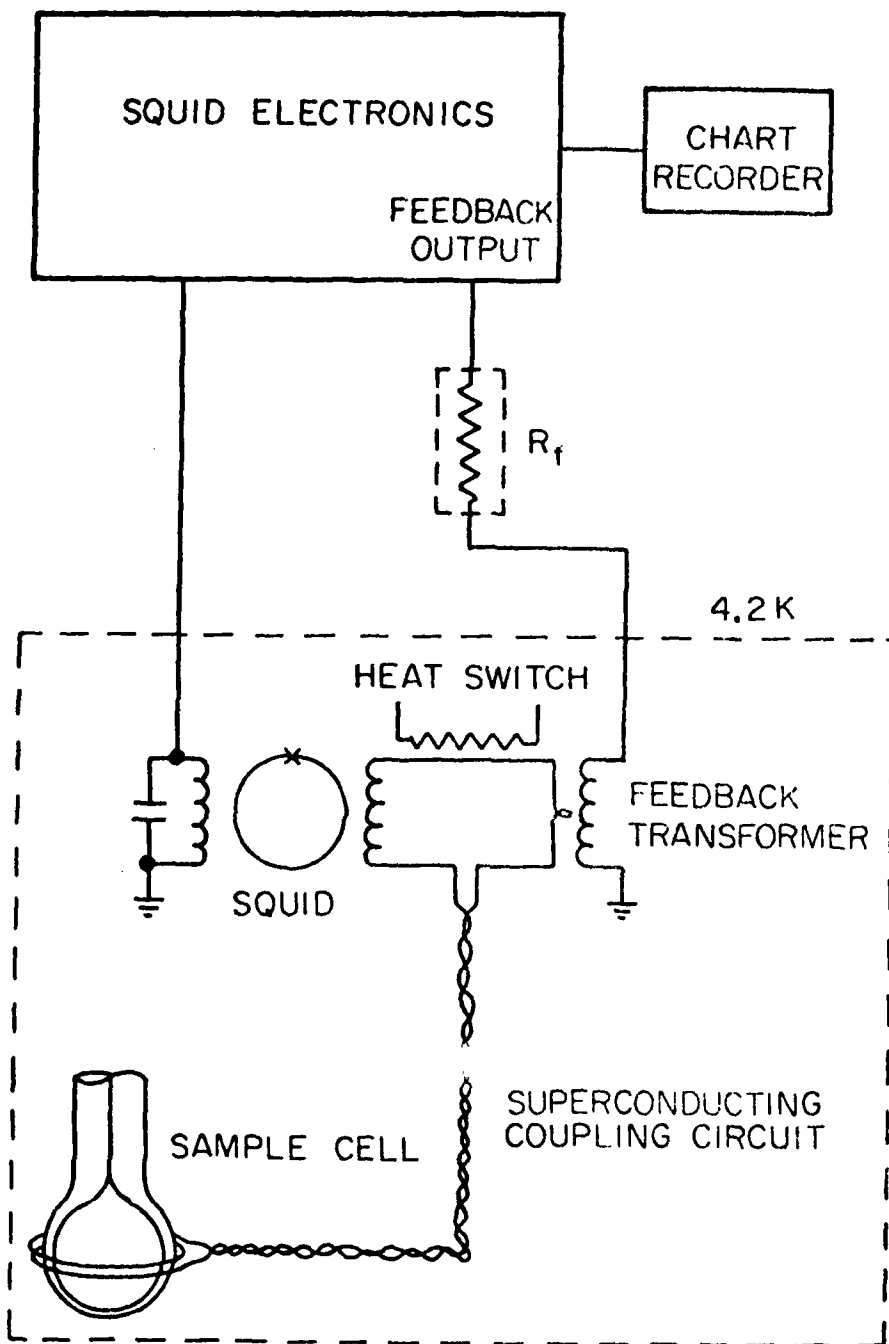


Fig. 2.6 Schematic diagram of SQUID magnetometer system. The feedback resistor,  $R_f$ , was omitted when the compensation system (Fig. 2.7) was used.

of no. 40 copper wire. This solenoid carried the feedback current from the magnetometer electronics and allowed the magnetometer to be run in the "current nulling"<sup>39</sup> mode that was briefly described in Chapter 1. The feedback resistor was selected to yield 2.5 V at the output per flux quantum in the SQUID.

The superconducting input circuit was also equipped with a heater as shown in Fig. 2.6 which could be used to drive a small portion of the circuit normal when necessary.

All together, the SQUID magnetometer system had an estimated total equivalent input flux noise of  $\sim 2.5 \times 10^{-4} \phi_0 \text{ Hz}^{-\frac{1}{2}}$  where  $\phi_0 = 2.07 \times 10^{-7} \text{ G cm}^2 = 2.07 \times 10^{-15} \text{ Wb}$  is the quantum of flux in the SQUID. By using the vertical Helmholtz field coil calibration of  $1.45 \text{ G A}^{-1}$  (the source of this number will be discussed in Sec. 2.2), and by measuring the amount of current into the vertical field coil that was necessary to produce a quantum of flux in the SQUID, it was determined that  $10.5 \mu\text{G}$  of uniform field normal to the plane of the pickup coil produced one  $\phi_0$  in the SQUID. Thus the equivalent magnetic field noise of the magnetometer referred to the pickup coil  $\sim 3 \times 10^{-9} \text{ G Hz}^{-\frac{1}{2}}$ .

After some initial experimental trials involving the actual observation of the magnetization of the polarized  $\text{He}^3$ , it became apparent that it would be very useful to add some specialized electronics beyond the basic magnetometer system. In particular, it was decided to add some circuitry which would sense the currents being applied to the field coils and then supply proportional currents to the feedback transformer in such a fashion as to make the magnetometer virtually insensitive

to the applied magnetic fields.

The primary reason for this decision was due to the manner which was selected to measure the sample magnetization. This technique, which will be discussed below, involved suddenly shifting the direction of the applied field by switching on the horizontal field coils, and then observing the resulting precession of the magnetization with the magnetometer. Since the pickup coil was nominally orthogonal to the horizontal field, the magnetometer was not very sensitive to the horizontal field component. Thus, as long as the sample magnetization was large, this technique presented no problems. When the magnetization signal became small compared to the signal due to stray coupling between the horizontal field and the coupling circuit (but was still large compared to the noise), however, it became both difficult and a nuisance to adjust the chart recorder gain and offset so that a useful record could be obtained.

Thus a compensation circuit was clearly useful for the purpose of eliminating the magnetometer response to the horizontal field coils. In addition, it was decided to build a compensation circuit for the vertical field coils for additional operating convenience. Block diagrams of these circuits are shown in Fig. 2.7. For details on these types of circuits, the reader is referred to any standard reference on operational amplifier applications.<sup>40</sup> The circuits which we built were capable of handling up to about 10 mA and had bypass switches in case compensation was not desired.

#### 2.1.5 *Cryostat Probe*

The outer jacket and primary structural member of the cryostat

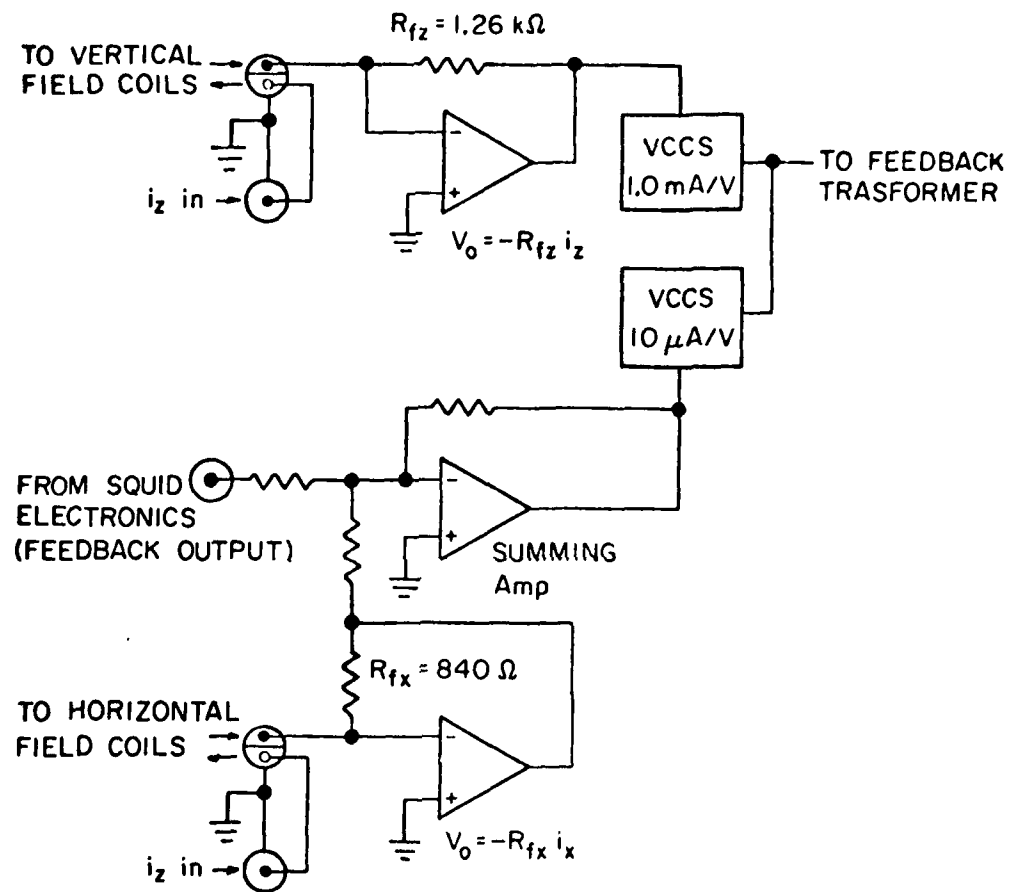


Fig. 2.7 Compensation electronics used to null the response of the magnetometer to the horizontal and vertical field coils. Boxes labeled VCCS represent voltage-controlled constant current sources.

probe was a 66 in  $\times$  4 in o.d.  $\times$  1/8 in wall tube made of G-10 glass-epoxy laminate. This material was chosen because of its low thermal conductivity, good mechanical properties, and nominally non-magnetic character. Aluminum flanges were attached on the ends of this tube with epoxy adhesive. A sliding aluminum flange with a rubber O-ring seal was captive between these end flanges and served to mate to the dewar top-plate. This allowed the probe to be slowly lowered into and withdrawn from the liquid bath while preventing convective mixing between the helium vapor and normal atmospheric gases.

The sample cell, field coils, and magnetometer were housed in a demountable aluminum can which bolted to the lower G-10-tube flange with an indium seal. The primary function of this can was to provide mechanical protection for the internal apparatus. Aluminum was chosen because it exhibits very low remanent magnetization at low temperatures.<sup>17</sup>

The sample bulb and a portion of the capillary fill line together with the coil assembly are shown in Fig. 2.8. The fill line was a nominal 0.5 mm-bore Pyrex capillary with a  $\sim$  0.1 mm-bore constricted section 1 cm long just above the sample cell. This constriction was included in order to limit diffusion in and out of the sample cell after it had been filled with liquid. The sample cell was blown out of Pyrex and had an outside diameter of  $\sim$  9.5 mm and an estimated inside diameter of 9 mm.

After the capillary and sample bulb had been connected to the optical pumping system, but before the rest of the probe was assembled, the capillary and sample cell were subjected to a plasma cleaning procedure. This involved filling the capillary and sample cell with 10 Torr of clean helium and then simultaneously torch baking with a soft flame

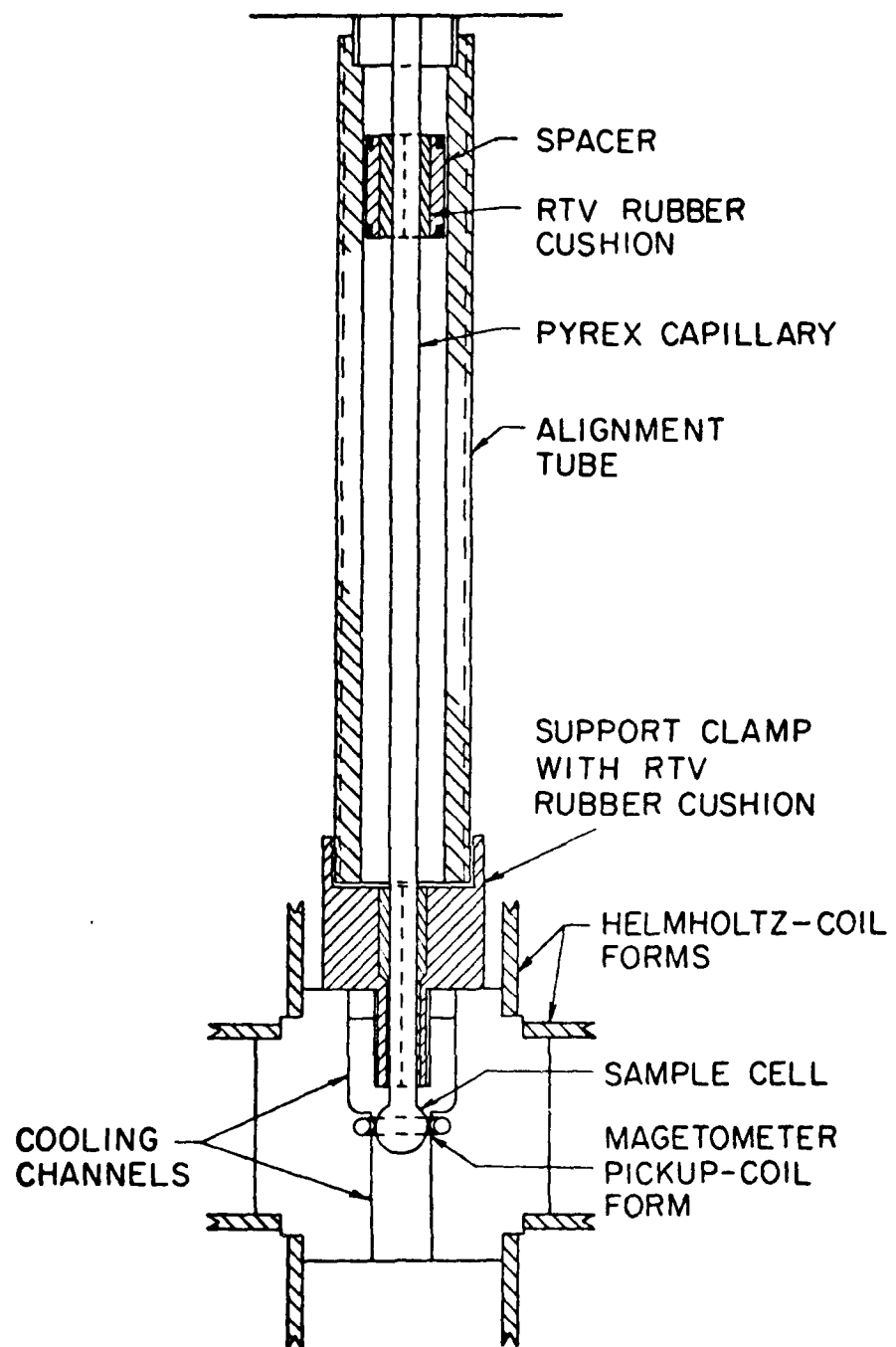


Fig. 2.8 Detail of sample cell and coil assembly. Alignment tube acts as a coil form for the guide solenoid and provides horizontal alignment (but no vertical support) for the coil assembly.

and igniting a plasma discharge in the helium with a hand-held tesla coil. The helium was then pumped out while this process was continued. This whole procedure was repeated several times until no further progress was noted in the purity of the helium spectral lines emitted from the discharge as observed with a pocket spectroscope. In addition to the plasma cleaning, this technique has the advantage of flushing out impurity species since at 10 Torr pressure, the helium is well in the viscous flow region even in the 0.1 mm-bore constriction.

The coil assembly shown in Fig. 2.8 held both the vertical and horizontal field coils as well as the pickup coil. The entire assembly was made of unpigmented Delrin with the exception of the small pieces of RTV silicone rubber shown and natural Nylon screws.

It should be noted that the entire coil assembly was supported by the fill-line capillary and an additional glass capillary which served only as mechanical support. The assembly was clamped on the capillary with the RTV silicone rubber acting as a cushion. This was done in order to keep the coils centered on the sample bulb regardless of differential thermal contraction between the glass capillary and the rest of the cryostat probe. It was considered prudent to avoid subjecting the capillary to the stress that would occur if both ends were clamped with respect to the G-10 housing. This technique was not totally successful as will be discussed in Chapter 4.

The vertical channels in the Delrin block were included in order to allow the exchange gas to convectively cool the sample cell during the condensation of the  $\text{He}^3$ - $\text{He}^4$  mixture.

Both the vertical and horizontal Helmholtz coils consisted of a

total of 12 turns of no. 40 copper wire wound in V-grooves machined in Delrin coil forms. The two halves of each Helmholtz pair were wired in series but with center taps so that the current in each half could be controlled separately if desired. This made it possible to feed current in opposition to the two halves so that a known magnetic-field gradient could be applied to the sample.

The vertical coil pair had a 7.09 cm diameter yielding a calculated field-to-current ratio of  $1.52 \text{ G A}^{-1}$  and a maximum variation of the axial-field component of  $\sim \pm 3 \times 10^{-4}$  over the sample volume. The horizontal pair had a diameter of 8.10 cm yielding a calculated field-to-current ratio of  $1.33 \text{ G A}^{-1}$  and a somewhat better uniformity than the vertical pair.

Because of the presence of the superconducting shield, however, these numbers can only be approximate. By considering the superconducting shield to be spherical, it is not difficult to see that the correction to the magnitude of the magnetic field is on the order of  $(a/R_s)^3$ , where  $a$  is the radius of the coil and  $R_s$  is the radius of the shield. (This result is obtained in Appendix C as a part of the more general calculation needed for Chapter 5.) In our present case this correction amounts to an effective reduction in the field-to-current ratios by  $\sim 5\%$ . Since the nuclear gyromagnetic ratio of  $\text{He}^3$  is accurately known, these ratios were experimentally determined (see Sec. 2.2.5) and were found to be  $1.45 \text{ G A}^{-1}$  for the vertical pair and  $1.27 \text{ G A}^{-1}$  for the horizontal.

Only the horizontal coils were used experimentally to generate field gradients. The gradient generated by a Helmholtz pair fed in

opposition is given by<sup>41</sup>

$$(\partial B_x / \partial x)_{x=0} = 48\pi NI / (125 \sqrt{5} a^2) , \quad (2.1)$$

where  $x$  is the axial coordinate for the horizontal pair,  $N$  is the total number of turns, and  $a$  is the cylindrical radius of the coils. In this expression, the current is in amps, dimensions are in cm, and the field is in Gauss. Numerically (2.1) yields  $(\partial B_x / \partial x)_{x=0} I^{-1} = 0.394 \text{ G cm}^{-1} \text{ A}^{-1}$  for the horizontal pair. The lowest order relative gradient error is second order and is expected to cause a maximum variation of  $\pm 4\%$  over the sample volume. It can be shown that the effect of the superconducting shield on the gradient is small--a reduction on the order of  $(a/R_s)^5$  which is  $\sim 1\%$  in the present case.

In addition to the field coils for the sample cell, a 2.5 cm diam solenoidal winding having a pitch of 7.87 turns  $\text{cm}^{-1}$  ( $9.9 \text{ G A}^{-1}$ ) was provided for virtually the full length of the fill capillary. This solenoid was used only during the sample filling process in order to prevent the possibility of exposing the polarized  $\text{He}^3$  to any non-adiabatic variations in magnetic field.

## 2.2 Experimental Procedures

### 2.2.1 $\text{He}^4$ Requirement

The  $\text{He}^4$  pressure in the optical pumping bulb prior to condensation of the mixture is determined by the setting of the relief valve used to limit the pressure of the purified  $\text{He}^4$  in the storage volume.

Initially it was thought that the proper  $\text{He}^4$  pressure would be that which was sufficient to just fill the sample cell. It was estimated

that  $\sim 2$  atm of  $\text{He}^4$  in the optical pumping cell would accomplish this. There was some concern, however, about how long the filling time would be under these circumstances. A long filling time was considered to be undesirable because of the possibility that it could become a significant fraction of the  $\text{He}^3$  wall-induced relaxation time in the 0.5 mm-bore capillary with its large surface-area-to-volume ratio.

As a consequence, a dummy apparatus consisting of the sample cell and its constriction, a helical segment of 0.5 mm-bore capillary having the same length as the fill line in the cryostat probe, a spare optical-pumping cell, and two stopcocks was constructed. This dummy apparatus was sufficiently compact to allow the sample bulb and helical fill line to be immersed in a liquid helium bath in a small glass dewar so that the filling process could be visually observed. It was found that although the sample cell initially filled quite quickly ( $\sim \frac{1}{2}$  full in 10 sec), the upper 1/3 of the cell was very slow to fill. This was probably due to two factors: 1) the drop in the pressure in the pumping cell, and 2) the greater wall thickness of the sample cell in the top portion (see Fig. 4.5 for an enlarged schematic depiction of the sample cell). This latter factor meant that the path of lowest thermal resistance was through the bottom of the cell. This situation could lead to stratification of the liquid and slow thermal relaxation of the upper portion of the sample cell.

It was found, however, that if an initial pressure of 2.7 atm was used, the sample cell would fill quite quickly ( $\sim 20$  sec). Although this pressure would eventually lead to the liquid-vapor interface being somewhere in the fill line, it was not judged to be a significant

problem, and this figure was adopted as standard. It was then experimentally determined that a pressure of 4.9 atm in the  $\text{He}^4$  storage volume would be quite sufficient to yield 2.7 atm in the pumping cell. The relief valve was then set to this value. According to manufacturer's specifications, the cracking pressure of the relief valve is subject to a 5% variation.

### 2.2.2 $\text{He}^3$ Density

The range of  $\text{He}^3$  concentrations that can be used is constrained by the limited pressure range over which the optical-pumping process is capable of producing a useful polarization. Given the fact that this process works in the vicinity of 1 Torr pressure, it was estimated that  $\text{He}^3$ - $\text{He}^4$  ratios on the order of  $10^{-3}$  would be obtained at 4.2 K. In making this estimate, it is important to note that in dilute mixtures of  $\text{He}^3$  in  $\text{He}^4$  under the saturated vapor,  $C_V/C_L = 1.4$  at 4.21 K, where  $C_V$  is the  $\text{He}^3$  concentration in the vapor and  $C_L$  is the concentration in the liquid.<sup>42</sup> Thus, since the density of  $\text{He}^4$  at NBP is approximately 7.5 times that of the saturated vapor,<sup>43</sup> the  $\text{He}^3$  number density is approximately 5 times greater in the liquid than in the vapor. This leads to a considerable increase in the  $\text{He}^3$  density over the value that would be obtained if no  $\text{He}^4$  or only  $\text{He}^4$  gas were used.

Because of uncertainties involved in making *a priori* estimates of the  $\text{He}^3$  density in the sample cell, it was decided that a measurement of the  $\text{He}^3$ - $\text{He}^4$  ratio should be made. After one of our experimental runs where 1 Torr of  $\text{He}^3$  had been originally loaded into the optical pumping bulb (this was a typical value), the vapor in the pumping cell was pumped out and discarded and the liquid sample was then withdrawn

into a sampling vessel for mass spectrometer analysis. The results<sup>37</sup> showed the He<sup>3</sup> concentration to be  $6.9 \times 10^{-4}$ . This corresponds to a molar density of  $2.2 \times 10^{-5}$  mol cm<sup>-3</sup> which is equal to the density of 0.48 atm of an ideal gas at STP.

In those few experimental runs where the initial He<sup>3</sup> pressure was other than 1 Torr, it was assumed that the He<sup>3</sup> density in the sample cell mixture was directly proportional to the initial He<sup>3</sup> pressure. This pressure was measured with an oil manometer which could be read to  $\pm 0.05$  Torr.

#### 2.2.3 Start-up Procedure

If a cryogenic wall coating (e.g., hydrogen, or argon) was to be used, or if it was necessary to remove the cryogenic wall coating from the previous run, the first step in the start-up procedure was to pump out the sample cell while the cryostat probe was at room temperature and backfill with an appropriate pressure of the wall-coating gas. The stopcock at the top of the capillary was then closed off and the probe was cooled down by slowly lowering into the dewar. A generous amount (1 atm at room temperature) of helium exchange gas was kept inside of the probe. The cooldown process usually took about two hours. The heat capacity of the probe was sufficiently small that it usually displaced more liquid helium than it boiled off, and the liquid level in the dewar would typically be two to three inches higher after the probe was fully lowered than at the start.

After the cryostat probe was in position in the dewar, the pumping cell was cleaned and loaded with He<sup>3</sup>, and the He<sup>4</sup> storage tank was pressurized with purified He<sup>4</sup>. The optical pumping apparatus was then

checked. If an acceptable absorption signal was obtained the run was then begun.

Before condensation of the sample, the magnetic fields were set as follows: optical-pumping Helmholtz coils, 10 G; capillary solenoid, 1 G; sample cell vertical coils, 0.1 G. Care was taken to insure that all of these fields had the same polarity. After the He<sup>3</sup> was polarized, the weak discharge was turned off and the high pressure He<sup>4</sup> was admitted to the pumping cell by briefly opening the appropriate stopcock. The He<sup>3</sup>-He<sup>4</sup> mixture was then condensed into the sample cell by opening the capillary stopcock. This stopcock was left open during the duration of a run so that the pumping bulb could act as a ballast volume. This prevented large increases in pressure in the sample cell due to changes in the temperature profile along the cryostat probe as the helium bath level fell during normal boil-off.

It was usually possible to monitor the condensation process with the magnetometer. A typical condensation curve is shown in Fig. 2.9. The magnetometer invariably lost lock at the start of the condensation, probably due to the large thermal impulse. If the magnetometer was immediately reset, however, the buildup of the magnetization due to accumulation of liquid could be clearly observed. Buildup of the magnetization usually ceased after about three minutes. After about five minutes, all magnetic fields were turned off except for the field at the sample cell which was reduced to a few mG.

In the early runs an exponentially decaying signal having a time constant on the order of minutes was noted soon after condensation. It was determined that this signal was not due to nuclear relaxation

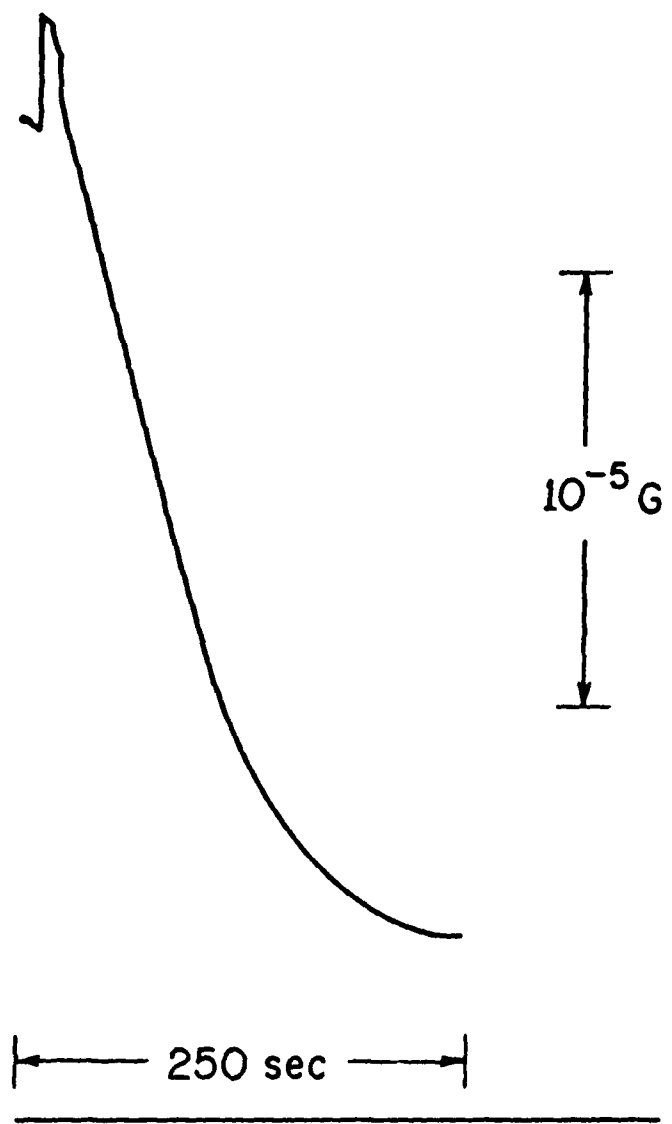


Fig. 2.9 Typical condensation signal.

of the  $\text{He}^3$ , and it was therefore attributed to magnetometer drift due to thermal relaxation of the interior of the cryostat probe. Subsequently a one hour equilibration time was allowed at the beginning of a run before any data was taken. This was done not only for the sake of reducing magnetometer drift but also for the sake of allowing the  $\text{He}^3$  density in the sample to equilibrate.

#### 2.2.4 $T_1$ Measurement Procedure

Most of our measurements were of the longitudinal nuclear relaxation time. In principle, this measurement could be made by simply monitoring the decay of the sample magnetization with the magnetometer as it remained aligned in the applied field. In practice, however, because the nuclear relaxation times were generally quite long and the potential for magnetometer drift due to thermal effects existed (particularly during and after a helium transfer), we elected to use a transitory precession technique for measuring the magnitude of the magnetization.<sup>44</sup> The dc output of the magnetometer was useful as a guide to deciding when to make the precession measurements.

The transitory precession technique is shown schematically in Fig. 2.10. In order to make a precession measurement of the magnetization, the vertical field  $\vec{B}_0 = B_0 \hat{k}$  was first adjusted to a standard value  $B_{sz} = 55 \mu\text{G}$ . Then a horizontal field  $B_{sx} = B_{sz}$  was switched on causing a sudden shift in the direction of the applied field by  $45^\circ$ . The magnetization would then precess in a cone having a half-angle of  $45^\circ$  at a frequency  $(\sqrt{2} \gamma/2\pi)B_{sx} = 0.25 \text{ Hz}$ . The output of the magnetometer, which was recorded on a chart recorder, would vary sinusoidally with an amplitude directly proportional to the magnitude of the magnet-

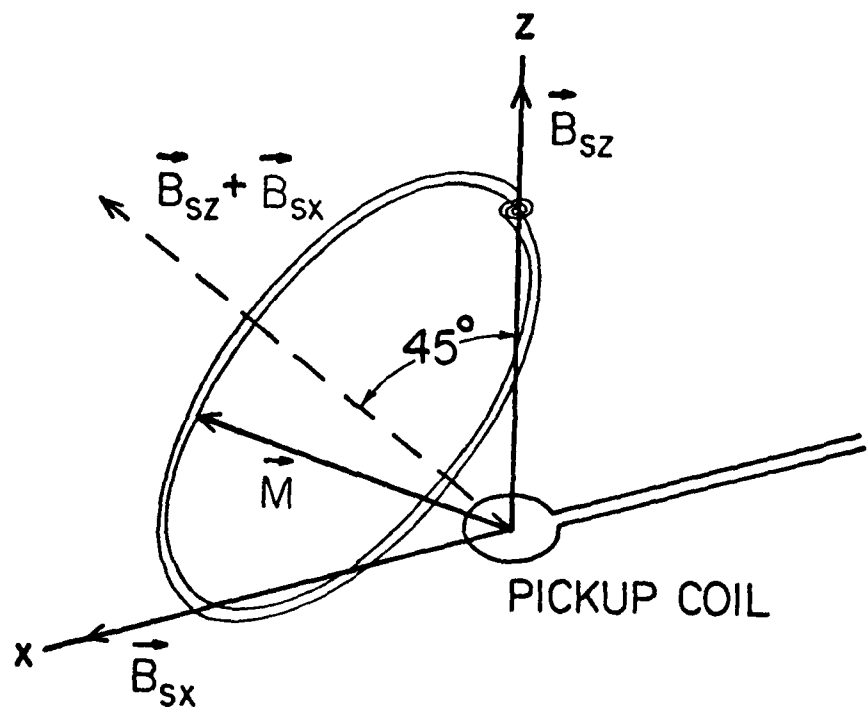


Fig. 2.10 Diagram of the transitory precession technique used to measure the magnitude of the sample magnetization.

ization. After two complete cycles had elapsed,  $B_{sx}$  was switched off, leaving the magnetization once again aligned with  $B_{sz}$ . Examples of the chart recorder output from two sequential precession measurements are shown in Fig. 2.11.

The magnitude of  $B_{sz}$  was chosen to be sufficiently small that  $B_{sx}$  could be switched manually, yet still be much larger than the ambient field.

It should be noted that it was not essential that the field be shifted by  $45^\circ$  as long as the angular shift was the same from one measurement to the next. This was a convenient choice, however, for the following reason: Because of a gradient in the ambient magnetic field (this will be discussed in detail in Chapter 4) the magnitude of the average magnetization decayed somewhat during precession due to dephasing. This loss in magnetization is clearly seen in Fig. 2.11 as a baseline offset that remained after  $B_{sx}$  was switched off.

In order to estimate the relaxation time, it is necessary then to compare the initial magnetization of one measurement with the final magnetization of the preceding one. Since the precession cone had a half-angle of  $45^\circ$ , however, it was possible to estimate the initial magnetization (with sufficient accuracy for our purposes) by measuring the height of the first peak with respect to the *initial* baseline, and to estimate the final magnetization by measuring the height of this peak with respect to the *final* baseline.

Thus, if  $S_{nf}$  is the height of the first peak with respect to the final baseline in the  $n$ -th measurement, and  $S_{n+1,i}$  is the height of the first peak with respect to the initial baseline in the  $(n+1)$ -th

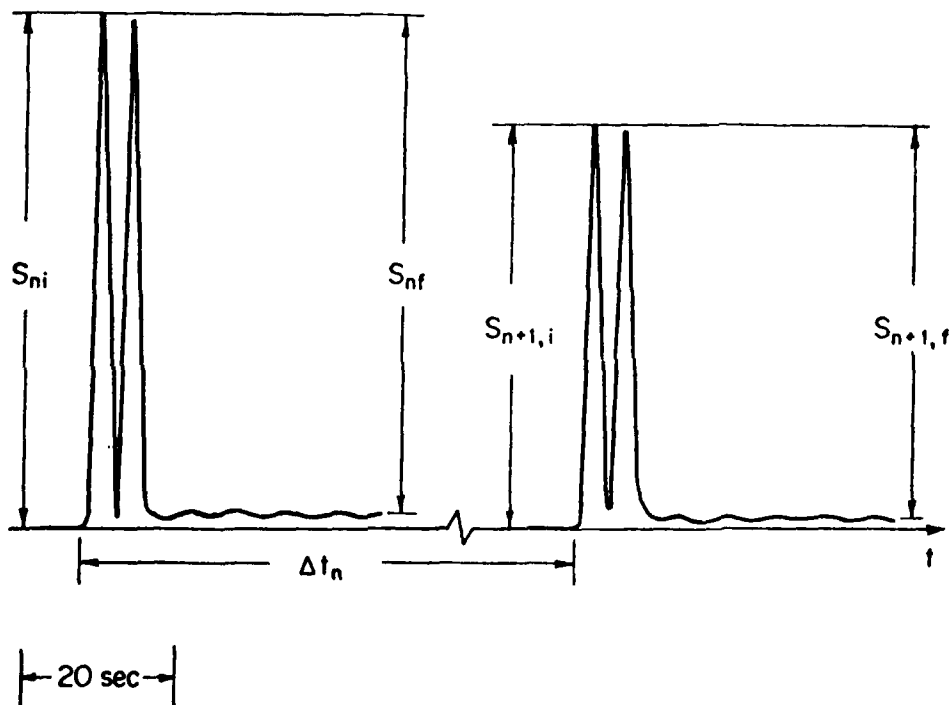


Fig. 2.11 Typical data record of two sequential measurements of the sample magnetization using the transitory precession technique. The time between measurements,  $\Delta t_n$ , ranged between one hour and more than a day depending on the estimated relaxation rate.

measurement, then the longitudinal relaxation time between these two measurements is

$$T_1 = \Delta t_n [\ln(S_{nf}/S_{n+1,i})]^{-1},$$

where  $\Delta t_n$  is the time interval between the measurements. The use of this expression obviously assumes that the decay of  $M_z$  is exponential in time. Corroboration of this assumption will be shown in Chapter 4.

The effect of dephasing due to a magnetic field gradient is shown schematically in Fig. 2.10 as a slight inward spiralling of the transverse component of  $\vec{M}$ .

#### 2.2.5 Full Free-Precession Decay Measurements

It was occasionally useful to use the precession technique where the transverse component of the magnetization was allowed to decay to zero. There were two reasons to do this: 1) it yielded a reasonably accurate measurement of the average field over the sample volume thereby allowing calibration of the field coils, and 2) it permitted an estimate of the average field gradient to be made. The relationship between the waveform obtained in a free-precession decay and the magnetic field profile (or shape factor) will be noted in general terms in Chapter 3.

The procedure that was used to make the average field measurements started exactly as was described in the previous section. In order to make a more accurate frequency measurement, however,  $B_{sx}$  was left on and the transverse magnetization was allowed to decay to zero. Fig. 2.12 shows an example of such a decay. Since the applied fields are much larger than the ambient field, the precession rate is approximately  $|\omega_0| \approx \gamma(|\vec{B}_s| + \vec{B}_a \cdot \hat{s})$ , where  $\vec{B}_a$  is the ambient field,  $\vec{B}_s$  is

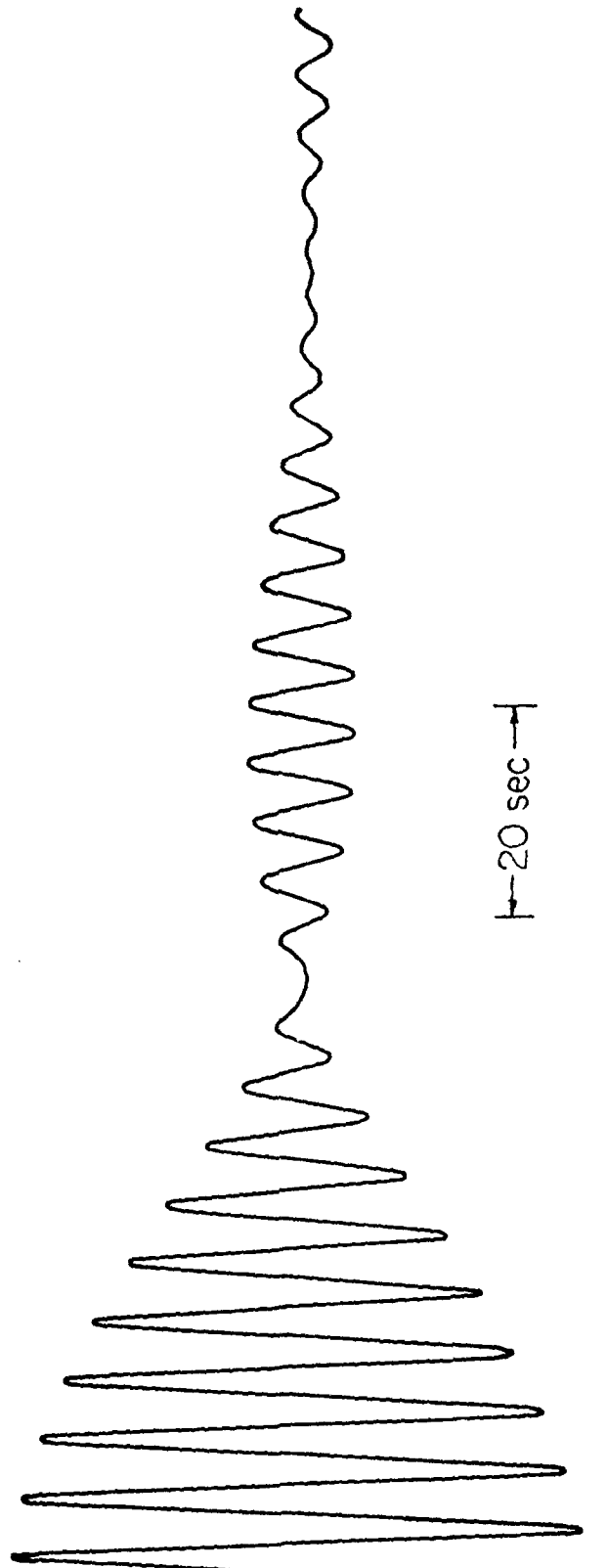


Fig. 2.12 Example of a full precession decay.

the applied field, and  $\hat{s} = \vec{B}_s / |\vec{B}_s|$ .

The process of suddenly switching the applied field and letting the transverse magnetization decay to zero while recording the waveform of  $M_z$  was carried out in the following sequence:  $B_{sz}\hat{k} + (B_{sx}\hat{i} + B_{sz}\hat{k}) + B_{sx}\hat{i} + (-B_{sx}\hat{i}) + (-B_{sx}\hat{i} - B_{sz}\hat{k}) + (-B_{sx}\hat{i})$ . (The field reversal step  $B_{sx}\hat{i} + -B_{sx}\hat{i}$  caused a precession of small amplitude that was not recorded.) The precession frequencies obtained when  $\vec{B}_s = B_{sx}\hat{i}$  and  $\vec{B}_s = -B_{sx}\hat{i}$  were averaged in order to eliminate the effect of  $B_{ax}$ . In this way, the horizontal pair of field coils were directly calibrated. Similarly, the frequencies obtained when  $\vec{B}_s = \pm (B_{sx}\hat{i} + B_{sz}\hat{k})$  were averaged, and the vertical field coils could be calibrated by vector subtraction of  $B_{sx}$ . No precessions about the  $z$  axis were used since the pickup coil was only sensitive to the  $z$  component of  $\vec{M}$ .

The field calibration obtained for the vertical coils was 4.5% lower than that expected for Helmholtz coils in free space, and similarly the calibration for the horizontal pair was 4.9% lower than the calculated value. As has been noted, these discrepancies are consistent with the estimated effect of a 8 in diam superconducting shield. It is also possible that dimensional changes between room temperature and 4.2 K could play a role although this would presumably cause the field level to increase rather than decrease.

#### 2.2.6 *Ambient Field Estimation*

It was useful for us to make an experimental estimate of the magnitude of the ambient magnetic field at the sample cell independently of Cabrera's measurements.<sup>17</sup> There was a possibility that remanent fields associated with our cryostat probe could have a sig-

nificant impact on the ambient field. Once the magnitude of this field was known, the applied fields could be kept sufficiently large so that the effect of the ambient field would be minimal.

The technique that was used to estimate  $|\vec{B}_a|$  was to suddenly turn off  $B_0$  and allow the sample magnetization to slowly precess in the ambient field. This was done in several different experimental runs, typically near the end when the signal-to-noise ratio was becoming marginal. A typical example is shown in Fig. 2.13.

The ambient field was not sufficiently homogeneous to make this a very accurate measurement as can be seen in this figure. It can be estimated from these precessional decays, however, that the ambient field was on the order of 3  $\mu\text{G}$ . This compares to a value of 5  $\mu\text{G}$  obtained by Cabrera.

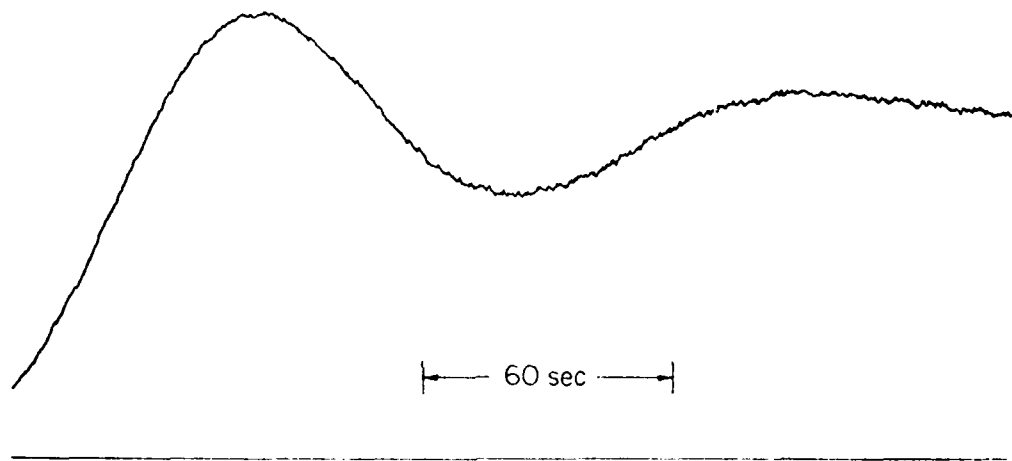


Fig. 2.13 Precession and decay in the ambient magnetic field

## CHAPTER 3

### THEORY OF $\text{He}^3$ NUCLEAR RELAXATION

Nuclear relaxation is the process of thermal equilibration between the nuclear degrees of freedom and those of the lattice. The random thermal motions of the lattice coordinates are coupled to the nuclear spins through the spatial and angular variation of various nuclear electromagnetic interactions. Details of this process depend on the initial state of the system, the presence of externally applied fields, electromagnetic moments of the nuclear species involved, and the nature of the lattice.

For the specific case at hand, these various attributes can be characterized as follows:

- 1) The nuclear spins are initially preferentially oriented, *i.e.*, polarized, such that the sample has a macroscopic magnetization.
- 2) The applied uniform magnetic field,  $\vec{B}_0$ , will be considered to be of arbitrary magnitude (including zero) but in any case will be sufficiently small that the equilibrium magnetization,  $\vec{M}_0$ , is completely negligible.
- 3) The nuclear species is spin-½ with only a magnetic-dipole moment.
- 4) The nuclei belong to a monatomic species in a *classical* liquid or gas. The lattice can be considered to be a true thermal reservoir.

As was noted in the first chapter, the specific magnetic interactions include the  $\text{He}^3$ - $\text{He}^3$  dipole-dipole interaction, the  $\text{He}^3$ -magnetic gradient interaction, and  $\text{He}^3$ -foreign spin dipolar or scalar interactions.

In this chapter, we will review the theory of nuclear relaxation in sufficient depth to deal with the physical circumstances described above. The general theory will first be discussed and applied to a simple example. We will then review some of the theoretical models that have been developed to deal with gradient-induced, intrinsic, and wall-induced relaxation of  $\text{He}^3$ .

### 3.1 General Theory

We will now briefly summarize the semi-classical formulation of spin-relaxation theory in liquids and gases as discussed by Abragam.<sup>1</sup> We will also follow his notation in most cases.

In the semi-classical formulation, the spin system is described quantum mechanically by use of the density matrix with its equation of motion, while the lattice coordinates are introduced into the Hamiltonian as classical stationary random functions of time. A suitable ensemble average can then be made to obtain the desired result.\*

The Hamiltonian for the spin system is written

$$\hbar H = \hbar [H_0 + H_1(t)],$$

---

\* It will be recalled that the spin density matrix represents an average over an ensemble of spins or spin systems. The equation of motion must then be averaged over an ensemble of *lattice* systems in order to take into account the statistical nature of the lattice coordinates. A full quantum treatment would describe both the lattice and spin systems with a single density matrix.<sup>1</sup>

where  $\hbar H_0 = - \vec{\mu} \cdot \vec{B}_0 = - \gamma \vec{h} \vec{I} \cdot \vec{B}_0$ . The perturbation Hamiltonian,  $\hbar H_1$ , is assumed to represent a stationary random interaction with a zero-mean expectation value. If a physical situation arises where this latter assumption does not hold,  $H_0$  can be redefined to include the non-zero mean of the perturbation.

The equation of motion for the spin density matrix operator  $\rho(t)$  is

$$i d\rho/dt = [H, \rho(t)].$$

In the interaction representation (denoted by an asterisk), this becomes

$$i d\rho^*/dt = [H_1^*(t), \rho^*(t)],$$

where an arbitrary Schrödinger operator  $Q(t)$  is converted to the interaction representation by the expression

$$Q^*(t) = e^{iH_0 t} Q(t) e^{-iH_0 t}.$$

We note that working in the interaction representation is equivalent in this case to working in a frame of reference rotating with an angular velocity  $\vec{\omega}_0 = -\gamma \vec{B}_0$ . (It should be remembered that this applies only to the spins. That is, the position coordinates are not transformed by  $H_0$ .)

If we now assume that the perturbation  $H_1(t)$  is characterizable by a correlation time  $\tau_c$ , and most importantly that  $\tau_c$  is sufficiently short that  $\rho^*(\tau_c) - \rho^*(0) \ll \rho^*(0)$  for all matrix elements of  $\rho^*$ , then it can be shown that<sup>1</sup>

$$\overline{\frac{d\rho^*(t)}{dt}} = - \int_0^\infty d\tau \overline{[H_1^*(t), [H_1^*(t-\tau), \rho^*(t)]]}, \quad [3.1]$$

where the bar indicates a lattice ensemble average. The bar over  $\rho^*$  will henceforth be omitted and it will be understood that  $\rho^*(t)$  will refer to an average of spin density matrix operators. It should be emphasized that equation [3.1] is valid only on a scale of times that are much longer than  $\tau_c^*$ .

The requirement that  $\rho^*$  changes very little in a time interval  $\tau_c^*$  implies a sufficient condition that  $\overline{|H_1|^2} \tau_c^2 \ll 1$ . This condition is called the "motional narrowing" condition because of the effect it has on NMR linewidths. Although the motional narrowing condition is necessary for general validity of the theory, there exists a narrow context in which it may be replaced by a different requirement. This point will be discussed in the section on gradient-induced relaxation (Sec. 3.3).

Of course, one is generally not interested in the motion of the density matrix itself but rather in the motion of the expectation values of the observable variables, which may be calculated from the density matrix. Thus, if  $Q$  is an operator representing an observable of interest, then

$$\langle Q \rangle = \text{Tr}(\rho Q),$$

and

$$\frac{d\langle Q \rangle}{dt} = \text{Tr}[(d\rho/dt)Q],$$

where  $\text{Tr}$  signifies the trace of the following operator. Since the motion of  $\rho$  in the Schrödinger representation (lab frame) includes

the precessional motion around the static field  $\vec{B}_0$ , it is actually more convenient to calculate a different expectation value:

$\langle Q \rangle^* = \text{Tr}(\rho^* Q)$ , where  $Q$  is still a Schrödinger operator and  $\rho^*$  is in the interaction representation (rotating frame).  $\langle Q \rangle^*$  is the value of  $Q$  that would be measured in the rotating frame where only the motion due to the perturbation Hamiltonian  $H_1^*$  is seen. Hence

$$d\langle Q \rangle^*/dt = \text{Tr}[(d\rho^*/dt)Q], \quad [3.2]$$

where it is assumed that  $Q$  is a time-independent Schrödinger operator.

By combining [3.1] and [3.2] we have

$$d\langle Q \rangle^*/dt = - \langle A \rangle^* \quad [3.3]$$

where

$$A = \int_0^\infty \frac{1}{d\tau [H_1^*(t - \tau), [H_1^*(t), Q]]}. \quad [3.4]$$

### 3.2 A Simple Example

As an illustration of the foregoing, we will apply the general theory to a simple model. In this model, we consider the disorientation produced by subjecting a spin to an externally applied random magnetic field,  $\vec{B}_1(t)$ . The Hamiltonian is then

$$\hbar H = \hbar H_0 + \hbar H_1(t),$$

where

$$H_0 = - \gamma B_0 I_z = \omega_0 I_z, \quad \omega_0 = - \gamma B_0,$$

$$H_1 = - \gamma \vec{I} \cdot \vec{B}_1(t) = - \gamma \sum_q B_1^{(-q)}(t) I^{(q)},$$

and

$$\overline{\vec{B}_1(t)} = 0.$$

In the latter expression for  $H_1(t)$ , we have used spherical vectors:

$$B_1^{(\pm 1)} = \frac{1}{2}(B_{1x} \pm iB_{1y}), \quad B_1^{(0)} = B_{1z}; \quad [3.5]$$

$$I^{(\pm 1)} = I_x \pm iI_y, \quad I^{(0)} = I_z. \quad [3.6]$$

In this notation, the commutation relations between the components of  $\vec{I}$  are

$$[I^{(\alpha)}, I^{(\beta)}] = (\alpha - \beta)(-1)^{\alpha+\beta} I^{(\alpha+\beta)}.$$

By letting  $Q = I^{(k)}$  in equations [3.3] and [3.4], we have

$$\begin{aligned} d\langle I^{(k)} \rangle^*/dt = -\gamma^2 \text{Tr} \left\{ \rho^*(t) \sum_{qq'} \int_0^\infty d\tau \overline{B_1^{(-q)}(t-\tau) B_1^{(-q')}(t)} \cdot \right. \\ \left. \cdot [I^{(q)}^*(t-\tau), [I^{(q')^*}(t), I^{(k)}]] \right\}. \end{aligned} \quad [3.7]$$

Using the identity

$$e^A B e^{-A} = B + [A, B] + \frac{1}{2!} [A_1 [A, B]] + \frac{1}{3!} [A, [A, [A, B]]] + \dots,$$

it is seen that

$$I^{(q)}^*(t) = e^{iH_0 t} I^{(q)} e^{-iH_0 t} = I^{(q)} e^{iq\omega_0 t}.$$

Making the substitutions into [3.7] and evaluating the commutators yields the result

$$\begin{aligned} d\langle I^{(k)} \rangle^*/dt = - \sum_{qq'} e^{i\omega_0 (q+q')t} (q' - k)(q - q' - k)(-1)^{q+2(q'+k)} \cdot \\ \cdot F_{-q-q'}(-q\omega_0) \langle I^{(q+q'+k)} \rangle^*, \end{aligned} \quad [3.8]$$

where  $F_{qq'}(\omega)$  is a one-sided Fourier transform of the correlation

function  $G_{qq'}(\tau)$ :

$$F_{qq'}(\omega) = \int_0^\infty d\tau e^{i\omega\tau} G_{qq'}(\tau), \quad [3.9]$$

and

$$G_{qq'}(\tau) = \gamma^2 B_1^{(q)}(t - \tau) \overline{B_1^{(q')}(t)}. \quad [3.10]$$

We note that  $F_{-q-q'}(-q\omega_0) = F_{qq'}^{*}(q\omega_0)$  where the asterisk denotes a complex conjugate when used with variables that are not operators.

In equation [3.8] two kinds of terms appear: those which have an oscillating factor  $\exp[i\omega_0(q + q')t]$  (nonsecular terms), and those for which  $\omega_0(q + q') = 0$  (secular terms). Now if the Larmor frequency,  $\omega_0$ , is much larger than the relaxation rates, *i.e.*, the rate of change of  $\langle \vec{I} \rangle^*$ , then the effect of the nonsecular terms is negligible compared to the secular terms and they may be omitted. If this condition is not satisfied, however, there is still one situation which admits a simple analysis: the case where  $\omega_0 = 0$ . In this case, *all* terms in [3.6] are secular.

In either of these two cases we see that equation [3.8] represents a set of first order coupled linear differential equations with constant coefficients in the expectation values  $\langle I^{(k)} \rangle^*$ . The solution of these equations is thus straightforward in these two cases.

If we now consider in detail the most common circumstance, *i.e.*,  $\omega_0 \gg T_{1,2}^{-1}$ , and retain only those terms in [3.8] for which  $q + q' = 0$ , we find

$$d\langle I^{(k)} \rangle^*/dt = - \sum_q (-q-k)(2q-k)(-1)^{q+2(k-q)} F_{-q+q}(-q\omega_0) \langle I^{(k)} \rangle^* \quad [3.11]$$

In these equations, we see that the variables  $\langle I^{(k)} \rangle^*$  are decoupled

from each other;  $d\langle I^{(k)} \rangle^*/dt$  depends only on  $\langle I^{(k)} \rangle^*$ . More explicitly, [3.11] yields

$$d\langle I^{(0)} \rangle^*/dt = -4\text{Re}[F_{-11}(-\omega_0)]\langle I^{(0)} \rangle^*, \quad [3.12]$$

and

$$d\langle I^{(1)} \rangle^*/dt = -[F_{00}(0) + 2F_{-11}(-\omega_0)]\langle I^{(1)} \rangle^*, \quad [3.13]$$

where  $\text{Re}$  denotes the real part. The equation for  $\langle I^{(-1)} \rangle^*$  is simply the complex conjugate of [3.13] and is therefore redundant.

Equation [3.12] shows that  $\langle I_z \rangle$  decays exponentially in time:

$$\langle I^{(0)}(t) \rangle^* = \langle I^{(0)}(0) \rangle^* e^{-t/T_1}$$

where

$$T_1^{-1} = 4\text{Re}F_{-11}(-\omega_0).$$

The physical significance of this expression for the longitudinal relaxation time can be made clearer if the right hand side is expressed in terms of the spectral densities of the Cartesian components of  $\vec{B}_1(t)$ . To do this, we define the correlation functions

$$G_{\alpha\beta}(\tau) = \gamma^2 \overline{B_{1\alpha}(t-\tau)B_{1\beta}(t)}, \quad (\alpha, \beta = x, y, z) \quad [3.14]$$

and their one-sided cosine and sine Fourier transforms

$$j_{\alpha\beta}(\omega) = \int_0^\infty d\tau \cos(\omega\tau)G_{\alpha\beta}(\tau), \quad [3.15a]$$

$$k_{\alpha\beta}(\omega) = \int_0^\infty d\tau \sin(\omega\tau)G_{\alpha\beta}(\tau). \quad [3.15b]$$

Using definitions [3.5], [3.9], and [3.10] we find that

$$T_1^{-1} = j_{xx}(\omega_0) + j_{yy}(\omega_0) + k_{xy}(\omega_0) - k_{yx}(\omega_0). \quad [3.16]$$

Now if it is assumed that  $G_{\alpha\beta}(\tau) = \delta_{\alpha\beta}G_{\alpha\beta}(\tau)$ , and/or that  $G_{\alpha\beta}(\tau) =$

$= G_{\alpha\beta}(-\tau) = G_{\beta\alpha}(\tau)$  (the latter equality being a consequence of the assumption of stationarity in [3.14]), then this expression for  $T_1^{-1}$  reduces to

$$T_1^{-1} = j_{xx}(\omega_0) + j_{yy}(\omega_0). \quad [3.16']$$

This is a simple and physically very plausible result. In essence, the longitudinal relaxation rate is simply the sum of the power spectral densities of the  $x$  and  $y$  components of the perturbation field  $\vec{B}_1(t)$  at the Larmor frequency.

The equation for the transverse component  $\langle I^{(1)} \rangle^*$  is slightly more complicated. Equation [3.13] has the solution

$$\langle I^{(1)}(t) \rangle^* = \langle I^{(1)}(0) \rangle^* \exp[(i\delta\omega - T_2^{-1})t] \quad [3.17]$$

where

$$T_2^{-1} = \text{Re}[F_{00}(0) + 2F_{-11}(-\omega_0)] \quad [3.18]$$

and

$$\delta\omega = -\text{Im}[F_{00}(0) + 2F_{-11}(-\omega_0)]. \quad [3.19]$$

Equivalently [3.18] and [3.19] can be written

$$\begin{aligned} T_2^{-1} &= j_{zz}(0) + \frac{1}{2}T_1^{-1} \\ &= j_{zz}(0) + \frac{1}{2}[j_{xx}(\omega_0) + j_{yy}(\omega_0)], \end{aligned} \quad [3.20]$$

and

$$\begin{aligned} \delta\omega &= \frac{1}{2}[k_{xx}(\omega_0) + k_{yy}(\omega_0) - j_{xy}(\omega_0) + j_{yx}(\omega_0)] \\ &= \frac{1}{2}[k_{xx}(\omega_0) + k_{yy}(\omega_0)], \end{aligned} \quad [3.21]$$

where we have used the same assumption that was used in obtaining [3.16'] from [3.16].

The motion of the transverse component of  $\langle \vec{I} \rangle^*$  is characterized not only by an exponential decay at a rate  $T_2^{-1}$ , but also by an additional precession around the  $z$  axis at a rate  $\delta\omega$  as seen from the rotating frame. The total precession rate as seen from the lab frame is therefore  $\omega_0 + \delta\omega$ .  $\delta\omega$  is called the dynamic frequency shift, and in many circumstances it is too small to be of any consequence.

Although the detailed dependence of  $T_1^{-1}$ ,  $T_2^{-1}$ , and  $\delta\omega$  on  $\omega_0$  cannot be specified without knowledge of the correlation functions  $G_{\alpha\alpha}(\tau)$ , the fact that  $G_{\alpha\alpha}$  must be maximum when  $\tau = 0$  and small when  $\tau = \tau_c$  allows some general statements to be made. In particular, since  $\delta\omega$  arises from sine transforms [3.15b],  $\delta\omega \propto \omega_0$  in the low frequency limit  $\omega_0 \ll \tau_c^{-1}$ . On the other hand,  $T_1^{-1}$  and  $T_2^{-1}$  consist only of cosine transforms [3.15a] and thus become relatively independent of  $\omega_0$  in this limit. These general conclusions will be verified below when a specific form of the correlation function is considered.

It should be remembered that these results were obtained under the assumption that the Larmor frequency is much larger than the relaxation rates. This made it permissible to neglect the nonsecular terms. We now consider the case  $\omega_0 = 0$  as a separate matter.

When  $\omega_0 = 0$ , all terms in equation [3.8] are secular, and consequently it becomes

$$d\langle I^{(k)} \rangle / dt = - \sum_{qq'} (q' - k)(q - q' - k) (-1)^{q+2(q'+k)} \cdot F_{-q-q'}(0) \langle I^{(q+q'+k)} \rangle.$$

Obviously, since  $H_0 = 0$  there is no distinction to be made between

$\langle \vec{I} \rangle$  and  $\langle \vec{I} \rangle^*$ . Also, since  $\vec{B}_0 = 0$ , there is no unique direction defined so that it is merely sufficient to calculate  $d\langle I_z \rangle / dt = d\langle I^{(o)} \rangle / dt$ ; the derivatives of  $\langle I_x \rangle$  and  $\langle I_y \rangle$  are obtainable by cyclic permutation of the coordinates. Thus

$$d\langle I_z \rangle / dt = - 2\text{Re}[- F_{0-1}(0)\langle I^{(1)} \rangle + 2F_{-11}(0)\langle I^{(o)} \rangle]$$

$$= - [- j_{zx}\langle I_x \rangle - j_{zy}\langle I_y \rangle + (j_{xx} + j_{yy})\langle I_z \rangle]$$

where it is understood that  $j_{\alpha\beta} \equiv j_{\alpha\beta}(0)$ . Hence, we obtain the matrix equation

$$d\langle \vec{I} \rangle / dt = - R_c^{(o)} \langle \vec{I} \rangle, \quad [3.22a]$$

where

$$R_c^{(o)} = \begin{pmatrix} j_{yy} + j_{zz} & -j_{xy} & -j_{xz} \\ -j_{yx} & j_{zz} + j_{xx} & -j_{yz} \\ -j_{zx} & -j_{zy} & j_{xx} + j_{yy} \end{pmatrix}. \quad [3.22b]$$

If it is also assumed that  $G_{\alpha\beta} = \delta_{\alpha\beta}G_{\alpha\alpha}$ , then equations [3.22] become

$$d\langle I_\alpha \rangle / dt = - T_\alpha^{-1} \langle I_\alpha \rangle, \quad \alpha = x, y, z; \quad [3.23a]$$

where

$$T_x^{-1} = j_{yy} + j_{zz} (+ \text{cyclic perm.}) . \quad [3.23b]$$

In order to make the foregoing more concrete, we now assume a specific form for the correlation functions. For simplicity, it will be assumed that  $G_{\alpha\beta}(\tau) = \delta_{\alpha\beta}G(\tau)$ , i.e., that  $\vec{B}_1(t)$  is isotropic. A correlation function that is analytically convenient and which

actually arises in approximations to various physical processes is

$$G(\tau) = G(0)e^{-|\tau|/\tau_c}, \quad [3.24a]$$

where

$$G(0) = \gamma^2 \frac{B_1^2}{B_{1c}} = \frac{1}{3} \gamma^2 \frac{B_1^2}{B_1^2}. \quad [3.24b]$$

Evaluating the one-sided sine and cosine transforms [3.15] gives

$$j_{\alpha\alpha}(\omega) = G(0)\tau_c (1 + \omega^2 \tau_c^2)^{-1}, \quad [3.25a]$$

$$k_{\alpha\alpha}(\omega) = G(0)\omega \tau_c^2 (1 + \omega^2 \tau_c^2)^{-1} \quad [3.25b]$$

$$= \omega \tau_c j_{\alpha\alpha}(\omega)$$

Thus,

$$T_1^{-1} = 2\gamma^2 \frac{B_1^2}{B_{1c}} \tau_c (1 + \omega_0^2 \tau_c^2)^{-1}, \quad [3.26a]$$

$$T_2^{-1} = \frac{1}{3} T_1^{-1} + \omega_0^2. \quad [3.26b]$$

and

$$\delta\omega = \omega_0 \tau_c = T_1^{-1}. \quad [3.26c]$$

With regard to the dynamic frequency shift, it is clear from

[3.26c] that  $\delta\omega/\omega_0 \ll 1$  since the theory can be valid only if  $T_1 \gg \tau_c$ .

In the case of the relaxation time  $\tau_c \ll \omega_0, \tau_1, \tau_2$ , the observation is frequently made that when  $\omega_0 \tau_c \ll 1$ ,  $T_1 \approx T_2$  is obtained here.

While this is often the case for many relaxation mechanisms, Aragam<sup>1</sup> points out that it is inaccurate to assume that it is universally true. We will see that relaxation due to magnetic field gradients is in fact an example of a situation where  $T_1 \neq T_2$  in the  $\omega_0 \tau_c \ll 1$  limit. For the case  $\omega_0 = 0$ , equations [3.23] show that identical results are

obtained if one simply lets  $\omega_0 = 0$  in equations [3.26a,b]. This is obviously the result of the assumption of isotropy which was made to simplify the present discussion.

In the general expression for  $T_2^{-1}$  [3.20] there is a term  $j_{zz}(0)$  which appears as  $\gamma^2 \overline{B_{1\alpha}^2 \tau_c}$  in [3.26b]. This term is called the "secular broadening" term because it is determined by the zero-frequency component of the spectral density of  $B_{1z}$ . Physically, this is due to the fact that  $B_{1z}$  is the same in the rotating frame as in the lab frame, and it is those components of the perturbation field which appear at zero frequency in the rotating frame that are capable of causing reorientation of the spins. Thus, in the  $\omega_0 \tau_c \gg 1$  limit ("extreme narrowing" limit) where  $T_1^{-1} \propto \omega_0^{-2}$  and is considerably smaller than it would be in the  $\omega_0 \rightarrow 0$  limit,  $T_2^{-1}$  is dominated by the secular broadening term and is therefore useful for estimating the zero-field relaxation rate.

We now inquire into the behavior of the relaxation rates as a function of  $\tau_c$  in the context of the present example. In particular, we wish to note the effect of allowing  $\tau_c$  to become sufficiently large that  $\gamma^2 \overline{B_{1\alpha}^2 \tau_c^2} \approx 1$  in violation of the motional narrowing condition. If  $\omega_0^2 \ll \gamma^2 \overline{B_{1\alpha}^2}$ , [3.26a,b] show that  $T_1/\tau_c \approx T_2/\tau_c \approx (\gamma^2 \overline{B_{1\alpha}^2 \tau_c^2})^{-1}$  so that  $T_1, T_2 \rightarrow \tau_c$  as  $\tau_c$  becomes long. On the other hand, if  $\omega_0^2 \gg \gamma^2 \overline{B_1^2}$ , then  $T_1/\tau_c \approx \omega_0^2/(2\gamma^2 \overline{B_{1\alpha}^2})$  as  $\tau_c \rightarrow \infty$ . Thus, the longitudinal relaxation time appears to become *longer* as  $\tau_c$  becomes longer irrespective of violation of the motional narrowing condition provided that  $\omega_0^2 \gg \overline{B_{1\alpha}^2}$ .

The question therefore arises as to whether the present theory

can yield correct results for  $T_1$  when  $B_0^2 \gg \overline{B_{1\alpha}^2}$  even though the motional narrowing condition is violated. As this situation can readily arise in the case of slow diffusion through a magnetic gradient (e.g., in a liquid) this question will be considered further in the following section.

### 3.3 Relaxation Due to Diffusion Through Magnetic-Field Gradients

The theory that was discussed in the previous section can now be applied to a real physical situation: relaxation due to motion through magnetic-field gradients. To do this, the identification  $\vec{B}_1(t) = \vec{B}_1(\vec{r}(t))$  is made and a means found to characterize  $\vec{r}(t)$ , an atomic trajectory, and  $\vec{B}_1(\vec{r})$  so that the necessary functions and their Fourier transforms can be calculated.

This type of problem has been dealt with by a number of different authors concerned with varying physical situations; some will be referred to here, others will be mentioned later in this section. Kleppner, Goldenberg, and Ramsey<sup>45</sup> obtained approximate expressions for nuclear relaxation when the atomic mean free path is limited by the walls of the container. Schearer and Walters<sup>46</sup> dealt with the situation in a gas where the mean free path is much shorter than the container dimensions. They were concerned with a uniform gradient and a Larmor frequency such that  $\omega_0 \gg \tau_D^{-1}$ , where  $\tau_D$  is the diffusion time through the sample cell. Barbé, Leduc, and Laloë<sup>47</sup> (BLL) on the other hand dealt with an arbitrary field configuration (within the limits of the motional narrowing condition) and assumed that  $\omega_0 \ll \tau_f^{-1}$ , where  $\tau_f$  is the mean time between collisions. They also assumed a short mean free

path compared to the sample dimensions.\*

For the situation we are interested in, *i.e.*, a classical liquid with very low Larmor frequencies, the diffusion equation with appropriate boundary conditions provides an accurate description of the long term statistical motion of the  $\text{He}^3$  atoms. This was the technique used by BLL and we will follow their approach here. We will start by discussing the problem in an unspecified sample geometry. Subsequently the expressions appropriate to a spherical sample geometry will be written. The spherical case is important because it is the actual geometry which must be used. In Chap. 4 and in particular in Appendix A, a cubical geometry will be utilized since it lends itself to approximations which are useful in calculating the relaxation due to a nearby ferromagnetic dipole.

### 3.3.1 *Unspecified Sample Geometry*

We start by writing a general expression for the required correlation functions:

$$G_{\alpha\beta}(\tau) = \gamma^2 \overline{B_{1\alpha}(\vec{r}(t - \tau)) B_{1\beta}(\vec{r}(t))} .$$

Let  $p(\vec{r}_0, t) d^3 r_0$  be the probability that a given  $\text{He}^3$  atom is in the volume element  $d^3 r_0$  centered at  $\vec{r}_0$  at time  $t_0$ . Also let  $P(\vec{r}_0, t_0; \vec{r}, t_0 + \tau) d^3 r$  be the conditional probability that given that a certain atom was located at  $\vec{r}_0$  at time  $t_0$ , that it will be found in the volume element  $d^3 r$  located at  $\vec{r}$  at time  $t_0 + \tau$ . If we assume homogeneity and stationarity these probability densities may be written

---

\* In actuality, the BLL paper is concerned with the effects of an inhomogeneous rf field in NMR experiments, but their results are readily applicable to relaxation in static field gradients as well.

and

$$p(\vec{r}_o, t_o) = V^{-1},$$

$$p(\vec{r}_o, t_o; \vec{r}, t_o + \tau) = p(\vec{r}_o; \vec{r}, \tau)$$

where  $V$  is the sample volume. Hence

$$\begin{aligned} G_{\alpha\beta}(\tau) &= \gamma^2 \int_V d^3 r_o p(\vec{r}_o, t_o) B_{1\alpha}(\vec{r}_o) \int_V d^3 r p(\vec{r}_o, t_o; \vec{r}, t_o + \tau) B_{1\beta}(\vec{r}) \\ &= \gamma^2 V^{-1} \int_V d^3 r_o B_{1\alpha}(\vec{r}_o) \int_V d^3 r p(\vec{r}_o; \vec{r}, \tau) B_{1\beta}(\vec{r}). \end{aligned} \quad [3.27]$$

It is now assumed that  $p(\vec{r}_o; \vec{r}, t)$  satisfies the diffusion equation

$$\frac{\partial p(\vec{r}_o; \vec{r}, t)}{\partial t} = D \vec{\nabla}_r^2 p(\vec{r}_o; \vec{r}, t) \quad [3.28]$$

with the boundary conditions

$$p(\vec{r}_o; \vec{r}, 0) \approx \delta(\vec{r} - \vec{r}_o), \quad [3.29]$$

$$[\hat{n} \cdot \vec{\nabla}_r p(\vec{r}_o; \vec{r}, t)]_S = 0, \quad [3.30]$$

$$p(\vec{r}_o; \vec{r}, \infty) = V^{-1}, \quad [3.31]$$

where  $D$  is the diffusion coefficient,  $\vec{\nabla}_r$  is the gradient operator on  $\vec{r}$ , and  $\hat{n}$  is the unit normal on the surface  $S$  of the sample volume.

Using the separation of variables technique, we write

$$p(\vec{r}_o; \vec{r}, t) = g(t) f(\vec{r}_o, \vec{r}).$$

Substituting into [3.28],

$$(gD)^{-1} dg/dt = f^{-1} \vec{\nabla}_r^2 f = -k^2,$$

where the sign of the separation constant is dictated by [3.31].

Considering the equation for  $g(t)$

$$dg/dt + Dk^2 g = 0 ,$$

we have  $g(t) = g(0)\exp(-t/\tau_k)$  where

$$\tau_k \equiv (Dk^2)^{-1} . \quad [3.32]$$

Now considering the equation for  $f(\vec{r}_0, \vec{r})$ , we have

$$(\vec{\nabla}_{\vec{r}}^2 + k^2)f = 0 \quad [3.33]$$

and [3.30] becomes

$$(\vec{\nabla}_{\vec{r}} f \cdot \hat{n})_s = 0 . \quad [3.34]$$

The Helmholtz equation [3.33] with the boundary condition [3.34] constitute a classical eigenvalue problem where the eigenvalues  $k^2$  form a discrete spectrum, and the associated eigenfunctions  $\phi_{k\ell}(\vec{r})$  can be assumed to be a complete orthonormal set. Thus

$$\int \phi_{k\ell}^*(\vec{r}) \phi_{k',\ell}(\vec{r}) d^3r = \delta_{kk'} \delta_{\ell\ell} , \quad [3.35a]$$

and

$$\sum_{k\ell} \phi_{k\ell}^*(\vec{r}) \phi_{k\ell}(\vec{r}') = \delta(\vec{r} - \vec{r}') , \quad [3.35b]$$

where we have added the index  $\ell$  to distinguish between any degenerate modes.

The complete solution of [3.28] satisfying the boundary condition [3.30] can now be written

$$P(\vec{r}_0; \vec{r}, t) = \sum_{k\ell} A_{k\ell}(\vec{r}_0) \phi_{k\ell}(\vec{r}) e^{-t/\tau_k} . \quad [3.36]$$

Using equation [3.29] and [3.35a] yields the coefficients  $A_{kl}(\vec{r}_o)$ :

$$P(\vec{r}_o; \vec{r}, 0) = \delta(\vec{r}_o - \vec{r}) = \sum_{kl} A_{kl}(\vec{r}_o) \phi_{kl}(\vec{r})$$

giving

$$A_{kl}(\vec{r}_o) = \phi_{kl}^*(\vec{r}_o) .$$

Substituting this into [3.36] and [3.36] into [3.27] yields the desired expression for the correlation functions:

$$G_{\alpha\beta}(\tau) = \gamma^2 V^{-1} \sum_{kl} \tilde{B}_{1\alpha}(k, l) \tilde{B}_{1\beta}^*(k, l) e^{-|\tau|/k} ; \quad [3.37]$$

where  $\tilde{B}_{1\alpha}(k, l)$  and  $\tilde{B}_{1\beta}(k, l)$  are expansion coefficients for  $B_{1\alpha}(\vec{r})$  and  $B_{1\beta}(\vec{r})$  in terms of the orthonormal functions  $\phi_{kl}(\vec{r})$ :

$$\tilde{B}_{1\alpha}(k, l) = \int_V d^3r B_{1\alpha}(\vec{r}) \phi_{kl}^*(\vec{r}) , \quad [3.38a]$$

$$B_{1\alpha}(\vec{r}) = \sum_{kl} \tilde{B}_{1\alpha}(k, l) \phi_{kl}(\vec{r}) . \quad [3.38b]$$

Before proceeding to specific cases, some general observations should be made. First, we note that  $k = 0$  is an eigenvalue; equation [3.33] becomes Laplace's equation which has one solution that satisfies the boundary condition [3.34]:

$$\phi_0(\vec{r}) = \text{const} = V^{-\frac{1}{3}} .$$

It is recalled, however, that it is always assumed that  $\vec{B}_1 = 0$ .

Hence

$$\tilde{B}_{1\alpha}(k = 0) = V^{-\frac{1}{3}} \int_V d^3r B_{1\alpha}(\vec{r}) = 0 ,$$

so that the  $k = 0$  term in [3.37] is always zero.

Secondly, it is seen that  $G_{\alpha\beta}(\tau)$  and hence  $j_{\alpha\beta}(\omega)$  and  $k_{\alpha\beta}(\omega)$  transform as the components of a symmetric second-rank tensor under rotations of the coordinate system. That  $G_{\alpha\beta}(\tau)$  is symmetric can be seen from the fact that  $B_{1\alpha}$  and consequently  $G_{\alpha\beta}(\tau)$  are real.

Thus

$$\begin{aligned} G_{\alpha\beta}(\tau) &= \gamma^2 V^{-1} \sum_{kl} \tilde{B}_{1\alpha}(k, l) \tilde{B}_{1\beta}^*(k, l) e^{-\tau/\tau_k} \\ &= \gamma^2 V^{-1} \sum_{kl} \tilde{B}_{1\alpha}^*(k, l) \tilde{B}_{1\beta}(k, l) e^{-\tau/\tau_k} = G_{\beta\alpha}(\tau) . \end{aligned}$$

The tensor property can be seen from [3.38a] and [3.37].

The symmetry property  $G_{\alpha\beta} = G_{\beta\alpha}$  allows cancelation of the cross-correlation terms in [3.16] which results in [3.16'], [3.20] and [3.21]. The fact that  $G_{\alpha\beta}$  also transforms as a symmetric tensor is useful in that it means that there is a coordinate system  $x'y'z'$  such that  $G_{\alpha'\beta'} = \delta_{\alpha'\beta'} G_{\alpha\beta}$ . This allows the simplification of the relaxation equations for  $\omega_0 = 0$ , [3.22] to the diagonal form [3.23]. By examination of [3.23] it is seen that in both the general cases considered in the previous section, *i.e.*,  $\omega_0 \gg T_{1,2}^{-1}$  and  $\omega_0 = 0$ , it is sufficient to consider only the autocorrelation functions  $G_{\alpha\alpha}(\tau)$  and their transforms  $j_{\alpha\alpha}(\omega)$  and  $k_{\alpha\alpha}(\omega)$ . In the  $\omega_0 = 0$  case, of course, the proper coordinate system must be utilized.

Incorporating the result that the  $k = 0$  term may be omitted with the fact that only  $\alpha = \beta$  terms are needed, allows [3.37] to be written

$$G_{\alpha\alpha}(\tau) = \gamma^2 V^{-1} \sum'_{k, l} |\tilde{B}_{1\alpha}(k, l)|^2 e^{-\tau/\tau_k} , \quad [3.39]$$

where  $\Sigma'$  signifies that the  $k = 0$  is omitted.

Having seen that  $\tau_k^{-1} = Dk^2 \neq 0$  for all terms in [3.39], we may proceed to write the one-sided Fourier transforms:

$$j_{\alpha\alpha}(\omega) = \gamma^2 V^{-1} \sum_{k,\ell}' |\tilde{B}_{1\alpha}(k,\ell)|^2 \tau_k (1 + \omega^2 \tau_k^2)^{-1} \quad [3.40]$$

and

$$k_{\alpha\alpha}(\omega) = \gamma^2 V^{-1} \sum_{k,\ell}' |\tilde{B}_{1\alpha}(k,\ell)|^2 \omega \tau_k^2 (1 + \omega^2 \tau_k^2)^{-1}. \quad [3.41]$$

This general formalism may now be applied to a spherical sample geometry.

### 3.3.2 Spherical Sample

The eigenfunctions are

$$\phi_{n\ell m}(\vec{r}) = A_{\ell n} j_{\ell}(\beta_{\ell n} r/R_o) Y_{\ell m}(\theta, \phi)$$

where  $j_{\ell}(z)$  is the  $\ell^{\text{th}}$  order spherical Bessel function of the first kind (not to be confused with the cosine transform which will always have a double subscript),  $\beta_{\ell n}$  is the  $n^{\text{th}}$  zero of the first derivative of  $j_{\ell}(z)$ :  $j_{\ell}'(\beta_{\ell n}) = 0$ ,  $Y_{\ell m}(\theta, \phi)$  is the usual spherical harmonic,  $R_o$  is the radius of the spherical sample cell, and  $A_{\ell n}$  is the normalization coefficient:

$$A_{\ell n} = \left[ R_o^3 \int_0^1 \rho^2 j_{\ell}^2(\beta_{\ell n} \rho) d\rho \right]^{-\frac{1}{2}}$$

$$= \left\{ \frac{1}{2} R_o^3 [1 - \ell(\ell + 1) \beta_{\ell n}^{-2}] j_{\ell}^2(\beta_{\ell n}) \right\}^{-\frac{1}{2}}. \quad [3.42]$$

The separation constant,  $k^2$ , is given by

$$k^2 = (\beta_{\ell n}/R_o)^2, \quad [3.43]$$

so that the time constants  $\tau_{\ell n}$  are

$$\tau_{\ell n} = R_o^2 / (\beta_{\ell n}^2 D) . \quad [3.44]$$

Now  $\beta_{01} = 0$  and is therefore excluded. The next smallest zero is  $\beta_{11} = 2.0816$  which means that the slowest diffusion mode has a time constant  $\tau_{11} = 0.2308 R_o^2 / D$ . For numbers that are typical of our experimental situation,  $R_o = 0.5 \text{ cm}$ ,  $D = 10^{-4} \text{ cm}^2 \text{ sec}^{-1}$ , we have  $\tau_{11} \approx 10 \text{ min}$ . It is interesting to note that the slowest isotropic mode  $\tau_{02} = 0.0495 R_o^2 / D$  decays in less than one-quarter the time the 1,1 mode does.

To make any further progress, we must specify the perturbation field  $\vec{B}_1(\vec{r})$  in some fashion. The easiest way to do this is to assume that the sample volume is free of any magnetic-field sources so that each of the Cartesian components of  $\vec{B}_1(\vec{r})$  must satisfy Laplace's equation. Hence,

$$B_{1\alpha} = \sum_{\ell m} C_{\alpha}(\ell, m) r^{\ell} Y_{\ell m}(\theta, \phi) , \quad [3.45]$$

where obviously the  $C_{\alpha}(\ell, m)$ 's are constrained by the reality condition on  $B_{1\alpha}$  and Maxwell's equations. Using equation [3.38a] and the fact  $B_{1\alpha}$  is real,

$$\tilde{B}_{1\alpha}(n, \ell, m) = C_{\alpha}^*(\ell, m) A_{\ell n} I_{\ell n} R_o^{\ell+3} , \quad [3.46]$$

where

$$I_{\ell n} = \int_0^1 \rho^{\ell+2} j_{\ell}(\beta_{\ell n} \rho) d\rho . \quad [3.47]$$

$I_{\ell n}$  can be explicitly evaluated:

$$I_{\ell n} = \ell j_{\ell}(\beta_{\ell n}) / \beta_{\ell n}^2 . \quad [3.48]$$

Substituting from [3.48] and [3.42],

$$|B_{1\alpha}(n, \ell, m)|^2 = 2|C_\alpha(\ell, m)|^2 \ell^2 R_0^{2\ell+3} \left\{ \beta_{\ell n}^2 [\beta_{\ell n}^2 - \ell(\ell + 1)] \right\}^{-1}. \quad [3.49]$$

From equations [3.39], [3.40], [3.41] we then have the correlation functions and their transforms:

$$G_{\alpha\alpha}(\tau) = \frac{3\gamma^2}{2\pi} \sum_{n\ell m} \frac{|C_\alpha(\ell, m)|^2 R_0^{2\ell} \ell^2}{\beta_{\ell n}^2 [\beta_{\ell n}^2 - \ell(\ell + 1)]} e^{-\tau/\tau_{\ell n}} \quad [3.50]$$

$$j_{\alpha\alpha}(\omega) = \frac{3\gamma^2}{2\pi D} \sum_{n\ell m} \frac{|C_\alpha(\ell, m)|^2 R_0^{2\ell+2} \ell^2}{(\beta_{\ell n}^4 + \omega^2 R_0^{4D-2}) [\beta_{\ell n}^2 - \ell(\ell + 1)]} \quad [3.51]$$

$$k_{\alpha\alpha}(\omega) = \frac{3\gamma^2}{2\pi D^2} \sum_{n\ell m} \frac{|C_\alpha(\ell, m)|^2 R_0^{2\ell+4} \ell^2 \omega}{\beta_{\ell n}^2 (\beta_{\ell n}^4 + \omega^2 R_0^{4D-2}) [\beta_{\ell n}^2 - \ell(\ell + 1)]} \quad [3.52]$$

As a specific example, we consider a uniform field gradient axially symmetric about the  $x$  axis:

$$\vec{B}_1(\vec{r}) = g(\hat{i}x - \frac{1}{2}\hat{j}y - \frac{1}{2}\hat{k}z), \quad [3.53]$$

where  $g$  is a constant. In this case, the only non-zero expansion coefficients in equation [3.45] are

$$\begin{aligned} C_x(1, \pm 1) &= \pm \frac{1}{2} \sqrt{8\pi/3} g \\ C_y(1, \pm 1) &= -\frac{1}{4} i \sqrt{8\pi/3} g \\ C_z(1, 0) &= -\frac{1}{2} \sqrt{4\pi/3} g \end{aligned} \quad [3.54]$$

Hence

$$j_{yy}(\omega_0) = j_{zz}(\omega_0) = \frac{1}{2} g^2 \gamma^2 R_o^4 D^{-1} \sum_n \{ (\beta_{1n}^2 - 2) (\beta_{1n}^4 + \omega_0^2 R_o^4 D^{-2}) \}^{-1} ,$$

$$j_{xx}(\omega_0) = 4j_{zz}(\omega_0) .$$

[3.55]

The sum in [3.55] is most readily evaluated in either of two limits:

$$\omega_0 \tau_{11} = \omega_0^2 R_o^2 / (\beta_{11}^2 D) \ll 1, \text{ or } \omega_0 \tau_{11} \gg 1.$$

In the case  $\omega_0 \tau_{11} \ll 1$

$$\sum_n \{ (\beta_{1n}^2 - 2) (\beta_{1n}^4 + \omega_0^2 R_o^4 D^{-2}) \}^{-1} \approx \sum_n [\beta_{1n}^4 (\beta_{1n}^2 - 2)]^{-1} = 0.0229$$

[3.56]

We can now write the "low field" relaxation times. For  $\omega_0 = 0$ , equations [3.55], [3.56] and [3.23b] give

$$T_{zG}^{-1} = T_{yG}^{-1} = 5j_{zz}(0) = (5/2)(0.0229 \gamma^2 g^2 R_o^4 D^{-1}) ,$$

$$T_{xG}^{-1} = 2j_{zz}(0) ,$$

[3.57]

$$\text{so } T_{zG}^{-1} = T_{yG}^{-1} = (5/2)T_{xG}^{-1} .$$

In the case  $\omega_0 \gg T_{1,2}^{-1}$  but  $\omega_0 \tau_{11} \ll 1$ , equations [3.16'], [3.20], and [3.55] give

$$T_{1G}^{-1} = T_{zG}^{-1} = 5j_{zz}(0) ,$$

[3.58]

$$T_{2G}^{-1} = j_{zz}(0) + \frac{1}{2} T_{zG}^{-1} = (7/2)j_{zz}(0) .$$

$$\text{Hence } T_{1G}^{-1} = (10/7)T_{2G}^{-1} .$$

This illustrates the assertion that was previously made: the condition  $\omega_0 \tau_{11} \ll 1$  does not guarantee that  $T_1 = T_2$ .

In the opposite limit, i.e.  $\omega_0 \tau_{11} \gg 1$ , the sum in [3.55] can

be approximated as follows:

$$\sum_n \{(\beta_{1n}^2 - 2)(\beta_{1n}^4 + \omega_0^2 R_0^4 D^{-2})\}^{-1} \approx (\omega_0^2 R_0^4 D^{-2})^{-1} \sum_n (\beta_{1n}^2 - 2)^{-1}. \quad [3.59]$$

This approximation is not as good as that used in the opposite limit [3.56], nor is the convergence nearly as rapid. Nonetheless, a numerical summation reveals

$$\sum_n (\beta_{1n}^2 - 2)^{-1} \sim \frac{1}{2}.$$

Using this result in equations [3.55] and [3.16'] yields

$$T_{1G}^{-1} = 5j_{zz}(\omega_0) = (5/4)g^2\gamma^2 D \omega_0^{-2}. \quad [3.60]$$

This is identical to the result obtained by Schearer and Walters<sup>46</sup> in the limit  $\omega_0 \tau_f \ll 1$ , where  $\tau_f$  is the mean time between collisions in the gas.\* It is noteworthy that this result is independent of  $R_0$  and proportional to  $\omega_0^{-2}$ .

With regard to  $T_{2G}^{-1}$ , it has already been noted that the secular term will dominate in the extreme narrowing ( $\omega_0 \tau_{11} \gg 1$ ) limit. Equations [3.58] show that  $T_{2G}^{-1}$  shifts from  $(7/2)j_{zz}(0)$  when  $\omega_0 \tau_{11} \ll 1$  to  $j_{zz}(0)$  when  $\omega_0 \tau_{11} \gg 1$ .

For the sake of completeness, we also write the expressions for the dynamic frequency shift using this particular gradient configuration. Combining equations [3.21], [3.52], and [3.54] we find

\* The Schearer and Walters calculation is based on a gradient that has axial symmetry about the z axis and therefore has a different numerical coefficient than [3.60]. Our choice of gradient configuration was made in order to facilitate the analysis of experimental data in Chap. 4.

$$\delta\omega = \frac{1}{2} [k_{xx}(\omega_0) + k_{yy}(\omega_0)] = (5/2)k_{yy}(\omega_0)$$

$$\delta\omega/\omega_0 = 5g^2\gamma^2R_0^6D^{-2} \sum_n \{\beta_{1n}^2(\beta_{1n} - 2)(\beta_{1n}^4 + \omega_0^2R_0^4D^{-2})\}^{-1}.$$

In the limit  $\omega_0\tau_{11} \ll 1$ , this becomes

$$\delta\omega/\omega_0 \approx 0.0263 \gamma^2 g^2 R_0^6 D^{-2}$$

$$\approx \frac{1}{2} (\tau_{11}/T_1),$$

and in the opposite limit,  $\omega_0\tau_{11} \gg 1$ , we have

$$\delta\omega/\omega_0 \approx 0.50 (g\gamma R_0/\omega_0)^2$$

$$\approx 0.43 (\tau_{11}/T_1)$$

### 3.3.3 Relaxation When the Motional Narrowing Condition is Violated

In our discussion of gradient-induced relaxation, we have assumed until now that the motional narrowing condition holds. In the case of a uniform gradient such as we have just discussed, the motional narrowing condition requires  $\gamma^2 R_0^2 \tau_{11}^2 \approx (3/10)R_0^2 g^2 \gamma^2 \tau_{11}^2 \approx 0.02 g^2 \gamma^2 R_0^6 D^{-2} \ll 1$ . For our experimental situation this means that  $g \ll 3 \times 10^{-7} \text{ G cm}^{-1}$ .

As it turned out, our experimental conditions did not meet the motional narrowing criterion. Since we still wish to be able to analyze the data in spite of this, we must now deal with the gradient-induced relaxation in the opposite limit, *i.e.*, when  $D \rightarrow 0$ . Specifically, we wish to understand the behavior of the longitudinal (or spin-lattice) relaxation and the nature of the transverse decay of

the precessing magnetization when the motional narrowing condition is strongly violated but when  $|\vec{B}_1(\vec{r})| \ll |\vec{B}_0|$  everywhere in the sample volume. The matter of spin-lattice relaxation will be dealt with first.

The situation we are now concerned with has a simple physical interpretation: As a spin slowly diffuses through a gradient it sees a local field that varies in direction (and magnitude) at a rate that is slow compared to  $\omega_0$ . In this case the spin can "adiabatically follow"<sup>1</sup> the local field. More precisely, the value of the component of  $\vec{I}_i$  (the subscript referring to a specific spin) that lies along the local field direction is now an approximate constant of the motion. Thus, after transverse components of the magnetization have been damped out, the magnetization will become nonuniform and will tend to assume the same configuration as  $\vec{B}_1(\vec{r}) + \vec{B}_0$ .

The ability of a spin to adiabatically follow the local field is obviously not perfect, and over a period of time it will become disoriented. From a thermodynamic point of view, in fact, it makes sense to identify the longitudinal relaxation rate with the rate of decay of the component of the magnetization in the direction of the local field,  $\vec{B}_1(\vec{r}) + \vec{B}_0$ , rather than with the rate of decay of  $M_z$ . This is the point of view taken by Schearer and Walters<sup>46</sup> (SW) in one of their derivations of an expression for  $T_1$  of a gas in a uniform gradient.

In this derivation SW reasoned as follows: As an atom moves on a flight between collisions, it sees the local field rotate slightly because of the gradient. By transforming to a frame that is under-

going instantaneous rotation such that the local field always lies along the  $z$  axis, there appears an effective field  $\vec{B}_1^{(e)}$  that is orthogonal to the  $z$  axis and lies along the axis of rotation. As the direction of  $\vec{B}_1^{(e)}$  depends on the velocity of the atom, this effective field will be seen to fluctuate rapidly. From this reference frame, the correlation time is now  $\tau_f$ , the mean time between collisions. The correlation function  $G_{\alpha\alpha}^{(e)}(\tau) = \gamma^2 \overline{B_{1\alpha}^{(e)}(t - \tau)B_{1\alpha}^{(e)}(t)}$  is readily calculated for a gas and the expression for  $T_1^{-1}$  is obtained by using the relations

$$(T_{1G}^{(e)})^{-1} = j_{xx}^{(e)}(\omega_0) + j_{yy}^{(e)}(\omega_0) ,$$

where

$$j_{\alpha\alpha}^{(e)}(\omega) = \int_0^\infty d\tau G^{(e)}(\tau) \cos(\omega\tau) .$$

We now adopt this point of view but under somewhat broader conditions than those assumed by SW. That is, although we still assume  $|\vec{B}_1(\vec{r})| \ll |\vec{B}_0|$  (e.g., the local Larmor frequency is taken to be  $-\gamma\vec{B}_0$  rather than  $-\gamma(\vec{B}_1 + \vec{B}_0)$ ), we do not assume that the substance is necessarily a gas or that the gradient is uniform.

Because of the assumption that  $|\vec{B}_1(\vec{r})| \ll |\vec{B}_0|$ , the effective fields in the rotating frame are given in first order by

$$\gamma B_{1x}^{(e)}(t) = \dot{B}_{1y}(t)/B_0$$

$$\gamma B_{1y}^{(e)}(t) = -\dot{B}_{1x}(t)/B_0 ,$$

anywhere in the sample cell. Now it is well known that if the power spectral density of the variable  $x(t)$  is  $j(\omega)$ , then the spectral density of  $cx(t)$  is  $c^2\omega^2 j(\omega)$ .<sup>48</sup> Hence

AD-A101 064

STANFORD UNIV CALIF DEPT OF PHYSICS  
I. SPIN-LATTICE RELAXATION OF DILUTE SOLUTIONS OF POLARIZED HE3--ETC(U)  
AUG 78 M A TABER

F/G 14/2

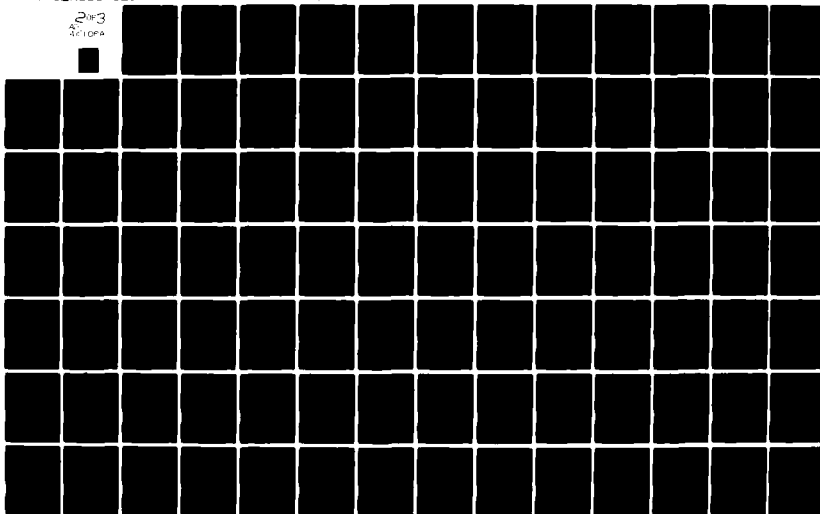
F44620-75-C-0022

NL

UNCLASSIFIED

AFOSR-TR-81-0522

2003  
ACIOPA



$$j_{xx}^{(e)}(\omega) = (\omega/\omega_0)^2 j_{yy}(\omega) ,$$

[3.61]

$$j_{yy}^{(e)}(\omega) = (\omega/\omega_0)^2 j_{xx}(\omega) ,$$

and

$$\begin{aligned} (T_{1G}^{(e)})^{-1} &= j_{xx}^{(e)}(\omega_0) + j_{yy}^{(e)}(\omega_0) \\ &= j_{yy}(\omega_0) + j_{xx}(\omega_0) \\ &= T_{1G}^{-1} , \end{aligned}$$

where  $T_{1G}^{-1}$  is the longitudinal relaxation rate that was calculated assuming the validity of the motional narrowing condition.

Thus, by considering the longitudinal relaxation rate to be defined with regard to the local field, we obtain the same result that would be obtained by blindly applying the BLL theory without regard to the motional narrowing requirement. Of course, the validity of this approach depends on the motional narrowing condition being satisfied in the frame where the local field is stationary.

In order to test this requirement, we must estimate  $\overline{\gamma^2 (B_1^{(e)})^2 \tau_f^2}$ . This is readily done by calculating  $\overline{(B_{1\alpha}^{(e)})^2}$  from  $j_{\alpha\alpha}^{(e)}(\omega)$ :

$$\overline{\gamma^2 (B_1^{(e)})^2} = G_{\alpha\alpha}^{(e)}(0) = 4 \int_0^\infty j_{\alpha\alpha}^{(e)}(\omega) d\omega / 2\pi .$$

(The factor of 4 arises from the fact that one-sided transforms have been used.)

Now when the diffusion equation is used to describe atomic motion, we have seen that

$$j_{\alpha\alpha}(\omega) = V^{-1} \sum_{k,\ell} \gamma^2 |\tilde{B}_{1\alpha}(k,\ell)|^2 \tau_k (1 + \omega^2 \tau_k^2)^{-1} . \quad [3.40]$$

If it is assumed that a value of  $\kappa$  exists such that  $|\tilde{B}_{1\alpha}(k,\ell)|^2$  is negligible for all  $k > \kappa$ , then for  $\omega \tau_k \gg 1$ , where  $\tau_k = (\kappa^2 D)^{-1}$  is the shortest significant diffusion time constant,  $j_{\alpha\alpha}^{(e)}(\omega \gg \tau_k^{-1}) \propto \text{const.}$  Thus in this model  $G^{(e)}(0) = \infty$  due to the cancelation of the  $\omega^{-2}$  behavior in the high frequency limit of  $j_{\alpha\alpha}(\omega)$  by the  $\omega^2$  factor in [3.61].

This problem arises because the diffusion equation is incorrect for frequencies  $\omega \gtrsim \tau_f^{-1}$ . In particular, the instantaneous velocity is infinite in the diffusion model. In actuality, the spectral density will decline faster than  $\omega^{-2}$  above  $\tau_f^{-1}$ . For example, for a gas where the atoms undergo random flights,  $j_{\alpha\alpha}(\omega \gg \tau_f^{-1}) \propto \omega^{-4}$  as is shown by SW.

For our present purposes, we will simply cut off the frequency integral at  $\tau_f^{-1}$ . Thus, for example, assuming that  $\tau_k \gg \tau_f$ ,

$$\begin{aligned} \gamma^2 \overline{(B_{1x}^{(e)})^2} &\approx \frac{2}{\pi} \sum_{k,\ell} \frac{\gamma^2 |\tilde{B}_{1y}(k,\ell)|^2}{\omega_0^2} \int_0^{\tau_f^{-1}} \frac{\tau_k \omega^2}{1 + \omega^2 \tau_k^2} d\omega \\ &\approx \frac{2}{\pi} V^{-1} \sum_{k,\ell} \frac{\gamma^2 |\tilde{B}_{1y}(k,\ell)|^2}{\omega_0^2 \tau_f \tau_k} \\ &\lesssim (2/\pi) (\omega_0^2 \tau_k \tau_f)^{-1} V^{-1} \sum_{k,\ell} \gamma^2 |\tilde{B}_{1y}(k,\ell)|^2 . \end{aligned}$$

$$\text{But } \overline{\gamma^2 B_{1y}^2} = V^{-1} \sum_{k,\ell} \gamma^2 |\tilde{B}_{1y}(k,\ell)|^2 .$$

Hence,

$$\gamma^2 \overline{(B_{1x}^{(e)})^2} \tau_f^2 \lesssim (2/\pi) (\tau_f/\tau_K) \overline{(B_{1y}^2/B_0^2)} \ll 1.$$

Thus under the conditions we have assumed, the motional narrowing condition is amply satisfied in the frame where the local field is stationary. As a consequence, the usual motional narrowing condition is unnecessary provided that 1) we are only dealing with the spin-lattice relaxation time, and 2)  $|\vec{B}_1(\vec{r})| \ll |\vec{B}_0|$ .

In the case of the decay of the transverse component of the magnetization (or the decay of the magnetization when  $\omega_0 \rightarrow 0$ ) the situation is quite different. Because of the presence of a secular term in the relaxation rate, it is essential that the motional narrowing criterion be satisfied. If it is not the decay of the transverse magnetization is in general not exponential.

In the limit where the diffusion coefficient is zero and  $|\vec{B}_0| \gg |\vec{B}_1(\vec{r})|$  (as before, spin-spin interaction is ignored) the evolution of the average transverse magnetization in a free-precession decay is easily understood: it is simply the Fourier transform of the "shape function" of the Larmor frequencies taken over the sample volume.<sup>1</sup> To be more explicit, if  $\vec{M}(\vec{r}, t = 0) = M_0 \hat{i}$ , then

$$\begin{aligned} \overline{M}_+(t) &= \overline{M}_x + i\overline{M}_y = M_0 \int f(\omega_0^0) e^{i\omega_0^0 t} d\omega_0 \\ &= M_0 \exp(i\omega_0^0 t) \int f(\omega_0^0 + u) e^{iut} du \end{aligned}$$

where  $f(\omega_0)$  is the shape function ( $\int f(\omega) d\omega = 1$ ), and  $\omega_0^0$  is the central Larmor frequency. In this case the magnetization is extremely nonuniform. In addition, the decay of the average magnetization does

not represent a relaxation process since the entropy of the spin system does not change. The magnetization can be made to reappear at some later time by use of the well known spin-echo technique.<sup>1</sup>

If the diffusion coefficient is nonzero, however, true relaxation will occur due to the differing phase histories of each of the spins. This situation is perhaps most easily studied by use of Torrey's modification of the Bloch equations.<sup>49</sup> He applied the Bloch equations to the magnetization of infinitesimal volume element in the sample cell and added the effect of diffusion of the magnetization into and out of this volume element. This diffusion is of consequence whenever there are magnetization gradients present in the sample.

The Torrey-Bloch equations are simply

$$\partial M_{x,y} / \partial t = \gamma (\vec{M} \times \vec{B})_{x,y} - M_{x,y} / T_2 + \vec{\nabla} \cdot \vec{D} \vec{M}_{x,y} \quad [3.62a]$$

$$\partial M_z / \partial t = \gamma (\vec{M} \times \vec{B})_z - (M_z - M_0) / T_1 + \vec{\nabla} \cdot \vec{D} \vec{M}_z. \quad [3.62b]$$

The relaxation rates  $T_1^{-1}$  and  $T_2^{-1}$  that appear in these equations are the rates due to mechanisms not associated with the magnetic-field gradient, and we will assume that they are sufficiently small that they may be neglected here.

As an example, Torrey applied (3.62a) to the case of precession in a small uniform gradient which is symmetric about the z axis. That is

$$\vec{B}(\vec{r}) = \vec{B}_1(\vec{r}) + B_0 \hat{k} = g(-\frac{1}{2}x\hat{i} - \frac{1}{2}y\hat{j} + z\hat{k}) + B_0 \hat{k}$$

where  $|\vec{B}_0| \gg |\vec{B}_1(\vec{r})|$ . He then obtained the well-known result

$$M_z(\vec{r}, t) = M_x(\vec{r}, t) + iM_y(\vec{r}, t) = M_0 \exp[i(\omega_0 - \gamma g z)t - \frac{1}{3}D\gamma^2 g^2 t^3]. \quad [3.63]$$

The first term in the exponential factor in [3.63] is the dephasing that would occur in the absence of diffusion and the second term is the irreversible damping. It is easily seen however, that if it is postulated that the motional narrowing condition is strongly violated, then the dephasing effect will cause the *average* magnetization to disappear before the  $-1/3 D\gamma^2 g^2 t^3$  term becomes particularly significant. Thus, the only clear way a pronounced  $\exp(-t^3)$  behavior can be observed is through the spin-echo technique.

Hence, with regard to the free-precession decay of the transverse magnetization one can make the following general statements: If the motional narrowing condition is well satisfied, the magnetization will be uniform throughout the sample volume, and it will exponentially decay at a rate  $T_{G2}^{-1}$  as given by the BLL theory. If on the other hand, the motional narrowing condition is strongly violated, the magnetization will no longer be uniform. In this case, if the average magnetization is the quantity being measured, then the effect of diffusion can be ignored in the first approximation and the average transverse magnetization will decay according to the Fourier transform of the shape function of the Larmor frequency.

### 3.4 Intrinsic Relaxation

We will now briefly review the subject of intrinsic relaxation due to the dipole-dipole interaction between  $\text{He}^3$  nuclei as they move relative to one another. This subject was initially treated in a

paper by Bloembergen, Purcell, and Pound<sup>50</sup> (BPP) which contains a lucid discussion of the physical interpretation of the results. More recent reviews of the general theory of this subject as treated by the density matrix formalism can be found in an article by Hubbard<sup>51</sup> as well as in Abragam.<sup>1</sup>

More specifically, we outline the calculation of  $T_1$  starting with the general expressions [3.3] and [3.4]:

$$d\langle Q \rangle^* / dt = - \langle A \rangle^* , \quad [3.3]$$

where

$$A = \int_0^\infty d\tau \overline{[H_1^*(t - \tau), [H_1^*(t), Q]]} . \quad [3.4]$$

Since we are interested in  $T_1$ , the operator  $Q$  is specified by

$$Q = \sum_i^N I_i^{(o)} \equiv I^{(o)}$$

where  $I_i^{(o)}$  is the  $z$  component of the nuclear spin operator  $\vec{I}_i$  for the  $i$ -th nuclear spin and similarly  $I_i^{(\pm 1)} = I_{xi} \pm iI_{yi}$ . The dipole-dipole interaction Hamiltonian is taken for  $H_1$  and can be written in the form

$$\hbar H_1 = \frac{1}{2} \sum_{i \neq j}^N F_{ij}^{(q)} V_{ij}^{(-q)} \equiv F^{(q)} V^{(-q)} , \quad [3.64]$$

where

$$F_{ij}^{(q)} = \alpha |q| r_{ij}^{-3} Y_{2q}(\theta_{ij}, \phi_{ij}) , \quad [3.65]$$

$$\begin{aligned} V_{ij}^{(o)} &= \frac{2}{3} I_i^{(o)} I_j^{(o)} - \frac{1}{6} (I_i^{(1)} I_j^{(-1)} + I_i^{(-1)} I_j^{(1)}) , \\ V_{ij}^{(\pm 1)} &= I_i^{(o)} I_j^{(\pm 1)} + I_i^{(\pm 1)} I_j^{(o)} , \\ V_{ij}^{(\pm 2)} &= I_i^{(\pm 1)} I_j^{(\pm 1)} , \end{aligned} \quad [3.66]$$

and  $(r_{ij}, \theta_{ij}, \phi_{ij})$  are the spherical coordinates of the relative position vector of spin  $j$  with respect to spin  $i$ . The coefficients in [3.65] are given by  $\alpha_0 = -6\sqrt{\pi/5}\gamma^2\hbar^2$ ,  $\alpha_1 = -3\sqrt{2\pi/15}\gamma^2\hbar^2$ , and  $\alpha_2 = -6\sqrt{2\pi/15}\gamma^2\hbar^2$ . We note that  $F_{ij}^{(-q)} = F_{ij}^{(q)*}$ ,  $V_{ij}^{(-q)} = V_{ij}^{(q)\dagger}$ ,  $V_{ij}^{(q)} = V_{ji}^{(q)}$ , and  $F_{ij}^{(q)} = F_{ji}^{(q)}$ .

As usual, the unperturbed Hamiltonian is

$$\hbar H_0 = -\hbar\gamma B_0 I^{(0)},$$

or

$$H_0 = \omega_0 I^{(0)}.$$

By using the expression

$$[I^{(0)}, F^{(q)} V^{(-q)}] = -q F^{(q)} V^{(-q)},$$

which is readily obtained from the usual commutation relations for the spin operators, the expression for the operator  $A$  in [3.4] can be written

$$A = \hbar^{-2} \sum_{qq'} q \exp[-i\omega_0(q+q')t] \int_0^\infty dt e^{i\omega_0 q' \tau} \overline{[F^{(q')}(t-\tau) V^{(-q')}, F^{(q)}(t) V^{(-q)}]} . \quad [3.67]$$

In order to evaluate

$$[F^{(q')}(t-\tau) V^{(-q')}, F^{(q)}(t) V^{(-q)}] = \frac{1}{4} \sum_{i \neq j} \sum_{k \neq l} \overline{F_{ij}^{(q')}(t-\tau) F_{kl}^{(q)}(t)} [V_{ij}^{(-q')}, V_{kl}^{(-q)}], \quad [3.68]$$

the following assumptions are made:

a) Three-body correlations are zero or small compared to two-body correlations, *i.e.*,

$$\overline{F_{ij}^{(q')}(t - \tau)F_{il}^{(q)}(t)} = \overline{\delta_{jl}F_{ij}^{(q')}(t - \tau)F_{il}^{(q)}(t)} .$$

b) The sample is homogeneous and the relative motion of the spins is random and isotropic. More explicitly, if  $p(\vec{r}_o)d^3r_o$  is the probability of the relative position vector of spin  $i$  with respect to spin  $j$  being  $\vec{r}_o$  at  $t = 0$ , then it is assumed  $p(\vec{r}_o) = \text{const.}$  In addition, if  $P(\vec{r}_o; \vec{r}, t)$  is the conditional probability that given  $\vec{r}_{ij} = \vec{r}_o$  at  $t = 0$ , that  $\vec{r}_{ij} = \vec{r}$  at time  $t$ , then it is assumed  $P(\vec{r}_o; \vec{r}, t) = P(|\vec{r} - \vec{r}_o|, t)$ .

If these two conditions hold it can be shown that

$$\overline{F_{ij}^{(q')}(t - \tau)F_{ij}^{(q)}(t)} = \delta_{-q, q'} \overline{F_{ij}^{(q')}(t - \tau)F_{ij}^{(q)}(t)} \equiv G_{ij}^{(q)}(\tau) ,$$

and  $G_{ij}^{(q)}$  is real. This result automatically eliminates the non-secular terms in the expression for  $A$ , equation [3.67]. These assumptions are clearly invalid in proximity to the sample walls. This exception will be ignored here but will be discussed briefly in Sec.

### 3.5.

With these assumptions [3.68] becomes

$$[F^{(q')}(t - \tau)V^{(-q')}, F^{(q)}(t)V^{(-q)}] = \frac{1}{2} \delta_{-q, q'} \sum_{i \neq j} G_{ij}^{(q)}(\tau) [V_{ij}^{(q)}, V_{ij}^{(-q)}] .$$

Substituting this into [3.67] and evaluating the commutators yields<sup>1</sup>

$$\langle A \rangle^* = \frac{2}{3} I(I + 1) \langle I^{(0)} \rangle \sum_j' [J_{ij}^{(1)}(\omega_o) + J_{ij}^{(2)}(2\omega_o)] . \quad [3.69]$$

By using this result in [3.3] and noting that all the terms the sum over  $j$  in [3.69] are identical, we finally obtain the desired expression:

$$T_{1B}^{-1} = (2/3)\hbar^{-2}I(I+1)N_3[J_{ij}^{(1)}(\omega_0) + J_{ij}^{(2)}(2\omega_0)] , \quad [3.70]$$

where  $N_3$  is the total number of spins,

$$J_{ij}^{(q)} = 2 \int_0^{\infty} d\tau \cos(\omega\tau) G_{ij}^{(q)}(\tau) , \quad [3.71]$$

and we have added the subscript "B" to designate intrinsic relaxation in the bulk.

In like fashion, the expression for  $T_{2B}^{-1}$  can be obtained:<sup>1</sup>

$$T_{2B}^{-1} = (\frac{1}{6})\hbar^{-2}I(I+1)N[J_{ij}^{(2)}(2\omega_0) + 10J_{ij}^{(1)}(\omega_0) + J_{ij}^{(0)}(0)] . \quad [3.72]$$

From the assumption of isotropy and homogeneity and from equations [3.65] it is easily shown that

$$\begin{aligned} J_{ij}^{(0)}(0) : J_{ij}^{(1)}(0) : J_{ij}^{(2)}(0) &= \overline{|F_{ij}^{(0)}|^2} : \overline{|F_{ij}^{(1)}|^2} : \overline{|F_{ij}^{(2)}|^2} \\ &= 6 : 1 : 4 \end{aligned} \quad [3.73]$$

Hence, as long as the motional narrowing condition is satisfied with respect to the dipole-dipole interaction, and  $\omega_0$  is sufficiently small that the spectral densities  $J_{ij}^{(q)}(\omega)$  may be approximated by their zero-frequency value, then  $T_{1B} = T_{2B}$ .

It now remains to calculate the correlation functions and their Fourier transforms. In the case of a liquid, a reasonable first approximation is to assume continuous diffusive atomic motion where

the distance of closest approach between spins is limited by a hard-sphere interatomic potential. This approach results as a limiting case to Torrey's jump-diffusion model based on the theory of random flights,<sup>52</sup> and has the advantage of allowing an exact calculation.

This calculation proceeds in virtually the same fashion as in Sec. 3.3:

$$G_{ij}^{(q)}(\tau) = \int d^3r_o p(\vec{r}_o) F_{ij}^{(-q)}(\vec{r}_o) \int d^3r P(\vec{r}_o; \vec{r}, t) F_{ij}^{(q)}(\vec{r}) , \quad [3.74]$$

where  $p(\vec{r}_o)$  and  $P(\vec{r}_o; \vec{r}, t)$  are defined as in assumption b) above. As before, we take  $p(\vec{r}_o) = V^{-1}$ ,  $V$  being the sample volume. For  $P(\vec{r}_o; \vec{r}, t)$  we use the solution to the diffusion equation satisfying the initial condition  $P(\vec{r}_o; \vec{r}, 0) = \delta(\vec{r} - \vec{r}_o)$ :

$$P(\vec{r}_o; \vec{r}, t) = (8\pi D t)^{-3/2} \exp[-(\vec{r} - \vec{r}_o)^2 / 8Dt] , \quad [3.75]$$

where  $2t$  has been substituted for  $t$  in the usual expression since  $\vec{r}, \vec{r}_o$  are relative vectors between two spins which are independently diffusing with a diffusion coefficient,  $D$ .<sup>52</sup> Making these substitutions for  $p(\vec{r}_o)$  and  $P(\vec{r}_o; \vec{r}, t)$  into [3.74] and using the definitions of  $F_{ij}^{(q)}(\vec{r})$  the correlation functions become<sup>52,1</sup>

$$G_{ij}^{(q)}(\tau) = (2/\pi) \alpha_q^2 (Va^3)^{-1} \int_0^\infty j_1^2(u) \exp[-2Du^2 \tau/a^2] du \quad [3.76]$$

where  $a$  is the distance of closest approach between two nuclei, and  $j_1(u)$  is a spherical Bessel function of the first order and kind. Using [3.71] we obtain the desired spectral densities.

$$J_{ij}^{(q)}(\omega) = (2/\pi) \alpha_q^2 (aDV)^{-1} \int_0^\infty j_1^2(u) u^2 (u^2 + \omega^2 \tau_a^2)^{-1} du , \quad [3.77]$$

where  $\tau_a = a^2/(2D)$ .

The integral in [3.77] can be expressed in terms of elementary functions.<sup>52</sup> Letting  $x = (2\omega_0\tau_a)^{1/2}$

$$I(x) = (2/\pi) \int_0^\infty j_1^2(u) u^2 (u^2 + x^4/4)^{-1} du$$
$$= x^{-5} \{x^2 - 2 + e^{-x} [(x^2 - 2)\sin x + (x^2 + 4x + 2)\cos x]\}. \quad [3.78]$$

Now except for viscous liquids in high magnetic fields, the condition  $\omega_0\tau_a \ll 1$  would be satisfied. Hence

$$I(x) = (2/15)[1 - (5/12)x], \quad x \ll 1.$$

Substituting  $I(0) = 2/15$  into [3.77] and [3.77] into [3.70], the classical result

$$T_{1B}^{-1} = T_{2B}^{-1} = (8\pi/15)\gamma^4 h^2 I(I + 1) n_3 (Da)^{-1} \quad [3.74]$$

is obtained. In this expression  $n_3 = N_3/V$  is the spin density.

For the sake of later reference, we note that in the opposite limit  $\omega_0\tau_a \gg 1$ ,  $I(x) = x^{-3} = (2\omega_0\tau_a)^{-3/2}$ . For He<sup>3</sup> and other liquids of low viscosity, however, this result is somewhat academic because of the extremely high magnetic field ( $\gtrsim 10^7$  G) necessary to reach this limit.

This result suffers from two obvious defects, both of which tend to be accentuated by the fact that the dominant contribution to the correlation functions come from the region  $r_{ij} \gtrsim a$ :

- 1) The model of continuous diffusion is an inadequate description of atomic motion for time scales on the

order of or less than the mean time between collision and for distances on the order of or less than the mean free path. This means that the zero-frequency result [3.79] would be in error by a factor on the order of unity and that the high-frequency ( $\omega_0^{-3/2}$ ) result could be completely incorrect.

2) The uniform radial distribution function implied by the hard-sphere interaction is also inaccurate.

It is clear that it is necessary to use a more realistic model of the dynamics and structure of the liquid state if the result [3.79] is to be improved upon. One effort that has been made to accomplish this was that of Oppenheim and Bloom<sup>53</sup> who used the concept of a time dependent pair distribution function in order to introduce the effect of a non-uniform radial distribution function. In the case of a classical liquid in the low frequency limit ( $\omega_0 a^2 / 2D \ll 1$ ), they obtained the expression

$$T_1^{-1} = 4\pi\gamma^4 h^2 I(I+1) n_3(ba)^{-1} \int_0^\infty F(y) y^{-1} dy$$

where

$$F(y) = \left[ \int_0^\infty [g(x)]^{1/2} J_{5/2}(xy) x^{-3/2} dx \right]^2,$$

and where  $g(x) = g(r/a)$  is the radial distribution function. This expression is identical to (3.79) when the hard-sphere radial distribution function is assumed.

Oppenheim and Bloom specifically applied their theory to liquid

$\text{He}^3$  by numerically evaluating  $\int_0^\infty F(y)y^{-1}dy$  as a function of temperature and density by using the Lennard-Jones potential and Kirkwood's superposition principle. Their results show that this integral is "remarkably insensitive to density and temperature" and yields a  $T_1$  which is approximately 15% lower than [3.79] where the parameter  $a$  is taken to be the Lennard-Jones radial parameter ( $2.56 \times 10^{-8}$  cm for He).

Horvitz<sup>24</sup> has found that the Oppenheim and Bloom result agrees well with  $T_1$  measurements made on liquid  $\text{He}^3$  in a Pyrex cell that has been subjected to a stringent plasma cleaning procedure.

Harmon and Muller<sup>54</sup> adopted a different approach in their analysis of nuclear relaxation of liquid ethane. They started with Torrey's jump-diffusion model and extended it by introducing the effect of a nonuniform radial distribution function. The size of the correction to [3.79] obtained by this approach naturally depends on the parameter  $\langle r^2 \rangle / a^2$ , where  $\langle r^2 \rangle$  is the mean-square jump distance. Although Harmon and Muller find it necessary for this parameter to be nonzero in order to obtain agreement with their ethane data, the agreement of the Horvitz data with the Oppenheim and Bloom result (which does not provide for jump-diffusion) makes it doubtful that this is the case for liquid  $\text{He}^3$ .

### 3.5 Wall-Induced Relaxation

We now consider the nuclear relaxation of  $\text{He}^3$  at low temperatures where the  $\text{He}^3$  comes in contact with a dielectric surface via an adsorbed phase. This situation is more complex than the other relaxation mechanisms for two reasons:

- 1) The adsorbed phase is in reality not a distinct homogeneous phase. Heterogeneity arises not only from the fact that substrates are typically heterogeneous, but also from the variation of the adsorbate-substrate interaction as a function of the separation of the two.<sup>55</sup> In fact, experimental evidence shows that for helium a density like that of the bulk liquid at the saturated vapor pressure is not obtained until approximately three atomic layers away from the substrate surface.<sup>56</sup>
- 2) Wall-induced relaxation arises not only due to the intrinsic  $\text{He}^3$ - $\text{He}^3$  dipolar interaction, but also due to the interaction of the  $\text{He}^3$  with foreign nuclear and electronic magnetic moments that are associated with the wall. These foreign moments can either be part of the wall constituents or an adsorbed contaminant such as  $\text{O}_2$ . Electronic spins are particularly important since they are more effective in relaxing the  $\text{He}^3$  than nuclear spins are by a ratio of  $(\mu_e/\mu_n)^2 \approx 10^6$ .<sup>1</sup>

These complexities not only introduce theoretical complications but also introduce problems in experimental design and analysis. In particular, the nature and density of foreign spins on the wall is frequently unknown, and the degree of surface heterogeneity can also be sufficiently unknown to cloud experimental results. Some experimental results will be noted below, however, that indicate that the use of a cryogenic wall coating consisting of a solid inert gas is useful in reducing some of these difficulties.

With regard to a theoretical model, we will keep things simple by maintaining the convenient fiction that the adsorbed phase is a separate homogeneous phase with an enhanced relaxation rate that can exchange atoms with the bulk sample. By using this approximation it is not difficult to derive the relationship between the relaxation rate in the adsorbed phase,  $T_{1\text{Ad}}^{-1}$ , and the measured relaxation rate in the bulk,  $T_{1W}^{-1}$ , that is due to this relaxation mechanism. The situation is further simplified by two additional assumptions:

- 1) The rate of diffusion in the bulk is assumed to be sufficiently rapid that the sample polarization may be considered to be homogeneous throughout the bulk.

While this assumption is not true in experimental situations where  $T_{1\text{Ad}}^{-1}$  is particularly short,<sup>57</sup> it is demonstrably true in ours.\*

- 2) It is also assumed that  $N_{3B}/N_{3\text{Ad}} \gg 1$ , where  $N_{3B}$  and  $N_{3\text{Ad}}$  are the total number of  $\text{He}^3$  atoms in the bulk and adsorbed phase respectively. In the case of a spherical cell,  $N_{3\text{Ad}}/N_{3B} = 3 s_3/(n_3 R_0^2)$  where  $s_3$  is the number of  $\text{He}^3$  atoms per unit area of surface.

With these assumptions, the solution of the two coupled rate equations relating the polarizations of the bulk and adsorbed phases yields the result<sup>28</sup>

---

\* In the case of diffusion in a sphere where the magnetization is specified to be zero at the surface, the diffusion mode with the longest time constant decays in a time  $T_D = R_0^2/(\pi^2 D)$ . In our case  $T_D \approx 240$  sec. This compares with an experimentally-estimated value of  $T_{1W}$  that is well in excess of  $10^5$  sec. Thus it is clear that  $T_{1W}$  is not limited by diffusion in the bulk.

$$T_{1W} = (N_{3B}/N_{3Ad})(T_{1Ad} + \tau_{Ad}) , \quad [3.80]$$

where  $\tau_{Ad}$  is the mean time that an atom spends in the adsorbed phase.

It should be noted that in general  $T_{1Ad}$  is anisotropic; i.e.,  $T_{1Ad}$  is a function of the local surface normal with respect to  $\vec{B}_0$  if the relaxation mechanism is due to dipole-dipole interactions.<sup>58</sup>

Since in our case, however, only the bulk magnetization is observed, we can take  $T_{1Ad}^{-1}$  to signify the relaxation rate that is obtained from an average over a spherical surface.

At this point we will briefly discuss the intrinsic component of  $T_{1Ad}^{-1}$ . It is not particularly useful to discuss this subject at great length since the experimental data that will be discussed in the next chapter were not taken over a broad enough range of conditions (particularly  $B_0$ ) to allow a significant check of any detailed theoretical model.

In general, the theory of intrinsic relaxation of adsorbed  $He^3$  is identical to that discussed in the previous section except that the relative motion between  $He^3$  atoms is now confined to a planar surface. That is,  $T_1^{-1}$  is given by [3.70], and after averaging over all orientations of the surface with respect to  $\vec{B}_0$ , the ratios between the three spectral densities [3.73] still pertains. The correlation functions and consequently the spectral densities may be calculated using [3.74]. This has been done by a number of authors<sup>58-61</sup> by modifying Torrey's analysis<sup>52</sup> to describe two-dimensional motion.

In practice, two limiting cases can be considered: the limit of continuous (two dimensional) diffusion, and the long-jump limit where

it can be considered that two initially adjacent atoms no longer interact after a single jump.

In the former (continuous diffusion) case, the calculation is quite analogous to the one outlined in the previous section although the results are no longer expressible in terms of elementary functions. When  $\omega_0 \tau_a \gg 1$ , where  $\tau_a = a^2/(2D)$  as before, it is found that  $J_{ij}^{(q)}(\omega_0) \propto \omega_0^{-2}$  in contrast to the  $\omega_0^{-3/2}$  dependence found in three-dimensional diffusion. If it is assumed that  $\tau_a \ll \tau_{Ad}$ , then in the frequency range  $\tau_{Ad}^{-1} \ll \omega_0 \ll \tau_a^{-1}$  it is found that  $J_{ij}^{(q)}(\omega_0) \propto [\text{const} - \ln(\omega_0 \tau_a)]$ . This low-frequency logarithmic divergence is cut off for  $\omega_0 \ll \tau_{Ad}^{-1}$  and  $T_{1Ad}$  becomes constant in this limit.

In the long-jump limit, the correlation functions are readily calculated using Poisson statistics. The spectral densities are proportional to  $\tau_c^{-1} [1 + \omega_0^2 \tau_c^2]^{-1}$  where  $\tau_c$  is the mean time between jumps.

Chapman and Bloom have measured  $T_{1W}$  of  $\text{He}^3$  gas inside of a  $1 \text{ cm}^3$  spherical Pyrex cell that had been coated with an annealed neon film.<sup>61</sup> The gas density was  $6 \times 10^{-3} \text{ g cm}^{-3}$  and measurements were made at 2.6, 4.2 and 8.0 K and over a range of values for  $B_0$ . They found that the continuous diffusion model correctly described the dependence of  $T_{1W}$  on  $B_0$ , but that the long-jump model did not. (It was assumed that  $T_{1Ad} \gg \tau_{Ad}$  so that  $T_{1W}$  and  $T_{1Ad}$  are directly proportional to each other.) At 8.0 K, a fit of the model to their data gave  $\tau_a = 2 \times 10^{-7} \text{ sec}$ . At the lower temperatures, however,  $\tau_a$  became about an order of magnitude shorter (e.g.,  $10^{-8} \text{ sec}$  at 4.2 K) than this. Chapman and Bloom point out that this is not a reasonable result since a shorter

correlation time should lead to weaker relaxation than that observed.

They suggest that this could be due to the partial formation of the second, more loosely bound, adsorbed layer. Thus while the 2D-diffusion model appears to be adequate for the description of a monolayer of  $\text{He}^3$  on annealed neon (or other similar surface), it is probably too crude to deal with relaxation at a liquid-solid interface.

Wall-induced relaxation due to foreign spins can be modeled in a similar fashion.<sup>61</sup> In the case of electronic spins, however, there are additional complications; *e.g.* the coupling may be scalar as well as dipolar and the relevant correlation time may be determined by the electronic-spin relaxation time.<sup>1</sup> The use of an inert-gas wall coating of sufficient thickness should reduce this problem to a negligible level provided that the  $\text{O}_2$  contamination of the gases can be kept sufficiently low.

## CHAPTER 4

### EXPERIMENTAL RESULTS AND ANALYSIS

#### 4.1 Initial Experimental Results

##### 4.1.1 *Effect of Sample Condensation on He<sup>3</sup> Polarization*

The first experimental question that had to be answered concerned the loss of He<sup>3</sup> polarization during the process of condensing the He<sup>3</sup>-He<sup>4</sup> mixture into the sample cell after traversing nearly 2 m of  $\frac{1}{2}$  mm-bore glass capillary. It turned out that this process was more efficient than had been feared. When the He<sup>3</sup> was polarized to  $\sim 5\%$  at 1 Torr pressure, the sample magnetization was such as to yield a magnetometer signal equivalent to a uniform applied field of  $1-2 \times 10^{-5}$  G. This gave a signal-to-noise ratio in excess of  $10^3$  with the magnetometer output filter having a 0.1 sec time constant. This was fortunate in that it allowed a number of relaxation-time measurements, typically between 10 and 15, to be made in a given experimental run.

Since the sample cell is approximately spherical in shape, the internal macroscopic flux density is approximately uniform and related to the magnetization by<sup>62</sup>

$$B_{mo} \approx 8\pi M/3 \approx (8\pi/3) (\frac{1}{2}h\gamma) P x_3 n_4 , \quad x_3 \ll 1 \quad [4.1]$$

where P is the He<sup>3</sup> polarization,  $x_3$  is the He<sup>3</sup> concentration, and  $n_4$  is the He<sup>4</sup> number density. A uniform applied magnetic field  $B_{az}$

that produces the same magnetometer signal as  $B_{mo}$  is related to  $B_{mo}$  by  $B_{az} = (R_o/R_c)^3 B_{mo}$  (see Sec. 5.3), where  $R_c$  is the pickup coil radius and  $R_o$  is the sample radius. Thus

$$P \approx (R_c/R_o)^3 [(8\pi/3)^{1/2} \hbar \gamma x_3 n_4]^{-1} B_{az}.$$

Estimating  $(R_c/R_o)^3 = 1.66$  and taking typical values  $x_3 = 6.9 \times 10^{-4}$ ,  $B_{az} = 1.7 \times 10^{-5}$  G, and  $n_4 = 1.88 \times 10^{22} \text{ cm}^{-3}$ , we find  $P \approx 2.4\%$  in a typical run. The efficiency of the condensation process is retaining the  $\text{He}^3$  polarization is therefore on the order of 40-50%.

#### 4.1.2 Initial $T_1$ Measurements

In the first experimental run that made use of the  $T_1$ -measurement technique described in Chap. 2, a series of  $T_1$  measurements were made under nominally constant conditions with an applied field,  $B_o = 50.9 \mu\text{G}$ . (In this run, 2 Torr of  $\text{He}^3$  was polarized so the  $\text{He}^3$  concentration in the sample was twice the typical value of  $6.9 \times 10^{-4}$ .) The purposes of this run were to obtain accurate measurements of  $T_1$  and to check the reproducibility of these measurements. The results are shown in Fig. 4.1.

The error bars in Fig. 4.1 were obtained by a standard propagation-of-errors calculation<sup>63</sup> based on estimates of timing error, magnetometer noise and chart recorder resolution. Also included was an estimate of the small systematic error introduced by the uncertainty in the direction of the applied magnetic fields due to the presence of an ambient field having an unknown direction and a poorly known magnitude. All of the error estimates of the individual  $T_1$  measurements that will be discussed in this chapter were made in this

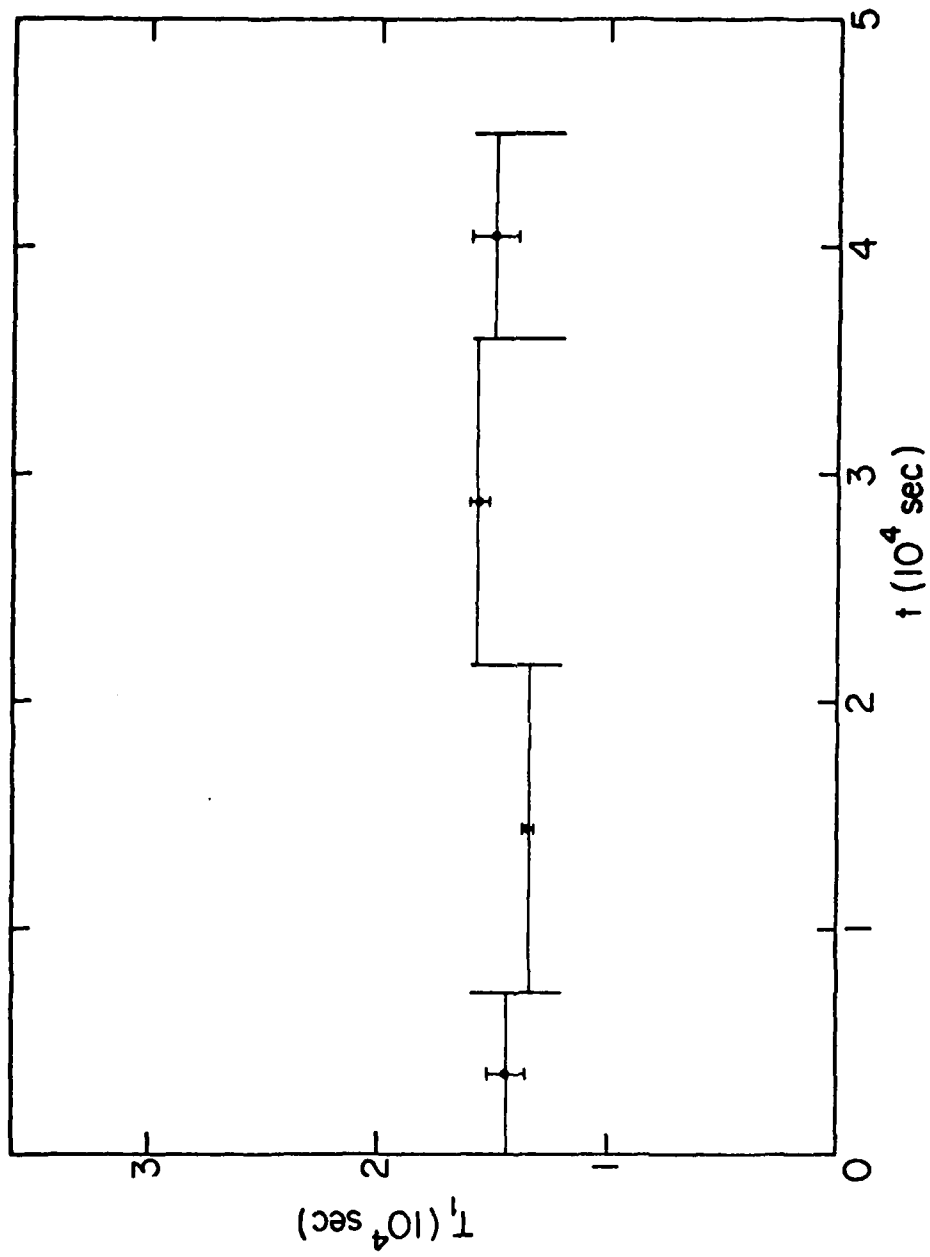


Fig. 4.1 Data from a sequence of  $T_1$  measurements made under nominally constant conditions. Error bars were estimated as described in the text. Applied field was  $B_0 = 50.8 \mu G$ , and the  $\text{He}^3$  concentration was estimated to be  $1.4 \times 10^{-3}$ .

fashion. The weighted average of the measurements made in this run was  $1.39 \times 10^4$  sec (3.9 h).

This relaxation time seemed to be much too short to be attributable to intrinsic relaxation. This was verified in a subsequent experimental run that was virtually identical to the one we have just described except only 1 Torr of  $\text{He}^3$  was used. Since the  $\text{He}^3$  density was halved, the relaxation time should have increased if intrinsic relaxation was playing any significant role. The relaxation time, however, did not change.

#### 4.1.3 *Field-Dependent Longitudinal Relaxation*

After the above measurements were made, it was discovered that  $T_1$  was strongly dependent on the magnitude of  $B_0$ . In particular, it was found that the relaxation time was an increasing function of  $B_0$  up to the 1 mG level above which  $T_1$  would level off in excess of  $1.25 \times 10^5$  sec (35 h).

Now a general conclusion that can be drawn from our discussion of simple relaxation mechanisms in liquids and gases in Chap. 3 is this: If the relaxation rate  $T_1^{-1}$  is a strong function of  $B_0$ , then there is a relaxation mechanism that has a correlation time  $\tau_c$  such that  $\omega_0 \tau_c \gtrsim 1$ . Since our results show a field dependence for  $\omega_0 < 1 \text{ rad sec}^{-1}$ , the responsible mechanism must have a correlation time in excess of 1 sec. The only mechanism that can reasonably fit this requirement is relaxation due to a magnetic-field gradient. We have already seen that the slowest diffusion mode has a decay time on the order of several hundred seconds. One might therefore expect that  $T_1^{-1} \propto \omega_0^{-2} + \text{const}$  because the first order gradient would generally

have the dominant effect due to its association with the slowest diffusion mode.

Unfortunately, things were not that simple. In the first place, the measured values of  $T_1^{-1}$  did not have an inverse-square dependence on  $B_0$ . Secondly, the first-order gradient that would be necessary on the basis of the theory in Chap. 3 (e.g. equation [3.60]) to account for the measured relaxation times would be inconsistent with the gradient inferred from the free-precession decay measurements discussed in Chap. 2. It turns out, however, that the observed field dependence is quite consistent with what would be expected from a dipolar field arising from a ferromagnetic contaminant located a distance from the sample cell that is small compared to the size of the sample. This hypothesis will be discussed in further detail in Sec. 4.3.

#### 4.2 Measurement of the $\text{He}^3$ Diffusion Coefficient

As we have seen in Chap. 3, it is necessary to know the diffusion coefficient of  $\text{He}^3$  in liquid  $\text{He}^4$  if we are to analyze the relaxation data. Since this information does not appear to be available in the literature for our experimental conditions, we have made our own measurement of this parameter.

Before describing this measurement, however, we note that it can be shown from the theory of diffusion in binary mixtures that provided the mass concentration of the component of interest ( $\text{He}^3$  in our case) is vanishingly small, then the motion of that component (i.e.,  $n_3$ ) is given by the ordinary diffusion equation

$$\frac{\partial n_3}{\partial t} = - D \nabla^2 n_3 ,$$

where  $D$  is independent of the concentration,  $x_3$ .<sup>64</sup> In this limit, the theory also shows that  $\frac{\partial n_3}{\partial t}$  is unaffected by a thermal gradient provided, of course, that the gradient is not big enough to cause convective motion. Since in all of our experiments  $x_3 < 3 \times 10^{-3}$ , we will assume that these results apply.

As was noted in Chap. 2, the horizontal field coils were wired so that they could be fed in opposition in order to produce a known gradient. In Chap. 3, the relaxation rate due to the gradient configuration produced by these coils was calculated. Since all of our data amply satisfied the condition  $\omega_0 \tau_{11} \gg 1$ , we use the expression [3.60]

$$T_{1G}^{-1} = (5/4) g^2 \gamma^2 D \omega_0^{-2} = (5/4) (g/B_0)^2 D , \quad [4.2]$$

where it is seen from equations [3.53] and [2.1] that

$$g = 48\pi NI / (125 \sqrt{5} a^2) \approx 0.394 I (G \text{ cm}^{-1}) ,$$

$I$  being the current in amps that is fed to each coil. If a series of relaxation measurements is made with various values of  $g$ ,  $D$  can be experimentally determined by a least-squares fit of the data to

$$T_1^{-1} = (T_1^{-1})_{g=0} + (5/4) (g/B_0)^2 D \quad [4.3]$$

The results of such a sequence of measurements are shown in Fig. 4.2 along with the curve obtained by a weighted least-squares fit.<sup>63</sup> These measurements were made with  $B_0 = 1.45 \text{ mG}$  so that the

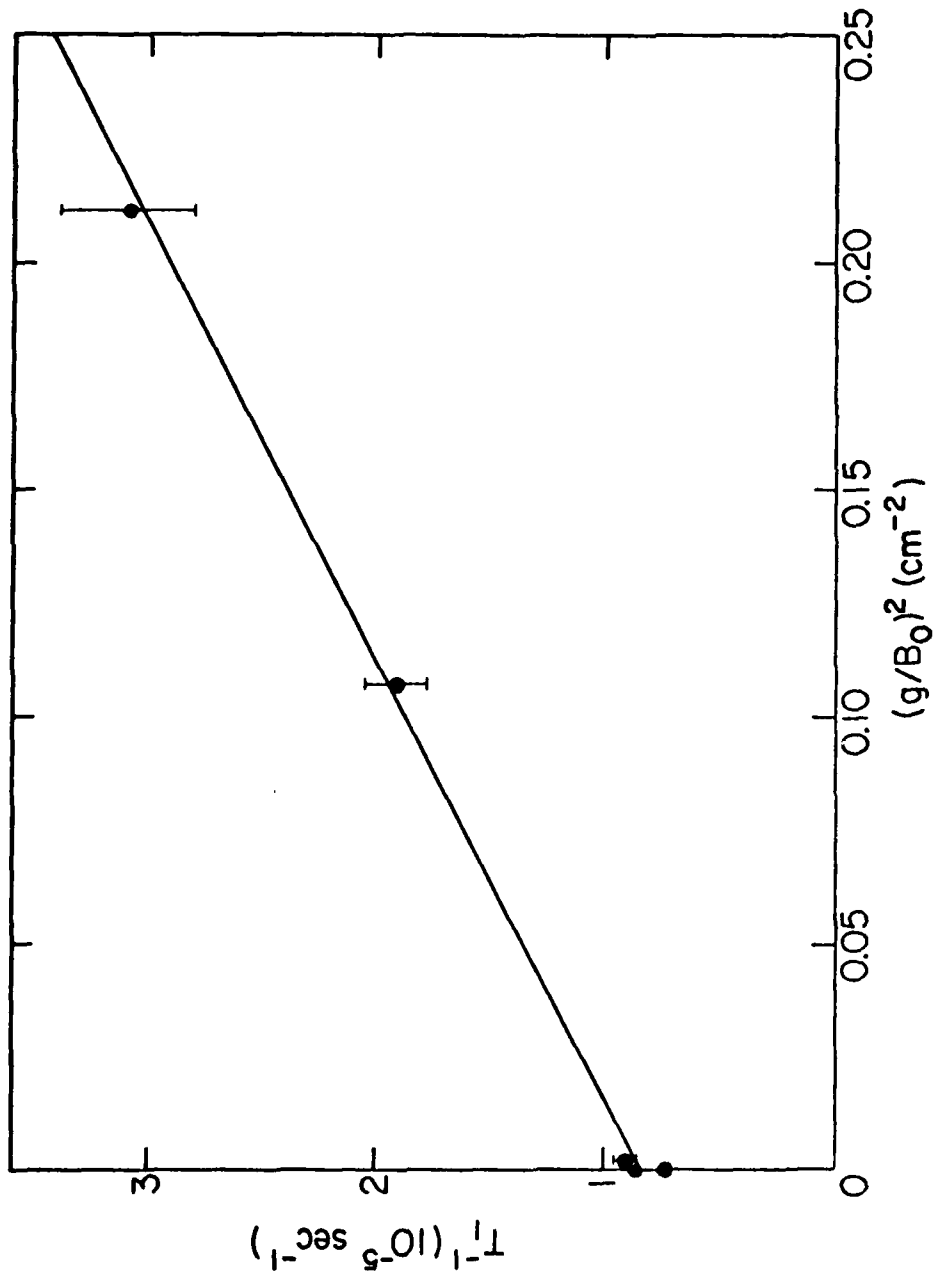


Fig. 4.2 Measurement of the  $\text{He}^3$  diffusion coefficient in liquid  $\text{He}^4$  by application of a sequence of known gradients. The expression  $T_1^{-1} = (T_1^{-1})_{g=0} + (5/4)(g/B_0)^2 D$  was fit to the data to yield  $D = (8.4 \pm 0.8) \times 10^{-5} \text{ cm}^2 \text{ sec}^{-1}$ . Uniform field was  $B_0 = 1.45 \text{ mG}$ .

effect of the ferromagnetic contaminant dipole was minimal. The weighted fit yielded the results  $(T_1^{-1})_{\text{g=0}} = (8.02 \pm 0.2) \times 10^{-6} \text{ sec}^{-1}$ , and  $D = (8.4 \pm 0.8) \times 10^{-5} \text{ cm}^2 \text{ sec}^{-1}$ .\*

Although there do not appear to be any published measurements of the diffusion coefficient of  $\text{He}^3$  in liquid  $\text{He}^4$  at 4.2 K, Harrison and Hatton<sup>65</sup> have reported on measurements made up to  $\sim 3$  K on mixtures having  $\text{He}^3$  molar concentrations as low as  $x_3 = 0.137$ . A rough extrapolation of their data on this lowest molar concentration to 4.2 K yields an estimate that agrees reasonably well with our result.

#### 4.3 Relaxation Due to a Nearby Ferromagnetic Dipole

##### 4.3.1 *Results of Model Calculation*

Having seen that the observed field-dependent relaxation is inconsistent with a uniform-gradient model, we now turn to an analysis of the relaxation that would be expected from the next most likely perturbation field: a dipolar field arising from a nearby ferromagnetic contaminant. We will show that there is sufficiently good circumstantial evidence in support of the validity of this model to allow us to deduct this effect from our data so that the field independent mechanisms, *i.e.*, wall-induced relaxation and

\* It should be pointed out that the experimental conditions under which these measurements were made were not accurately known. That is, although the conditions were intended to be at the NBP of  $\text{He}^4$ , the sample pressure and temperature were not directly monitored. In particular, the practice of overfilling the sample cell (see Chap. 2) could lead to the liquid-vapor interface being sufficiently high in the fill-line capillary that the sample pressure could be somewhat in excess of 1 atm. All we were really interested in, of course, was the value of  $D$  under the same conditions that all the other measurements were made.

intrinsic relaxation, may be studied.

In order to simply model the effect of relaxation due to diffusion through a dipolar field, we consider a cubical sample cell having sides of length  $L$  with a ferromagnetic dipole  $\vec{m}$  located a distance  $b$  from the center of one face of the sample (see Fig. 4.3). It is assumed that the relative orientations of  $\vec{m}$ ,  $\vec{B}_0$ , and the vector between  $\vec{m}$  and the center of the sample do not have a major effect on the magnitude of the relaxation rate so that all three may be taken to be in the  $z$  direction as a first approximation. In addition, it is assumed that a)  $\omega_0(\pi/L)^2 D^{-1} \gg 1$ , b)  $b \ll L$  and c)  $|\vec{B}_0| \gg |\vec{B}_1(\vec{r})|$  everywhere in the sample volume, where  $\vec{B}_1(\vec{r})$  is the dipolar perturbation field. Assumption a) is demonstrably true for our experiments. Assumption b) is justified *a posteriori*: all of our experimental information is consistent with the results obtained with this assumption. Assumption c) arises from our validity discussion in Chap. 3. An estimate of  $|\vec{m}|$  on the basis of fitting the data to the results of this model will indicate that c) is moderately well satisfied.

With these assumptions it is not difficult although somewhat tedious to use the results of Chap. 3 to calculate  $T_{1G}^{-1}$ . The details of the calculation are presented in Appendix A, and only the results will be discussed here. Explicit results can be obtained in two limiting cases: 1)  $\omega_0 \tau_b \ll 1$ , and 2)  $\omega_0 \tau_b \gg 1$ , where  $\tau_b \equiv b^2/D$ .

In case 1), we obtain

$$T_{1G}^{-1} = \pi \gamma^2 m^2 / (8VbD), \quad \omega_0 \tau_b \ll 1, \quad [4.4]$$

where  $V = L^3$  is the sample volume. In the opposite limit,

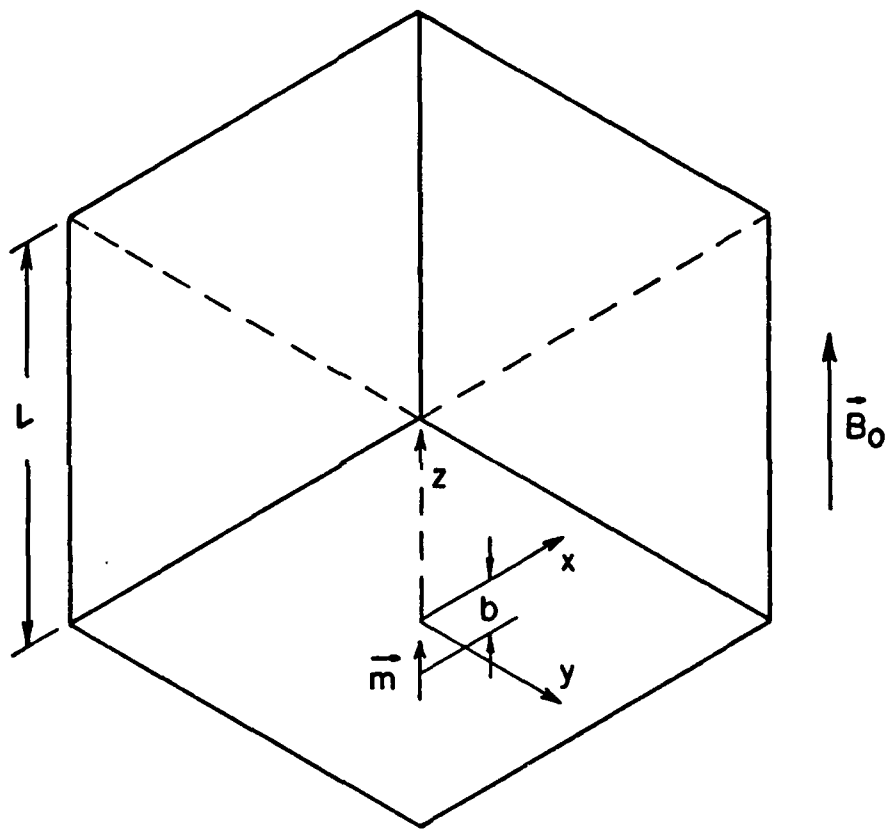


Fig. 4.3 Geometry and coordinate system used to estimate the relaxation due to an external ferromagnetic dipole.

$$T_{1G}^{-1} = [3 \pi \gamma^2 m^2 D^{1/2} / (4 \sqrt{2} b^4 V)] \omega_0^{-3/2}, \quad \omega_0 \tau_b \gg 1. \quad [4.5]$$

Thus the dipolar perturbation field leads to a  $\omega_0^{-3/2}$  dependence in the limit  $\omega_0 \tau_b \gg 1$  and  $L \gg b$ . It is not difficult to see from the discussion in Appendix A that relaxation arising from a remotely located dipole,  $b \gg L$ , would yield a  $\omega_0^{-2}$  dependence. Since  $B_0$  spans a range of almost two decades in our data, a discrepancy of  $\omega_0^{1/2}$  is quite marked, and our data clearly favors the  $\omega_0^{-3/2}$  dependence.

Before making a detailed comparison with our data, a general comment is in order. In our review of the intrinsic nuclear relaxation of monatomic liquids in Chap. 3, it was noted that a model based on continuous diffusive relative motion between atoms led to a  $\omega_0^{-3/2}$  dependence in the limit that  $\omega_0 \tau_a \gg 1$ . Here  $\tau_a \equiv a^2 / (2D)$ , where  $a$  is the distance of closest approach between two atoms. Since dipolar interactions are involved in both intrinsic nuclear relaxation and in the present case, it is clear that the present case is a kind of macroscopic analog of intrinsic relaxation. There are, of course, gross differences of scale. For liquid He,  $\tau_a \approx 10^{-11}$  sec while for the present case  $\tau_b \approx 10^2$  sec. It should also be noted that while it is inappropriate to use the diffusion equation to describe atomic motion for times  $\lesssim \tau_a$ , its use for times  $\lesssim \tau_b$  is very well justified except in the case of a low pressure gas.

#### 4.3.2 Comparison of the Dipole Model with the Data

In order to test our ferromagnetic dipole hypothesis, the function

$$T_1^{-1} = T_{1\infty}^{-1} + \alpha B_0^{-3/2} \quad [4.6]$$

was fitted by means of the weighted least-squares technique to the data from the first experimental run where a systematic measurement of  $T_1$  vs.  $B_0$  was made. The data and the resulting fitted curve are shown in Fig. 4.4. The fit parameters were  $T_{1\infty} = (1.45 \pm 0.04) \times 10^5$  sec (40.4 h), and  $\alpha = (2.04 \pm 0.1) \times 10^{-11}$  sec $^{-1}$  G $^{3/2}$ . The fit to data obtained from some of the other experimental runs using [4.6] will be shown in following sections.

The question that now arises is whether there is a reasonable probability that there is at least one ferromagnetic dipole of sufficient magnitude and in sufficiently close proximity to the sample to account for the value of  $\alpha$  that has been obtained. To answer this we note that there are only three materials that are sufficiently close to the sample to satisfy the  $b \ll L$  condition: Pyrex glass, Delrin plastic, and niobium wire. Cabrera<sup>17</sup> has measured the remanent magnetization of typical samples of all of these materials at 4.2 K using a SQUID magnetometer. Of these materials, Delrin is the most suspect since it was found to be invariably contaminated with numerous isolated ferromagnetic inclusions. Particularly suspect was the Delrin coil form (Fig. 4.5), since it came to within an estimated 0.06 cm of the sample.

In order to be more quantitative we use equations [4.6] and [4.5] to write

$$\alpha \approx 3\pi(\gamma D)^{1/2} m^2 / (4\sqrt{2} b^4 V) . \quad [4.7]$$

If we take  $b = 0.1$  cm and estimate the sample volume to be  $V = 0.38$  cm $^3$ , equation [4.7] together with the measured value of  $\alpha$  yields the esti-

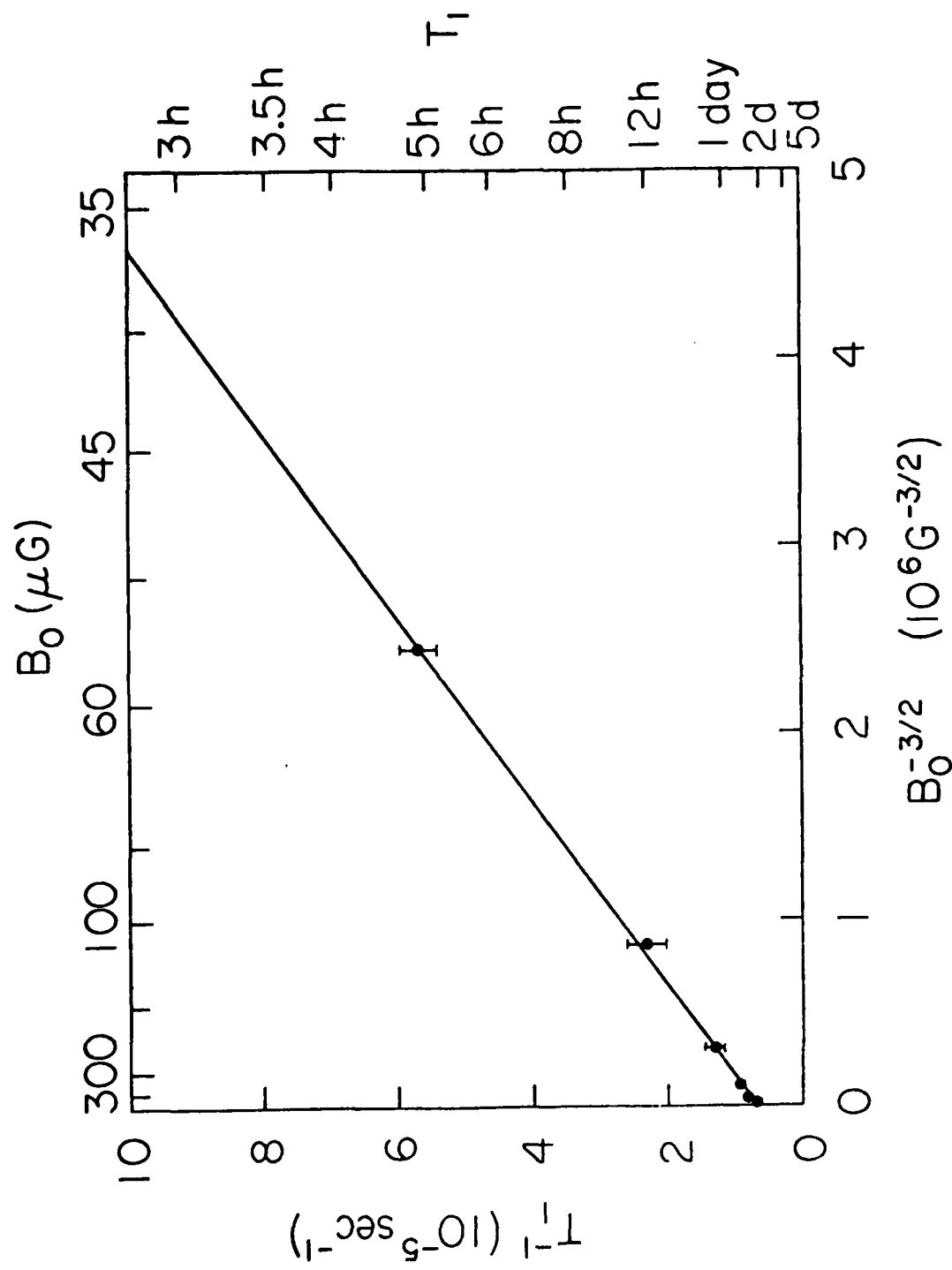


Fig. 4.4  $T_1$  as a function of  $B_0$  in the bare Pyrex sample cell. The straight line is a fit of  $T_1^{-1} = T_{1\infty}^{-1} + \alpha B_0^{-3/2}$  to the data yielding  $T_{1\infty} = 40.4 \pm 1$  hours.

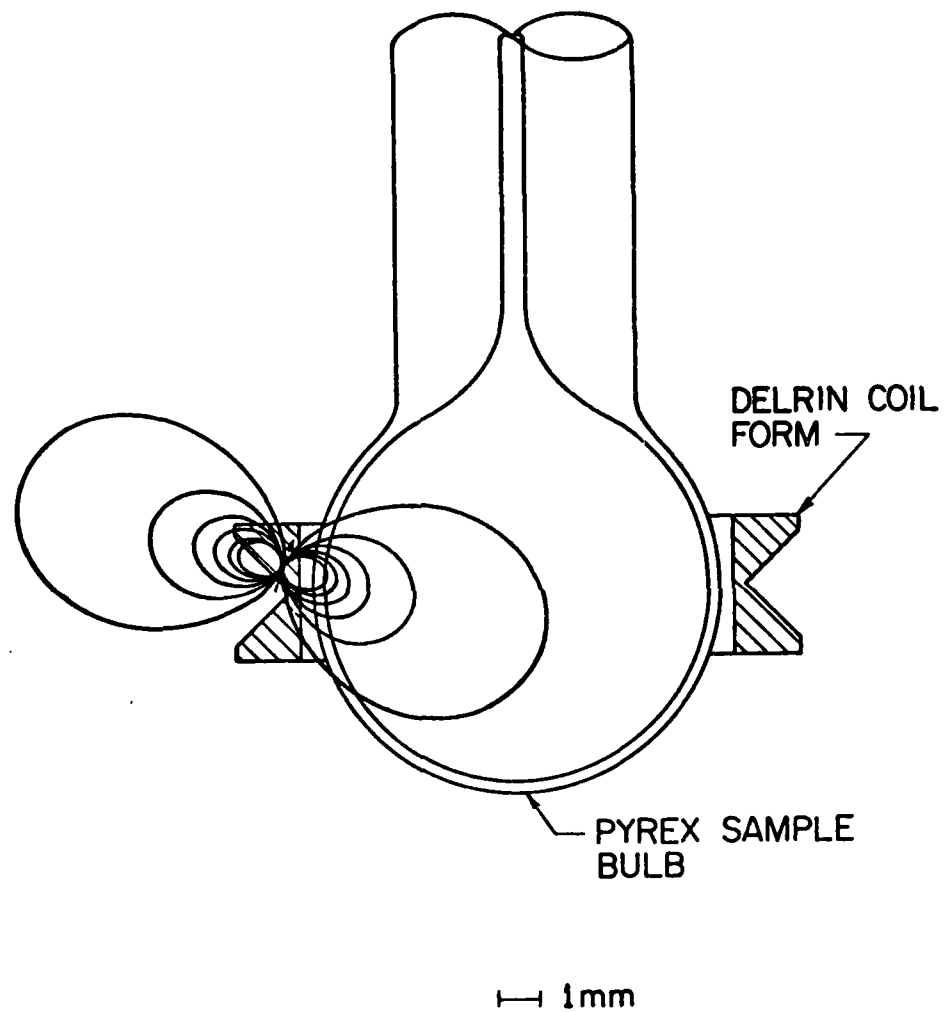
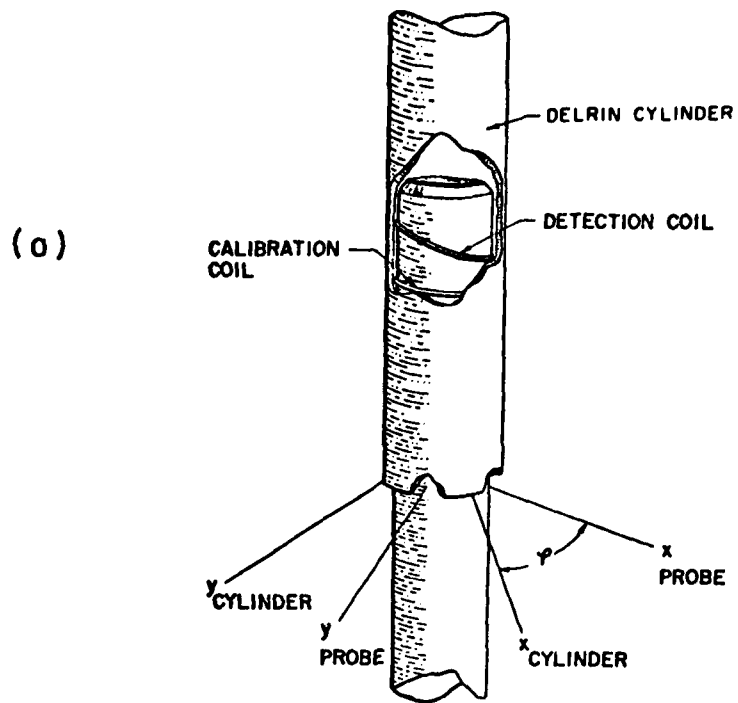


Fig. 4.5 Detail of sample cell and pickup coil form showing possible location of a ferromagnetic dipole.

mate  $m \approx 2 \times 10^{-8} \text{ G cm}^3$ . This can then be compared with the results of measurements made by Cabrera on two thin-wall cylindrical samples of Delrin of dimensions  $\frac{1}{2}'' \text{ diam} \times 4'' \text{ length} \times .010'' \text{ wall}$ . These samples were axially scanned by slowly sliding the cylinders over a close fitting cylindrical post that had a superconducting pickup coil wound on it (Fig. 4.6a). Fig. 4.6b shows the results of these scans. The reference marks in Fig. 4.6b show the peak signal that would be obtained from a point dipole of magnitude  $m = 2 \times 10^{-8} \text{ G cm}^3$  that was embedded in the sample wall and oriented in the axial direction. Cabrera points out that this type of measurement always given a *lower* bound on the size of the dipole. Although the evidence shown in Fig. 4.6 cannot be conclusive since the measurement was not made on our coil form and since the value of  $m$  inferred from [4.7] is very sensitive to the value chosen for  $b$ , it is clear that our hypothesis is very reasonable indeed.

There is additional supporting evidence for the ferromagnetic dipole hypothesis. For one thing, a microscopic examination of the coil form revealed a brown contaminant speck near the inner surface. (The coil form was made of unpigmented Delrin which has a white, translucent appearance similar to that of natural nylon.)

Another piece of corroborating evidence was also obtained in an unexpected fashion. In the first 15 experimental runs the cryostat was kept cold continuously in order to avoid disturbing the apparatus unnecessarily. Between each of the subsequent runs (excepting between 19 and 20), however, the cryostat probe was removed and reinserted into the dewar in order to remove and apply cryogenic wall coatings.



(b)

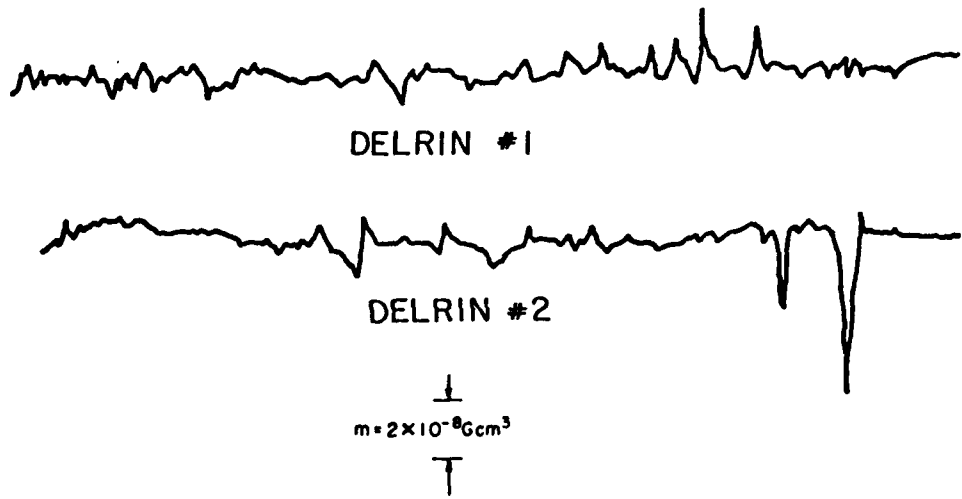


Fig. 4.6 (a) Detail of apparatus used by Cabrera to measure remanent magnetization associated with 4" long  $\times$  1/2" diam  $\times$  0.01" wall Delrin cylinders. Detection coil was coupled to a SQUID magnetometer.  
 (b) Scans made with this apparatus along the length of two different Delrin samples.

In the analysis of data from these runs it was noted that the fit parameter  $\alpha$  in equation [4.6] was slowly declining from one run to the next. It was speculated that this was due to a shifting of the coil assembly (which was clamped to the fill capillary with an RTV rubber cushion) with respect to the sample bulb because of the effects of thermal cycling. A subsequent disassembly of the apparatus indeed revealed that there had been a downward shift of the coil assembly by 0.15 - 0.2 cm. The numerical decline that was noted in  $\alpha$  was consistent with this amount of motion.

It should also be noted that the  $B_0^{-3/2}$  behavior was otherwise immune to changes in experimental parameters. For instance, this behavior was unaffected by wall coatings and  $\text{He}^3$  density. In addition, factors such as changes in the bath temperature, vertical location of the cryostat probe in the dewar, whether the magnetometer was on or off, and current changes in the pickup loop corresponding to 1  $\phi_0$  at the SQUID either had little or no effect on the relaxation rate.

The preponderance of this evidence suggests that the source of the field-dependent relaxation has been correctly identified. In the following sections, we will identify  $T_{1\infty}^{-1}$  with the sum of the wall-induced and intrinsic relaxation rates, both of which should be quite independent of the small applied field,  $B_0$ . This is equivalent to assuming that the microscopic correlation times associated with these two remaining relaxation mechanisms are very short compared to the smallest value of  $\omega_0^{-1}$  that was used in our experiments ( $\omega_0^{-1} \geq 2 \times 10^{-2}$  sec).

#### 4.4 Wall-Induced Relaxation and Intrinsic Relaxation in the Bulk

Having made the identification  $T_{1\infty}^{-1} = T_{1W}^{-1} + T_{1B}^{-1}$ , we now wish to analyze our data in light of some of the models that were discussed in Chap. 3. Comparison of our data with that published by other workers will be made in order to facilitate this analysis.

As a result of this, we will see that there are two effective ways of reducing  $T_{1W}^{-1}$  for  $\text{He}^3$  at 4.2 K: 1) use a wall coating of solid  $\text{H}_2$ , and 2) use  $\text{He}^4$  as a buffer for the adsorbed phase. In addition, our data will show that the two techniques may be used together with advantage.

##### 4.4.1 *Effect of $\text{He}^4$*

In order to discuss the interplay between wall-induced relaxation and intrinsic relaxation in the bulk, it is useful to summarize the results obtained by Chapman and Richards<sup>31</sup> (CR) from  $T_1$  measurements of  $\text{He}^3$  gas at 4.2 K over a range of densities  $2 \times 10^{-5} < \rho < 7 \times 10^{-2} \text{ g cm}^{-3}$ . Their results are particularly useful to us because their sample cell was virtually identical to ours and similar cleaning procedures were used. Their measurements, however, were made with  $B_0 = 1 \text{ kG}$ . CR found that their results could be represented by

$$T_{1\infty}^{-1} = C_1 n_{m3} + C_2 / n_{m3} \quad [4.8]$$

where  $n_{m3}$  is the  $\text{He}^3$  molar density,  $C_1$  is a constant that did not vary from run to run, and  $C_2$  is a constant that was found to depend on the cleanliness of the sample-cell wall.

CR identified the first term with the intrinsic rate in the bulk,

$T_{1B}^{-1}$ , and the second with the wall-induced rate,  $T_{1W}^{-1}$ . The reason that  $T_{1B}^{-1}$  is proportional to  $n_{m3}$  has been discussed in Sec. 3.4.

The reason that  $T_{1W}^{-1} \approx C_2/n_{m3}$  can be seen from equation [3.80],

$$T_{1W} = (N_{3B}/N_{3Ad})(T_{1Ad} + \tau_{Ad}) , \quad [3.80]$$

if certain conditions are met. The primary condition is that the  $He^3$  molar surface density,  $s_{m3}$ , be independent of  $n_{3m}$ ; *i.e.*,  $n_{m3}$  should be large enough for the surface to be saturated so that the adsorption isotherm is relatively flat. Secondly, it is necessary that  $T_{1Ad} + \tau_{Ad}$  be independent of  $n_{m3}$ . If these conditions hold and [3.80] is written in the form

$$T_{1W}^{-1} = 3s_{m3}/[n_{m3}R_o(T_{1Ad} + \tau_{Ad})] , \quad [4.9]$$

where  $3/R_o$  is the surface-to-volume ratio for a sphere of radius  $R_o$ , then the inverse relationship between  $T_{1W}^{-1}$  and  $n_{m3}$  is apparent.

Actually, CR assumed (as will we) that  $T_{1Ad} \ll \tau_{Ad}$  so that [3.80] and [4.9] become

$$T_{1W} = N_{3B}T_{1Ad}/N_{3Ad} \quad [3.80']$$

and

$$T_{1W}^{-1} = 3s_{m3}/(n_{m3}R_oT_{1Ad}) . \quad [4.9']$$

The justification for this assumption in the case of Pyrex or other weakly relaxing surfaces is that  $C_2$  in [4.8] is in fact sensitive to surface preparation.<sup>24,31</sup> If the opposite limit were true,  $\tau_{Ad} \gg T_{1Ad}$ , the state of surface cleanliness would have little or no effect on the measured relaxation. Thus, with the various assump-

tions that have been made

$$C_2 = 3s_{m3}/(R_o T_{1Ad}) \quad [4.10]$$

CR determined  $C_1$  by fitting [4.8] to their data and found  $C_1 = (4.9 \pm 0.2) \times 10^{-2} \text{ sec}^{-1} \text{ cm}^3 \text{ mol}^{-1}$ . Although they don't specify the values of  $C_2$  that were obtained,  $C_2$  can be readily inferred from their data plot by noting that  $T_{1\infty}$  is a maximum when  $n_{m3}^2 = C_2/C_1$ . We thus find that  $1.4 \times 10^{-7} < C_2 < 2 \times 10^{-6} \text{ sec}^{-1} \text{ mol cm}^{-3}$ , depending on the surface cleanliness.

By using these values for  $C_1$  and  $C_2$  in [4.8] we can estimate the relaxation time that would be obtained for the typical  $\text{He}^3$  density used in our experiments (*i.e.*,  $n_{m3} = 2.16 \times 10^{-5} \text{ mol cm}^{-3}$  when the optical pumping bulb was initially loaded with 1 Torr  $\text{He}^3$ ) but in the absence of the liquid  $\text{He}^4$ :  $10 < T_{1\infty} < 150 \text{ sec}$ . Since the value of  $T_{1\infty}$  quoted in the previous section is  $\sim 10^3$  times 150 sec, it is clear that the presence of the liquid  $\text{He}^4$  buffer has drastically reduced  $T_{1W}^{-1}$ . As an alternative comparison, we note that the longest relaxation time obtained by CR was  $\sim 5 \times 10^3 \text{ sec}$  (1.4 h) at a density of  $3.3 \times 10^{-3} \text{ mol cm}^{-3}$ .

It scarcely needs to be pointed out, however, that for our intended application the presence of the  $\text{He}^4$  is certainly not an unmixed blessing. For example, the use of liquid  $\text{He}^4$  has the effect of reducing the  $\text{He}^3$  diffusion coefficient by  $\sim 10^4$  and thereby increasing the zero-field relaxation rate due to magnetic-field gradients by that factor. In addition we will see that the use of liquid  $\text{He}^4$  will also shorten  $T_{1B}$  somewhat ( $\sim 40\%$  at 4.2 K under SVP),

although the presence of  $\text{He}^4$  gas should have little effect on  $T_{1B}$ .

By using the range of values for  $C_2$  inferred from CR together with [4.10], a range of values for  $T_{1\text{Ad}}$  can be estimated. Taking  $R_o = 0.5 \text{ cm}$ ,  $s_{m3} \approx 1.7 \times 10^{-9} \text{ mol cm}^{-2}$  ( $10^{15} \text{ atoms cm}^{-2}$ ), we find  $5 \times 10^{-3} < T_{1\text{Ad}} < 7 \times 10^{-2} \text{ sec.}$

These simple considerations can be readily extended to  $\text{He}^3\text{-He}^4$  mixtures. To do this, we take advantage of the relatively high temperature involved and make the approximation that  $\text{He}^3$  and  $\text{He}^4$  are identical with regard to their adsorption properties.\* In this case, then, we write

$$s_{m3}/s_{m4} = n_{m3}/n_{m4} ,$$

$$s_{m3} + s_{m4} = s_{mt} = \text{const} ,$$

and

$$N_{3\text{Ad}}/N_{3B} = 3s_{mt}/(n_{mt} R_o) \quad [4.11]$$

where  $n_{mt} = n_{m3} + n_{m4}$ . Thus,

$$T_{1\infty}^{-1} = C_1' n_{m3} + [3s_{mt}/(n_{mt} R_o)] T_{\text{Ad}}^{-1} , \quad [4.12]$$

where  $C_1'$  may or may not be the same as  $C_1$  depending on whether the  $\text{He}^4$  has liquid or gas density. (It is assumed that  $n_{m3}$  is much smaller than liquid density.)

If we assume that the presence of  $\text{He}^4$  cannot increase  $T_{1\text{Ad}}^{-1}$  and

\* This approximation is reasonable given the crudeness of the present analysis. At lower temperatures, this approximation becomes invalid as the  $\text{He}^4$  tends to exclude  $\text{He}^3$  from the wall.<sup>65</sup> This occurs because  $\text{He}^3$  has a slightly larger effective atomic volume due to its greater zero-point motion.

that  $s_{mt}$  is virtually independent of  $n_{m3}/n_{m4}$ , we see by comparing [4.9'] and [4.12] that the *minimal* effect of a  $\text{He}^4$  buffer is to multiply  $T_{1W}^{-1}$  by the factor  $n_{m3}/(n_{m3} + n_{m4}) \ll 1$ . With the use of  $\text{He}^4$ , then, one can lengthen the intrinsic relaxation time in the bulk by reducing  $n_{m3}$  without incurring a penalty from  $T_{1W}^{-1}$ .

Experimentally, however, we now face a somewhat more difficult situation. In the case of pure  $\text{He}^3$  one is reasonably justified in assuming that  $T_{1Ad}^{-1}$  is fairly independent of  $n_{m3}$  so that relaxation in the bulk can be experimentally separated from  $T_{1W}^{-1}$  by fitting [4.8] to the data. In the case of  $\text{He}^3$ - $\text{He}^4$  mixtures, however, this may not be the case for clean or coated walls where the intrinsic relaxation process in the adsorbed phase may be significant. Since the intrinsic process in the adsorbed phase would also be proportional to  $n_{m3}$ , one cannot identify the component of  $T_{1\infty}^{-1}$  that is proportional to  $n_{m3}$  exclusively with the first term in [4.12], *i.e.*,  $T_{1B}^{-1}$ .

Although the technique of using sample cells of differing radii could be used, we did not do so. Relaxation measurements were made, however, at three different  $\text{He}^3$  densities:  $p_3 = 0.4, 1$ , and 4 Torr pressure in the optical pumping bulb. In order to interpret these results, we will resort to using the Oppenheim and Bloom<sup>53</sup> theoretical estimate of  $T_{1B}^{-1}$  for pure liquid  $\text{He}^3$  (see Sec. 3.4), which has been experimentally verified.<sup>24</sup> Hence,

$$T_{1B}^{-1} = C_1' n_{3m} ,$$

where

$$C_1' \approx 1.97 N_A \gamma^4 \hbar^2 I(I+1)/aD , \quad [4.13]$$

and where  $N_A$  is Avogadro's number. Taking for D our measured value  $8.4 \times 10^{-5} \text{ cm}^2 \text{ sec}^{-1}$  and  $2.56 \times 10^{-8} \text{ cm}$  for the Lennard-Jones radial parameter, we find  $C_1' \approx 7.9 \times 10^{-2} \text{ sec}^{-1} \text{ cm}^3 \text{ mol}^{-1}$ . For our typical  $\text{He}^3$  density  $n_{m3} = 2.16 \times 10^{-5} \text{ mol cm}^{-3}$  this yields  $T_{1B} \approx 5.85 \times 10^5 \text{ sec}$  (162 h).

Although this is not a particularly desirable way to proceed, this is sufficiently accurate to allow estimates of  $T_{1Ad}^{-1}$  for the purpose of comparison with the CR data. In addition, it will be seen in Sec. 4.3.2 that this theoretical estimate of  $T_{1B}$  is only  $\sim 15\%$  greater than an experimental lower bound on  $T_{1B}$ . Hence we can say with reasonable certainty that  $C_1' \lesssim 10^{-1} \text{ sec}^{-1} \text{ cm}^3 \text{ mol}^{-1}$ .

By using the value of  $C_1'$  obtained from [4.13] we have plotted  $T_{1W}^{-1} \approx T_{1\infty}^{-1} - C_1' n_{m3}$  in Fig. 4.7 from each of the three experimental runs where different values of  $n_{m3}$  were used. Also shown are the estimated values of  $T_{1Ad}^{-1}$  where we have used [4.11] to estimate  $N_{3Ad}/N_{3B} \approx 3.3 \times 10^{-7}$ .

On the basis of the results shown in Fig. 4.7 two comments can be made:

- 1) No conclusion may be drawn concerning the dependence of  $T_{1W}$  on  $n_{m3}$  from this data alone. It should be noted that the experimental run where the largest  $\text{He}^3$  density was used ( $p_3 = 4 \text{ Torr}$ ) was widely separated in time from the other two. In addition, this particular run occurred after  $\text{O}_2$ -contaminated  $\text{He}^4$  had been admitted to the sample cell (see Sec. 4.4.3).
- 2) Despite the large difference in  $s_{m3}$ , it is seen that the

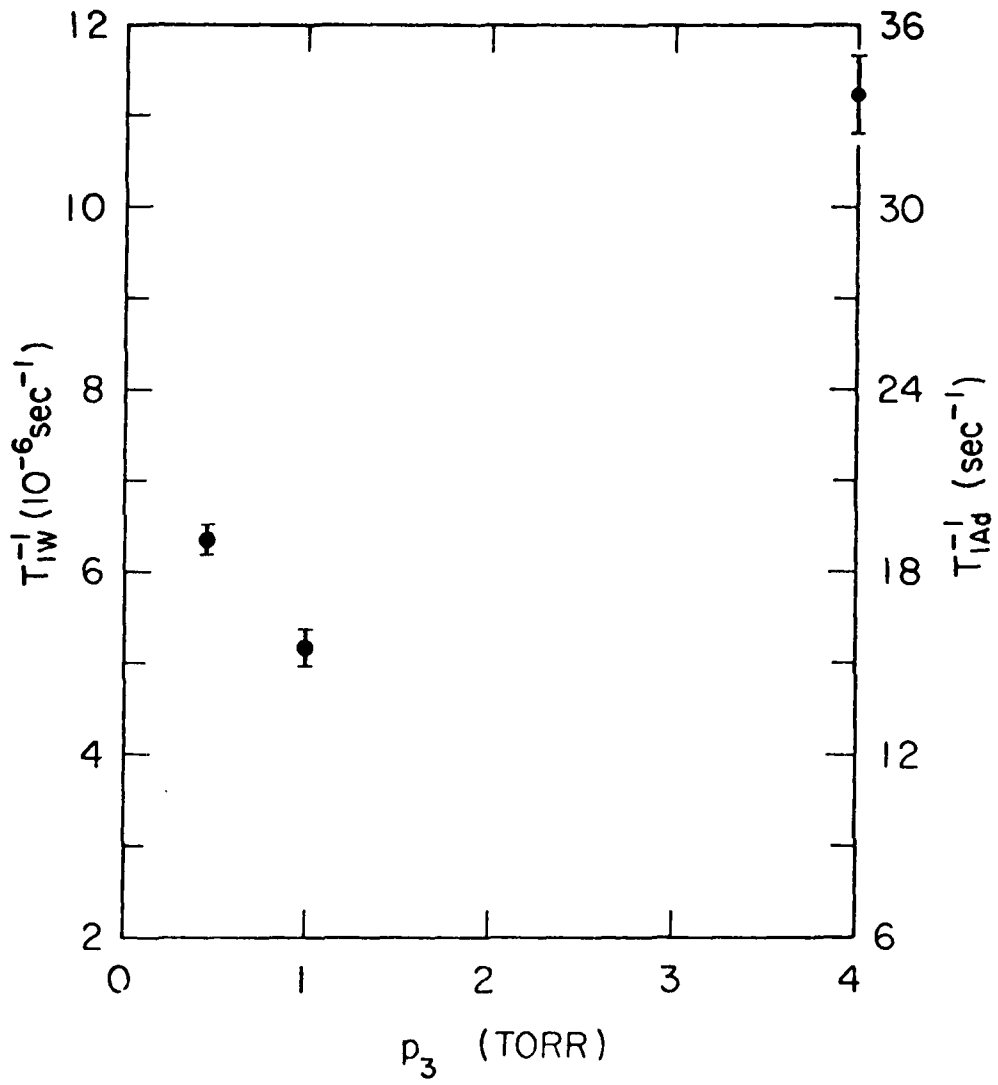


Fig. 4.7 Estimates of the wall-induced relaxation,  $T_{lw}^{-1}$ , and the relaxation rate in the adsorbed phase,  $T_{1Ad}^{-1}$ , as a function of the  $\text{He}^3$  pressure in the optical pumping cell,  $p_3$ .

estimates of  $T_{1Ad}$  that we have obtained ( $3-6 \times 10^{-2}$  sec) are quite similar to those that can be inferred from the CR data ( $5 \times 10^{-3} - 7 \times 10^{-2}$  sec). It is tempting to conclude that this shows that in spite of the plasma cleaning,  $T_{1Ad}^{-1}$  is still dominated by foreign-spin interactions, in particular by electronic paramagnetic centers. Since the CR data were taken in a field of 1 kG ( $\omega_0 = 2 \times 10^7$  rad sec $^{-1}$ ), however, it is not possible to do so without demonstrating that  $T_{1W}$  has no significant field dependence below 1 kG. Since Chapman and Bloom<sup>61</sup> have found that He<sup>3</sup> on annealed Ne has a correlation time of  $\tau_a = 2 \times 10^{-7}$  sec (see Sec. 3.5) this possibility cannot be discounted.

#### 4.4.2 Cryogenic Wall Coatings

Because  $T_{1W}$  becomes very short for the low He<sup>3</sup> gas densities that must be used for optical pumping of He<sup>3</sup>, it normally becomes impossible to obtain any measurable nuclear polarization by use of this technique at temperatures below  $\sim 20$  K. It was discovered by Barbé, Laloë, and Brossel<sup>32</sup> (BLB), however, that the use of certain solid cryogenic wall coatings could be used to dramatically reduce the wall-induced relaxation of He<sup>3</sup> at low temperatures and thus allow significant nuclear polarization to be achieved. In particular, they found that the use of a solid H<sub>2</sub> wall coating of  $\sim 30$  molecular layers at 4.2 K caused the relaxation time  $T_1 = T_{1W}$  ( $T_{1B}^{-1}$  was completely negligible) of He<sup>3</sup> gas at a density of  $2.7 \times 10^{-8}$  mol cm $^{-3}$  to increase from  $< 1$  sec (estimated to be  $10^{-2}$  sec) to  $60 \pm 10$  h. The sample cell diameter

was 3 cm.

BLB also found that the various cryogenic wall coatings were effective in allowing significant nuclear polarizations only over a limited temperature range below the freezing point of the coating gas. For instance,  $H_2$  was effective in the range of  $2 < T < 6.5$  K, and  $D_2$  was found to be effective for  $6 < T < 8.5$  K. Additionally, the noble gases Ne, Ar, Kr, and Xe were found to be effective over the ranges 8-13, 14-36, 16-50, and 17-33 K respectively.

In a detailed discussion of this phenomenon, Barbe<sup>33</sup> notes that the upper limit is simply due to the increasing vapor pressure of the wall coating which quenches the metastable ( $2^3S_1$ ) atoms and thereby inhibits the optical pumping process. He finds, however, that the low-temperature limit is due to a rapidly increasing  $T_{1W}^{-1}$ , which has a temperature dependence of the sort  $T_{1W}^{-1} \propto \exp(E/kT)$ . For example, in the case of a  $H_2$  wall coating,  $T_{1W} < 5$  sec when the temperature approaches 3.7 K.

It is therefore clear that the obvious function of a wall coating, *i.e.*, that of covering a magnetically dirty surface with a relatively nonmagnetic material, is not the dominant reason for the dramatic improvement in  $T_{1W}$ . The most important function is to reduce energy of adsorption,  $E_a$ , for a helium atom on the surface. In the case of low density  $He^3$  gas where the wall is unsaturated, this can have two, possibly three effects on  $T_{1W}$ :

- 1) The mean sticking or adsorption time, which is given by  $\tau_{Ad} = \tau_{Ad}^0 \exp(E_a/kT)$  when the coverage is much less than a monolayer, is reduced so that the probability

that a helium atom is adsorbed,  $N_{3\text{Ad}}/N_{3\text{B}}$ , is likewise reduced.

- 2) The correlation time,  $\tau_c$ , for an adsorbed atom becomes shorter so that under the assumption that  $\omega_0 \tau_c \ll 1$ ,  $T_{1\text{Ad}}^{-1}$  becomes proportionately smaller.
- 3) The intrinsic relaxation mechanism in the adsorbed phase is reduced since the  $\text{He}^3$  surface density is smaller.

The first two of these are discussed in detail by Barbé.<sup>33</sup>

Whether the third effect is significant or not depends on the nuclear and electronic spin density of the wall coating, the latter presumably being negligible if the  $\text{O}_2$  contamination is small.

In our experimental situation, it would not be expected that the  $\text{He}^3$  surface density would be greatly altered by the presence of a wall coating. It still could be possible, however, that a wall coating might be helpful in reducing the correlation time for atoms in the adsorbed phase as well as serving to cover magnetic sites in the glass surface. For these reasons, we decided to do some preliminary experiments with wall coatings.

In our experiments, several different wall coatings were tried at 4.2 K using the procedure described in Chap. 2. It should be pointed out, however, that since our experimental procedure required condensation of the  $\text{He}^3\text{-He}^4$  mixture after the coating had been frozen on the sample cell walls, it is possible that the wall coating was ablated to some extent during the interval when relatively warm gas was entering the cell.\* Thus it is unknown whether any given wall

coating was uniform or not or even whether all of the cell surfaces were covered or not. It can only be assumed that our results represent a lower bound on the effectiveness that a given wall coating would have under ideal circumstances.

Hydrogen wall coatings were used in two experimental trials (Fig. 4.8). In the first trial, an estimated equivalent of 30 molecular layers of solid  $H_2$  was used, and in the second a much thicker coating of  $\sim 280$  molecular layers was tried.<sup>+</sup> In the former case we obtained  $T_{1\infty} = 141 \pm 3$  h, although the longest relaxation time that was actually measured was  $128 \pm 8$  h. When the thicker  $H_2$  coating was used,  $T_{1\infty}$  dropped to  $57 \pm 1$  h. The reason for the thicker  $H_2$  wall coating yielding a shorter  $T_{1\infty}$  than the thin one has not been determined.

In any case, it is clear that  $\sim 30$  molecular layers of  $H_2$  wall coating had a definite impact on  $T_{1W}$ . By comparing  $T_{1\infty}$  for the bare cell (40.4 h) with the value obtained with the thin  $H_2$  coating we see that  $T_{1W} \lesssim 57$  h in the bare cell. In other words, wall-induced relaxation was responsible for  $\gtrsim 70\%$  of the relaxation rate that was measured in the bare cell.

---

<sup>\*</sup> Although some attempts were made to throttle the flow of the sample gas through the stopcock connecting the optical pumping bulb with the fill-line capillary, the presence of the stopcock grease made it virtually impossible to obtain anything other than an on-off response.

<sup>†</sup> The estimates of the equivalent coating thickness were based on the assumption that all of the wall-coating gas ended up on the sample-cell surface. This assumption is reasonable since the sample cell, because of its location and its thin walls, would cool before the fill capillary as the probe was lowered into the dewar.

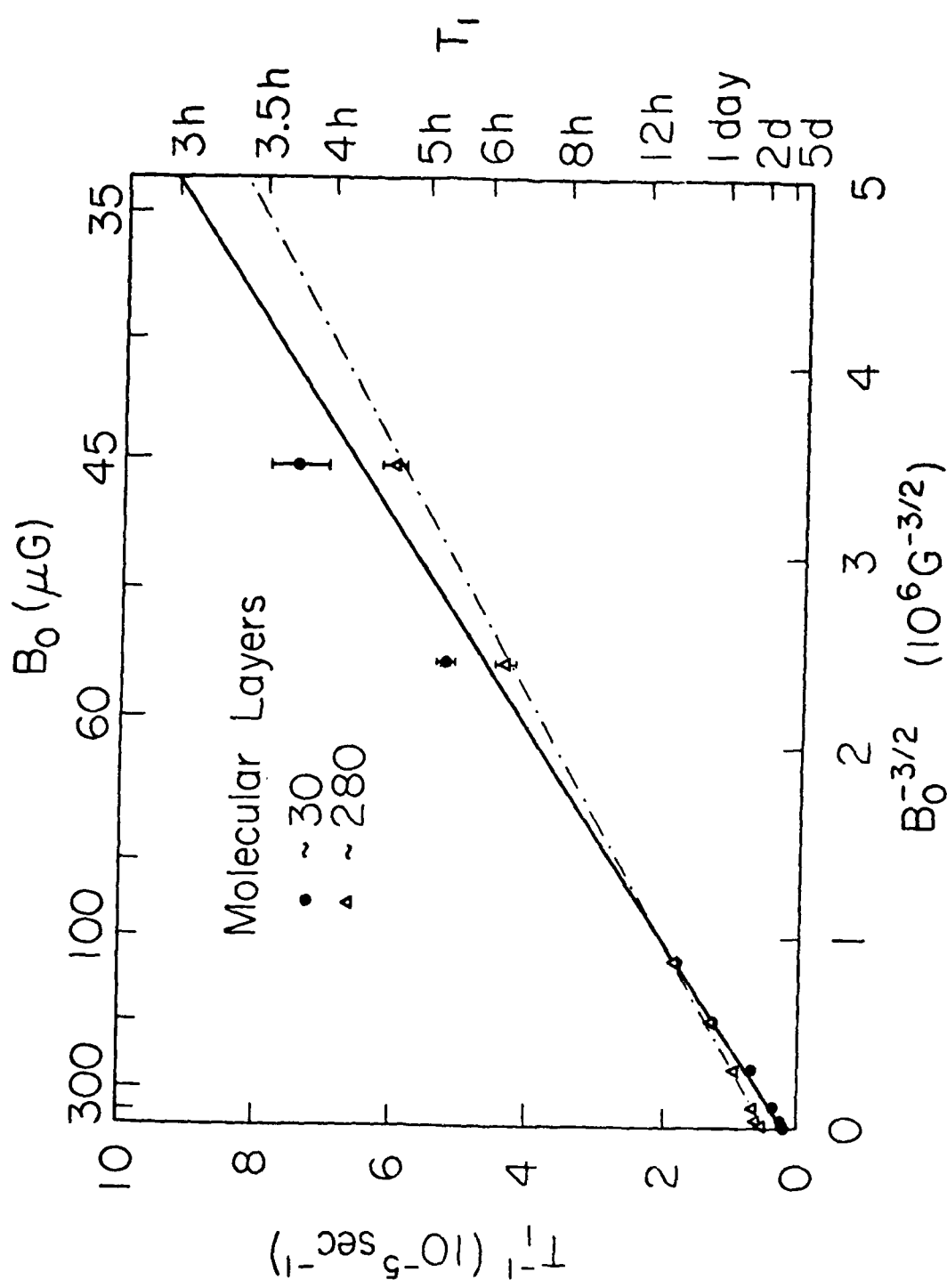


Fig. 4.8 Relaxation rate data obtained with solid-H<sub>2</sub> wall coatings. The coating with  $\sim 30$  molecular layers yielded  $T_{1\infty} = 141 \pm 3$  h and the coating with  $\sim 280$  molecular layers gave  $T_{1\infty} = 57.4 \pm 0.7$  h.

We also note that the theoretical estimate of  $T_{1B}$  made in the previous section exceeds the value of  $T_{1\infty}$  obtained with the thin  $H_2$  coating by  $\sim 15\%$  and the longest measured relaxation time by  $\sim 27\%$ . Thus it seems likely that  $T_{1B}^{-1}$  was dominant over  $T_{1W}^{-1}$  in this case. Because of this and the lack of an accurate measure of  $T_{1B}$ , a quantitative estimate of  $T_{1W}$  (for the thin  $H_2$  coating) is not possible. This result, however, does suggest that yet longer relaxation times are possible at lower  $He^3$  densities.

In two other experimental runs, a generous ( $\sim 700$  atomic layers) coating of solid argon was tried. Argon was chosen because it has no nuclear magnetic moment. In the first trial argon that was specified to have an  $O_2$  level of  $< 0.1$  ppm was used and yielded  $T_{1\infty} = 39.1 \pm 0.4$  h which is virtually identical to the bare cell result ( $40.4 \pm 1$  h). In order to see if  $O_2$  contamination in the Ar would have any effect, Ar that had been doped with 3.9 ppm of  $O_2$  was used in the second trial. In this case, we obtained  $T_{1\infty} = 39.5 \pm 0.6$  h. These results are shown in Fig. 4.9.

Our results were thus similar to those obtained by BLB: at 4 K an argon coating had no effect when compared to a clean Pyrex surface. In light of our remarks on the disposition of the wall coating after admission of the He sample, however, it must be admitted that a firm conclusion cannot be drawn on the basis of our negative result. However, if the hypothesis that the effectiveness of a wall coating was predominantly due to the covering of a magnetically dirty surface with a non-magnetic substance were true, our sensitivity was such that a coverage of only  $\sim 10\%$  would have been sufficient to cause an observable change in  $T_{1\infty}$ .

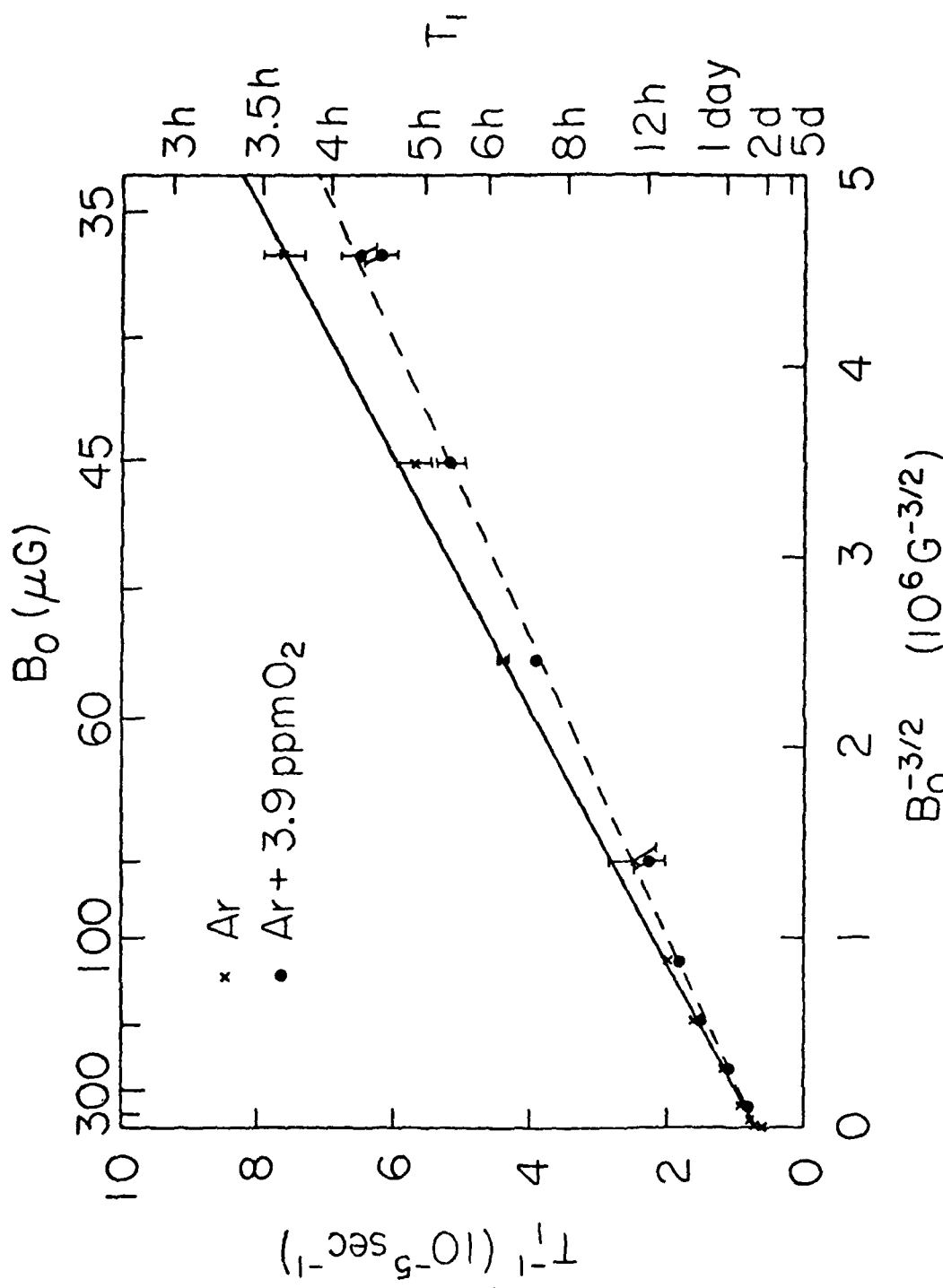


Fig. 4.9 Relaxation rate data obtained when the sample cell was pre-filled with the equivalent of  $\sim 10^3$  atomic layers of argon prior to cooldown. without O<sub>2</sub> doping,  $T_{1\infty} = 39.1 \pm 0.4$  h, and with O<sub>2</sub> doping  $T_{1\infty} = 39.5 \pm 0.6$  h.

#### 4.4.3 *Effect of O<sub>2</sub> Contamination*

Because of the time and effort necessary to operate the super-leak He<sup>4</sup> purifier, commerical grades of He gas were tried on two occasions in order to see if the superleak purification procedure was important or not. On the first occasion Matheson "Ultra High Purity" grade helium (total impurity content < 10 ppm, O<sub>2</sub> concentration < 2 ppm) was used and on the second occasion helium having a total impurity content < 1 ppm was obtained from Liquid Carbonic Corp.

The use of the lower purity helium gave some rather pronounced results. The initial magnetization was so small ( $\sim 10^{-2} \times$  the usual value) that only one relaxation-time measurement was made. Even more surprising, the sign of the magnetization was the opposite of that observed on all other occasions. The reason for this is not known. No difference in experimental conditions (e.g., current polarity to the optical pumping field coils, guide solenoid, and sample cell field coils) could be found, although the possibility of a mistake cannot be absolutely ruled out until the experiment is repeated. The one relaxation-time measurement yielded  $T_1 = 2.7 \pm 0.3$  h in a field of 145  $\mu$ G. In this magnetic field we would have expected  $T_1 \approx 19$  h in the bare sample cell with the superleak-purified He<sup>4</sup>.

In preparation for the subsequent run in which the higher purity commerical He<sup>4</sup> was to be used, the cryostat probe was removed from the dewar and the sample cell was pumped out. In order to reduce the possible effects of residual O<sub>2</sub> contamination from the previous run, argon was admitted before cooling the probe down again. It is now

thought that this maneuver was of dubious value and that the probe should have been disassembled for a new plasma cleaning of the sample cell. Consequently, the fact that  $T_{1\infty}$  was found to be shorter in this run ( $30.6 \pm 0.3$  h) than in runs where superleak-purified  $\text{He}^4$  was used is probably insufficient to judge the relative purity of the gas from these two sources.

#### 4.5 Conclusions

The primary objective of our experimental work was to determine whether the long intrinsic nuclear relaxation times that are predicted in the bulk of dilute  $\text{He}^3$ -liquid  $\text{He}^4$  mixtures can be attained in actual practice when other relaxation mechanisms may be present. With respect to this objective the experimental results have been encouraging. It has been found that with a  $\text{H}_2$  wall coating, the wall-induced relaxation was reduced to the point where a  $T_1$  in excess of 5 days was achieved in a 0.069% mixture of  $\text{He}^3$  in liquid  $\text{He}^4$  at 4.2 K in a 1 cm diameter Pyrex cell. Since this result appears to be limited for the most part by intrinsic relaxation in the bulk, yet longer relaxation times should be achievable by using lower  $\text{He}^3$  concentrations.

The problem of obtaining long relaxation times in a zero-average magnetic field (or equivalently, the problem of obtaining a long  $T_2$ ) is well understood. For example, by using care in selecting materials and in making the superconducting shield, a gradient on the order of  $10^{-8} \text{ G cm}^{-1}$  should be possible. If this had been the case for our experiments, we would have found that the gradient-induced relaxation time would have been on the order of 9 days when  $B_0 = 0$ . Thus it

appears that zero-field relaxation times on the order of several days are quite possible.

It is clear that a number of unresolved issues have been raised in our discussion of our experimental work and that of others. In particular, an issue which is of importance to us concerns the nature of the dominant magnetic interaction in wall-induced relaxation when wall coatings are used. The question of whether the thickness of the wall coating is of importance also needs to be studied.

It is clear however, that although some aspects of our experimental technique are useful, there are more efficient ways of studying wall-induced relaxation *per se*. Since our experiments were motivated by the desire to achieve long relaxation times, the rate of data acquisition was inversely proportional to our success. The use of sample cells with much larger surface-to-volume ratios, for example, would reduce the duration of an experimental run from a week or so to hours or less.

## CHAPTER 5

### $\text{He}^3$ ZERO FIELD NUCLEAR GYROSCOPE

#### 5.1 Introduction

We have already discussed the basic concept and techniques involved in the  $\text{He}^3$  ZFNG in Chap. 1 and have described the use of some of these techniques in greater detail in Chap. 2. A schematic depiction of the  $\text{He}^3$  ZFNG is shown in Fig. 5.1.

Although the original  $\text{He}^3$  ZFNG prescription called for a polarized  $\text{He}^3$ -liquid  $\text{He}^4$  mixture, we saw in Chapters 3 and 4 that the small  $\text{He}^3$  diffusion coefficient in the liquid phase can lead to considerable shortening of the relaxation time in low magnetic fields because of relaxation due to magnetic field gradients. In this chapter we will therefore allow the possibility of  $\text{He}^3$ - $\text{He}^4$  gas mixtures as well. Because of the much more rapid diffusion in the gas phase, however, a simple constriction would probably no longer be adequate to control diffusion in and out of the sample cell. Thus it is likely that some sort of mechanical closure would be required.

An additional departure from our previous discussions is that we will now entertain the possibility of a much larger sample volume and a smaller sample magnetization than were used in our experimental relaxation studies. Hence, in the numerical estimates that will be made in this chapter, the sample diameter will be taken to be 3.8 cm (1½"), and the sample internal flux density will be taken to be  $10^{-6}$  G.

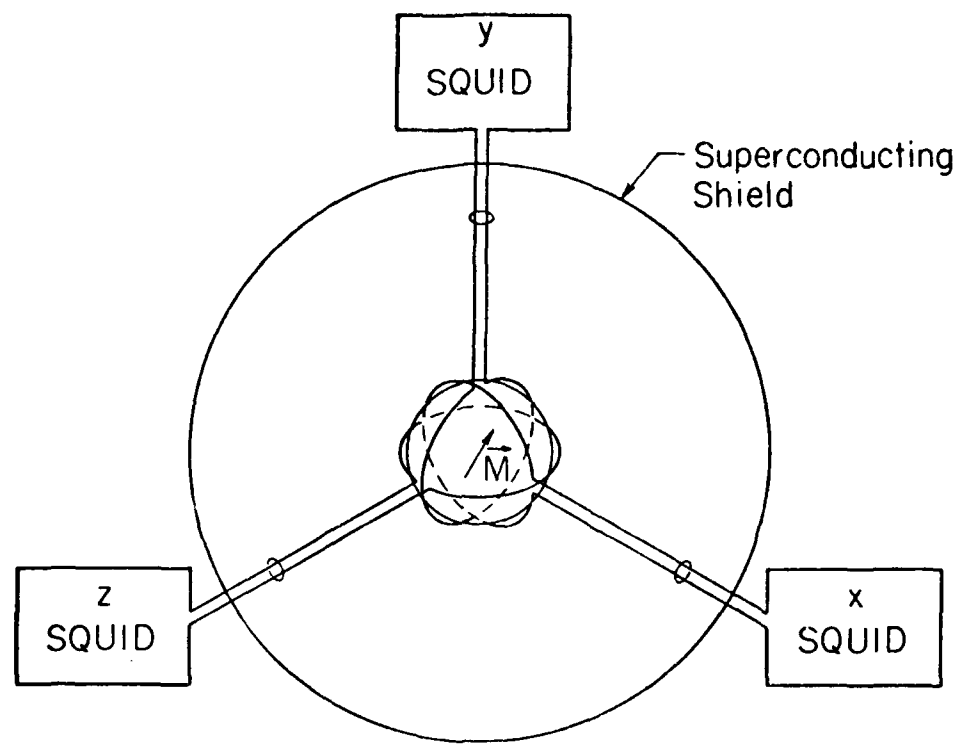


Fig. 5.1 Schematic depiction of the He<sup>3</sup> zero-field nuclear gyroscope.

Although it is clear that we estimate these modifications to be advantageous, it should be pointed out that these choices are somewhat arbitrary and are not guaranteed to be optimal. It will become clear that there are too many uncertainties at this point for an optimal set of gyro design factors to be determined.

In the following sections of this chapter we will examine in detail the following key elements of the  $\text{He}^3$  ZFNG performance:

1)  $\text{He}^3$  relaxation time, 2) the angular accuracy with which the direction of the sample magnetization may be determined, and 3) residual motion of the magnetization due to time-varying or magnetization-dependent magnetic fields which are therefore impossible to null. The related topics of anisotropic relaxation and the dynamic frequency shift are most conveniently discussed as relaxation topics even though their effects could in practice be difficult to distinguish from motion due to uniform magnetic fields.

Within the constraints of our present state of knowledge, our objectives in this chapter are to 1) illuminate the relationships between the various design parameters and the performance elements we have just listed so that important tradeoffs may be better understood, and 2) to roughly estimate how well a  $\text{He}^3$  ZFNG might be expected to actually perform within the capabilities of current technology.

### 5.2 $\text{He}^3$ Nuclear Relaxation Considerations

We now consider the relaxation of  $\text{He}^3$ - $\text{He}^4$  mixtures in zero-average magnetic field at 4.2 K. Since this topic has been discussed

in detail in Chapters 3 and 4, we will merely review the results which pertain to the ZFNG performance.

### 5.2.1 *Intrinsic Relaxation*

For our present purposes, it is sufficient to consider the intrinsic nuclear relaxation of a monatomic species in the simplest approximation, *i.e.*, under the assumption of a classical gas or liquid with a hard sphere interatomic potential. For a gas the result is<sup>53</sup>

$$T_B^{-1} = 2\gamma^4 \hbar^2 I(I + 1) (\pi m/k\Theta)^{1/2} n_3 a^{-3} . \quad [5.1]$$

where  $k\Theta$  is Boltzmann's constant times the temperature, and  $m$  is the mass of the  $\text{He}^3$  atom. For a liquid, we have equation [3.79]

$$T_B^{-1} = 8\pi\gamma^4 \hbar^2 I(I + 1) n_3 / (15D a) , \quad [5.2]$$

where as we have noted in Chap. 3,  $D$  is independent of  $n_3$  in the limit  $n_3/n_4 \rightarrow 0$ . In both [5.1] and [5.2]  $a$  is the hard-sphere radius.

It is noteworthy that the relaxation rate for the gas is independent of the mean free path so that the addition of a magnetically inert gas such as  $\text{He}^4$  will have no effect on this relaxation mechanism. This is not true for a liquid buffer where the mean free path is comparable to atomic dimensions. According to equation [5.1] the density of a liquid buffer can have an effect insofar as it affects  $D$ . This situation is reflective of the fact that only the relative motion between two  $\text{He}^3$  atoms during a collision has any significant impact on the relaxation process.

Now if we use equation [4.1]

$$B_{mo} = (8\pi/3)(\frac{1}{2}\gamma\hbar)n_3 P ,$$

and require that  $B_{mo} = 10^{-6}$  G, then  $n_3 \approx 10^{16} \text{ p}^{-1} \text{ cm}^{-3}$ . On the basis of our experimental experience we can assume  $P \approx 10^{-2}$  so that we need  $n_3 \approx 10^{18} \text{ cm}^{-3}$  ( $2 \times 10^{-6} \text{ mol cm}^{-3}$ ). This is  $\sim 10\%$  of the  $\text{He}^3$  density that we used in our relaxation studies. Substituting this into [5.1] yields  $T_{1B} \approx 6$  months. The use of equation [5.2] along with our experimental value for D (Sec. 4.2) yields a result that is about 45% of this.

Despite the fact that these results are somewhat optimistic due to the neglect of the attractive interatomic potential between helium atoms, it is improbable that these relaxation rates will be significant in either the liquid or gas case when compared to the other relaxation processes.

#### 5.2.2 *Wall-Induced Relaxation*

As we have discussed in Chap. 4, both  $\text{He}^4$  buffer and a solid  $\text{H}_2$  wall coating are effective in reducing  $T_{1W}^{-1}$ , the rate at which the sample would relax due to wall effects alone, by many orders of magnitude in the region of 4.2 K. Unfortunately, there appears to be no data on the relaxation rate of  $\text{He}^3\text{-He}^4$  gas mixtures in Pyrex let alone  $\text{He}^3\text{-He}^4$  gas mixtures with cryogenic wall coatings. In addition, the data that Barbé, Laloë and Brossel obtained on  $T_{1W}$  with a solid  $\text{H}_2$  wall coating were obtained with a  $\text{He}^3$  density  $\sim 1/70$  of the value we are planning on using.<sup>32</sup> How  $T_{1W}$  will behave as a function of  $\text{He}^3$  density when a solid  $\text{H}_2$  wall coating is used is not clear and needs experimental work.

It is our estimation, however, that if a  $\text{He}^4$  density of  $10^{-5}$  mol  $\text{cm}^{-3}$  is used in conjunction with the solid  $\text{H}_2$  coating,  $T_{1W}$  will be in excess of  $10^5$  sec. We will see in the next section that this value of  $\text{He}^4$  density should lead to an acceptable relaxation rate due to magnetic gradients.

### 5.2.3 Gradient-Induced Relaxation

As we have seen in Chap. 3, nuclear relaxation due to diffusion through magnetic-field gradients is readily treated. This mechanism differs from the previous two in that it is anisotropic even in the  $B_0 = 0$  limit. The results that were obtained in Chap. 3 and will be utilized here are valid under the conditions that 1) the motional narrowing condition,  $\gamma^2 B_1^2 \tau_{11}^2 \ll 1$ , holds; 2) the average of the perturbation field  $\vec{B}_1(\vec{r})$  is zero; and 3) the mean free path is small compared to the sample cell diameter.

Now if it is assumed that the field sources are located at a distance that is much greater than the sample size, as would be the case for both trapped flux in the superconducting shield and the field nulling coils, then we may adequately model the situation with a uniform gradient. For the purposes of calculation, we take a similar gradient configuration to the one used as an example in Chap. 3

$$\vec{B}_1(\vec{r}) = g(-\frac{1}{2}\hat{i}x - \frac{1}{2}\hat{j}y + \hat{k}z) . \quad [5.3]$$

We now need to specify the state of relative angular motion between the sample magnetization and the gyro case with respect to which the gradient field is fixed. In the situation where the sample magnetization is stationary with respect to the gyro case, it has been

shown that

$$\frac{dM_\alpha}{dt} = - T_{\alpha G}^{-1} M_\alpha, \quad \alpha = x, y, z. \quad [5.4]$$

With the gradient configuration [5.3] we have seen in Chap. 3 that

$$T_{xG}^{-1} = T_{yG}^{-1} = 5/2 T_{zG}^{-1} = 0.057 \gamma^2 g^2 R_0^4 D^{-1} \quad [5.5]$$

where  $R_0$  is the sample radius.

Now it is reasonable to assume that a value of  $g = 10^{-8} \text{ G cm}^{-1}$  can be attained. Thus, if we wish to obtain  $T_G \approx 10^6 \text{ sec}$  (12 d), then it is required that  $R_0^4 D^{-1} \lesssim 400 \text{ cm}^2 \text{ sec}$ . If one were to use a 1 cm diameter cell, it would be necessary that  $D \gtrsim 1.5 \times 10^{-4} \text{ cm}^2 \text{ sec}^{-1}$ , a condition which can be readily met for all densities of  $\text{He}^4$  buffer short of liquid density. On the other hand a 3.8 cm cell would require that  $D \gtrsim 0.03 \text{ cm}^2 \text{ sec}^{-1}$  or  $n_4 \lesssim 8 \times 10^{-5} \text{ mol cm}^{-3}$ . It will be seen in discussion of other issues that it is advantageous to use the larger diameter and lower density for which we have  $\tau_{11} \lesssim 27 \text{ sec}$ .

Of perhaps greater concern than the lifetime-limiting aspect of relaxation due to magnetic field gradients is its anisotropic nature. If the magnetization does not lie along one of the principal axes, the orientation of the magnetization will not in general remain constant in time even in the absence of any average magnetic field. If, for example, the gradient field is given by [5.3], then it is easily seen from [5.4] and [5.5] that

$$\begin{aligned} \frac{d\theta}{dt} &= - \frac{1}{2} [T_{xG}^{-1} - T_{zG}^{-1}] \sin 2\theta \\ &= - (3/10) T_{xG}^{-1} \sin 2\theta \end{aligned} \quad [5.6]$$

where  $\theta$  is the angle between  $\vec{M}$  and the  $z$  axis. Thus for the parameters used above, the worst case ( $\theta = 45^\circ$ ) would yield a drift rate of  $3 \times 10^{-7}$  rad sec $^{-1}$  (0.06  $\widehat{\text{sec sec}}^{-1}$ ).

Up to now we have considered the situation where the magnetization remains stationary with respect to the gyro case. We now briefly discuss the situation where the magnetization appears to rotate with respect to the case with an angular velocity  $\vec{\omega}_0$ . (Since we are discussing a gyro, it is perhaps more appropriate to think in terms of the case rotating with respect to the magnetization with a velocity  $-\vec{\omega}_0$ .) If the duration of the rotation is much longer than  $\omega_0^{-1}$ , then we have seen that the relaxation rates  $T_{\alpha G}^{-1}$  are no longer appropriate. Instead, the appropriate relaxation rates are  $T_{1G}^{-1}$ , the relaxation rate of the component of  $\vec{M}$  in the direction of  $\omega_0$ , and  $T_{2G}^{-1}$ , the relaxation rate of the transverse component. In general,  $T_{1G} \neq T_{2G}$ . Aside from this, however, it is seen in Chap. 3 that these relaxation rates are of the same order as the  $T_{\alpha G}^{-1}$ , provided that  $\omega_0 \tau_{11} \ll 1$ . For example, if the gradient were given by [5.3] and the rotation  $\vec{\omega}_0$  were along the  $x$  axis then  $T_{1G}^{-1} = \frac{1}{2}(T_{zG}^{-1} + T_{yG}^{-1}) = (7/10)T_{xG}^{-1}$ , and  $T_{2G}^{-2} = \frac{1}{2}T_{1G}^{-1} + T_{xG}^{-1} = (27/20)T_{xG}^{-1}$ . On the other hand, if the opposite situation,  $\omega_0 \tau_{11} \gg 1$ , holds then  $T_{1G}^{-1} \propto (\omega_0 \tau_{11})^{-2}$  whereas  $T_{2G}^{-1}$  will have dropped only slightly. In this regime  $T_{1G}^{-1}$  becomes negligible compared to  $T_{2G}^{-1}$ .

We note that since  $T_{1G} \neq T_{2G}$  the relaxation is still anisotropic, *i.e.*, if  $\theta'$  is the angle between  $\vec{M}$  and  $\vec{\omega}_0$  then we have instead of [5.6]

$$d\theta'/dt = -\frac{1}{2}(T_{2G}^{-1} - T_{1G}^{-1})\sin 2\theta'.$$

There is one remaining consequence of magnetic field gradients when  $\omega_0 \neq 0$ , i.e., the dynamic frequency shift. In the frame where  $\vec{M}$  would be stationary in the absence of any field gradients,  $\vec{M}$  will actually precess about  $\vec{\omega}_0$  with an angular velocity  $\delta\omega$  when field gradients are present. In the case of a uniform gradient, we have the approximate relation (Chap. 3)

$$\delta\omega/\omega_0 \approx \frac{1}{2}(\tau_{11}/T_{1G})$$

Since  $T_{1G}^{-1}$  is constant for  $\omega_0\tau_{11} \ll 1$  and varies as  $\omega_0^{-2}$  for  $\omega_0\tau_{11} \gg 1$ ,  $\delta\omega$  is at a maximum when  $\omega_0 \approx \tau_{11}$ . At worst, then,  $\delta\omega \approx T_{1G}^{-1} \approx T_{2G}^{-1}$ .

As a result of this discussion we can draw the following general conclusion: if the magnetization rotates with respect to the gyro case at a constant rate  $\omega_0$  (which may be zero), then the maximum drift that will occur in any direction due to magnetic field gradients will be on the order of  $T_{2G}^{-1}$  rad sec<sup>-1</sup>.

### 5.3 $\text{He}^3$ ZFNG Angular Readout Resolution

One of the three magnetometer systems is shown schematically in Fig. 5.2. For the purpose of our analysis of the ZFNG performance, we will use data obtained by Clarke, Goubau, and Ketchen<sup>23</sup> (CGK) on their tunnel junction dc SQUID. This device is somewhat different than the rf-biased SQUID that was used for our relaxation experiments, but at the present it has the advantage of having a somewhat better low-frequency performance than any of the other SQUID magnetometers.

Typically the noise performance of a SQUID by itself is specified by  $S_\phi^{\frac{1}{2}}/\phi_0$ , where  $S_\phi(v)$  is the equivalent flux noise spectral density

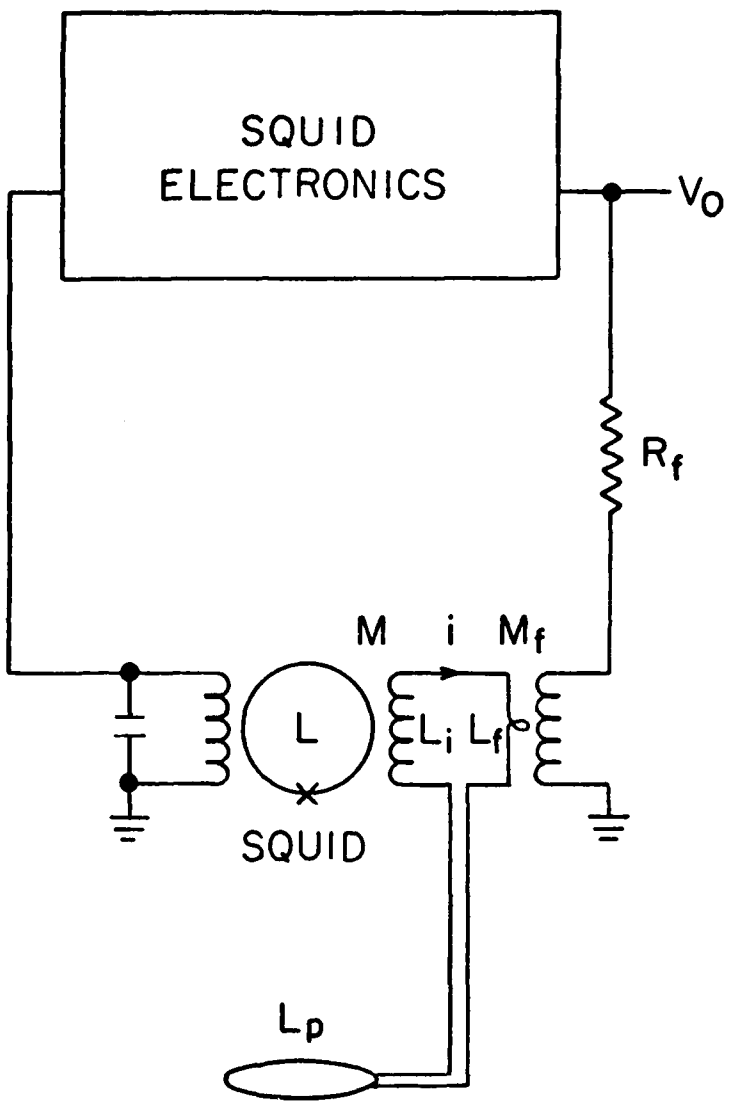


Fig. 5.2 One of the SQUID readout systems for the  $\text{He}^3$  ZFNG.

from all sources referred to the SQUID inductance  $L$ , and  $\phi_0$  is the quantum of flux ( $\phi_0 = 2.07 \times 10^{-7}$  G cm $^2 = 2.07 \times 10^{-15}$  Wb).\* This, however, does not take into account the consideration of how efficiently the flux in the coupling inductance,  $L_i$ , can be coupled into  $L$ .

In order to specify the performance of  $L_i$  plus the SQUID together, the energy resolution per Hz,  $E_n(v)$ , is frequently used as a figure of merit.<sup>66</sup>  $E_n(v)$  is defined by

$$\begin{aligned} E_n(v) &= L_i S_i(v) = \frac{1}{2} L_i S_\phi(v) / M^2 \\ &= \frac{1}{2} S_\phi(v) / k^2 L, \end{aligned} \quad [5.7]$$

where  $M = k(L L_i)^{\frac{1}{2}}$  is the mutual inductance between  $L_i$  and  $L$ , and  $S_i(v)$  and  $S_\phi(v)$  are the equivalent input current and SQUID flux noise spectral densities respectively.

It is easily shown<sup>66</sup> that flux applied to  $L_p$ , the sensing coil, is most efficiently coupled to  $L_i$  when  $L_i = L_p$ , and under this condition the SQUID noise specified as an equivalent noise spectral density of a uniform magnetic field applied normally to  $L_p$  is

$$\begin{aligned} S_{B'}(v) &= (2/N_p A_p)^2 L_p [S_\phi(v) / k^2 L] \\ &= (2/N_p A_p)^2 L_p [2E_n(v)], \end{aligned} \quad [5.8]$$

where  $L_p$  has  $N_p$  turns and encompasses an area  $A_p$ . (The  $B'$  subscript

---

\* Although we have been using cgs units for the most part, it is more convenient to use MKS units in magnetometer discussions.

is used to denote an *equivalent* uniform magnetic field in order to distinguish it from a real magnetic field.) Writing

$$L_p = \alpha_p N_p^2 \quad [5.9]$$

we have

$$S_B^{\frac{1}{2}} = 2[2\alpha_p E_n]^{\frac{1}{2}} A_p^{-1} \quad [5.10]$$

We must now be more explicit about  $L_p$  in order to evaluate  $\alpha_p$ . It will be assumed that  $L_p$  consists of a compact array of circular turns whose cross-section dimension is much smaller than the mean radius of the coil. In this case<sup>67</sup>

$$\alpha_p = R_c \kappa \quad [5.11]$$

where  $R_c$  is the mean radius of the coil (in meters) and  $\kappa$  is given by

$$\kappa/\mu_0 = \ln(R_c/b) + c \quad [5.12]$$

Here  $\mu_0 = 4\pi \times 10^{-7} \text{ NA}^{-2}$  and  $b$  is the dimension of the cross section of the windings. If the cross section is square  $c = 0.885$  and if it is circular,  $c = 1.02$ . Since  $\kappa$  varies only logarithmically as a function of  $R_c/b$  it may be considered roughly as a constant. Combining [5.10] and [5.11] we then have

$$S_B^{\frac{1}{2}} = \frac{2}{\pi} (2E_n \kappa)^{\frac{1}{2}} R_c^{-3/2} \quad [5.13]$$

It is seen that the magnetic field resolution of a magnetometer having a compact circular sensing coil varies roughly as  $R_c^{-3/2}$ .

For a 4 cm diam coil, we are safe in assuming  $5 < \kappa/\mu_0 < 8$ , and for specificity will take  $\kappa/\mu_0 = 6.5$ . (Because of the proximity of

the diamagnetic pickup coil to the sample, the dimension  $b$  should be as small as practically possible.)

Before proceeding to calculate the angular resolution that might be expected, we note that there are two sources of coupling inefficiency that have been ignored. One is simply the stray lead inductance between  $L_i$  and  $L_p$ . The other is that the pickup coil diameter must be somewhat larger than the sample cell diameter. It is easily shown that if  $\vec{B}_{mo}$  is the internal magnetic field in the sample cell of radius  $R_o$ , then the flux coupled into a filamentary coil of radius  $R_c$  whose plane is normal to  $\vec{B}_{mo}$  is

$$\phi_p = B_a A_p = \pi R_o^3 R_c^{-1} B_{mo}$$

Hence

$$B_a = (R_o/R_c)^3 B_{mo} \quad [5.14]$$

where  $B_a$  is the equivalent uniform field that would have to be applied to  $L_p$  in order to yield the same signal as  $B_{mo}$ . This can be explicitly taken into account by referring  $S_B^{\frac{1}{2}}$  to  $B_{mo}$  instead of  $B_a$  and replacing [5.13] with

$$S_B^{\frac{1}{2}} = (2/\pi)(2E_n \kappa)^{\frac{1}{2}} R_c^{3/2} R_o^{-3} \quad [5.15]$$

This correction is not particularly important as long as the three orthogonal pickup coils can be nested fairly closely about the sample cell. For simplicity we will assume that all the pickup coils have the same diameter.

If we now define  $\psi$  to be the readout error, *i.e.*, the instantaneous angle between  $\vec{B}_{mo}$  and the vector that would be inferred from the

magnetometer outputs, and assume that 1) magnetometer noise is normally distributed (*i.e.*, gaussian), 2) gains and noise characteristics of each of the 3-axis readout magnetometers are equal and their noise uncorrelated, and 3)  $B_{mo} \gg \sigma_B^2$ , where  $\sigma_B^2$  is the variance of the magnetometer noise referred to  $B_{mo}$ , then we have the result that

$$\sigma_\psi^2 = 2\sigma_B^2 B_{mo}^{-2} . \quad [5.16]$$

Now  $\sigma_B^2$  is related to  $S_B(v)$  by

$$\sigma_B^2 = \int_0^\infty S_B(v) |H(\omega)|^2 dv \quad [5.17]$$

where  $H(\omega)$  is the frequency transfer function of the magnetometer and its output low-pass filter normalized such that  $H(0) = 1$ . For convenience, we simply take

$$H(\omega) = 1 \quad v < v_c ,$$

$$= 0 \quad \text{otherwise}$$

SQUID-based instruments, like any other dc instrument, exhibit divergent "1/f" noise below some frequency  $v_{1/f}$ . This has the effect of limiting the resolution of a dc measurement even if one is willing to spend an arbitrarily long period of time to make the measurement.

Thus if  $v_c \gg v_{1/f}$ , the contribution of the white noise portion of the spectrum above  $v_{1/f}$  will generally dominate in [5.18] and  $\sigma_B^2 \propto v_c$ . On the other hand, if  $v_c \lesssim v_{1/f}$  then  $\sigma_B^2 \propto \ln v_c$ , and it becomes impossible to make any further significant improvements in  $\sigma_B$ , by narrowing the bandwidth.

In the case where the white portion of the noise spectrum dominates, we have

$$\sigma_{B'}^2 \gtrsim S_{Bw} v_c = (8/\pi^2) E_{nw} \kappa R_c^3 R_o^{-6} v_c, \quad v_c \gg v_{1/f}. \quad [5.18]$$

Here  $S_{Bw} = S_{B'} (v > v_{1/f})$  and likewise for  $E_{nw}$ . Thus

$$\sigma_\psi \gtrsim (4/\pi) (E_{nw} \kappa v_c R_c^3)^{1/2} / (R_o^3 B_{mo}) \quad v_c \gg v_{1/f}. \quad [5.19]$$

As a numerical example, we take the CGK data  $E_{nw} \approx 7 \times 10^{-30} \text{ J Hz}^{-1}$ ,  $v_{1/f} \approx 2 \times 10^{-2}$  and use the values  $v_c = 1 \text{ Hz}$ ,  $\kappa = 6.5 \mu_o$ ,  $R_c = 2 \times 10^{-2} \text{ m}$ , and  $B_{mo} = 10^{-10} \text{ T}$  to obtain the estimate  $\sigma_\psi \approx 4 \times 10^{-5} \text{ rad} = 8 \text{ sec}$ . This corresponds to  $\sigma_{B'} \approx 3 \times 10^{-11} \text{ G}$ .

Another issue which is of importance is the matter of drift in the SQUID output. This drift is generally thought to be principally attributable to temperature changes that occur at the SQUID and along its electrical leads as the level of the helium bath drops. CGK claim an average drift rate of  $\sim 2 \times 10^{-5} \phi_o \text{ h}^{-1}$  over a 20 h period for a dc SQUID that was temperature stabilized to  $\pm 50 \mu\text{K}$ . This corresponds to an apparent magnetic field drift of  $\sim 1.9 \times 10^{-11} \text{ G h}^{-1}$  in the measurement of  $B_{mo}$ . This could mimic a gyro drift as large as  $5 \times 10^{-9} \text{ rad sec}^{-1}$  for  $B_{mo} = 10^{-6} \text{ G}$ . If the three magnetometers tended to drift together, the angular drift could conceivably be smaller than this.

It should be remembered at this point that SQUIDs are only capable of measuring magnetic field *changes*. Thus a technique of purposely precessing the sample magnetization could be used in order to establish or recheck the zero level for each of the readout systems. Since this is an ac measurement, the zero-level measurement can presumably be made

with sufficient accuracy to insure that it does not contribute significantly to the overall readout error.

#### 5.4 Residual Magnetic Torques

The presence of any residual magnetic field  $\vec{B}(\vec{r})$  for which the spatial average over the sample volume  $\overline{\vec{B}(\vec{r})} \neq 0$  will cause precession of the magnetization at a rate  $\sim \gamma \overline{\vec{B}(\vec{r})}$ . We will assume that those sources of  $\vec{B}$  which are truly constant in time (such as trapped flux in the superconducting shield and dc current in the magnetometer coupling circuits) can be nulled by using trimming coils.

Those sources of  $\vec{B}$  which are not constant and therefore not capable of being nulled will be our chief concern in this present discussion. There are three sources which fall in this category: 1) the magnetization of the sample as it interacts with asymmetric aspects of its surroundings, 2) the magnetic noise field produced by the magnetometers, and 3) the London moment. The last of these is the least troublesome since it is quite predictable and can therefore be readily compensated for. The first of these is not predictable, but should be reproducible. It should therefore be possible to compensate for it once sufficient experience has been acquired with a given apparatus.

We will now discuss each of these topics separately.

##### 5.4.1 *Drifts Proportional to the Sample Magnetization*

###### 5.4.1.1 Interaction of the Magnetization with Passive Elements

For our purposes we can consider a given  $\text{He}^3$  nucleus as lying isolated inside the center of its spherically symmetric electronic shell which is surrounded by a medium that is uniformly magnetized

on the average. Thus, even though the macroscopic magnetic-flux density arising from the magnetization inside of a *perfect, uniformly magnetized sphere* is  $\vec{B} = (8\pi/3)\vec{M}$ , it is seen by superposition that the average field at a given nucleus is *zero*. This, of course, is an idealization. In reality, the sample cell is not perfectly spherical and the diamagnetic superconducting shield has a myriad of imperfections: sphericity errors, access holes, superconducting leads, *etc..* It is necessary therefore to estimate the effect these various assymmetries will have.

We start out with a result that is proven in Appendix B: the *average magnetic field seen by a given nucleus*,  $\vec{B}_{loc}$ , in an arbitrarily shaped but uniformly magnetized sample located in an arbitrarily shaped superconducting shield is related to the sample magnetization  $\vec{M}$  by symmetric, second rank tensor. That is,

$$\vec{B}_{loc} = U\vec{M} . \quad [5.20]$$

$U$  can be reduced by writing  $U = sI + Q$  where  $I$  is the unit tensor,  $s = 1/3 \text{ Tr}(U)$ , and  $Q$  is a traceless symmetric tensor.

If it is assumed that the average magnetic field from all other sources is zero and that motional narrowing condition holds (which it must since we have assumed a uniform magnetization), the equation of motion of  $\vec{M}$  exclusive of relaxation effects is simply

$$\begin{aligned} \vec{dM}/dt &= \vec{\gamma M} \times \vec{B}_{loc} \\ &= \vec{\gamma} [\vec{sM} \times \vec{M} + \vec{M} \times (\vec{QM})] \\ &= \vec{\gamma M} \times (\vec{QM}) . \end{aligned} \quad [5.21]$$

Since  $Q$  is symmetric there exists a principal axis coordinate system in which it is diagonal. If the components of [5.21] are written in the principal axis coordinate system, we have

$$\frac{dM_x}{dt} = M_y M_z (Q_{zz} - Q_{yy}) , \quad [5.22]$$

+ cyclic perm.

These equations are formally identical to Euler's equations of motion of a torque-free rigid body.<sup>68</sup> Thus  $\vec{M}$  will execute a polhode-type precession with respect to the gyro case. By design, of course, this motion is to be made as slow as possible.

As an example of this formalism, we consider a situation having axial symmetry about the  $z$  axis:  $Q_{xx} = Q_{yy} = - \frac{2}{3}Q_{zz}$ . In this case  $\frac{dM_z}{dt} = 0$  so that  $M_z$  is a constant of the motion, and

$$\frac{dM_{x,y}}{dt}^2 = - \omega_p^2 M_{x,y}$$

where

$$\omega_p = - 3/2 \gamma M_z Q_{zz} . \quad [5.23]$$

Thus  $\vec{M}$  precesses around the  $z$  axis with an angular velocity  $\omega_p$ . If  $M_z$  changes due to relaxation or motion of the gyro case, the precession rate will also change.

Even without explicitly calculating  $Q$  it is possible to derive some useful information from this formalism. For instance,  $Q$  can have contributions from several different sources. Two of these sources are asymmetry in the sample cell and asymmetry in the superconducting shield and other superconducting parts. Now the former source is difficult to alter once the gyro case is manufactured. Since  $Q$  involves

only five independent variables, however, it is quite possible to invent a simple scheme using adjustable superconducting components to null out  $Q$  regardless of what the original source of the asymmetry is. In addition, this formalism gives us the prescription for balancing out the perturbations due to necessary components such as access holes through the shield and superconducting leads: one need only maintain cubic symmetry in order to assure that  $Q$  is zero. These perturbative components will, of course, introduce gradients as they interact with the sample magnetization, but this effect can be kept acceptably small provided that the dimensions of the superconducting components in proximity to the sample (*i.e.*, the pickup coils) are kept small.

We will now present the results of some explicit calculations (Appendix C) in order to obtain a sense of how critical this problem is. First the effect of asphericity of the sample cell will be discussed and then the analogous expressions arising from asphericity of the superconducting shield will be written for purposes of comparison. In both cases the results are valid to first order and higher order terms are neglected.

If the radius of the sample cell is expressed in the form

$$R_o(\theta, \phi) = R_o [1 + \sum_{\substack{\ell, m \\ \ell \neq 0}} \alpha_{\ell m} Y_{\ell m}(\theta, \phi)] \quad [5.24]$$

where  $|\alpha_{\ell m}| \ll 1$  and  $\alpha_{\ell m} = (-1)^m \alpha_{\ell m}^*$ , then as might be expected,  $Q_c$  depends only on  $\alpha_{2m}$  in first order. ( $Q_c$  is that part of  $Q$  due to cell asphericity only.) In order to keep things simple we will consider the case where this quadrupole deformation is axially symmetric

around the  $z$  axis so that  $\alpha_{2\pm 1} = \alpha_{2\pm 2} = 0$ . In this case

$$Q_C = 4 \sqrt{\pi/5} \alpha_{20} \begin{pmatrix} -\frac{1}{2} & 0 & 0 \\ 0 & -\frac{1}{2} & 0 \\ 0 & 0 & 1 \end{pmatrix}. \quad [5.25]$$

If we let  $\delta R_o = R_o \alpha_{20} Y_{20}(\theta = 0)$ , then

$$\alpha_{20} = \sqrt{4\pi/5} (\delta R_o / R_o).$$

Thus the precession rate due to cell asphericity,  $\omega_{pc}$ , is given by

$$\begin{aligned} \omega_{pc} &= - (24\pi/10) (\delta R_o / R_o) \gamma M_z \\ &= - (9/10) (\delta R_o / R_o) \gamma B_{mo} \cos \theta \end{aligned} \quad [5.26]$$

where  $\theta$  is the polar angle of the magnetization.

If, by the way of a numerical example, we take  $|\delta R_o| = 0.13 \mu\text{m}$  (5 micro inch) and the usual values for  $B_{mo}$  and  $R_o$ , then we would have  $|\omega_{pc}| \approx 10^{-7} \text{ rad sec}^{-1}$  or  $0.03 \text{ sec}^{-1}$ .

As would be expected, the situation with the superconducting shield is not as critical. Writing the shield radius  $R_s(\theta, \phi)$  in the same form as [5.24]

$$R_s = R_{so} [1 + \sum_{\substack{\ell, m \\ \ell \neq 0}} \beta_{\ell m} Y_{\ell m}(\theta, \phi)],$$

where the same restrictions to  $\alpha_{\ell m}$  are applied to  $\beta_{\ell m}$ , and likewise limiting our consideration to the case where  $\beta_{2\pm 2} = \beta_{2\pm 1} = 0$ , we obtain the expression analogous to equation [5.27]:

$$Q_s = -12 \sqrt{\pi/5} \left(\frac{R_o}{R_{so}}\right)^3 \beta_{20} \begin{pmatrix} -\frac{1}{2} & 0 & 0 \\ 0 & -\frac{1}{2} & 0 \\ 0 & 0 & 1 \end{pmatrix} .$$

The precession rate due to an axially symmetric quadrupolar error in the shield is then

$$\omega_{ps} = (27/10) \left(\frac{\delta R_s}{R_{so}}\right) \left(\frac{R_o}{R_{so}}\right)^3 \gamma B_{mo} \cos\theta \quad [5.27]$$

where we have defined  $\delta R_s$  analogously to  $\delta R_c$ . It is seen by comparing [5.26] and [5.27] that if a tolerance of  $\delta R_o$  can be achieved for the cell radius then the equivalent specification for the shield radius is given by

$$\delta R_s = 1/3 \left(\frac{R_{so}}{R_o}\right)^4 \delta R_c .$$

Thus if the shield diameter is 15 cm and the best that can be done on the sample cell is  $\delta R_c \approx 0.13 \mu\text{m}$  then there is no point in specifying  $\delta R_s$  any smaller than 10  $\mu\text{m}$ .

Up to now our analysis has been appropriate to the situation where the magnetization would otherwise remain fixed in direction with respect to the gyro case. We now ask the question of what would happen if there were relative motion between the sample magnetization and the gyro case. In particular, in a fashion that is quite analogous to the analysis of relaxation due to magnetic field gradients, we briefly consider the case where there is a constant but arbitrarily directed rate of rotation,  $\vec{\omega}_o$ , between  $\vec{M}$  and the gyro case.

This problem is readily analyzed by using the transformation

properties of the tensor  $U$  and transforming to the coordinate system where  $\vec{M}$  is stationary. The elements of the transformed tensor,  $U'$ , will contain both secular and nonsecular terms. Under the usual conditions that allow neglect of the nonsecular terms with respect to the secular ones, we find that  $U'$  has axial symmetry about the axis of rotation. More precisely, if the  $z$  axis lies along the axis of rotation, then the neglect of the nonsecular terms gives

$$U' = \begin{pmatrix} U_a & 0 & 0 \\ 0 & U_a & 0 \\ 0 & 0 & U_{zz} \end{pmatrix}, \quad [5.28]$$

where  $U_a = \frac{1}{2}(U_{xx} + U_{yy})$ .

Since we have already explicitly considered the case where  $U$  (or  $Q$ ) is axially symmetric, we know that the net effect is to cause  $\vec{M}$  to precess at a rate,  $\omega_p$ , given by [5.23] about the  $z$  axis. The primary difference, of course, is that the  $z$  axis is no longer necessarily a principal axis of  $U$  but is specified by  $\vec{\omega}_0$ .

#### 5.4.1.2 Interaction of the Magnetization with the Readout Magnetometers: Effect of Finite Loop Gain

Because the response of a SQUID is periodic in the applied flux, most of the instrument applications of the SQUID make use of feedback in order to form a flux-locked loop.<sup>22</sup> The effect of this is to substantially increase the dynamic range of linear response, and the resulting device is therefore sometimes referred to as a linearized SQUID. Since the use of feedback does not affect signal-to-noise ratio considerations,<sup>66</sup> this aspect of SQUID operation was omitted in

our discussion of the ZFNG readout resolution (Sec. 5.3).

There are two ways feedback can be applied in instrument applications:<sup>22,66</sup> by applying feedback flux directly into the SQUID, and by applying feedback flux into the superconducting coupling circuit. As noted in Chap. 1, the latter approach is very attractive for the ZFNG application in that it considerably reduces the reaction current in the persistent coupling circuit. This technique is shown schematically in Fig. 5.2. The price that must be paid for actively controlling the current in the coupling circuit is that the sample is exposed to a greater extent to SQUID magnetometer noise and drift than it would be if the feedback went to the SQUID instead. This issue will be discussed in the next section.

Referring to Fig. 5.2, we would like to calculate the current,  $i(t)$ , in the input circuit due to the applied field at the pickup coil,  $B_a(t)$ , subject to the closed loop condition imposed by the magnetometer. Knowing this, we can then calculate the average reaction field (*i.e.*, the spatial average),  $B_i(t)$ , that will be seen at the sample.

The flux quantization condition requires that

$$B_a(t)A_p N_p + V_o(t)M_f/R_f + i(t)L_t = n\phi_o = 0 , \quad [5.29]$$

where the choice of  $n = 0$  is a matter of convenience. As before,  $A_p$  and  $N_p$  are the area and number of turns of  $L_p$  and  $L_t \equiv L_i + L_p + L_f \approx 2L_p$ . This value for  $L_t$  is due to the requirements that  $L_p = L_i \gg L_f$  for maximum coupling efficiency.

If equation [5.29] is Fourier transformed, and we define the forward and reverse transfer functions

$$G_{iV}(\omega) = V_o(\omega)/i(\omega) , \quad [5.30]$$

and

$$g_{Vi} = M_f/R_f L_t , \quad [5.31]$$

respectively, then [5.29] yields

$$\begin{aligned} j(\omega) &= - \frac{B_a A_p N_p}{p} \{L_t [1 + G_L(\omega)]\}^{-1} \\ &\approx - \frac{B_a A_p N_p}{p} \{2L_p [1 + G_L(\omega)]\}^{-1} . \end{aligned} \quad [5.32]$$

Here,  $G_L(\omega) = G_{iV} g_{Vi}$  is the loop gain.

Now the average field appearing in the sample volume due to  $i(\omega)$  is equal to the field at the center of the sample cell. Thus,

$$B_i(\omega) = \mu_o N_p i(\omega) / 2R_c \quad [5.33]$$

$$= \mu_o N_p^2 A_p \{4R_c L_p [1 + G_L(\omega)]\}^{-1} . \quad [5.34]$$

Following our previous discussion of pickup coil considerations, equations [5.9], [5.11] and [5.12], this becomes

$$B_i(\omega) = - \pi/4 \{[1 + G_L(\omega)] \kappa / \mu_o\}^{-1} B_a . \quad [5.35]$$

At this point, we consider the application of [5.35] to two different cases: a) in the low frequency limit where the sample magnetization  $\vec{M}$  is sufficiently stationary that we can assume  $G_L(\omega) \approx G_L(0)$ , and b) where  $\vec{M}$  lies in the x-y plane, rotating with angular velocity  $\omega_o \hat{k}$ . In both of these cases we have for each orthogonal pickup loop  $(B_a)_\alpha = (R_o/R_{c\alpha})^3 (B_{mo})_\alpha$  (equation [5.14]), where  $\alpha$  denotes both the pickup loop and the Cartesian axis along which its normal lies.

In case a)  $\omega$  is taken to be small enough that the phase shift in the SQUID electronics is negligible and  $G_L(\omega)$  is therefore real. Just how small  $\omega$  must be in order to satisfy this requirement depends on the design of the magnetometer electronics, *i.e.*, on the modulation frequency  $\omega_m$  and on the design of the low pass filter that is necessary to make  $|G_L(\omega_m)| \lesssim 1$ .<sup>22</sup>

Under the assumption that  $G_L$  is real, we can write

$$\vec{B}_i = U_m \vec{B}_{mo} \quad [5.36]$$

where  $U_m$  is a diagonal tensor in the coordinate system of the orthogonal pickup coils. The elements of  $U_m$  in this coordinate system are given by

$$(U_m)_{\alpha\alpha} = -\pi/4 \{ [1 + G_L(\omega)] \kappa_\alpha / \mu_0 \}^{-1} (R_o / R_{ca})^3. \quad [5.37]$$

Thus in case a), the problem is formally identical to the passive perturbations that were considered previously.

In case b) we no longer assume that  $G_{L\alpha}(\omega)$  is real. This case thus serves to illustrate the effect of a phase shift in the loop. Since in this example we are assuming that  $\vec{M}$  lies in the x-y plane ( $M_z = 0$ ) and is rotating at a rate  $\omega_0 \hat{k}$  with respect to the gyro case, the in-phase components of  $\vec{B}_i$  have no effect on the average; *i.e.*, equation [5.23] shows that  $\omega_p = 0$  when  $M_z = 0$ . In presence of phase shifts, however,  $\vec{B}_i$  can lead or lag  $\vec{M}$  on the average and cause  $\vec{M}$  to slowly move out of the x-y plane. This effect is termed radiation damping in NMR.

If, as usual, we assume that nonsecular terms may be ignored, it can be shown that the rate of change of  $\theta$ , the polar angle of  $\vec{M}$  with respect to  $\vec{\omega}_0$ , is given by

$$d\theta/dt = \frac{1}{2} \gamma B_{mo} \text{Im}[(U_m)_{xx} + (U_m)_{yy}] \quad [5.38]$$

It is noteworthy that although both the precession effect in case a) and the damping effect in case b) are gyro drifts, the former is determined by the traceless tensor  $Q_m = \text{Re}[U_m - \frac{1}{3} I(\text{Tr}U_m)]$ , whereas the latter is determined by  $\text{Im}(U_m)$ . Thus the precession effect can be minimized if the magnetometers are balanced such that  $(U_m)_{xx} = (U_m)_{yy} = (U_m)_{zz}$ , but the damping effect can be minimized only by minimizing  $\text{Im}[G_L(\omega_0)]^{-1}$  for all values of  $\omega_0$  that are likely to be encountered.

As an order-of-magnitude estimate of both of these effects, we can evaluate  $\gamma B_{mo} (U_m)_{\alpha\alpha}$  from [5.37]. Taking  $|G_L| \approx 10^5$ ,  $B_{mo} = 10^{-6}$  G, and  $(\pi/4)(\mu_0/\kappa)(R_o/R_c)^3 = 10^{-1}$ , we find the gyro drift rate due to finite loop gain to be on the order of  $2 \times 10^{-8}$  rad sec $^{-1}$ . This compares to an estimated drift rate of  $10^{-7}$  rad sec $^{-1}$  due to sample cell asphericity.

#### 5.4.2 Motion of the Sample Magnetization Due to Magnetometer Noise and Drift

The technique of feeding back into the input coupling circuit implies that the noise current in this circuit is simply equal (except for a correction on the order of the reciprocal of the loop gain) to the total magnetometer output noise multiplied by the reverse transfer function,  $g_{Vi}$ , equation [3.51]. The presence of noise currents in

the input coupling circuits will cause a magnetic noise field  $\vec{B}_n$  to appear at the sample and this field can cause random motion of the sample magnetization. At the outset we will confine our discussion to stationary random noise; the matter of magnetometer drift will be considered separately at the end of this section.

Before proceeding to the specific problem at hand, it is helpful to review a few aspects of low-frequency-divergent noise. For that purpose, we will follow an analysis made by Radeka<sup>69</sup> to which the reader is referred for further details and references.

The approach that is taken is to consider low-frequency-divergent noise to be the result of applying broadband white noise to a physical system or filter having an appropriate frequency transfer function. It is convenient to think of the white noise as being generated by  $\delta$ -function impulses that are Poisson-distributed in time in the manner of temperature-limited shot noise. The filter has a transfer function  $H(\omega)$  and impulse response  $h(t)$ :

$$H(\omega) = \int_{-\infty}^{\infty} e^{-j\omega t} h(t) dt \quad (j \equiv \sqrt{-1})$$

$$h(t) = \int_{-\infty}^{\infty} H(\omega) e^{j\omega t} \frac{d\omega}{2\pi} = \int_{-\infty}^{\infty} H(\omega) e^{j\omega t} d\omega .$$

Thus if  $x(t)$  is the input, then the output,  $y(t)$ , is simply the convolution of  $x(t)$  and  $h(t)$ :

$$y(t) = \int_{-\infty}^t x(t') h(t - t') dt' . \quad [5.39]$$

Letting the (one-sided) input noise spectral density be  $n_{x0}$ , then the (one-sided) output spectral density is

$$S_y(v) = |H(\omega)|^2 n_{x0} .$$

We are interested in a class of filters  $H(\omega)$  such that

$$H_\alpha(\omega) = (j\omega)^{-\alpha/2}, \quad \alpha > 0 .$$

Thus,

$$S_{y\alpha}(\omega) = |\omega|^{-\alpha} n_{x0} \quad [5.40]$$

as desired. The Fourier transform of  $H_\alpha(\omega)$  can be obtained by considering  $(b + j\omega)^{-\alpha/2}$  and taking the limit  $b \rightarrow 0$ , resulting in<sup>70</sup>

$$h_\alpha(t) = \begin{cases} 0 & , \quad t < 0 \\ t^{\alpha/2-1}/\Gamma(\alpha/2), & t > 0 . \end{cases}$$

Now if white noise is generated by a random sequence of pulses  $t_j q \delta(t - t_j)$  where the times  $t_j$  are Poisson-distributed and occur at an average rate  $\bar{n}$  sec<sup>-1</sup>, then it can be shown that the noise power spectral density is given by<sup>71</sup>

$$n_{x0} = 2\bar{n}q^2 .$$

(We assume that there is no dc component, *i.e.*, that the positive and negative pulses both occur at an average rate  $\bar{n}/2$ .) If this noise is applied to the filter specified above starting at  $t = 0$ , it can be shown using Campbell's theorem<sup>72</sup> that the ensemble variance of the output  $\sigma_{y\alpha}^2(t)$  at a time  $t$  later is given by

$$\begin{aligned} \sigma_{y\alpha}^2(t) &= \bar{n}q^2 \int_0^t h^2(t') dt' \\ &= \frac{1}{2} n_{x0} \int_0^t h_\alpha^2(t') dt' . \end{aligned}$$

Hence for  $H(\omega) = (j\omega)^{-\alpha/2}$ ,

$$\begin{aligned}\sigma_{y\alpha}^2(t) &= \frac{n_{x0}}{2\Gamma^2(\alpha/2)} \int_0^t t'^{(\alpha-2)} dt' \\ &= \frac{n_{x0} t^{\alpha-1}}{2(\alpha-1)\Gamma^2(\alpha/2)}, \quad \alpha > 1. \quad [5.41]\end{aligned}$$

We now discuss the specific cases of  $\alpha = 1, 2, 3$ .

$\alpha = 1$ :

This generates 1/f noise.  $h_1(t) = (\pi t)^{-\frac{1}{2}}$ ,  $t > 0$ , so that input and output processes are related by

$$y_1(t) = \pi^{-\frac{1}{2}} \int_{-\infty}^t (t - t')^{-\frac{1}{2}} x(t') dt'.$$

In attempting to evaluate [5.41], however, we realize that 1/f noise is high-frequency as well as low-frequency divergent. This does not represent any real problem since all physical measurements have a high-frequency cutoff. By averaging over a time  $\epsilon$ , Radeka<sup>69</sup> obtains the approximate result

$$\sigma_{y1}^2(t) = (n_{x0}/2\pi) \begin{cases} t/\epsilon & t \leq \epsilon \\ 1 + \ln(t/\epsilon) & t \geq \epsilon \end{cases} \quad [5.42]$$

$\alpha = 2$ :

This case is also commonly occurring.  $h_2(t)$  is simply a unit step function at  $t = 0$  so that

$$y_2(t) = \int_{-\infty}^t x(t') dt'.$$

From [5.41] we have

$$\sigma_{y2}^2(t) = \frac{1}{2} n_{x0} t. \quad [5.43]$$

This is the familiar result obtained in a random walk. We may therefore conclude that a random walk has a  $\omega^{-2}$  spectrum.

$\alpha = 3$ :

This case will be seen to be relevant for the  $\text{He}^3$  FPNG. Here

$$y_3(t) = (2/\sqrt{\pi}) \int_{-\infty}^t (t - t')^{\frac{3}{2}} x(t') dt' ,$$

and

$$\sigma_{y3}^2(t) = (n_{x0}/\pi)t^2 . \quad [5.44]$$

We are now in a position to estimate the motion of the sample magnetization when subjected to a magnetic noise field such as would be generated by the magnetometers. In order to do this readily, we assume that the magnetization would otherwise be stationary with respect to the gyro case and that the magnetic noise field: 1) is isotropic with uncorrelated components, 2) is uniform over the sample volume, and 3) is sufficiently weak that the average motion of the magnetization is a small fraction of one radian for all times of interest.\* Assumption 2) is not necessary for frequencies  $\omega \ll \tau_{11}^{-1}$ .

If we define the coordinate system such that  $\vec{M}(t = 0) = \hat{M}$ , the equation of motion gives

$$dM_y/dt \approx \gamma M_y B_{nx} ,$$

or

$$M_y(t)/M \approx \gamma \int_0^t B_{nx}(t') dt' .$$

Thus, as we have just seen,  $M_y(t)/M$  is a random variable whose power

\* Normally, for well-behaved noise, one would specify that the motion be small in a correlation time of the noise field. Since 1/f noise does not have a correlation time, however, we substitute assumption 3) instead.

spectral density is related to that of  $B_{nx}$  by the coefficient  $(\gamma/\omega)^2$ .

By assumption 1) above, we also have  $\langle M_x^2(t) \rangle = \langle M_y^2(t) \rangle$  where the angle brackets are used to signify an ensemble average. Hence,

$$\begin{aligned}\langle \theta^2(t) \rangle &\simeq \langle M_x^2(t) + M_y^2(t) \rangle / M^2 \\ &\simeq 2 \langle M_y^2(t) \rangle / M^2.\end{aligned}$$

This leads to the desired relation

$$S_\theta = 2\gamma^2 S_B / \omega^2 \quad [5.45]$$

where  $S_B$  is the power spectral density of one of the Cartesian components of  $\vec{B}_n$ , and  $S_\theta$  is the power spectral density of the polar angle  $\theta$ .

Now from equations [5.7, 9, 11, and 33] and the requirement that  $L_i = L_p$  we can easily find the expression relating  $S_B$  to the noise energy of the individual SQUIDS:

$$S_B = \mu_0 E_n(v) / [2R_c^3(\kappa/\mu_0)] \quad [5.46]$$

Combining [5.45] and [5.46] we finally have

$$S_\theta = \left[ \frac{\mu_0 \gamma^2}{R_c^3(\kappa/\mu_0)} \right] \frac{E_n(v)}{\omega^2} \quad [5.47]$$

As was discussed in Sec. 5.3,  $E_n(v)$  has two principal components, a white spectrum and a  $1/f$  spectrum. As a consequence,  $S_\theta$  also has two components, a  $\omega^{-2}$  part due to the former component of  $E_n(v)$  and a  $\omega^{-3}$  due to the latter. We consider these two cases separately, using the CGK data<sup>23</sup> for numerical estimates.

Starting with the  $\alpha = 2$  case first, we compare equations [5.40] and [5.47] to make the identification

$$n_{x0} = \frac{\mu_0 \gamma^2}{R_c^3 (\kappa/\mu_0)} E_{nw} ,$$

where  $E_{nw}$  is  $E_n(v)$  in the white part of the SQUID noise spectrum.

Using [5.43] this yields

$$\sigma_{\theta 2}^2(t) = \frac{\mu_0 \gamma^2 E_{nw}}{2R_c^3 (\kappa/\mu_0)} t . \quad [5.48]$$

Using the CGK value of  $E_{nw} = 7 \times 10^{-30}$  J/Hz and the same values for  $R_c$  and  $\kappa/\mu_0$  we have used previously, we obtain

$$\sigma_{\theta 2}(t) \approx 6 \times 10^{-8} t^{\frac{1}{2}} . \quad [5.49]$$

Proceeding to the  $\alpha = 3$  case, we find from the CGK data that

$E_n(v) = k/\omega$ , where  $k \approx 4 \times 10^{-30}$  J Hz $^{-1} \cdot$  rad sec $^{-1}$ , for the 1/f noise.

Thus

$$S_{\theta 3} = \frac{\mu_0 \gamma^2 k}{R_c^3 (\kappa/\mu_0)} \omega^{-3} ,$$

and

$$\sigma_{\theta 3}^2(t) = \frac{\mu_0 \gamma^2 k}{\pi R_c^2 (\kappa/\mu_0)} t^2 . \quad [5.50]$$

This yields the numerical estimate

$$\sigma_{\theta 3}(t) \approx 5 \times 10^{-8} t . \quad [5.51]$$

If we compare these two cases, it is seen that  $\sigma_{\theta 3}$  will proceed

as  $t^{\frac{1}{2}}$  up to  $\sim 3$  sec after which it will proceed as  $t$ . It should be noted that the low-frequency behavior of the CGK data is only specified to be approximately  $1/f$  and is not measured below  $10^{-4}$  Hz. Equation [5.50] should therefore be taken as an order-of-magnitude estimate that should be reasonably valid for the range of times between 1 and  $10^4$  sec.

We will now briefly note the effect of magnetometer drift on the motion of the magnetization. We assume that the drift reported by CGK of  $2 \times 10^{-5} \phi_0 h^{-1}$  was not due to a random process and for simplicity will assume that the drift is linear in time. For our proposed geometry, this drift rate would result in a magnetic field drift of  $\sim 5 \times 10^{-16} G \text{ sec}^{-1}$  in each pickup coil. If it is now assumed that the magnetic field at the sample is somehow perfectly nulled at  $t = 0$ , then it is estimated that the magnetization will accumulate an error of  $\sim 6 \times 10^{-12} t^2 \text{ rad}$  after a time  $t$  sec due to magnetometer drift. This corresponds to an average drift rate of  $\sim 4 \times 10^{-7} \text{ rad sec}^{-1}$  over a 20 h period (the period over which the CGK drift measurement was made). The effect of drift will dominate over that of  $1/f$  noise after a period of a few hours.

#### 5.4.3 Effect of the London Moment

If a spherical superconductor, such as the shield for the  $He^3$  ZFNG is rotated with an angular velocity  $\vec{\omega}_0$ , then a uniform magnetic field,  $\vec{B}_L$ , will appear in the interior according to the expression derived by London:<sup>19</sup>

$$\vec{B}_L = (2mc/e)\vec{\omega}_0 \quad (\text{Gaussian units}) .$$

Here,  $m$  and  $e$  refer to the mass and charge of the electron, and the numerical value of the coefficient is  $1.14 \times 10^{-7}$  G rad $^{-1}$  sec.

Writing  $\vec{\omega}_L = -\gamma \vec{B}_L$ , we have the relation between the precession due to the London moment and the rate of rotation of the gyro case:

$$\vec{\omega}_L = -\gamma(2mc/e)\vec{\omega}_0 = 2.6 \times 10^{-3} \vec{\omega}_0 .$$

Even though this effect is fairly large it does not represent any significant limitation on the performance of the ZFNG since it is quite predictable and may be accurately compensated for.

### 5.5 Conclusion

We have theoretically analyzed the performance of a hypothetical  $\text{He}^3$  ZFNG having the following specifications: sample cell radius,  $R_0 = 1.9$  cm with a maximum elliptical ( $Y_{2m}$ ) error  $\delta R_0 = 1.3 \times 10^{-5}$  cm; internal flux density due to  $\text{He}^3$  magnetization,  $B_{mo} = 10^{-6}$  G ( $\text{He}^3$  density,  $2 \times 10^{-6}$  mol cm $^{-3}$ , 1% polarization); temperature, 4.2 K;  $\text{He}^4$  density  $\leq 8 \times 10^{-5}$  mol cm $^{-3}$ ; solid  $\text{H}_2$  wall coating; ambient magnetic field,  $\sim 5 \times 10^{-8}$  G, with a gradient  $\leq 10^{-8}$  G cm $^{-1}$ , maintained by a concentric spherical superconducting shield; readout, three-axis SQUID magnetometer utilizing feedback into the input coupling circuits.

With these specifications, it is estimated that the gyrc will have an initial readout resolution (*i.e.*, before significant relaxation of the sample magnetization) of  $\sim 4 \times 10^{-5}$  rad (8 sec) in a 1 Hz bandwidth and a residual drift rate in the range of  $10^{-6} - 10^{-7}$  rad sec $^{-1}$  ( $0.2^\circ - 0.02^\circ \text{ h}^{-1}$ ) when averaged over a one day period. The relaxation rates due to intrinsic relaxation in the bulk and magnetic

field gradients should both be less than  $10^{-6}$  sec<sup>-1</sup>. The actual relaxation rate that would be obtained under the specified conditions, however, is unknown because of inadequate information about wall-induced relaxation. In spite of this, it is thought that relaxation times on the order of a day or longer should be obtainable.

## CHAPTER 6

### $\text{He}^3$ NUCLEAR ELECTRIC DIPOLE MOMENT EXPERIMENT

#### 6.1 Introduction

Having analyzed the  $\text{He}^3$  ZFNG in some detail we now turn to the question of whether it would be a suitable vehicle for an attempt to measure the nuclear electric dipole moment (NEDM) of  $\text{He}^3$ . In making an evaluation, it is useful to have some reference sensitivity against which our estimates can be compared. For this purpose we use the most recently published results obtained by Dress, *et al.*<sup>8</sup> from neutron beam experiment. They concluded that  $|D| < 3 \times 10^{-24}$  cm, where  $D = \mu_e/e$ ,  $\mu_e$  being the electric dipole moment of the neutron and  $e$  is the electronic charge. More specifically, a weighted average of their data yielded  $D = (0.4 \pm 1.5) \times 10^{-24}$  cm. Thus, our target is an experiment capable of detecting an EDM having a magnitude  $|D| = 10^{-24}$  cm.

It will be recalled from Chap. 1 that the basic approach to measurement of the  $\text{He}^3$  NEDM by using the  $\text{He}^3$  ZFNG was to apply an electric field,  $\vec{E}$ , first in one direction, and then in the opposite direction to the  $\text{He}^3$  ZFNG. If a NEDM existed and there were no magnetic field then there would be a shift in the precession rate between the two intervals given by

$$\Delta\omega_{\text{ed}} = (1/\hbar) 2fEeD , \quad [6.1]$$

where  $f$  is the factor calculated by Schiff<sup>13</sup> which relates the applied

external electric field  $E$  to the electric field that actually would appear at the nucleus. Schiff found that  $f \approx 10^{-7}$ . If it is now assumed that an electric field of  $10^5$  V/cm can safely be applied to the dilute mixture of polarized  $\text{He}^3$  in liquid  $\text{He}^4$ ,<sup>73</sup> and we use  $|D| = 10^{-24}$  cm, then one would expect  $\Delta\omega_{ed} = 3 \times 10^{-11}$  rad sec<sup>-1</sup>. This is equivalent to the effect one would obtain if a magnetic field of  $7 \times 10^{-16}$  G were to be reversed instead. In actual practice, of course, the experiment would consist of periodically reversing the electric field at a rate of  $v_E$  Hz. The desired information would then be extracted by use of signal averaging techniques.

A perusal of the  $\text{He}^3$  ZFNG resolution and stability characteristics that were estimated in the previous chapter is quite discouraging in light of the above requirement. In fact, an analysis would show that an attempt to use the  $\text{He}^3$  ZFNG to do the NEDM experiment would require an unacceptably long period of time.

Instead of proving this statement, however, we will propose and analyze a somewhat modified approach which will be shown to ameliorate by several orders of magnitude most of the problems that make the application of the ZFNG concept to the NEDM experiment very difficult. This modified approach consists of forgoing the zero-field concept and instead applying a homogeneous, stable magnetic field  $\vec{B}_0 = B_0 \hat{k}$  such that the  $\text{He}^3$  Larmor frequency  $\omega_0 = -\gamma B_0$  is some convenient value, say 1 rad sec<sup>-1</sup>. (This would require that  $B_0 \approx 50 \mu\text{G}$ .) In order to start the experiment, the magnetization of the polarized  $\text{He}^3$  is established in the x-y plane and then allowed to precess about the z axis at frequency  $\omega_0$ . (See Fig. 6.1.) Now if a NEDM exists in  $\text{He}^3$ , the

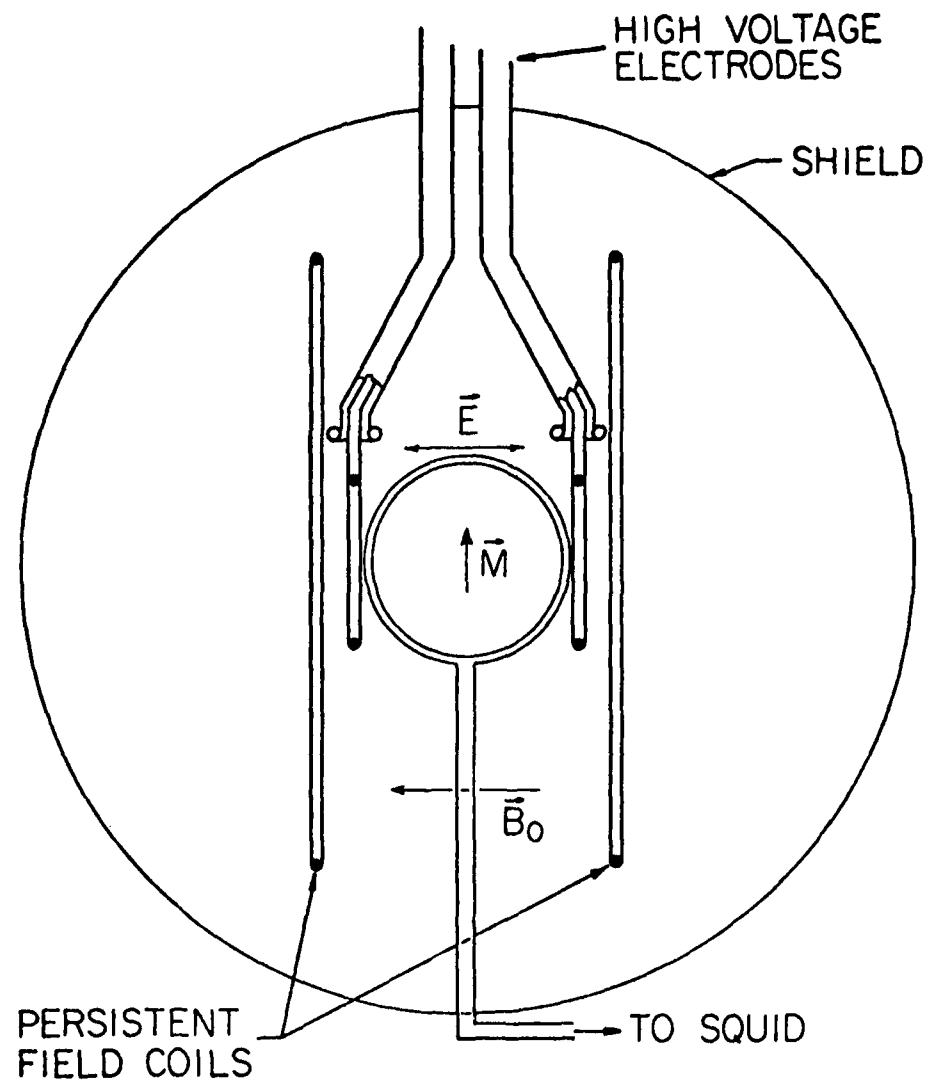


Fig. 6.1 Schematic depiction of an apparatus that might be used for a  $\text{He}^3$  nuclear electric dipole moment experiment.

application of an electric field  $\vec{E} = \hat{E}\hat{k}$  will cause the precession frequency to shift to  $\omega_0 + \delta\omega$  where  $\delta\omega = \hbar^{-1}fEDe$ . Reversing the electric field will cause a net frequency shift of  $2\delta\omega$ . Readout is accomplished by the use of a pickup coil located i.e. the y-z plane.

There are several advantages to this technique: 1) Although we will still require that the ambient magnetic field be  $\lesssim 5 \times 10^{-8}$  G, it is unnecessary to attempt to null this residual field. 2) The desired information is in the form of a frequency-modulated "carrier" at  $(\omega_0/2\pi)$  Hz which should be above the  $1/f$ -dominated region of the SQUID. This will significantly reduce the length of time necessary to resolve a given frequency shift. 3) The fact that the magnetization is in the x-y plane and that there is no pickup coil in this plane will considerably reduce the residual magnetic torques, i.e., the variations in the Larmor frequency. These advantages will be quantitatively evaluated in subsequent sections of this chapter.

Before proceeding with these evaluations, however, there is one additional problem that needs to be commented upon. We have noted that the  $\text{He}^3$  NEDM experiment must be done in the liquid phase. Yet our analysis of the ZFNG in the previous chapter was predicated on a relatively large (3.8 cm diam) sample cell which is only feasible if the  $\text{He}^3$  is able to rapidly diffuse throughout the sample. In Sec. 5.2.3 it was estimated that the  $\text{He}^3$  diffusion coefficient should satisfy the requirement  $D \gtrsim 0.03 \text{ cm}^2 \text{ sec}^{-1}$ . This clearly is impossible with normal liquid  $\text{He}^4$  but is quite feasible in the liquid  $\text{HeII}$  phase below the lambda point. For example, a measurement of the  $\text{He}^3$  spin diffusion coefficient at  $0.93 \text{ K}$ <sup>74</sup> indicates that  $D = 4.17 \times 10^{-2}$

$\text{cm}^2 \text{ sec}^{-1}$  for a  $\text{He}^3$  concentration of 0.03%. At sufficiently low temperature the  $\text{He}^3$  mean free path becomes limited by the  $\text{He}^3$  density alone. Dielectric breakdown data<sup>73</sup> indicate that there is only a slight decline in the breakdown field below the lambda point so that electric fields in the neighborhood of  $10^5 \text{ V cm}^{-1}$  still appear feasible.

## 6.2 Frequency Resolution Estimate

In this section we will obtain an estimate of the resolution of a frequency measurement in the presence of additive noise but in the limit of a large signal-to-noise ratio. The result that will be obtained is virtually identical to the one that is obtained using the much more rigorous and general techniques of estimation theory,<sup>75</sup> but our approach has the advantage of being simple and direct.

The process of measuring an inaccurately known frequency with additive noise can be conceptualized as follows: The unknown frequency is mixed with a known frequency such that the beat frequency is close to zero, *i.e.*, has a period that is long compared to the total measurement time,  $T$ . The difference frequency is then measured by estimating the rate of change of its phase as a function of time. This is done by averaging the difference signal over a time  $\Delta t$  for  $N$  consecutive intervals where  $N \gg 1$  and  $\Delta t$  is long compared to the period of the original frequency. This averaging limits the bandwidth to frequencies between  $\pm B$  Hz where the noise-equivalent bandwidth is given by  $2B = (\Delta t)^{-1}$ .

If we let  $S(\omega_0)$  be the one-sided noise power spectral density of the original signal at  $\omega_0$ , then the variance of the quadrature and

in-phase components of the narrow-band noise that exists after mixing and averaging are both equal to  $S(\omega_0)(\Delta t)^{-1}$ .<sup>75</sup> By assuming  $\sigma_x^2 = \sigma_y^2 \ll A(t)$ , where  $\sigma_x^2$  and  $\sigma_y^2$  are the in-phase and quadrature variances respectively and  $A(t)$  is the signal amplitude, the variance of the phase of each of the consecutive measurements is simply  $\sigma_\phi^2 \approx \sigma_y^2/A^2(t) = S(\omega_0)(\Delta t)^{-1}A^{-2}(t)$ . In this limit the error in the measurement of  $A$  has negligible effect on the phase error. For generality, we have allowed the signal amplitude to be a slowly varying function of time.

The information we desire is now obtained by fitting the data to the relation  $\phi(t) = \phi_0 + (\delta\omega_0)t$  where  $\delta\omega_0$  is the difference between the known and unknown frequencies. Using the linear least-squares technique<sup>63</sup> results in the following relationship between the variance of the estimate of  $\delta\omega_0$  (or  $\omega_0$ ) and  $\sigma_\phi^2$ :

$$\sigma_{\omega_0}^2 = \sigma_{\delta\omega_0}^2 = \Delta^{-1} \sum_i^N \sigma_{\phi i}^{-2} \quad [6.2]$$

where

$$\Delta = \left( \sum_i^N \sigma_{\phi i}^2 \right) \left( \sum_i^N t_i^2 / \sigma_{\phi i}^2 \right) - \left( \sum_i^N t_i / \sigma_{\phi i}^2 \right)^2,$$

and

$$\sigma_{\phi i}^2 = \sigma_y^2 / A^2(t_i) = S(\omega_0)(\Delta t)^{-1}A^{-2}(t_i).$$

We now approximate these sums with integrals:

$$\sum_i^N \approx \int_0^T \frac{dt}{\Delta t} = \frac{N}{T} \int_0^T dt$$

$$\sum_i^N \sigma_{\phi i}^{-2} \approx (N/T)^2 S^{-1}(\omega_0) \int_0^T A^2(t) dt = (N/T)^2 [2E/S(\omega_0)]$$

where

$$E = \frac{1}{2} \int_0^T A^2(t) dt \quad [6.3]$$

is the signal energy. (The  $\frac{1}{2}$  is due to the fact that  $A(t)$  is the amplitude of a sinusoid.) Defining a normalized amplitude

$$a(t) = (2E)^{-\frac{1}{2}} A(t) \quad \text{so that} \quad \int a^2(t) dt = 1 , \quad [6.4]$$

we find that  $\Delta$  can be written

$$\Delta = [(N/T) 2E t_d S^{-1}(\omega_0)]^2 ,$$

where

$$t_d^2 \equiv \int t^2 a^2(t) dt - [\int t a^2(t) dt]^2 . \quad [6.5]$$

Substituting the expressions for  $\sum \sigma_{\phi_i}^2$  and  $\Delta$  into [6.2] we obtain the desired result,

$$\sigma_{\omega_0}^2 = S(\omega_0) / (2E t_d^2) . \quad [6.6]$$

If, as a simple example, we take  $A = \text{constant}$  then

$$\sigma_{\omega_0}^2 = 12S(\omega_0) / A^2 T^3 . \quad [6.7]$$

Hence, the resolution of a frequency measurement in the presence of a small amount of additive noise varies as  $T^{-3/2}$  where  $T$  is the total measurement time.

By recalling our discussion in Sec. 5.4.2 this result is seen to be quite reasonable. If a steady-state quantity with additive white noise is averaged for a period  $T$  the variance of the average is proportional to  $T^{-1}$ . In the present case, however, the additive white noise constitutes a *phase* noise. Since the frequency is the time derivative of the phase, the frequency noise spectrum is related to the phase noise by  $S_v = \omega^2 S_\phi$ . This has the effect of depressing the

low frequency portion of the noise spectrum and causing the variance of a frequency measurement to vary as  $T^{-3}$ .

The advantage of  $\omega_0 \neq 0$  is noteworthy. In this case, only the portion of the noise spectrum in the vicinity  $\omega_0 \pm 2\pi T^{-1}$  affects the accuracy of the measurement. This avoids the problem of 1/f noise that was noted in the discussion of the  $\text{He}^3$  ZFNG readout resolution (Sec. 5.3).

We now would like to apply [6.6] to the problem of the  $\text{He}^3$  NEDM experiment. To do this, we need to do two things: 1) apply [6.6] to the situation where the signal is exponentially decaying with a time constant,  $T_2$ , and 2) use this result to determine the variance of a frequency difference measurement  $\Delta\omega \equiv \omega_+ - \omega_-$ , where  $\omega_+$  and  $\omega_-$  are to be alternately measured for intervals of  $T$  sec each. It is clear that these frequency measurements would be synchronized with the electric-field reversals so that  $T = (2v_E)^{-1}$ , where  $v_E$  is the field-reversal frequency. (For simplicity, the dead-time that would be necessary during the field-reversal process is ignored in this analysis.) We are primarily interested in a numerical estimate of the variance of  $\Delta\omega$ ,  $\sigma_{\Delta\omega}^2$ , and in determining the dependence of  $\sigma_{\Delta\omega}^2$  on the parameter  $u = T/T_2$ .

The application of equation [6.6] to a signal having an exponentially decaying amplitude,

$$A(t) = A_0 e^{-t/T_2}, \quad (T_2 \gg \omega_0^{-1}) \quad [6.8]$$

is straightforward, and yields the result

$$\sigma_{\omega}^2 = 4S(\omega_0)A_0^{-2}T_2^{-3}f(u) \quad [6.9]$$

where

$$f(u) = e^u \left( \sinh u - \frac{u^2}{\sinh u} \right)^{-1}, \quad [6.10]$$

and

$$u = T/T_2.$$

In order to analyze the field reversing scheme for measuring  $\Delta\omega$ , we designate each measurement period of duration  $T$  by the index  $k$ , where  $\omega_+$  is measured when  $k = 1, 3, 5, \dots$ , and  $\omega_-$  is measured then  $k = 2, 4, 6, \dots$  Thus the initial signal amplitude at the beginning of interval  $k$  is

$$A_{0k} = A_0 e^{-(k-1)T/T_2}. \quad [6.11]$$

We now imagine that the measurement process is continued for  $M$  complete cycles, that is for a total time  $2MT$ . Our estimate for  $\omega_+$  is then obtained from a weighted average of the measurements in the odd-numbered intervals and the estimate of  $\omega_-$  is likewise obtained from the even-numbered intervals. When this is done, the variances of  $\omega_+$  and  $\omega_-$  are given by<sup>63</sup>

$$\sigma_{\omega_+}^2 = \sum_{j=1}^M [\sigma(\omega_{2j-1})]^{-2}, \quad [6.12]$$

and

$$\sigma_{\omega_-}^2 = \sum_{j=1}^M [\sigma(\omega_{2j})]^{-2}. \quad [6.12]$$

where from [6.9]  $\sigma_k^2(\omega_k) = 4S(\omega_0)A_{0k}^{-2} T_2^{-3} f(u)$ . Since the desired quantity is  $\Delta\omega = \omega_+ - \omega_-$ , the desired variance is

$$\sigma_{\Delta\omega}^2 = \sigma_{\omega_+}^2 + \sigma_{\omega_-}^2 \quad [6.13]$$

AD-A101 064

STANFORD UNIV CALIF DEPT OF PHYSICS

I. SPIN-LATTICE RELAXATION OF DILUTE SOLUTIONS OF POLARIZED HES--ETC(U)

F44620-75-C-0022

F/6 14/2

AUG 78 M A TABER.

NL

UNCLASSIFIED

AFOSR-TR-81-0522

303  
4106A

END  
DATE  
7-88  
DTIC

By making the appropriate substitutions and doing the sums indicated in [6.12], the estimate of  $\sigma_{\Delta\omega}^2$  is readily obtained:

$$\sigma_{\Delta\omega}^2 = 8S(\omega_0)A_0^{-2}T_2^{-3}g_M(u) \quad [6.14]$$

where

$$g_M(u) = g_\infty(u)(1 - e^{-4Mu})^{-1}, \quad [6.15]$$

and

$$g_\infty(u) = 2 \sinh^2 2u / (\sinh^2 u - u^2). \quad [6.16]$$

We see from [6.15] that the total number of cycles should be such that  $4Mu \gtrsim 1$ . Now when  $u \ll 1$ ,  $g_\infty(u) \approx 24 u^{-2}$ , and in the opposite limit,  $u \gg 1$ ,  $g_\infty(u) \approx 2e^{2u}$ . Thus  $g_\infty(u)$  has a minimum at  $u = u_m$ , where it is found that  $u_m \approx 1.04$  and  $g(u_m) \approx 68.87$ . Hence

$$\min \sigma_{\Delta\omega} = 16.6 S^{\frac{1}{2}}(\omega_0)A_1^{-1}T_2^{-3/2}, \quad T \approx T_2. \quad [6.17]$$

Numerically, [6.17] yields  $\min \sigma_{\Delta\omega} \approx 1.6 \times 10^{-11} \text{ rad sec}^{-1}$  if we take  $T_2 = 10^5$  sec and  $S^{\frac{1}{2}}(\omega_0)/A_0 = 3 \times 10^{-11}/10^{-6} = 3 \times 10^{-5}$  (Sec. 5.3). This is an encouraging, although not particularly useful, result. It will be seen in the next section that  $\omega_0$  is not expected to be sufficiently stable to allow long-term measurements that optimize frequency resolution. Unless techniques are found to improve the stability of  $\omega_0$ , it will be necessary to alternate the electric field at a rate such that  $T \ll T_2$ . In this case, we have  $g_\infty(u) \approx 24 u^{-2}$  and

$$\sigma_{\Delta\omega} \approx 4\sqrt{6} S^{\frac{1}{2}}(\omega_0)A_0^{-1}T_2^{-1}T^{-1}, \quad T \ll T_2. \quad [6.18]$$

Numerical evaluation of [6.18] will be deferred to the next section.

### 6.3 Stability of the Larmor Frequency

As we have seen in Chap. 5, it can be expected that there will be small variations of the magnetic field seen by the sample as a function of time. The instantaneous Larmor frequency will therefore also vary as a function of time and can be thought of as having a Fourier spectrum of its own. These variations in the Larmor frequency can easily obscure the frequency shift of the size we are looking for. Sources of these variations include magnetic fields arising from magnetometer noise and drift, changes in the internal magnetic field arising directly or indirectly from the sample magnetization, mechanical motion of the apparatus, and various temperature-dependent effects. The first two of these were discussed in some detail in the previous chapter.

Now it is clear that only the  $z$  component (defined by the direction of  $\vec{B}_0$ ) of small perturbative static or quasistatic magnetic fields or rotations can have a first order effect on the Larmor frequency. Moreover, as long as these perturbative fields (or rotations) are small compared to  $B_0$  (or  $\omega_0$ ) then their static values will have only a minimal effect on the experiment. That is, the worst effect a small unknown static field can have is to introduce some misorientation in the direction of  $\vec{B}_0$ . Thus, if  $B_0 = 50 \mu\text{G}$  and the ambient field is  $5 \times 10^{-8} \text{ G}$ , there is a potential misorientation of  $\vec{B}_0$  by  $10^{-3} \text{ rad.}^*$

---

\* There is one other source of ambient field which has not been mentioned: the superconducting coupling circuit will freeze the instantaneous Johnson noise current (to the nearest quantum of flux) when it cools through its transition temperature. The rms value of the magnetic field at the sample due to this current can be readily calculated and for our proposed geometry with a niobium coupling circuit ( $T_c = 9.5 \text{ K}$ ), it should be less than  $10^{-8} \text{ G}$ .

The only way that perturbative magnetic fields or rotations that are orthogonal to  $\vec{B}_0$  can have anything other than a second order effect is for them to have a frequency component at  $\omega_0$ . In this case, they can cause the sample magnetization to move out of the x-y plane but will not have any direct effect on the Larmor frequency. We will estimate the magnitude of this effect with regard to magnetometer noise and will see that it is quite small.

#### 6.3.1 *Method of Analysis*

In Sec. 6.2 we determined that it would be possible to resolve the target frequency shift if  $T_2 \approx 10^5$  sec and  $T$  (the duration of a frequency measurement for a given polarity of the electric field) were approximately equal to  $T_2$ . In the following subsections the various sources of variations in the Larmor frequency will be examined to determine whether the Larmor frequency can be expected to be sufficiently stable over an interval of  $10^5$  sec to allow observation of the target frequency shift. It will be seen that in fact the Larmor frequency will be insufficiently stable by one or two orders of magnitude.

Although we will note some possible improvements and techniques that may ameliorate this situation somewhat, no presumption will be made that they will succeed. As a consequence we will proceed to analyze the case where  $v_E = (2T)^{-1} \gg T_2^{-1}$ . In this case, it will obviously take much longer to make the measurement. As a result it will either be necessary to have a longer  $T_2$  or to accumulate sufficiently good statistics over a number of separate experimental runs. In our analysis we will address this issue by estimating how long  $T_2$  would have to be in order to allow the measurement to be made in a

single run.

In order to analyze the case where  $\omega_0$  is no longer considered to be constant over the interval  $T$  (which is now assumed to be much shorter than  $T_2$ ), we view the output data as being the "instantaneous" frequency  $\omega_0(t)$ . That is, the frequency is considered to be measured over a continuous sequence of intervals of duration  $\Delta t$ , where  $\omega_0^{-1} \ll \Delta t \ll T$ . We assume that the precision of these measurements is limited by the presence of additive magnetometer noise so that the variance of the frequency measurement due to this noise (only) is given by equation [6.7]:

$$\sigma_{\omega_0}^2(t) = 12 S(\omega_0)/A^2(t)(\Delta t)^3. \quad [6.7]$$

Now our estimates of  $\omega_+$  and  $\omega_-$  are to be obtained from simple averages of the frequency data over all the intervals where the electric field is positive, and negative, respectively. Since the signal amplitude is not constant, however, the averages must be weighted by the factor of  $\sigma_{\omega_0}^{-2}(t)$ .<sup>63</sup> Thus our estimate of  $\omega_{\pm}$  would be given by

$$\omega_{\pm} = \frac{\sum_i \omega_0(t_i) \sigma_{\omega_0}^{-2}(t_i) \frac{1}{2}[1 \pm s(t_i)]}{\sum_i \sigma_{\omega_0}^{-2}(t_i) \frac{1}{2}[1 \pm s(t_i)]}, \quad [6.19]$$

where  $s(t) = \text{sgn } E_z(t)$  is a square wave of unit amplitude specifying whether the applied electric field is positive or negative. (We again are ignoring the dead time involved in the switching process.) By approximating the sums in [6.19] with integrals and using definition

[6.4] where  $2E = \int_0^\infty A^2(t)dt$ , the estimate for  $\Delta\omega = \omega_+ - \omega_-$  can be written in the form

$$\Delta\omega = 2 \int_0^\infty \omega_0(t) a^2(t) \left[ \frac{s(t) - \lambda}{1 - \lambda^2} \right] dt , \quad [6.20]$$

where

$$\lambda = \int_0^\infty a^2(t) s(t) dt . \quad [6.21]$$

Since we have specified that  $\omega_E T_2 = 2\pi v_E T_2 \gg 1$ , we note that  $\lambda \ll 1$ . Its presence in [6.20] (particularly in the numerator) cannot be neglected, however, since it assures that [6.20] will yield a null estimate for  $\Delta\omega$  if  $\omega_0(t) = \text{constant}$ . The factor of  $1 - \lambda^2$  in the denominator is a normalization factor that assures that  $\Delta\omega = 2\omega_{ed}$  if  $\omega_0(t) = \omega_{ed} s(t)$ . Since  $\lambda$  must be estimated from the data and is therefore not exactly known, it is useful to choose a phase for  $s(t)$  that minimizes  $\lambda$ . It can be shown that  $\lambda$  is minimum when the electric field is reversed at  $t = 1/2 T, 3/2 T, 5/2 T, \dots$  Thus we consider  $s(t)$  to be an even function of time (where the experiment starts at  $t = 0$ ), and  $s(t)$  may be expressed as a cosine Fourier series. We note that this represents a slight departure from the analysis in Sec. 6.2.

Equation [6.20] is useful as it stands for determining the spurious estimate of  $\Delta\omega$  that would be obtained if  $\omega_0(t)$  were to vary in some deterministic fashion for reasons other than the presence of a NEDM. If, on the other hand,  $\omega_0(t)$  is a random function of time where only its power spectrum  $S_{\omega_0}(v)$  is known, we need an expression yielding the ensemble variance  $\langle (\Delta\omega)^2 \rangle$ . (This quantity should not be confused with  $\sigma_{\Delta\omega}^2$  which is the variance of frequency measurements due to

the presence of additive noise.) If we rewrite equation [6.20]

$$\Delta\omega = \int_0^\infty I(t)\omega_0(t)dt \quad [6.22]$$

where

$$I(t) \equiv a^2(t)[s(t) - \lambda]/(1 - \lambda^2), \quad [6.23]$$

it is easily shown that

$$\langle(\Delta\omega)^2\rangle = \int_0^\infty dv S_{\omega_0}(v) |\tilde{I}(\omega)|^2 \quad [6.24]$$

where  $\tilde{I}(\omega) = \int_0^\infty e^{i\omega t} I(t)dt$ , and  $S_{\omega_0}(v)$  is the one-sided power spectral density of  $\omega_0$ .

Since we are considering the situation where  $\omega_E T_2 \gg 1$ ,  $|\tilde{I}(\omega)|^2$  has the form of a series of Lorentzian peaks located at  $\pm (2j - 1)\omega_E$ ,  $j = 1, 2, \dots$ , with heights  $(4/\pi)^2 (2j - 1)^{-2}$  and FWHM =  $T_2^{-1}$ . In addition to these peaks, the presence of  $\lambda$  in the numerator of [6.23] introduces another small term in  $\tilde{I}(\omega)$  which has the effect of canceling all of the tails of these peaks at  $\omega = 0$ . In the limit  $\omega \ll T_2^{-1}$  it is easily shown that  $|\tilde{I}(\omega)|^2 \propto \omega^2$ .

In applying [6.22] and [6.24] to cases where there are deterministic and random variations in  $\omega_0(t)$ , we will approximate  $s(t)$  with its lowest frequency Fourier component:  $S(t) \approx (4/\pi) \cos \omega_E t$ . This approximation is quite adequate for our present purposes and will underestimate the effect of variations in  $\omega_0$  on  $\Delta\omega$  by  $\sim 20\%$  at the most. With this approximation

$$\begin{aligned} \tilde{I}(\omega) \approx (4/\pi) & \{ [1 - (i/2)(\omega + \omega_E)T_2]^{-1} + [1 - (i/2)(\omega - \omega_E)T_2]^{-1} \\ & - 2\lambda[1 - (i/2)T_2]^{-1} \}, \end{aligned} \quad [6.25]$$

where

$$\lambda \approx (4/\pi) [1 + (\frac{1}{2} \omega_{E2}^2)^2]^{-1} \ll 1 .$$

### 6.3.2 Effects Due to Magnetometer Noise and Drift

The normal to the plane of the pickup coil is nominally orthogonal to the constant magnetic field  $\vec{B}_0$ . Because of residual magnetic fields and imperfect alignments in the experimental apparatus, it is estimated that the cosine of the angle between  $\vec{B}_0$  and  $\vec{B}_n$  (the uniform component of the magnetic field due to magnetometer-induced noise and drift currents in the pickup coil) will probably not be less than  $10^{-3}$  rad. If this cosine is designated by  $\beta$ , we have from [5.46]:

$$S_{\omega_0}(v) = \frac{\mu_0 \gamma^2 \beta^2}{2R_c^3(\kappa/\mu_0)} E_n(v) . \quad [6.26]$$

Now if an attempt is made to measure  $\omega_+$  or  $\omega_-$  over a long interval ( $10^5$  sec) it is clear that the 1/f component of  $E_n(v)$  will be dominant and we can proceed in the same manner as in Sec. 5.4.2. Writing  $E_n(v) = k/v$  in [6.26] and comparing the result with [5.45] we can identify the value of  $n_{x0}$  to be used in [5.40]. Ignoring the weak time dependence in [5.42], we have an approximate result for the actual variance of  $\omega_0$ :

$$\langle (\omega_0 - \langle \omega_0 \rangle)^2 \rangle \approx \frac{\mu_0 \gamma^2 \beta^2 k}{4\pi R_c^3(\kappa/\mu_0)} . \quad [6.27]$$

Using the same numerical values that were used in Chap. 5, and  $\beta = 10^{-3}$ , the estimate  $\langle (\omega_0 - \langle \omega_0 \rangle)^2 \rangle^{1/2} \approx 2 \times 10^{-11} \text{ rad sec}^{-1}$  is obtained.

Although this appears encouraging, we recall that for time scales

this long, magnetometer drift will be more significant than  $1/f$  noise. Using the value of  $\sim 5 \times 10^{-16}$  G sec $^{-1}$  quoted in Sec. 5.4.2 and multiplying by  $\beta\gamma$ , a drift rate of  $10^{-14}$  rad sec $^{-2}$  is obtained for  $\omega_0$ . Thus after  $10^5$  sec,  $\omega_0$  will have deviated from its original value by  $\sim 10^{-9}$  rad sec $^{-1}$ . Thus, unless significant reductions can be made in magnetometer drift (and there appears to be some reason for optimism on this score<sup>23</sup>) or some technique of orthogonalizing  $\vec{B}_n$  and  $\vec{B}_0$  (by use of trim coils to adjust the direction of  $\vec{B}_0$ ) is used, the long-term measurement appears to be impossible.

Assuming that it is necessary to have  $\omega_E T_2 \gg 1$  in order to reduce the effect of magnetometer drift, we find from [6.22] and the approximate form for  $s(t)$  that

$$\Delta\omega_d \approx -\frac{32}{\pi} \omega_{ed} T_2 (\omega_E T_2)^{-2} . \quad [6.28]$$

In order to obtain this estimate, we took  $\omega_0(t) = \omega_{00} + \dot{\omega}_{od} t$ . The best way to use this expression is to use the relation  $\omega_E = \pi/T$  and combine [6.28] with the resolution estimate, equation [6.18], in order to determine what value of  $T_2$  is necessary to assure satisfactory values for both  $\sigma_{\Delta\omega}$  and  $\Delta\omega_d$ . Doing this we obtain

$$T_2 \approx \frac{32}{\pi} \sigma_{\Delta\omega}^{-1} \left[ \frac{S^{\frac{1}{2}}(\omega_0)}{A_0} \right] \left[ \frac{3}{\pi} \frac{\dot{\omega}_{od}}{\Delta\omega_d} \right]^{\frac{1}{2}} . \quad [6.29]$$

Using  $\sigma_{\Delta\omega} = \Delta\omega_d = 2 \times 10^{-11}$  rad sec $^{-1}$  and  $\dot{\omega}_{od} = 10^{-14}$  rad sec $^{-2}$  (as above), we estimate that  $T_2 \approx 3.3 \times 10^5$  sec ( $\sim 10^2$  h) should yield adequate results. Substituting this into [6.28] we find that this would require  $T \approx 2.5 \times 10^4$  sec ( $\omega_E T_2 \approx 41$ ).

As to the effect of  $1/f$  noise when  $\omega_E T_2 \gg 1$ , we have from [6.24] and [6.26]

$$\langle (\Delta\omega)^2 \rangle \approx S_{\omega_0}(\nu_E) \int_0^\infty |\tilde{I}(\omega)|^2 d\nu = (4/\pi)^2 T_2^{-1} S_{\omega_0}(\nu_E) .$$

By using [6.26] and taking  $S_{\omega_0}(\nu_E) = k/\omega_E$  it is seen that expression [6.27] is obtained except that it is multiplied by a factor of  $(32/\pi)(\omega_E T_2)^{-1}$ . Thus while  $\Delta\omega_d \propto (\omega_E T_2)^{-2}$ ,  $\langle (\Delta\omega)^2 \rangle^{\frac{1}{2}} \propto (\omega_E T_2)^{-\frac{1}{2}}$ . Numerically, we estimate  $\langle (\Delta\omega)^2 \rangle^{\frac{1}{2}} \approx 9 \times 10^{-12} \text{ rad sec}^{-1}$  if  $\omega_E T_2 = 41$ , which is somewhat less than the estimate that was made of the effect of  $1/f$  noise on a long-term measurement.

There is yet one other effect of magnetometer noise on the sample magnetization that should be numerically estimated. As we have noted, the spectral component of the magnetometer noise at  $\omega_0$  can cause random motion of the polar angle of the sample magnetization,  $\theta$ . This effect can be estimated by use of the discussion in Sec. 5.4.2. In fact, the result we desire is simply  $1/\sqrt{2}$  of that given by [5.48] since  $\omega_0$  is in the white portion of the magnetometer noise spectrum. Hence  $(\theta - \pi/2)_{\text{rms}} \approx 4 \times 10^{-8} t^{\frac{1}{2}} \text{ rad}$ . Since we will only assume that  $|\cos\theta| \lesssim 10^{-3}$  at the outset, the motion induced by the magnetometer noise is clearly negligible.

### 6.3.3 Variations in the Larmor Frequency Due to Asymmetries

As we have discussed in Chap. 5, the average local field in the sample volume due to the sample magnetization,  $\vec{M}$ , is related to  $\vec{M}$  by a symmetric tensor. This general relationship encompasses the effects of sample asphericity, superconducting shield asphericity, the presence of other superconducting parts, and the effect of the real part of the

reciprocal of the magnetometer loop gain.

In particular, the analysis of the effect of these asymmetries under the condition of constant relative rotation between  $\vec{M}$  and the gyro case (Sec. 5.4.1.1) is relevant to our present problem. There we saw that in the frame rotating with angular velocity  $\omega_0 \hat{k}$  with respect to the gyro case (where  $\vec{M}$  would appear stationary except for the effect we are discussing here), there is an additional precession around the  $z$  axis occurring with angular velocity  $\omega_p$  given by

$$\omega_p = -\frac{3}{2} \gamma Q_{zz} |\vec{M}| \cos\theta. \quad [6.30]$$

We recall that  $Q$  is the traceless portion of  $U$ , where  $U$  is the symmetric tensor relating the spatial average of the local magnetic field (*i.e.*, as seen by a given nucleus) to the sample magnetization:  $\vec{B}_{loc} = \vec{U} \vec{M}$ . We also recall that [6.30] holds regardless of whether or not  $\vec{\omega}_0$  lies along a principle axis of  $U$ .

This additional precession,  $\omega_p$ , represents a frequency shift that is proportional to  $M_z$ .  $M_z$  can vary as a function of time due to a number of effects. The most significant of these is the exponential relaxation of  $M_z$  with the time constant  $T_1$ .

Since we have assumed that it is possible to initialize the experiment so that  $|\cos\theta| \lesssim 10^{-3}$ ,  $\omega_p$  should be reduced by a factor of  $\sim 10^3$  of the value that was estimated for the ZFNG. Now in Chap. 5 it was pointed out that the largest contribution to  $Q$  would probably arise from sample cell asphericity, and it was estimated that  $\frac{3}{2} \gamma Q_{zz} |\vec{M}| \approx 10^{-7} \text{ rad sec}^{-1}$  would be about the best that could be done if  $B_{mo} = 10^{-6} \text{ G}$ . By making  $\cos\theta \lesssim 10^{-3}$ , the maximum value of  $\omega_p$  (at

the start of the experiment) would be  $\sim 10^{-10}$  rad sec $^{-1}$ . This is only a half of an order of magnitude away from what is required for the He $^3$  NEDM experiment.

As was the case with magnetometer drift, it is clear that reversing the electric field at a rate such that  $\omega_E T_2 \gg 1$  will be efficacious in reducing the effect of this slow variation of  $\omega_p$  on the measurement of  $\Delta\omega$ . By using [6.20] together with the approximate form for  $s(t)$  and assuming that  $T_1 \approx T_2$ , we find that

$$\Delta\omega_p \approx (80/3\pi)\omega_p(\omega_E T_2)^{-2}. \quad [6.31]$$

Thus if  $\omega_p \approx 10^{-10}$  rad sec $^{-1}$ , the value of  $\omega_E T_2 \approx 41$  suggested previously would make  $\Delta\omega_p \approx 5 \times 10^{-13}$ .

This result, which indicates that the effect of asymmetries will be negligible when compared to that of magnetometer drift, depends on being able to maintain the tight tolerances suggested in Chap. 5. If this should prove to be difficult, certain trimming techniques may be feasible. The problem of trimming is considerably simplified in the present scheme (as opposed to the ZFNG approach) since only one parameter (e.g.,  $Q_{zz}$ ) need be adjusted.

#### 6.3.4 Effect of Mechanical Motion

Any small changes in the rotational velocity of the experimental apparatus in the direction of  $\vec{\omega}_0$  will appear as shifts in the Larmor frequency. For example, the basement floor of a building can tilt with an amplitude of  $\sim 10^{-5}$  rad (2 sec) with approximately diurnal periodicity. This can have two effects. First, the component of the earth's rotational velocity  $\vec{\Omega}_e$  in the direction of  $\vec{\omega}_0$  will vary, and secondly,

the time derivative of the motion itself can appear as a frequency shift.

The first effect is commonly dealt with in gyro testing programs by orienting the sensitive axis ( $\vec{\omega}_0$ ) along  $\vec{n}_e$  so that the effect of tilt is only second order. Thus, if the (small) angle between  $\vec{n}_e$  and  $\vec{\omega}_0$  is  $\vartheta$  and it is subjected to a variation  $\delta\vartheta$ , then  $|\delta\omega_0| = \Omega_e \vartheta \delta\vartheta$ . Hence with  $\delta\vartheta \approx 10^{-5}$  rad and  $\vartheta \leq 2 \times 10^{-2}$  ( $1^\circ$ ), we would have  $|\delta\omega_0| \approx 10^{-11}$  rad sec $^{-1}$ . In gyro applications, the second effect is not of great concern since presumably the tilt is largely periodic and does not accumulate very rapidly.

In the EDM experiment however, the second effect can also be troublesome. For example, a periodic sinusoidal tilt (*i.e.*, rotation) about  $\vec{\omega}_0$  with an amplitude of  $10^{-5}$  rad on a daily basis would cause a maximum shift in  $\omega_0$  of  $\sim 7 \times 10^{-10}$  rad sec $^{-1}$ . This would appear as a peak in the Fourier spectrum of  $\omega_0$  at  $10^{-5}$  Hz.

The use of a concrete isolation pad which is separate from the building floor could alter this situation. Since the motion of such a pad could presumably depend on factors such as temperature stability it is not possible to estimate the Fourier spectrum of its tilting motion without making careful measurements under controlled conditions.

#### 6.3.5 Effect of Temperature Stability on $\omega_0$

We will now discuss one topic where the present formulation of the  $\text{He}^3$  NEDM experiment is inferior to the ZFNG approach. Since we are considering the application of a non-zero uniform field,  $\vec{B}_0$ , by means of persistent current loops, the matter of the intrinsic stabil-

ity of  $B_0$  (exclusive of the other effects we have already discussed) needs to be considered. In particular, there are three temperature-dependent mechanisms that can affect  $B_0$ : 1) the thermal expansion of the field coils,<sup>\*</sup> 2) variation of the magnetic-field penetration depth in the field coils, and 3) the Curie-law susceptibility of the quartz housing.

The evaluation of these effects depends to a greater or lesser extent on details of the design of the apparatus which go beyond the scope of our present discussion. In order to obtain rough estimations of their relative importance, however, we will assume that the sample cell consists of a solid block of fused quartz with a spherical sample cavity and deposited niobium circuits on the outer surface to act as field sources. This assembly would then be concentrically mounted in the spherical shield.

In the case of thermal expansion, we find that  $\delta\omega_0/\omega_0 = \delta B_0/B_0 = -2\alpha\delta\theta$  where  $\alpha \approx -4 \times 10^{-10} \text{ } \textcircled{3} \text{ K}^{-1}$  is the thermal coefficient of expansion for fused quartz at low temperature,<sup>76</sup> and  $\delta\theta$  is the temperature variation. Taking  $|\delta\omega_0/\omega_0| \lesssim 10^{-11}$ ,  $\theta = 0.9 \text{ K}$ , we find  $|\delta\theta| \lesssim 2 \times 10^{-2} \text{ K}$ , a modest requirement.

Considering the effect of temperature variations on the magnetic penetration depth, it is readily shown by use of an approximate expression for the temperature dependence of the penetration depth,  $\lambda(\theta) = \lambda(0)[1 - (\theta/\theta_c)^4]^{-\frac{1}{2}}$ ,<sup>77</sup> where  $\theta_c$  is the superconducting transition temperature, that  $\delta B_0/B_0 \approx -4\lambda(0)\theta^3(\delta\theta)/(R_f\theta_c^4)$  when  $\theta \ll \theta_c$ . Here

<sup>\*</sup> It is assumed that this is the most significant source of internal dimensional variation in a well designed apparatus.

$R_f$  is the radius of the source coils ( $\sim 6$  cm) and  $\lambda(0) = 4.7 \times 10^{-6}$  cm for Nb.<sup>78</sup> This expression yields the estimate  $\delta\omega_0/\omega_0 \approx 4 \times 10^{-10} \Theta^3$  which is approximately one-half the size of the thermal expansion effect and of opposite sign.

In the case of the Curie-law variation of the susceptibility of fused quartz, there are two effects to consider. The first is the effect on the current in the persistent field coils and the second is the distortion of the B-field in the vicinity of the sample cavity. Actually, we will ignore the first effect since the B-field produced by a persistent current in a superconductor embedded in an infinite homogeneous and isotropic medium is independent of the susceptibility because of the flux-conservation condition. Thus, in the limit that the field coils become much larger than the sample cavity, we can consider the problem to be that of a spherical cavity embedded in an infinite medium where the B-field tends to become constant and uniform at infinity.

Considering therefore only the first effect, we have

$$\delta B_0 = - (8\pi/3) (d\chi/d\Theta) B_{\text{ext}} \delta\Theta ,$$

where  $\chi$  is the susceptibility of the fused quartz, and  $B_{\text{ext}} \approx B_0$  is the external magnetic flux density at infinity. Now the susceptibility of high purity fused quartz is well characterized by Curie-law behavior so that

$$d\chi/d\Theta = - C\Theta^{-2} ,$$

where  $C \approx 1.5 \times 10^{-6}$  K.<sup>79</sup> Thus

$$\delta B_0/B_0 = (8\pi/3)C\theta^{-2}\delta\theta .$$

We note that in contrast to the other two temperature-dependent effects which are proportional to  $\theta^3$ , the Curie-law effect is proportional to  $\theta^{-2}$ . Numerically we find  $\delta B/B_0 \approx 1.2 \times 10^{-5} \theta^{-2} \delta\theta$ . Thus at 0.9 K we must have  $|\delta T| \lesssim 2 \mu\text{K}$  if we require  $|\delta\omega_0/\omega_0| \lesssim 3 \times 10^{-11}$ .

Careful temperature regulation is therefore important for achieving the required stability. As we have noted with regard to other mechanisms that affect  $\omega_0$ , however, it is the spectral density of the temperature fluctuations at  $\nu_E$  that is of significance.

#### 6.4 Relaxation Time Considerations

The various relaxation mechanisms have been adequately reviewed in Sec. 5.2. Both the intrinsic relaxation mechanism and the relaxation due to magnetic field gradients should not require any additional consideration beyond what was discussed in Chap. 5. Since it is necessary to work at liquid He II temperatures, however, it should be pointed out that a solid  $\text{H}_2$  wall coating is not likely to be nearly as effective in reducing wall-induced relaxation as it is at 4.2 K.<sup>32</sup> At the present, there appears to be no adequate data to allow us to predict what the wall-induced relaxation rate will be for very dilute mixtures of  $\text{He}^3$  in liquid He II in a quartz cell. It does not seem likely, however, that the wall-induced relaxation rate ( $T_{1\text{Ad}}^{-1}$ ) will become significantly greater than the value we obtained experimentally in our bare Pyrex cell (Chap. 4) at 4.2 K. Some support for this conjecture can be found in Horvitz's data<sup>24</sup> which shows  $T_1 \approx 660$  sec for a 33%  $\text{He}^3$  mixture at 1.8 K

(above the  $\lambda$ -point), and  $T_1 \approx 600$  sec for this same mixture at  $\sim 1.2$  K (below the  $\lambda$ -point).

In addition, the sample cell that we have been considering here has a surface-to-volume ratio that is approximately one-quarter of that possessed by our experimental cell. Since we estimated  $T_{1W} \approx 2 \times 10^5$  sec in our 1 cm diam experimental cell, it would be expected that  $T_{1W} \approx 7 \times 10^5$  sec in a 3.8 cm diam cell. Thus under the conditions we have postulated, relaxation times in the range  $10^5$ - $10^6$  sec are likely.

### 6.5 Electric Field Requirement

In this section we will discuss a couple of the obvious problems that are associated with the large ( $10^5$  V/cm) electric field that is necessary for the  $\text{He}^3$  NEDM experiment. We will not, however, delve into electric field homogeneity and electrode geometry considerations.

The most difficult problem arises because of the necessity of locating the superconducting pickup coil (made of small filamentary turns) in the electric field. (See Fig. 6.1.) This problem has two aspects: 1) the electric field at the edges of the coil will be much greater than the average field applied to the helium sample, and, 2) it is important to avoid exposing the SQUID and its input circuit to electric breakdown events. The pickup coil will be insulated from the electric field electrodes by fused quartz which has a dielectric breakdown strength of  $\sim 7 \times 10^6$  V/cm at low temperatures.<sup>80</sup>

The simplest way to model this situation is to consider a conducting oblate spheroid in a uniform applied electric field which is

normal to the spheroid axis. In the limit that the spheroid tends to a disk, it can be shown that the maximum electric field is given by  $(8/\pi)(R_c/\epsilon)$  where  $R_c$  is the disk radius,  $\epsilon$  is its thickness, and  $E_0$  is the uniform field at infinity.<sup>81</sup> Since the maximum electric field appearing at the edge of a conducting ring should be approximately equal to that appearing at the edge of a disk having the same thickness and diameter, we see that it is necessary to have  $\epsilon \gtrsim 1$  mm if  $R_c = 2$  cm in order to avoid breakdown in the quartz.

This means that the pickup coil will have to be shielded with a conducting toroidal shield having approximately this thickness. It is neither necessary nor desirable for this shield to have high electrical conductivity since that could cause additional magnetometer noise and radiation damping of the sample. In fact, the shield should be made discontinuous in such a fashion as to prevent circumferentially circulating currents.

Another concern is that pre-breakdown currents might occur in the liquid helium (but not in the quartz) and cause the electric field in the sample to decay. This problem can be simply modeled by a parallel plate capacitor. The decay time constant is then  $\tau = RC = \rho \kappa_e \epsilon_0$ , where  $\rho$  is the resistivity of the helium,  $\kappa_e$  is the dielectric coefficient and  $\epsilon_0$  is the permittivity of free space. With regard to the resistivity, Blank and Edwards<sup>73</sup> were unable to detect any pre-breakdown currents and thereby estimated that  $\rho \gtrsim 10^{18}$   $\Omega\text{-cm}$  or  $10^{16}$   $\Omega\text{-m}$ . Since  $\kappa_e \approx 1$  for liquid helium we therefore have  $\tau \gtrsim 9 \times 10^4$  sec. This should be adequate even in the event that the equality holds provided that the electric field is reversed with the periodicity suggested in Sec. 6.3.2, *i.e.*, approximately every  $2.5 \times 10^4$  sec.

## 6.6 Conclusions

While it is clear that the reformulated version of the  $\text{He}^3$  NEDM experiment should come much closer to being competitive with the highly developed neutron-beam technique than would the ZFNG approach, it is not possible at this point to predict whether this goal can actually be achieved.

There are several reasons for caution. The most obvious is that the Fourier spectra of some of the more important perturbations (e.g., thermal effects and mechanical motion) are not presently known. Another reason is that some of our optimistic assumptions may have to be compromised in the design of a physically feasible apparatus. In addition, there may be factors which have been overlooked.

If this matter is to be pursued, it is necessary that an experimental feasibility study be undertaken in order to determine whether sufficient stability may be achieved in  $\omega_0$  to allow an EDM measurement of significant sensitivity to be carried out in a reasonable length of time. Because of the time scales and frequencies that have been suggested in our analysis (e.g., electric field reversals every several hours,  $T_2$  on the order of days) it is clear that the process of testing and refining the apparatus could be quite time consuming.

## APPENDIX A

### GRADIENT-INDUCED RELAXATION DUE TO A NEARBY FERROMAGNETIC DIPOLE

In this appendix we will obtain an approximate expression for gradient-induced relaxation arising from a ferromagnetic speck located near the sample cell. The motivation for this calculation as well as a summary of the assumptions and results are found in Sec. 4.3. The calculation is based on the general theory reviewed in Sec. 3.3.

In order to simplify the problem we will consider the sample cell to be cubical with the ferromagnetic dipole  $\vec{m}$  located and oriented as shown in Fig. 4.3. The coordinate system is also shown in this figure.

Following the notation of Chap. 3, the magnetic field configuration in the sample volume is given by

$$\vec{B} = \vec{B}_1(\vec{r}) + B_0 \hat{k}$$

Since the motional narrowing condition was strongly violated in our experiments, we will confine our considerations to the calculation of the gradient-induced longitudinal relaxation time,  $T_{1G}$ , under the assumption that  $|\vec{B}_1(\vec{r})| \ll B_0$  throughout the sample volume.  $\vec{B}_1(\vec{r})$  is the dipolar field arising from  $\vec{m}$ .

According to equations [3.16'] and [3.40]

$$\begin{aligned} T_{1G}^{-1} &= \gamma^2 V^{-1} \sum_{k_x=0}^{\infty} \sum_{k_y=0}^{\infty} \sum_{k_z=0}^{\infty} [\tilde{B}_{1x}(\vec{k}) + \tilde{B}_{1y}(\vec{k})] \left[ \frac{(k_D^2)^{-1}}{1 + (k_D^2)^{-2} \omega_0^2} \right] , \\ &= \gamma^2 V^{-1} \sum_{k_x=0}^{\infty} \sum_{k_y=0}^{\infty} \sum_{k_z=0}^{\infty} |\tilde{B}_{1+}(\vec{k})|^2 \{k_D^2 [1 + (k_D^2)^{-2} \omega_0^2]\}^{-1} , \quad [A.1] \end{aligned}$$

where  $\tilde{B}_{1+}(\hat{k}) = \tilde{B}_{1x}(\hat{k}) + i\tilde{B}_{1y}(\hat{k})$ , and

$$\tilde{B}_{1\alpha}(\hat{k}) = \int_V \phi_{\hat{k}}(\vec{r}) B_{1\alpha}(\vec{r}) d^3r . \quad [A.2]$$

In these expressions  $D$ ,  $V$  are the diffusion coefficient and sample volume respectively and  $\phi_{\hat{k}}(\vec{r})$  are a complete orthonormal set of eigenfunctions satisfying

$$(\nabla^2 + k^2) \phi_{\hat{k}}(\vec{r}) = 0 ,$$

and

$$(\hat{n} \cdot \vec{\nabla} \phi_{\hat{k}})_S = 0 ,$$

where  $\hat{n}$  is a unit normal on the sample surface  $S$ .

In the case of cubical sample cell of dimension  $L$ ,

$$\phi_{\hat{k}}(\vec{r}) = A(\hat{k}) \cos[k_x(x + L/2)] \cos[k_y(y + L/2)] \cos(k_z z)$$

where  $(k_x, k_y, k_z) = (\pi/L)(\ell, m, n)$ ,  $\ell, m, n = 0, 1, 2, \dots$ . The normalization coefficient  $A(\hat{k})$  is given by

$$A(\hat{k}) = 2\sqrt{2} [(\delta_{0\ell} + 1)(\delta_{0m} + 1)(\delta_{0n} + 1)V]^{-\frac{1}{2}} . \quad [A.3]$$

By making use of the axial symmetry of  $\tilde{B}_1(\vec{r})$  about the  $z$  axis,

[A.2] becomes

$$\begin{aligned} \tilde{B}_{1\alpha}(\hat{k}) &= A(\hat{k}) \cos\left(\frac{\ell\pi}{2}\right) \cos\left(\frac{m\pi}{2}\right) \int_V \cos k_x x \cos k_y y \cos k_z z B_{1\alpha}(\vec{r}) d^3r \\ &= A(\hat{k}) \cos\left(\frac{\ell\pi}{2}\right) \cos\left(\frac{m\pi}{2}\right) \frac{1}{2} \int_V \left[ e^{i\hat{k}\cdot\vec{r}} + e^{-i\hat{k}\cdot\vec{r}} \right] B_{1\alpha}(\vec{r}) d^3r . \quad [A.4] \end{aligned}$$

Letting

$$\tilde{B}_{1\alpha}(\vec{k}) = A(\vec{k}) \cos\left(\frac{\ell\pi}{2}\right) \cos\left(\frac{m\pi}{2}\right) \frac{1}{2} \int_V e^{i\vec{k} \cdot \vec{r}} B_{1\alpha}(\vec{r}) d^3r \quad [A.5]$$

we then have

$$\tilde{B}_{1\alpha}(\vec{k}) = \tilde{B}_{1\alpha}^+(\vec{k}) + \tilde{B}_{1\alpha}^-(\vec{k}) . \quad [A.6]$$

We now make two assumptions:

a)  $\omega_0 \tau_{100} = \omega_0 (L/\pi)^2 D^{-1} \gg 1$ , where in general

$$\tau_{\ell mn} = (k^2 D)^{-1} = (L/\pi)^2 [\ell^2 + m^2 + n^2]^{-1} D^{-1}$$

are the decay times of the various diffusion modes.

b)  $b \ll L$ , where the dipole,  $\vec{m}$ , is located at  $(0, 0, -b)$ .

Assumption a) is well-satisfied in our experiments since  $\omega_0 \tau_{100} \gtrsim 900$  for all of our data. Assumption b) is justifiable because it leads to a result that agrees well with our data as has been discussed in Chap. 4.

The expression for  $T_{1G}^{-1}$ , equation [A.1], can now be put in more usable form. First, we note from [A.4] that the sum over  $\vec{k}$  may be taken over all  $\vec{k}$ -space (rather than just the first octant) and the result divided by 8:

$$T_{1G}^{-1} = \gamma^2 (8V)^{-1} \sum_{\vec{k}} |\tilde{B}_{1+}(\vec{k})|^2 \{k^2 D [1 + (k^2 D)^{-2} \omega_0^2]\}^{-1} . \quad [A.1']$$

In addition:

1) By assumption a) the factor  $\{k^2 D [1 + (k^2 D)^{-2} \omega_0^2]\}^{-1}$  varies slowly over an increment  $|\Delta k| = \pi/L$ , and by assumption b)  $|\tilde{B}_{1+}(\vec{k})|^2$  likewise varies slowly with respect to  $|\Delta k|$ . Thus we can make the approximation

$$\sum_{\vec{k}} \approx (V/\pi^3) \int d^3k .$$

2) The  $\cos^2(\ell\pi/2)\cos^2(m\pi/2)$  factor in the expressions for  $\tilde{B}_{1\alpha}^2(\vec{k})$  reduces the density of states in  $\vec{k}$ -space by a factor of 4.

3) The error introduced by taking  $A(\vec{k}) = (8/V)^{\frac{1}{2}}$  instead of [A.3] is negligible.

Hence

$$T_{1G}^{-1} \approx \gamma^2 (32\pi^3)^{-1} \int d^3k |\tilde{B}_{1+}(\vec{k})|^2 \{ (k_D^2) [1 + (k_D^2)^{-2} \omega_0^2] \}^{-1}. \quad [A.7]$$

By assumption b) the expression for  $\tilde{B}_{1\alpha}(\vec{k})$ , equation [A.2], can also be simplified:

$$\tilde{B}_{1\alpha}(\vec{k}) = \int_V B_{1\alpha}(\vec{r}) \phi_{\vec{k}}(\vec{r}) d^3r \approx \int_{UHS} B_{1\alpha}(\vec{r}) \phi_{\vec{k}} d^3r \quad [A.8]$$

where UHS signifies an integration over the upper half-space, *i.e.*,  $z \geq 0$ .

With these approximate expressions, we can now summarize the explicit calculation of  $T_{1G}^{-1}$ . The expression for the perturbation field is given by

$$B_{1+}(\vec{r}) = B_{d+}(\vec{r} + \hat{b}\vec{k}), \quad b > 0$$

where the dipolar field  $B_{d+}(\vec{r}) = B_{dx}(\vec{r}) + iB_{dy}(\vec{r})$ , is conveniently expressed by

$$B_{d+}(\vec{r}) = (3m/r^3)(-\sqrt{8\pi/15}) Y_{21}(\theta, \phi) . \quad [A.9]$$

With the approximations that have been made [A.5] becomes

$$\begin{aligned}
 \tilde{B}'_{1+}(\vec{k}) &= (2/V)^{\frac{1}{2}} \int_{\text{UHS}} \tilde{B}_{1+}(\vec{r}) e^{i\vec{k} \cdot \vec{r}} d^3 r \\
 &= (2/V)^{\frac{1}{2}} \int \Theta(z) B_{d+}(\vec{r} + b\hat{k}) e^{i\vec{k} \cdot \vec{r}} d^3 r \\
 &= (2/V)^{\frac{1}{2}} \int \Theta(z-b) B_{d+}(\vec{r}) e^{i\vec{k} \cdot (\vec{r}-b\hat{k})} d^3 r ,
 \end{aligned}$$

where

$$\Theta(z) = 0, \quad z < 0$$

$$= 1 \quad z > 1 .$$

Now it is convenient to use the Fourier representation of the theta function:

$$\Theta(z - b) = (2\pi)^{-3} \int d^3 k' e^{i\vec{k}' \cdot \vec{r}} \Theta(\vec{k}')$$

where

$$\Theta(\vec{k}') = (2\pi)^2 \delta(k'_x) \delta(k'_y) \left[ \frac{e^{-ik'_z b}}{i(k'_z - i\eta)} \right] , \quad [\text{A.10}]$$

and  $\eta = 0+$  is added for convergence.

Thus

$$\tilde{B}'_{1+}(\vec{k}) = (2/V)^{\frac{1}{2}} (2\pi)^{-3} \int d^3 k' I(\vec{k}, \vec{k}') \Theta(\vec{k}') , \quad [\text{A.11}]$$

where

$$I(\vec{k}, \vec{k}') = \exp(-ik_z b) \int d^3 r e^{i\vec{k} \cdot \vec{r}} B_{d+}(\vec{r}), \quad \vec{k} = \vec{k} + \vec{k}' .$$

Using the expansion

$$e^{i\vec{k} \cdot \vec{r}} = 4\pi \sum_{\ell, m} i^\ell Y_{\ell m}^*(\Omega) Y_{\ell m}(\Omega \vec{k}) j_\ell(kr) ,$$

where  $j_\ell(kr)$  is an  $\ell$ -th order spherical Bessel function, and the explicit form for  $B_{d+}$  [A.9] it is seen that

$$I(\vec{k}, \vec{k}') = 4\pi m (8\pi/15)^{\frac{1}{2}} Y_{21}(\Omega \vec{k}) e^{-ik_z b}$$

By substituting this and [A.10] into [A.11] an integral over  $k_z'$  results that may be readily evaluated by use of standard contour integration techniques. This yields

$$\tilde{B}_1^*(\vec{k}) = -2\pi m (2/V)^{\frac{1}{2}} \exp(ik_\phi - k_\rho b) (k_z + ik_\rho)^{-1}$$

where  $(k_\rho, k_\phi, k_z)$  are the cylindrical coordinates of  $\vec{k}$ .

Hence

$$\begin{aligned} |\tilde{B}_1(\vec{k})|^2 &= |\tilde{B}_1^*(\vec{k}) + \tilde{B}_1^*(-\vec{k})|^2 \\ &= (2/V) [4\pi m (k_\rho k_z / k^2) \exp(-k_\rho b)]^2 , \end{aligned} \quad [A.12]$$

where  $k^2 = k_z^2 + k_\rho^2$ .

This result may be substituted into [A.7] in order to obtain  $T_{1G}^{-1}$ . By letting  $u = bk_z$ ,  $v = bk_\rho$ ,  $\tau_b = b^2/D$ ,  $\alpha = \omega_0 \tau_b$ , and doing the trivial integration over  $k_\phi$ , we find

$$T_{1G}^{-1} = (2/V) \gamma^2 m^2 (D b)^{-1} \int_0^\infty dv e^{-2v} \int_{-\infty}^\infty du \frac{u^2}{(u^2 + v^2) [(u^2 + v^2)^2 + \alpha^2]} .$$

The integral over  $u$  may also be performed by use of contour integration

techniques with the result

$$T_{1G}^{-1} = (2\pi/V)\gamma^2 m^2 (Db)^{-1} \alpha^{-2} \int_0^\infty v^4 e^{-2v} \{2^{-\frac{1}{2}} [1 + (1 + \alpha^2 v^{-4})^{\frac{1}{2}}]^{\frac{1}{2}} - 1\} dv . \quad [A.13]$$

We can now make use of the fact that  $v^4 e^{-2v}$  is sharply peaked at  $v = 2$  to evaluate [A.13] in the limits  $\alpha \gg 1$  and  $\alpha \ll 1$  where approximate expressions for the factor in curly brackets may be used.

Considering first the case  $\alpha = \omega_0 \tau_b = \omega_0 b^2 / D \ll 1$ , we have

$$1/\sqrt{2} [1 + (1 + \alpha^2/v^4)^{\frac{1}{2}}]^{\frac{1}{2}} - 1 \approx \alpha^2/8v^4 ,$$

so that

$$T_{1G}^{-1} \approx \pi m^2 \gamma^2 / (8VDb) , \quad \omega_0 \ll D/b^2 . \quad [A.14]$$

This expression is valid if the condition  $\omega_0 \ll D/b^2$  is compatible with the requirement that  $|\vec{B}_1(\vec{r})| \ll B_0$ , i.e., that  $mb^{-3} \ll B_0$ . This compatibility is assured only if  $m \ll Db/\gamma$ . In Chap. 4 we assumed  $b \approx 0.1$  cm. Thus if  $D \approx 8 \times 10^{-5}$  cm<sup>2</sup> sec<sup>-1</sup>, we require  $m \ll 4 \times 10^{-10}$  G cm<sup>3</sup>. Since we estimated  $m \approx 2 \times 10^{-8}$  G cm<sup>3</sup> from the data it is clear that we would have not been able to experimentally verify [A.14]. In addition, the condition  $\omega_0 \ll D/b^2$  would require that  $B_0 \ll 4 \times 10^{-7}$  G, a value smaller than the ambient field of  $\sim 3$   $\mu$ G.

Now in the opposite limit,  $\omega_0 \gg D/b^2$ , we have

$$(1/\sqrt{2}) [1 + (1 + \alpha^2/v^4)^{\frac{1}{2}}]^{\frac{1}{2}} - 1 \approx \alpha^2/\sqrt{2} \beta .$$

Hence

$$T_{1G}^{-1} \approx 3\pi(\gamma m)^2 D^{\frac{1}{2}} / (4\sqrt{2} Vb^4 \omega_0^{3/2}) \quad [A.15]$$

This was the expression used in Chap. 4 in order to obtain an estimate of  $m$ .

## APPENDIX B

### FORMAL RELATIONSHIP BETWEEN $\overline{\vec{B}}_{loc}$ AND $\vec{M}$ FOR A UNIFORMLY MAGNETIZED REGION IN A PERFECTLY DIAMAGNETIC SHIELD

We consider a uniformly magnetized region  $R$  located entirely in a volume  $V$  bounded by a surface  $S$  (Fig. B.1). For purposes of this discussion we assume that there is no trapped flux through  $S$  and consider it to be perfectly diamagnetic for the low fields and frequencies that are of interest. We now wish to calculate the average local magnetic flux density,  $\overline{\vec{B}}_{loc}$ , that is seen by a nucleus in  $R$ .

To do this, we note that there are no currents in  $V$  so that the magnetic scalar potential may be used. Hence

$$\vec{H} = - \vec{\nabla} \phi_m ,$$

$$- \vec{\nabla} \cdot \vec{H} = \nabla^2 \phi_m = 4\pi \vec{\nabla} \cdot \vec{M} = - 4\pi \rho_m(\vec{r}) ,$$

where  $\rho_m = - \vec{\nabla} \cdot \vec{M}$  is the magnetic "charge" density. In our particular case, we are assuming  $\vec{M}(\vec{r}) = \vec{M}$  inside  $R$  and  $\vec{M}(\vec{r}) = 0$  everywhere else in  $V$ .

The problem therefore reduces to solving Poisson's equation,  $\nabla^2 \phi_m = - 4\pi \rho_m(\vec{r})$ , with the Neumann boundary condition on  $S$ :

$$(\partial \phi_m / \partial n)_S = 0 .$$

The solution to this problem may be formally expressed in terms of the Green's function for the problem,<sup>62</sup>

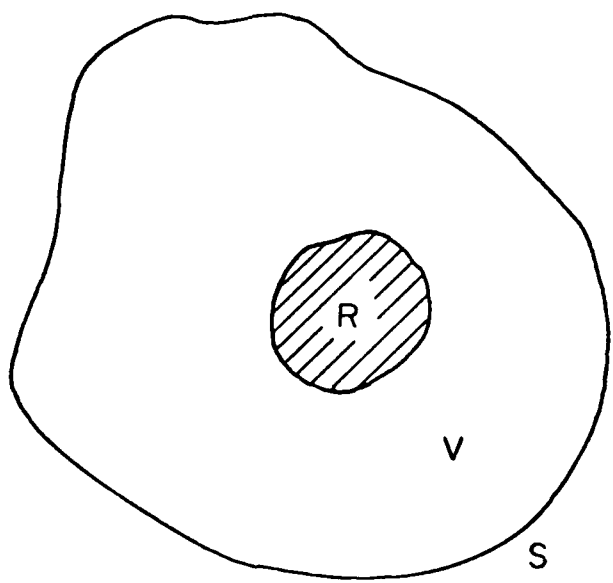


Fig. B.1 A uniformly magnetized region  $R$  located entirely in a volume bounded by a surface  $S$ .

$$\Phi_m(\vec{r}) = \int_V \rho_m(\vec{r}') G_N(\vec{r}, \vec{r}') d^3 r' + \overline{\Phi_m}_S \quad [B.1]$$

where  $\overline{\Phi_m}_S$  is the average of  $\Phi_m$  on  $S$ .

The Green's function in turn must satisfy

$$\nabla'^2 G_N(\vec{r}, \vec{r}') = -4\pi \delta(\vec{r} - \vec{r}')$$

with the boundary condition

$$\partial G_N(\vec{r}, \vec{r}') / \partial n' = -4\pi/s,$$

where  $s$  is the surface area of  $S$ . In general the Green's function has the form

$$G_N(\vec{r}, \vec{r}') = (|\vec{r} - \vec{r}'|)^{-1} + F(\vec{r}, \vec{r}')$$

where  $F$  is regular in  $V$ :  $\nabla'^2 F(\vec{r}, \vec{r}') = 0$ .

The boundary condition on  $G_N$  does not completely specify  $G_N$ ; i.e., if  $G_N$  satisfies the boundary condition, then  $G_N(\vec{r}, \vec{r}') + f(\vec{r})$  does also. Now since  $(\partial \Phi_m / \partial n)_S = 0$  implies that  $\int_V \rho_m(\vec{r}) d^3 r = 0$ , it is clear that this ambiguity has no effect on the expression for  $\Phi_m(\vec{r})$ . It does, however, have an effect on the symmetry (or reciprocity) of  $G_N(\vec{r}, \vec{r}')$ .

Since we would like to make use of this property (i.e.,  $G_N(\vec{r}, \vec{r}') = G_N(\vec{r}', \vec{r})$ ), we can be assured that this will be the case if the ambiguity in  $G_N$  is removed by requiring  $\oint_S G_N(\vec{r}, \vec{r}') ds' = 0$ . By using Green's second identity,

$$\int_V (\phi \nabla^2 \psi - \psi \nabla^2 \phi) d^3 r = \oint_S [\phi(\partial \psi / \partial n) - \psi(\partial \phi / \partial n)] ds,$$

and letting  $\phi = G_N(\vec{r}, \vec{u})$  and  $\psi = G_N(\vec{r}', \vec{u})$  it is readily seen that this

requirement implies that  $G_N(\vec{r}, \vec{r}') = G_N(\vec{r}', \vec{r})$ .

We may now proceed with the calculation by using equation [B.1].

Integrating by parts we have

$$\begin{aligned}\Phi_m(\vec{r}) &= \int_V [\nabla' \cdot \vec{M}(\vec{r}')] G_N(\vec{r}, \vec{r}') d^3 r' + \overline{(\Phi_m)}_S \\ &= - \int_V \nabla' \cdot [\vec{M}(\vec{r}')] G_N(\vec{r}, \vec{r}') d^3 r' + \int_V \vec{M}(\vec{r}') \cdot \vec{\nabla}' G_N(\vec{r}, \vec{r}') d^3 r' + \overline{(\Phi_m)}_S \\ &= \vec{M} \cdot \int_R \vec{\nabla}' G_N(\vec{r}, \vec{r}') d^3 r' + \overline{(\Phi_m)}_S.\end{aligned}$$

Inside  $R$ ,

$$\begin{aligned}\vec{B}_R &= \vec{H}_R + 4\pi \vec{M}_R = -R^{-1} \int_R \vec{\nabla} \Phi_m(\vec{r}) d^3 r + 4\pi \vec{M}_R \\ &= +4\pi \vec{M}_R - R^{-1} \int_R d^3 r \vec{\nabla} [\vec{M} \cdot \int_R \vec{\nabla}' G_N(\vec{r}, \vec{r}') d^3 r'] .\end{aligned}\quad [B.2]$$

Now as we have noted in Chap. 5, the local field seen inside of microscopic spherical cavity in  $R$  is given by

$$\vec{B}_{loc} = \vec{B}_R - (8\pi/3) \vec{M}_R .$$

Hence, from [B.2]

$$\vec{B}_{loc} = (4\pi/3) \vec{M}_R - R^{-1} \int_R d^3 r \vec{\nabla} [\vec{M} \cdot \int_R \vec{\nabla}' G_N(\vec{r}, \vec{r}') d^3 r'] .$$

Taking Cartesian components of this equation,

$$\begin{aligned}\overline{(\vec{B}_{loc})}_i &= (4\pi/3) M_i - R^{-1} \sum_j \left[ \int_R d^3 r \int_R d^3 r' \nabla_i \nabla'_j G_N(\vec{r}, \vec{r}') \right] M_j \\ &= \sum_j U_{ij} M_j ,\end{aligned}$$

where

$$U_{ij} = (4\pi/3) \delta_{ij} - R^{-1} \iint_R d^3 r d^3 r' \nabla_i \nabla'_j G_N(\vec{r}, \vec{r}') .$$

Now

$$\iint_R d^3r' d^3r \nabla_i \nabla_j G_N(\vec{r}, \vec{r}') = \iint_R d^3r d^3r' \nabla_i \nabla_j G_N(\vec{r}', \vec{r})$$
$$= \iint_R d^3r' d^3r \nabla_j \nabla_i G_N(\vec{r}, \vec{r}')$$

by the symmetry property of  $G_N(\vec{r}, \vec{r}')$ . Thus  $U_{ij} = U_{ji}$  as we wished to prove.

## APPENDIX C

### FIRST ORDER CALCULATION OF $\overline{\vec{B}}_{loc}$ IN A NEARLY SPHERICAL SAMPLE IN A NEARLY SPHERICAL SUPERCONDUCTING SHIELD

In this Appendix we will consider a specific example of the general situation discussed in Appendix B. In particular we will adopt the assumptions of Appendix B and will additionally assume that both  $R$  and  $V$  are nearly spherical and nearly concentric.

Inside  $R$ ,  $\overline{\vec{B}}_{loc}$  will be small compared to the macroscopic flux density,  $\vec{B} \approx 8\pi M/3$ . It is nonzero for two reasons: 1) asphericity in the sample cell, and 2) the presence of the superconducting shield.  $\overline{\vec{B}}_{loc}$  will not necessarily be uniform over  $R$ . Since we are only interested in the average of  $\overline{\vec{B}}_{loc}$  in a spherical volume, however, we will only be calculating the uniform component of  $\overline{\vec{B}}_{loc}$ . It is noteworthy that a gradient in  $M$  arising from a density gradient (due to, for example, a thermal gradient or the effect of gravity) does not affect  $\overline{\vec{B}}_{loc}$  as can be verified by direct calculation.

Outside of  $R$ , the field arising from the sample magnetization will be predominately dipolar. Higher multipole moments that arise due to sample asphericity or a magnetization gradient can affect  $\overline{\vec{B}}_{loc}$  only through interaction with imperfections in the superconducting shield. (The reasoning behind this statement will become apparent later in this appendix.) Since we are only interested in doing a first-order calculation these higher moments will be neglected. This neglect

of higher multipole moments allows the problem to be split to two:

First we will calculate  $\vec{B}_{loc}$  in a nearly spherical sample without the presence of the shield, and then the issue of a dipole in a nearly spherical superconducting shield will be considered separately.

### C.1 $\vec{B}_{loc}$ in a Nearly Spherical Sample

As in Appendix B, we may utilize the magnetic scalar potential  $\Phi_m(\vec{r})$  which is given by<sup>62</sup>

$$\Phi_m(\vec{r}) = - \vec{\nabla} \cdot \int_R \vec{M}(\vec{r}') |\vec{r} - \vec{r}'|^{-1} d^3 r' , \quad [C.1]$$

where  $\vec{H} = - \vec{\nabla} \Phi_m$ . Since we are assuming  $\vec{M}$  to be uniform in  $R$ ,  $\vec{\nabla} \cdot \vec{H} = 0$  everywhere in  $R$  except at the surface. Thus inside  $R$  we may write

$$\Phi_m(\vec{r}) = \sum_{\ell, m} A_{\ell m} r^{\ell} Y_{\ell m}(\theta, \phi) \quad [C.2]$$

where the reality of  $\Phi_m$  requires that  $A_{\ell -m} = (-1)^m A_{\ell m}^*$ . Combining [C.1] and [C.2],

$$\sum_{\ell, m} A_{\ell m} r^{\ell} Y_{\ell m}(\theta, \phi) = - \vec{M} \cdot \vec{\nabla} \int_R d^3 r' |\vec{r} - \vec{r}'|^{-1} .$$

Since we are interested in  $A_{1m}$  (which corresponds to the uniform component of  $\vec{H}$ ), we have

$$A_{1m} r = - \int_R d\Omega Y_{1m}^*(\Omega) [\vec{M} \cdot \vec{\nabla} \int_R d^3 r' |\vec{r} - \vec{r}'|^{-1}] . \quad [C.3]$$

At this point it is useful to express everything in terms of spherical vectors and spherical harmonics. Thus

$$\vec{M} \cdot \vec{\nabla} = M_0 \nabla_0 + \frac{1}{2} (M_+ \nabla_- + M_- \nabla_+)$$

where as usual  $M_0 = M_z$  and  $M_{\pm} = M_x \pm iM_y$ , and likewise for  $\vec{\nabla}$ . In addition, the well-known expansion for  $|\vec{r} - \vec{r}'|^{-1} = \vec{r} \cdot \vec{r}'^{-1}$  may be used:

$$|\vec{r} - \vec{r}'|^{-1} = 4\pi \sum_{kq} [r_<^k / r_>^{k+1} (2k+1)] Y_{kq}^*(\Omega') Y_{kq}(\Omega)$$

where  $r_>$  and  $r_<$  are the larger and smaller of  $|\vec{r}|$  and  $|\vec{r}'|$  respectively, and  $\Omega$  and  $\Omega'$  refer to the spherical angles specifying the orientations of  $\vec{r}$  and  $\vec{r}'$ . With these substitutions, [C.3] becomes

$$A_{1m} r = - \int d\Omega Y_{1m}^*(\Omega) [M_z \nabla_0 + \frac{1}{2}(M_+ \nabla_- + M_- \nabla_+)] 4\pi \sum_{kq} \frac{Y_{kq}(\Omega)}{2k+1} \cdot \int_R \frac{r_<^k}{r_>^{k+1}} Y_{kq}^*(\Omega') d^3 r' . \quad [C.4]$$

To proceed further, we may express  $\vec{\nabla}$  in terms of the angular momentum operator,  $\vec{L}$ :<sup>62</sup>

$$\vec{\nabla} = \hat{r} \partial / \partial r - (i/r^2) (\vec{r} \times \vec{L}) \quad [C.5]$$

where

$$\vec{L} = -i (\vec{r} \times \vec{\nabla}) . \quad [C.6]$$

With these expressions, it is not difficult to show that

$$\nabla_0 = \sqrt{\frac{4\pi}{3}} \left\{ Y_{10}(\Omega) \frac{\partial}{\partial r} - \frac{1}{\sqrt{2}r} [Y_{11}(\Omega) L_- + Y_{1-1}(\Omega) L_+] \right\} \quad [C.7a]$$

and

$$\nabla_{\pm} = \pm \sqrt{\frac{8\pi}{3}} \left\{ Y_{1\pm 1}(\Omega) \left[ -\frac{\partial}{\partial r} \pm \frac{1}{r} L_0 \right] + \frac{1}{\sqrt{2}r} Y_{10}(\Omega) L_{\pm} \right\} . \quad [C.7b]$$

Now from [C.4] we see that we need to evaluate integrals of the form

$$\int d\Omega Y_{1m}^*(\Omega) \nabla_i Y_{kq}(\Omega)$$

By use of the relations<sup>62</sup>

$$L_0 Y_{\ell m} = m Y_{\ell m} \quad [C.8a]$$

and

$$L_{\pm} Y_{\ell m} = \sqrt{(\ell \mp m)(\ell \pm m + 1)} Y_{\ell, m \pm 1} \quad [C.8b]$$

we see that integrals of this form can be decomposed further into terms containing the integrals

$$I_{1m1m'kq'} = \int d\Omega Y_{1m}^*(\Omega) Y_{1m'}(\Omega) Y_{kq'}(\Omega)$$

where  $m' + (q' - q) = i$ . Integrals of this type are readily evaluated:<sup>82</sup>

$$\begin{aligned} I_{\ell_3 m_3 \ell_2 m_2 \ell_1 m_1} &\equiv \int d\Omega Y_{\ell_3 m_3}^*(\Omega) Y_{\ell_2 m_2}(\Omega) Y_{\ell_1 m_1}(\Omega) \\ &= \sqrt{\frac{(2\ell_1 + 1)(2\ell_2 + 1)}{4\pi(2\ell_3 + 1)}} \langle \ell_1 \ell_2 00 | \ell_1 \ell_2 \ell_3 0 \rangle \cdot \\ &\quad \cdot \langle \ell_1 \ell_2 m_1 m_2 | \ell_1 \ell_2 \ell_3 m_3 \rangle, \end{aligned} \quad [C.9]$$

where the quantities in the angle brackets are the usual angular momentum coupling coefficients. By use of the triangle rule and parity, we see that  $I_{1m1m'kq'}$  can be nonzero only when  $k = 0, 2$ . It is also required that  $m' + q' = m$  or that  $m = i + q$ .

Having obtained these results, we now turn our attention to the last integral in the expression [C.4]:

$$\begin{aligned} J_{kq} &\equiv \int_R (r_<^k / r_>^{k+1}) Y_{kq}^*(\Omega') d^3 r' \\ &= \int Y_{kq}^*(\Omega') d\Omega' \int_0^R r'^2 (r_<^k / r_>^{k+1}) dr' \end{aligned}$$

where  $R_o(\Omega')$  specifies the radius of the surface at  $\theta', \phi'$ . For example, in the case  $k = 2$ , we have

$$J_{2q} = r^2 \int Y_{2q}^*(\Omega') d\Omega' \{1/5 + \ln[R_o(\Omega')/r]\} .$$

If we now specify  $R_o(\Omega')$  by its expansion in spherical harmonics,

$$R_o(\Omega') = R_o [1 + \sum_{\substack{\ell=1 \\ m}} \alpha_{\ell m} Y_{\ell m}(\Omega')] ,$$

where

$$\alpha_{\ell m} = (-1)^m \alpha_{\ell m}^*, \quad |\alpha_{\ell m}| \ll 1 ,$$

then

$$\ln R_o(\Omega') \approx \ln R_o + \sum_{\substack{\ell=1 \\ m}} \alpha_{\ell m} Y_{\ell m}(\Omega')$$

to first order. To this approximation, we then find  $J_{2q} = \alpha_{2q} r^2$ .

Likewise, the case  $k = q = 0$  may be evaluated to obtain

$$J_{00} = \sqrt{\pi} (R_o^2 - r^2/3) \text{ to first order.}$$

Having thus shown that only  $\alpha_{2m}$  have any effect on the result, we will now simplify the situation even further by considering that only  $\alpha_{20}$  is nonzero. This corresponds to a deformation of the spherical sample cell to a spheroid with the  $z$  axis as the axis of symmetry. The spheroid is prolate if  $\alpha_{20} > 0$  and oblate if  $\alpha_{20} < 0$ . With this simplification, carrying out the necessary algebra yields

$$A_{10} = -4\pi M_o \left( -\frac{2}{3} \sqrt{\frac{\pi}{3}} + \sqrt{\frac{4}{15}} \alpha_{20} \right) , \quad [C.10a]$$

$$A_{11} = -2\pi M_o \left( \frac{2}{3} \sqrt{\frac{2\pi}{3}} + \sqrt{\frac{2}{15}} \alpha_{20} \right) , \quad [C.10b]$$

$$A_{1-1} = -A_{11}^* .$$

Substitution of this result into [C.2] yields the desired component of  $\Phi_m(\vec{r})$ . It is convenient at this point to revert to Cartesian vectors. Doing this we have

$$\Phi_m^{(1)}(\vec{r}) = -\vec{H} \cdot \vec{r} ,$$

where  $\Phi_m^{(1)}$  is the  $\ell = 1$  component of  $\Phi_m$  and

$$\vec{H}_x = \sqrt{3/2\pi} \operatorname{Re} A_{11}$$

$$\vec{H}_y = -\sqrt{3/2\pi} \operatorname{Im} A_{11}$$

[C.11]

$$\vec{H}_z = -\sqrt{3/4\pi} A_{10}$$

Using the expressions for  $A_{10}$  and  $A_{11}$  given by equations [C.10] we have the result

$$\vec{H} = - (4\pi/3) \vec{M} + Q_C \vec{M} ,$$

where

$$Q_C = 4 \sqrt{\pi/5} \alpha_{20} \begin{pmatrix} -\frac{1}{2} & 0 & 0 \\ 0 & -\frac{1}{2} & 0 \\ 0 & 0 & 1 \end{pmatrix} . \quad [C.12]$$

In addition, since we have seen in Appendix B that  $\vec{B}_{\text{loc}} = \vec{H} + (4\pi/3) \vec{M}$

$$\vec{B}_{\text{loc}} = Q_C \vec{M} .$$

It should be noted that the same result may be obtained by considering a uniformly magnetized ellipsoid that differs only slightly from a sphere. In the case of an ellipsoid, of course, the internal field is always uniform no matter how pronounced the deviation from sphericity.

### C.2 Dipole in a Nearly Spherical Superconducting Shield

We now consider the case of a dipole  $\vec{m} = (4\pi R_0^3/3) \vec{M}$  located near the center of a nearly spherical, perfectly diamagnetic shield of mean radius  $R_{S0}$ . For our present purposes, we consider  $\vec{m}$  to be a point dipole and ignore the susceptibility of any materials located inside of the shield.

The calculation of the "reflected" field  $\vec{H}_r = -\vec{\nabla}\phi_{mr}$  that arises due to the presence of the shield may be approached in much the same manner as the previous calculation. We start with

$$\Phi_m(\vec{r}) = \sum_{\ell,m} [A_{\ell m}(r/R_{S0})^\ell + B_{\ell m}(r/R_{S0})^{-(\ell+1)}] Y_{\ell m}(\theta, \phi) .$$

With a dipole at the origin, all  $B_{\ell m}$  are zero except

$$B_{10} = R_{S0}^{-2} \sqrt{4\pi/3} m_z$$

$$B_{11} = -R_{S0}^{-2} \sqrt{2\pi/3} (m_x - im_y)$$

$$B_{1-1} = -B_{11}^* .$$

Thus

$$\Phi_m(\vec{r}) = \sum_m B_{1m}(R_{S0}/r)^2 Y_{1m}(\theta, \phi) + \sum_{\ell,m} A_{\ell m}(r/R_{S0})^\ell Y_{\ell m}(\theta, \phi) , \quad [C.13]$$

where we are specifically interested in determining

$$\Phi_{mr}^{(1)} = \sum_m A_{1m}(r/R_{S0}) Y_{1m}(\theta, \phi) ,$$

i.e., the coefficients  $A_{1m}$ .

The boundary condition  $(\hat{n} \cdot \vec{\nabla}\phi_{mr})_S = 0$ , where  $\hat{n}$  is the unit normal

to the surface S, must now be expressed in a useful form. We take S to be given by  $r = R_S(\theta, \phi)$  where

$$R_S = R_{S0} [1 + \sum_{\substack{\ell=1 \\ m}} \beta_{\ell m} Y_{\ell m}(\theta, \phi)] , \quad [C.14]$$

and as usual  $|\beta_{\ell m}| \ll 1$ ,  $\beta_{\ell -m} = (-1)^m \beta_{\ell m}^*$ . Letting

$$f(r, \theta, \phi) \equiv r - R_S(\theta, \phi)$$

so that

$$\hat{n} = (\vec{\nabla}f / |\vec{\nabla}f|)_{r=R_S} ,$$

the boundary condition may be written

$$(\vec{\nabla}f \cdot \vec{\nabla}\Phi_m)_{r=R_S} = 0 . \quad [C.15]$$

By expressing the  $\vec{\nabla}$  operator in terms of the angular momentum operator (equations [C.5] and [C.6]) the boundary condition [C.15] may be expressed in the form

$$R_S (\partial\Phi_m / \partial r)_{R_S} = R_S^{-1} [(\vec{L}f) \cdot (\vec{L}\Phi_m)]_{r=R_S} \quad [C.16]$$

where we have made use of the fact that both  $\vec{r} \cdot \vec{L}$  and  $\hat{r} \cdot (\vec{r} \times \vec{L})$  are zero.

Now

$$\vec{L}f = -R_{S0} \sum_{\substack{\ell=1 \\ m}} \beta_{\ell m} \vec{L}Y_{\ell m} ,$$

$$\vec{L}\Phi_m = \sum_m B_{1m} (R_{S0}/r)^2 \vec{L}Y_{1m}(\theta, \phi) + \sum_{\ell m} A_{\ell m} (r/R_{S0})^{\ell} \vec{L}Y_{\ell m}(\theta, \phi) ,$$

and

$$\begin{aligned}\frac{\partial \Phi_m}{\partial r} &= R_{S0}^{-1} \sum_m [A_{1m} - 2B_{1m}(R_{S0}/r)^3] Y_{1m}(\theta, \phi) \\ &+ R_{S0}^{-1} \sum_{\ell=2}^{\infty} \ell A_{\ell m} (r/R_{S0})^{\ell-1} Y_{\ell m}(\theta, \phi) .\end{aligned}$$

Thus, by substituting these expressions in [C.16] we see that if  $\beta_{\ell m} = 0$  for all  $\ell, m$  (i.e., the shield is perfectly spherical) then it is necessary that  $A_{1m}^0 = 2B_{1m}$ ,  $A_{\ell m}^0 = 0$ ,  $\ell \geq 2$ . As a result,  $(A_{1m} - A_{1m}^0)$  and all of the other  $A_{\ell m}$  are expected to be small if the  $\beta_{\ell m}$  are small. It is therefore convenient to define the small parameters  $A'_{\ell m}$ , where

$$A'_{1m} = A_{1m} - A_{1m}^0 = A_{1m} - 2B_{1m}$$

and

$$A'_{\ell m} = A_{\ell m}, \quad \ell \geq 2 .$$

By expressing  $\vec{L}f$ ,  $\vec{L}\Phi_m$  and  $\partial\Phi_m/\partial r$  in terms of these new parameters, we may easily obtain  $A'_{1m}$  to first order by 1) evaluating the boundary condition at  $r = R_{S0}$  (instead of  $R_S$ ), and 2) ignoring products involving  $A'_{\ell m} \beta_{kq}$  since they are second order. Hence [C.16] yields

$$\sum_m A'_{1m} Y_{1m} + \sum_{\ell=2}^{\infty} \ell A'_{\ell m} Y_{\ell m} = -3 \sum_{k=1}^{\infty} \sum_m \beta_{kq} B_{1m} (\vec{LY}_{\ell m}) \cdot (\vec{LY}_{kq}) \quad [C.17]$$

Multiplying [C.17] by  $Y_{1m}^*$ , and integrating yields the desired expression for  $A'_{1m}$ :

$$A'_{1m} = -3 \sum_{k=1}^{\infty} \sum_m \beta_{kq} B_{1m} \int d\Omega Y_{1m}^*(\Omega) \vec{LY}_{kq}(\Omega) \cdot \vec{LY}_{1m}(\Omega) . \quad [C.18]$$

The scalar product of the spherical vector harmonics is given by

$$(\vec{LY}_{kq}) \cdot (\vec{LY}_{1m}) = \frac{1}{2}(L_+ Y_{kq} L_- Y_{1m} + L_- Y_{kq} L_+ Y_{1m}) + L_0 Y_{kq} L_0 Y_{1m},$$

which may be evaluated by equations [C.8] and the consequent integrals are then given by [C.9]. We immediately infer from the triangle rule and parity that only the  $k = 2$  terms survive and that of these terms we must have  $m + q = m'$ .

An important consequence of this result is that the centering of the shield (which corresponds to the  $Y_{1m}$  term in the expression for  $R_S$ ) has no effect in first order and is therefore not as important as the quadrupolar error.

At this point we again choose as an illustration the case where only  $\beta_{20}$  is nonzero. Thus  $m' = m$ , and we obtain

$$A'_{10} = (9/\sqrt{5\pi})\beta_{20} B_{10},$$

$$A'_{1\pm 1} = - (9/2\sqrt{5\pi})\beta_{20} B_{1\pm 1}.$$

Substituting the resulting values for  $A'_{1m} = A'_{1m} + 2B_{1m}$  into [C.13] and returning to the Cartesian representation we find for the "reflected" field that

$$\vec{H}_r(r = 0) = - (8\pi/3)(R_0/R_{S0})^3 \vec{M} + Q_S \vec{M},$$

where

$$Q_S = - 12\sqrt{\pi/5} (R_0/R_{S0})^3 \beta_{20} \begin{pmatrix} -\frac{1}{2} & 0 & 0 \\ 0 & -\frac{1}{2} & 0 \\ 0 & 0 & 1 \end{pmatrix}$$

## REFERENCES

1. A. Abragam, *The Principles of Nuclear Magnetism* (Oxford University Press, Oxford, 1961).
2. B. S. Deaver and W. M. Fairbank, Phys. Rev. Lett. 7, 43 (1961).
3. R. Doll and M. Näbauer, Phys. Rev. Lett. 7, 51 (1961).
4. W. M. Fairbank and W. O. Hamilton, *Proceedings of the Xth International Conference on Low Temperature Physics*, ed. by N. V. Zavaritsky and I. P. Krylov, (Moscow, 1967), vol IIB, p. 327.
5. L. Landau, Nucl. Phys. 3, 127 (1957).
6. For a more extensive general review of EDM theory and experiments with an emphasis on neutrons, the reader is referred to R. Golub and J. M. Pendelbury, Contemp. Phys. 13, 519 (1972). Ref. 8 also provides a useful overview.
7. J. H. Christenson, J. W. Cronin, V. L. Fitch, and R. Turlay, Phys. Rev. Lett. 13, 138 (1964).
8. W. B. Dress, P. D. Miller, J. M. Pendelbury, P. Perrin, and N. F. Ramsey, Phys. Rev. D 15, 9 (1977).
9. M. C. Weisskopf, J. P. Carrico, H. Gould, E. Lipworth, and T. S. Stein, Phys. Rev. Lett. 21, 1645 (1968).
10. M. A. Player and P. G. H. Sandars, J. Phys. B3, 1630 (1970).
11. G. E. Harrison, P. G. H. Sanders, and S. J. Wright, Phys. Rev. Lett. 22, 1263 (1969).
12. I. B. Khriplovich, Zh. Eksp. Teor. Fiz. 71, 51 (1976). [Eng. Trans: Sov. Phys. JETP 44, 25 (1976).]
13. L. I. Schiff, Phys. Rev. 132, 2194 (1963).
14. F. D. Colegrove, L. D. Schearer, and G. K. Walters, Phys. Rev. 132, 2561 (1963).
15. Besides ref. 14, the review by W. Happer, Rev. Mod. Phys. 44, 169 (1972) provides useful references.
16. B. Cabrera, *Proceedings of the 14th International Conference on Low Temperature Physics*, M. Krusius and M. Vuorio, eds. (North Holland Publishing Co., Amsterdam, 1975), vol. 4, p. 270.

17. B. Cabrera, Ph.D. Thesis, Stanford University, 1975 (unpublished).
18. B. Cabrera, Rev. Sci. Instr. (to be published).
19. F. London, *Superfluids* (Dover, New York, 1961) vol. I, pp. 78-82.
20. S.H.E. Corp., Model 330X SQUID system.
21. J. E. Zimmerman, P. Thiene, and J. T. Harding, J. Appl. Phys. 41, 1572 (1970).
22. R. P. Giffard, R. A. Webb, and J. C. Wheatley, J. Low Temp. Phys. 6, 533 (1972).
23. J. Clarke, W. M. Goubau, and M. B. Ketchen, J. Low Temp. Phys. 25, 99 (1976).
24. E. P. Horvitz, Phys. Rev. A1, 1708 (1970).
25. See, for example, the collection of papers on NMR in liquid  $\text{He}^3$  in *Helium Three*, J. G. Daunt, ed. (Ohio State Univ. Press, Columbus, 1960).
26. R. H. Romer, Phys. Rev. 115, 1415 (1959).
27. R. H. Romer, Phys. Rev. 117, 1183 (1960).
28. W. A. Fitzsimmons, L. L. Tankersley, and G. K. Walters, Phys. Rev. 179, 156 (1969).
29. H. H. McAdams, Phys. Rev. 170, 276 (1968).
30. R. S. Timsit, J. M. Daniels, and A. D. May, Can. J. Phys. 49, 560 (1971).
31. R. Chapman and M. G. Richards, Phys. Rev. Lett. 33, 18 (1974).
32. R. Barbé, F. Laloë, and J. Brossel, Phys. Rev. Lett. 34, 1488 (1975).
33. R. Barbé, "Thèse de Doctorat d'Etat, Paris (1977)", Laboratoire de l'Ecole Normale Supérieure.
34. C. Cohen-Tannoudji, J. Dupont-Roc, S. Haroche, and F. Laloë, Phys. Rev. Lett. 22, 758 (1969).
35. R. C. Greenhow, Phys. Rev. 3A, 660 (1964).
36. D. F. Brewer, D. C. Champeny, and K. Mendelssohn, Cryogenics 1, 108 (1960).

37. West Coast Technical Service, Inc., Cerritos, Calif.
38. Delrin is the trademark of E. I. DuPont Nemours and Co., Inc., for polyformaldehyde thermoplastic.
39. J. H. Claassen, J. Appl. Phys. 46, 2268 (1975).
40. See, for example, W. G. Jung, *IC Op-Amp Cookbook* (Howard W. Sams and Co., Inc., Indianapolis, 1974).
41. M. W. Garrett, J. Appl. Phys. 22, 1091 (1951).
42. H. A. Fairbank, Phys. Rev. 71, 911 (1947). The quoted result was obtained on a sample having a  $\text{He}^3$  concentration of  $1.2 \times 10^{-6}$ .
43. D. B. Mann, *The Thermodynamic Properties of Helium from 3 to 300° K between 0.5 and 100 Atmospheres: NBS Technical Note 154* (U. S. Government Printing Office, Washington, D.C., 1962).
44. The particular technique that was adopted for the  $T_1$  measurements was suggested by R. C. Taber.
45. D. Kleppner, H. M. Goldenberg, and N. F. Ramsey, Phys. Rev. 116, 603 (1962).
46. L. D. Schearer and G. K. Walters, Phys. Rev. 139, A1398 (1965).
47. R. Barbé, M. Leduc, and F. Laloë, J. Phys. (Paris) 35, 699 (1974).
48. See, for example, A. M. Yaglom, *An Introduction to the Theory of Stationary Random Functions* (Dover Publications, Inc., New York, 1962).
49. H. C. Torrey, Phys. Rev. 104, 563 (1956).
50. N. Bloembergen, E. M. Purcell, and R. V. Pound, Phys. Rev. 73, 679 (1948).
51. P. S. Hubbard, Rev. Mod. Phys. 33, 249 (1961).
52. H. C. Torrey, Phys. Rev. 92, 962 (1953). Some of the expressions in this paper are incorrect due to an error originating in ref. 50. An extended and corrected version can be found in ref. 54.
53. I. Oppenheim and M. Bloom, Can. J. Phys. 39, 845 (1961).
54. J. F. Harmon and B. H. Muller, Phys. Rev. 182, 400 (1969).
55. See, for example, J. G. Dash, *Films on Solid Surfaces* (Academic Press Inc., New York, 1975).

56. D. F. Brewer, *J. Low Temp. Phys.* 3, 205 (1970).
57. See, for example, F. J. Low and H. E. Rohrschach, *Phys. Rev.* 120, 1111 (1960).
58. W. J. Mullin, D. J. Creswell, and B. Cowan, *J. Low Temp. Phys.* 25, 247 (1976).
59. A. A. Kokin and A. A. Ismest'ev, *Zhur. Fiz. Khimii* 39, 577 (1965); *Trans: Russ. J. Phys. Chem.* 39, 309 (1965).
60. D. Beckert, *Ann. Physik* 20, 220 (1967); *Ann. Physik* 23, 98 (1969).
61. R. Chapman and M. Bloom, *Can. J. Phys.* 54, 861 (1976).
62. See, for example, J. D. Jackson, *Classical Electrodynamics* (John Wiley and Sons, Inc., New York, 1962).
63. P. R. Bevington, *Data Reduction and Error Analysis for the Physical Sciences* (McGraw-Hill Book Co., New York, 1969).
64. L. D. Landau and E. M. Lifshitz, *Fluid Mechanics* (Pergamon Press, Oxford, 1959).
65. See, for example, M. A. Egginton and M. A. Moore, *J. Low Temp. Phys.* 15, 99 (1974) for a brief discussion of this effect and further references.
66. J. H. Claassen, *J. Appl. Phys.* 46, 2268 (1975).
67. F. W. Grover, *Inductance Calculations* (Dover, New York, 1946).
68. See, for example, H. Goldstein, *Classical Mechanics* (Addison-Wesley, Reading, Mass. 1950).
69. V. Radeka, *IEEE Trans. Nucl. Sci.* NS-16, 17 (1969).
70. Bateman Manuscript Project, *Tables of Integral Transforms*, A. Erdélyi, ed. (McGraw-Hill, New York, 1954) vol. I.
71. See, for example, F. N. H. Robinson, *Noise and Fluctuations* (Clarendon Press, Oxford, 1974) Chap. 2.
72. N. R. Campbell, *Proc. Cambridge Phil. Soc.* 15, 117 (1909). This theorem is also discussed in ref. 71.
73. C. Blank and M. H. Edwards, *Phys. Rev.* 119, 50 (1960).
74. J. E. Opfer, K. Luszczynski, and R. E. Norberg, *Phys. Rev.* 172, 192 (1968).

75. A. D. Whalen, *Detection of Signals in Noise* (Academic Press, New York, 1971).
76. G. K. White and J. A. Birch, *Phys. Chem. Glasses* 6, 85 (1965).
77. See, for example, E. A. Lynton, *Superconductivity* (Methuen, London, 1969), 3rd ed..
78. B. W. Maxfield and W. L. McLean, *Phys. Rev.* 139, A1515 (1965).
79. B. J. Marshall, R. Johnson, D. Follstaedt, and J. Randorff, *Rev. Sci. Instr.* 40, 375 (1969).
80. A. von Hippel and R. J. Maurer, *Phys. Rev.* 59, 820 (1941).
81. This result may be obtained by use of oblate spheroidal coordinates as explicated, for example, by W. R. Smythe, *Static and Dynamic Electricity* (McGraw-Hill, New York, 1950).
82. See, for example, E. Merzbacher, *Quantum Mechanics* (John Wiley, New York, 1961), Chap. 22.